TECHNICAL REPORT STANDARD PAGE

1. Report No.	2. Government Accession No.	3. Recipient's Catalog No.
FHWA/LA.14/529		

4. Title and Subtitle	5. Report Date
Structural Health Monitoring of I-10 Twin Span Bridge – Part I: Analysis of Lateral Load Test	November 2014
	6. Performing Organization Code LTRC Project Number: 07-1ST/8-3GT State Project Number: 736-99-1437

7. Author(s)	8. Performing Organization Report No.
Murad Y. Abu-Farsakh, Sungmin Yoon, Xinbao Yu, and Xiaochao Tang	

9. Performing Organization Name and Address	10. Work Unit No.
Department of Civil and Environmental Engineering Louisiana State University Baton Rouge, LA 70803	11. Contract or Grant No.

12. Sponsoring Agency Name and Address	13. Type of Report and Period Covered
Louisiana Department of Transportation and Development P.O. Box 94245 Baton Rouge, LA 70804-9245	**Final Report** **November 2007 – December 2013**
	14. Sponsoring Agency Code

15. Supplementary Notes

Conducted in Cooperation with the U.S. Department of Transportation, Federal Highway Administration

16. Abstract

The old I-10 Twin Span Bridge over Lake Pontchartrain was heavily damaged by the storm surges during Hurricane Katrina in 2005. A new 5.4-mile long replacement bridge was constructed with higher resistance to extreme events, such as storm surges and ship impacts. During the construction, a structural health monitoring system, including both superstructure and substructure, was implemented to study the lateral response of battered pile groups short-term and to monitor the "health" condition of the new bridge long-term. M19 pier on the main span of east bound, the second highest pier of the bridge, was selected to perform an in-situ large scale static lateral load test. The pier foundation consists of 24 square 3-ft. precast prestressed concrete (PPC) driven piles battered at 1:6 with an average embedment length of 87 ft. Among them, 8 piles were instrumented with micro electro mechanical systems (MEMS) In-Place Inclinometers (IPI) to monitor pile deflections. 12 piles were instrumented with sister bar type of strain gauges at two selected locations along the pile length to monitor moment and axial force. Other instruments also include triaxial accelerometers, tiltmeters, water pressure cells, and corrosion meters. A lateral load test was conducted by pulling two high strength steel strand tendons through the west bound and east bound M19 piers with hydraulic jacks; the lateral load was applied in 19 increments with a maximum load of 1870 kips.

A high-order-polynomial curve fitting method was selected to best-fit the measured rotation profiles by IPI. From the fitted rotation profiles, bending moments, shear forces, and soil reactions were derived using the classic beam theory. P-y curves were obtained from the derived soil reaction profiles and deflection profiles. The back-calculation results were verified with the measurement data from IPI and strain gauges. FB-MultiPier was used for the analysis of pier behaviors in the design of the I-10 Bridge. Therefore, it was selected to simulate the pier response during the lateral load test and verify its performance with measured data and results from the back-calculation. A sensitivity analysis of the input parameters for FB-MultiPier was first conducted to help make decisions on selecting design parameters. Based on the analysis on the simulation results, a select set of inputs were presented as a reference for the design of similar battered pile group in the future.

17. Key Words	18. Distribution Statement
	Unrestricted. This document is available through the National Technical Information Service, Springfield, VA 21161.

19. Security Classif. (of this report)	20. Security Classif. (of this page)	21. No. of Pages	22. Price
		165	

Project Review Committee

Each research project will have an advisory committee appointed by the LTRC Director. The Project Review Committee is responsible for assisting the LTRC Administrator or Manager in the development of acceptable research problem statements, requests for proposals, review of research proposals, oversight of approved research projects, and implementation of findings.

LTRC appreciates the dedication of the following Project Review Committee Members in guiding this research study to fruition.

LTRC Administrator/Manager

Zhongjie (Doc) Zhang

Pavement & Geotechnical Research Administrator

Members

Chris Nickel

Arthur D'Andrea

Jenny Fu

Arturo Aguirre

Gavin Gautreau

Directorate Implementation Sponsor

Janice P. Williams, P.E.

DOTD Chief Engineer

Structural Health Monitoring of I-10 Twin Span Bridge

by

Murad Y. Abu-Farsakh
Sungming Yoon
Xinbao Yu
and
Xiaochao Tang

Louisiana Transportation Research Center
4101 Gourrier Avenue
Baton Rouge, LA 70808

LTRC Project No. 07-1ST/08-3GT
State Project No. 736-99-1437

conducted for

Louisiana Department of Transportation and Development
Louisiana Transportation Research Center

November 2014

ABSTRACT

The old I-10 Twin Span Bridge over Lake Pontchartrain was heavily damaged by the storm surges associated with Hurricane Katrina that hit southern Louisiana in August of 2005. A new 5.4-mile long replacement bridge was constructed with higher resistance to extreme events such as storm surges and ship impacts. During construction, a structural health monitoring system, including both substructure and superstructure instrumentations, was installed to study the short-term lateral response of the battered pile groups during a static lateral load test and to monitor the long-term structural "health" condition of the new bridge. The M19 pier on the east bound main span, the second highest pier of the bridge, was selected to perform an in-situ large scale static lateral load test. The pier foundation consists of 24 square 3-ft. precast prestressed concrete (PPC) driven piles battered at 1:6 with an average embedment length of 87 ft. The substructure monitoring system includes instrumenting 8 piles with micro electro mechanical systems (MEMS) In-Place Inclinometers (IPI) to monitor the piles' deflections, instrumenting 12 piles with sister bar strain gauges at two selected locations along the pile length to measure the moments and axial forces, and instrumenting the pile-cap with accelerometers and tiltmeters, water pressure cells, and corrosion meters. The superstructure monitoring system includes instrumenting the columns, bent cap, steel girders, concrete girders, and one diaphragm with strain gauges and corrosion meters. An Osmos type weigh in motion (WIM) system was also installed at the concrete bridge deck of the M19 pier to capture the traffic live loads for the three lanes.

The substructural monitoring system was used to monitor the bridge response during the unique static lateral load test. The load test was conducted by pulling two high strength steel strand tendons through the west bound and east bound M19 piers with hydraulic jacks; the lateral load was applied in 19 increments with a maximum lateral load of 1870 kips.

A high-order-polynomial curve fitting method was selected to best-fit the measured rotation profiles by the IPIs. Then from the fitted rotation profiles, the bending moments, shear forces, and soil reactions were derived using classic beam theory. The p-y curves were obtained from the derived soil reaction profiles and the deflection profiles. The back-calculation results were verified with the measurement data from IPIs and strain gauges.

The FB-MultiPier software was used in the design and analysis of the pile group foundation of the I-10 Twin Span Bridge. Therefore, the FB-MultiPier was selected to simulate the response of M19 pier during the lateral load test and to verify its performance with the measured data and results from the back-calculation. A sensitivity analysis of the input parameters for FB-MultiPier was first conducted to help make decisions on selecting design

parameters. Based on the analysis of the simulation results, a select set of inputs were presented as a reference for the design of similar battered pile groups in the future.

ACKNOWLEDGMENTS

This research project is funded by the Federal Highway Administration (FHWA) through the Innovative Bridge Research and Deployment (IBRD) Program, the Louisiana Department of Transportation and Development (State Project Nos. 736-99-1437 and 736-99-1507) and the Louisiana Transportation Research Center (LTRC Project Nos. 07-1ST and 08-3GT). The field instrumentation was conducted by Geocomp Corporation. The help and support provided by Allen Marr, Da Ha, and Tom Weinmann Geocomp Corporation are highly appreciated. The comments and suggestions of Zhongjie (Doc) Zhang and Mark Morvant of LTRC are gratefully acknowledged.

The principal investigators extend their acknowledgements to the DOTD bridge design group for the supply of FB-MultiPier program.

IMPLEMENTATION STATEMENT

A structural health monitoring system (including both superstructure and substructure instrumentation) was installed at the M19 eastbound pier of the new I-10 Twin Span Bridge for short-term monitoring of the bridge during the lateral load test and for long-term monitoring of the structural health condition of the bridge. A unique lateral load test was designed and conducted at a selected M19 eastbound pier to verify the analysis method used to design the battered pile group foundation of the new bridge using the FB-MultiPier software. The substructure system was activated and used to monitor the M19 pier during the lateral load test. The piles' responses were monitored using the instrumented MEMS in-place inclinometers and strain gages. In addition, the horizontal movement of the cap was monitored using an automated survey station with prisms.

Based on the results and analysis of the lateral load test, it is recommended that DOTD bridge design engineers consider implementing less conservative p-multipliers (e. g., 0.9, 0.8, 0.8, and 0.7 for the 1^{st}, 2^{nd}, 3^{rd}, and 4^{th} row piles, respectively) when using the FB-MultiPier software for analysis and design of battered pile group foundations subjected to lateral loading.

It is recommended that DOTD bridge design engineers consider using the modified FB-MultiPier meshes (using single or multiple artificial shear wall beam shell elements to simulate rigidity of pile cap) presented at the end of this report, for modeling the pile cap and compare the results with the traditional model (the center of pile cap is rigidly connected to pile head using linear shell element) used by DOTD engineers. The discrepancies between the field measurements and the results from the FB-MultiPier analysis can be affected by the finite element model used in the analysis.

It is recommended that DOTD start applying a procedure to implement the effect of pile installation and the subsequent soil densification, consolidation, and setup in the analysis and design of battered pile group foundations. The effect of the pile installation can be incorporated through increasing the soil strength parameters, such as undrained shear strength, by a certain percentage (e. g., 20%).

TABLE OF CONTENTS

LIST OF TABLES

LIST OF FIGURES

INTRODUCTION

On August 29, 2005, the existing interstate I-10 Twin Span Bridge that crosses Lake Pontchartrain between New Orleans and Slidell sustained serious damage from the storm surge due to Hurricane Katrina, a Category 3 hurricane that hit the southern part of Louisiana with sustained winds of 125 mph. One year after, construction of a new $803-million federally funded replacement bridge began in August 2006. The new bridge was designed with a higher capability to withstand extreme events such as hurricane storm surges and ship impacts. The I-10 Twin Span Bridge, with a design life of 100 years, is around 5.4-miles long and located 300 ft. to the east of the old bridge. The new bridge was built entirely with high-performance concrete to resist salt water corrosion and has an elevation of 30 feet, which is 21 feet higher than the old bridge, and an 80-foot high-rise section near the Slidell side to allow for marine traffic, making it less susceptible to high storm surge. The new bridge is supported by battered pile groups consisting of 24 battered precast, pre-stressed concrete driven piles with high lateral resistance to prevent hurricane surges and ship impacts. The bridge consists of two parallel structures with three 12-ft. travel lanes and two 12-ft. shoulders on each side (60 ft. wide), allowing for a 50 percent increase in the traffic volume.

The adoption of a battered pile group as foundation support has the challenge of lacking design experience and the performance of the design battered pile groups by the software FB-MultiPier needs to be verified and calibrated. To address several questions raised during the design phase of the project, DOTD decided to install a substructure and superstructure health monitoring system on a selected bridge pier (M19 eastbound) at the main span for short-term and long-term monitoring of the bridge that can collect data such as acceleration, water pressure, strains, and lateral deformations of the piles, pile caps, columns, bent caps, girders, and concrete slab that result from strong wind, waves, and vessel collision loads. Additionally, a weight-in-motion (WIM) system by OSMOS was installed to determine truck loads on the eastbound bridge.

The focus of the short-term goal of the substructure monitoring is on the lateral load testing of the M19 eastbound pier. A large scale in-situ lateral load test was performed on the well instrumented pier-cap-pile system to study the system behavior under simulated lateral loads such as ship impacts and hurricane storm surges. An important task of the lateral load tests was to verify the design software FB-MultiPier currently used by the DOTD for its capability of designing battered pile groups, whereas the software was developed primarily based on the load test results of vertical piles and vertical pile groups. Findings from these lateral load tests will be used for designing battered pile group foundations in similar conditions.

Literature Review

Bridge Structural Health Monitoring

As of 2009, there were 603,310 bridges listed on the National Bridge Inventory (NBI), among which about 46.8% were built before 1966 and 27.6% were classified as either structurally deficient or functionally obsolete *[1]*. Depending on the bridge's current condition, structure type, and load rating, biannual inspections were required for over 500,000 bridges (approximately 83% of all the bridges on the NBI inventory) while about 72,000 bridges must be inspected yearly in accordance with the National Bridge Inspection Standards (NBIS). Although it has become a major challenge to inspect such a large amount of bridges, bridge inspections mainly have been conducted by visual inspection with the inherent drawback that only visible damages on the surface are considered and any damages under the surface often elude the inspectors. In addition, the labor-intensive visual inspections can be highly subjective and the condition ratings for the same bridge can vary greatly along with the inspections performed by different inspectors *[2]*.

During the period of 1989 to 2000, there were over 500 recorded bridge failures in the United States, which highlights the need to adopt a more reliable approach such as structural health monitoring (SHM) that can provide quantitative and continuous information on the bridges' structural state *[3]*. The highly-publicized tragic collapse of I-35 St. Anthony Falls Bridge over the Mississippi river in Minneapolis, Minnesota, in August of 2007 heightened the urgency of implementing SHM into bridge inspections and assessment. Structural health monitoring provides a means to quantitatively assess the structural state of bridges and detect structural changes that affect bridges' performance in both the short and long term. It allows continuous and real-time monitoring of bridges' structural conditions and their responses to traffic loads and special events such as earthquakes, floods and tornados. In fact, the importance of developing bridge structural health monitoring systems has been realized in the 1980s and SHM was first utilized for bridge damage detection *[4, 5, 6]*. Through laboratory experiments to field full-scale studies, a variety of research work has been conducted on bridge structural health monitoring to evaluate bridges' behavior and performance, as well as to predict the onset of structural damage with the aid of numerical modeling and damage detection algorithms *[7], [8], [9], [10]*. With the rapid advancement in the fields of the Electrical Engineering and Computer Science, the advent of technologies such as high-precision microelectromechanical system (MEMS) sensors, wireless sensor networks (WSN), and cyberinfrastructure (CI) tools makes it possible to have an effective, reliable yet affordable monitoring system for bridge structural health assessment *[11, 12]*.

Building instrumented bridges (smart bridges) is of great interest as it offers the advantage of implementing a monitoring plan in the design phase and providing baseline data for comparison. Integrating the monitoring systems with the bridge management system provides great benefits in terms of management efficiency and assurance of bridge safety. Recently, several newly-built bridges were instrumented with various types of sensors for structural health monitoring of the bridge. The new Svinesund Bridge, comprising of two approach bridges and a central arch section, was completed in 2005 joining Sweden and Norway across the Ide Fjord . It was claimed that the bridge was to be the longest single-arch bridge in the world. Due to the uniqueness of its design, it was decided to monitor the bridge during the construction phase and through the first four years of its service life. The bridge was heavily instrumented by various types of sensors at different locations of the arch, including vibrating-wire strain gauges, resistance strain gauges, load cells, linear servo accelerometers, temperature gauges, and anemometers *[13]*. The bridge structural responses to static and dynamic loading and environment factors were monitored. The instrumentation was aimed to validate the performance of the design and to monitor the health status of the bridge under special events, such as wind loading. In addition, the instrumentation data was implemented into a finite element (FE) model updating procedure coupling a non-linear optimizer, which can potentially be used for bridge evaluation and assessment *[14]*.

Since the use of structural health monitoring for bridge inspection and assessment, much of the emphasis has been on using SHM for the bridge superstructure elements rather than the entire bridge system, including the substructure. As the bridge substructures, i.e. foundations, play a critical role in maintaining the integrity of a bridge, the importance of substructure health monitoring (SSHM) should not be underestimated. Numerous studies have been conducted to monitor the behavior of bridge foundations through the construction phase to the long-term in-service life *[15]*, *[16]*, *[17]*. Some commonly-used sensors in bridge substructure health monitoring are strain gage (electrical resistance type and vibrating wire type), accelerometer, inclinometer, and earth pressure cell among others. A substructure health monitoring program was implemented at the new I-35 bridge in Minneapolis, Minnesota, built to replace the collapsed bridge to provide live monitoring of the substructure loads during construction and ultimately long-term health monitoring of the bridge *[18]*. Strain gages and thermocouples were installed on selected two pier columns and two shafts for short-term and long-term monitoring of the bridge substructure.

Lateral Load Tests

Tests conducted for understanding the lateral load behavior of pile or pile groups are generally categorized into full-scale test and centrifuge model tests. Full-Scale tests are not easy to perform because of the associated high cost, technical difficulties, and uncertainties,

so only few full-scale tests have been performed since the early nineteenth century, whereas comparatively more centrifugal tests that can simulate the actual field condition have been conducted. Important findings of researches corresponding to these tests are briefly reviewed herein.

Full-scale Lateral Load Test. Full-scale tests are considered to be the best method for understanding the behavior of laterally loaded piles. The literature review revealed no record of the full-scale test before Feagin, who conducted a field test on laterally loaded timber and concrete piles *[19]*. After that, many researchers performed full-scale tests on pile/pile group under different soil conditions *[20], [21], [22], [23], [24]*. Their findings showed an agreement in that average soil resistance per pile decreased in a pile group due to a group interaction effect which increases with larger deflection and decreases with the increment of center-to-center spacing. Also, the average load per pile for the group is lower than a single isolated pile at the same deflection. Matlock conducted lateral-load tests on steel pipe pile of 12.75 inches in diameter for both static and cyclic loading, and developed a p-y curve by assuming the pile remains linear *[25]*. Kim and Brungraber conducted full-scale test on pile group consisting of battered piles and noted that battered piles provide more lateral resistance with less bending stress *[20]*. The analysis of lateral load was revolutionized by Brown et al. who conducted full-scale tests on vertical pile groups on steel piles and generated p-y curves based on Winkler-type soil model with polynomial curve fitting to the bending moment data *[23], [26]*. Furthermore, Brown et al. introduced the p-multiplier concept to analyze the reduced resistance of the group pile and produced a modified p-y curve for pile group *[26]*. Their findings also showed that the depth of the maximum bending moment increased from front row to back row, and was greater and occurred at greater depths for the piles in the group than the single pile. The p-multiplier concept was adopted by Ruesta and Townsend through conducting full-scale tests on reinforced concrete pile and also noted that the outer piles took more load than inner pile of the same row due to greater influence of shadowing effect at inner piles *[27]*. Rollins et al. suggested a greater p-multiplier value after conducting a full-scale test on a vertical pile group in clay *[24]*. The other observations made by Rollins et al. *[24]* were: a) the displacement of pile group is 2-2.5 times higher than the single pile for the same average pile load, b) the load distribution in pile group is not uniform but is a function of the row position, and c) there are no consistent trends in the load distribution among piles in the same row which agrees with the previous results of Brown et al. *[23, 27]*.

In the early 21st century, Huang et al. conducted a full-scale test on bored and driven precast pile groups to investigate the influences of installation procedure of piles in lateral soil resistance *[28]*. The conclusion was that driven pile installation increased the group interaction by causing the soil to move laterally and hence become denser; while bored pile

installation loosens the soil and decreases group interaction. Rollins et al. conducted several full-scale lateral load tests of piles in clayey soil as well as sandy soil at different pile spacing *[29, 30]*. Some important findings of Rollins et al. are *[29*, *30]*:

- The middle pile of the same row carried the smallest load in the row at a given displacement, while the left and right piles carried 20-40% higher loads in the sandy soil, which agrees with most pile group tests in sands *[27]*, *[31]*. However, this observation conflicts with some previous full-scale pile group load tests in clays *[23]*, *[24]*, *[32]*. For verification, Rollins et al. explained that the increment of friction angle increases the width of the passive wedge which forms in soil in front of a laterally loaded pile; and as sands generally have higher friction angles than clays, there is more pile-soil-pile interaction, thereby more interaction in middle pile in a row with the adjacent piles, so carrying less loads than the outer piles *[30]*;
- The group effect becomes negligible when spacing between rows increased to more than 6B, where B is the pile width;
- The passive resistances on the pile cap can significantly increase the lateral load capacity provided by the pile group. They suggested that for the mobilization of full passive resistance in the dense compacted sandy gravel, nearly 6% of the pile cap height wall movement is necessary. Nip et al. conducted a full-scale test on 1.5 m diameter single vertical bored piles and successfully used the fourth order polynomial equation for the soil reaction profile to deduce the shear force profile, bending moment profile and to back calculate the p-y curves *[33]*.

Centrifuge Model Load Test. In contrast to full-scale tests, centrifuge and model tests are inexpensive and can be easily performed to study the lateral load behavior of piles at desired test conditions. Cox et al. (1984) conducted centrifuge testing using sand and suggested that the elastic theory does not account for the non-linearity behavior in pile group interaction, and also the total load carried by each pile within the group was not evenly distributed *[34]*. According to McVay et al., soil density influences the average load resistance which increases with the increase in soil density; however, the increment was not significant like pile spacing *[31]*, *[35]*. Also, in larger pile groups, the load resistance continues to decrease until about the fourth row, after which it stabilizes. McVay et al. also agreed with the p-multiplier concept of Brown et al. *[26]* and suggested using a different p-multiplier at different pile spacing, *[31]*. Moss et al. conducted model tests on cyclic loading and found that the soil resistance was more dependent upon the pile stiffness, instead of the p-y curves since the cyclic loading compress the soil and form the gap in front of the pile *[36]*. Llyas et al. performed centrifuge tests on pile groups in clay and noted that the reduction in pile group efficiency is less for piles installed in overconsolidated soils than

those installed in normally consolidated soils, and the group interaction effect becomes insignificant when center-to-center spacing reaches a value of 5D *[37]*. Llyas et al. also concluded that for the middle row, center piles often carried much less load and bending moment than those of the outer piles in the same row *[37]*.

Methods of Analyzing Laterally Loaded Pile

The pile response under lateral loads has been the focus of numerous studies in the past half century. The analysis methods reviewed in the literature generally can be grouped into the following five categories:

- Winkler approach. The soil is represented as linear springs and the pile is represented as a linear beam *[38]*.
- Elasticity theory. Based on an elastic continuum approach, which assumes both the soil and pile as elastic materials, Poulos developed a model to analyze lateral load behavior using the finite difference technique *[39]*.
- P-y method. This is the most popular method used in the design practice. In this method, Matlock and Reese modified the Winkler approach by representing the soil as a non- linear characteristic material *[25]*, *[40]*.
- Finite element method. The finite element method where the soil-pile interaction can be modeled easily is also used for the analysis of lateral load tests. Several computer programs were developed based on the finite difference method and the finite element technique; these programs will be discussed later.
- Strain wedge model. Norris developed a strain wedge model, later updated by Ashour et al., which analyzed the behavior of laterally loaded piles by considering the pile properties such as pile shape, bending stiffness, and head condition *[41]*, *[42]*. Details on each of the five methods for analyzing laterally loaded piles can be found in Appendix A.

Review on Battered Piles

Battered piles or inclined piles are generally classified into two types based on the loading direction: the pile which is battered toward the loading direction is negative battered or reverse battered pile, whereas, the pile battered against the loading direction is positive or forward battered pile, as shown in Figure 1. Battered piles are widely used in offshore structures due to their considerable resistance against lateral loading induced by ship impact, water wave, etc. The research on the laterally loaded battered piles began with Feagin who performed full-scale tests on battered timber piles *[19]* followed by model tests performed by

more researchers (e.g., [*43*], *[44]*, *[45]*). Kim and Brungraber and Manoliu et al. also performed full-scale tests on battered piles *[20]*, *[46]*. It was reported that negative battered piles offer more resistance than positive battered piles, which was also found by Ranjan et al. based on laboratory test results *[47]*. Lu also supported the concept and explained that the soil reaction at ground level is zero for a positive battered pile and maximum for a negative battered pile, indicating that the upper layer soil support in a negative battered is enormous so the negative battered pile has larger lateral resistance *[48]*.

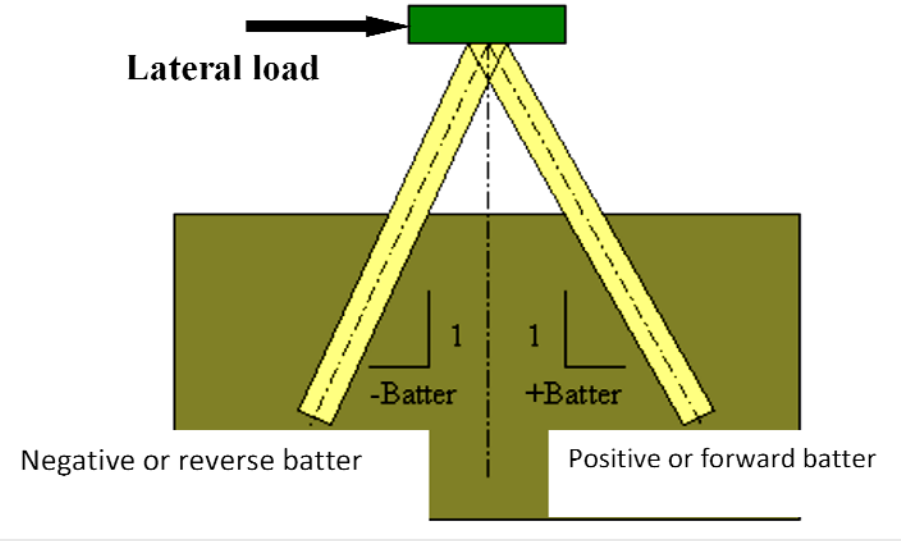

Figure 1
Battered pile categorized into positive and negative battered pile

Based on a centrifugal tests on laterally loaded single battered piles in sand with different relative density, Zhang et al. inferred that the effect of pile inclination on the lateral resistance is more effective in the dense sand and the lateral resistance of pile increases with the increment of the batterness of negative battered pile, whereas the lateral resistance decreases with the increment of batterness of forwarded battered pile *[49]*. Similarly, Rajashree and Sitharam performed a non-linear static analysis for both positive and negative battered piles at different angles (10°-30° inclination) and observed that the lateral deflection predicted at the ground line for a pile in positive battered is more than for vertical pile and less than for a negative battered pile, which agrees with Lu's observation that there is zero lateral resistance for positive battered pile and maximum for negative battered pile at the ground line *[48], [50]*.

As illustrated in Figure 2, when the lateral load is applied with no vertical load, the horizontal movement of the negative battered pile will cause a positive $\Delta\sigma_0$ in the soil in front of pile so the lateral resistance for the negative battered pile will be greater than the vertical pile.

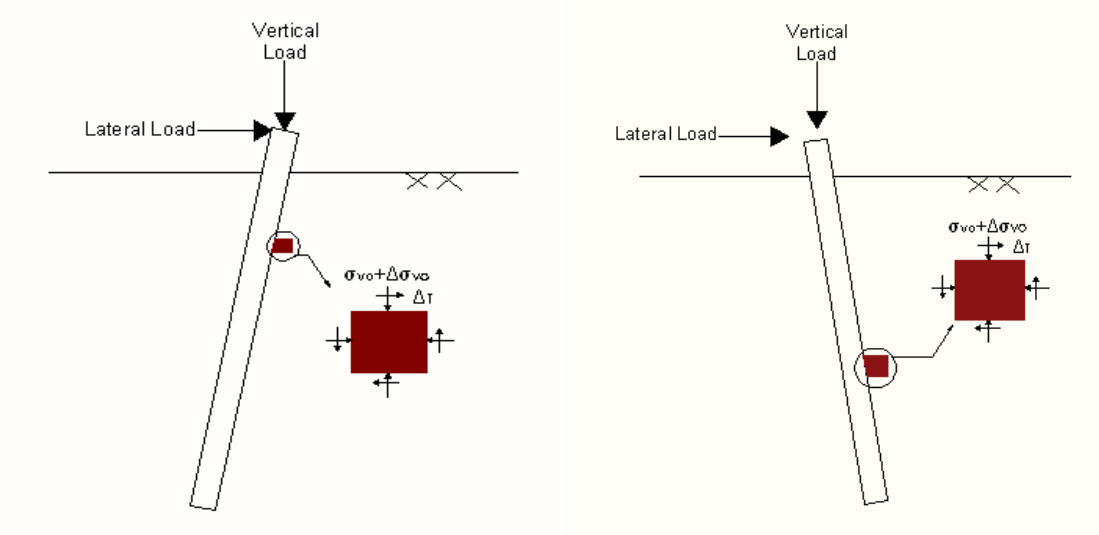

(a) For negative battered pile (b) For positive battered pile

Figure 2
Movement of soil around battered pile (after *[49]*)

To the contrary, the lateral movement of the positive battered pile will cause an upward movement of soil, which will reduce the vertical stress and hence the lateral resistance of the positive battered pile will be smaller than the vertical load. However, when the vertical load is applied, the lateral resistance of the negative battered pile reduced because the bending moment generated by the vertical load component causes an additional lateral defection, whereas the lateral resistance of the positive battered pile since the bending moment caused by the vertical load negates the effect of the lateral load component.

Pinot et al. conducted centrifuge tests on battered pile groups and concluded that the group effects for 5B spacing and fixed-head conditions appear to be minimal and suggested the p-multipliers values of 1.0, 0.85, and 0.7 for rows 1, 2, and 3 of 3×3 pile configuration *[51]*.

P-y Curves of Battered Piles. The effect of pile inclination on the p-y curves was investigated by Kubo, Awoshika, and Zhang et al. *[52], [53], [54]*. Their findings indicate that the shape of the p-y curves for battered piles and vertical piles are similar, but the battered angle influences the ultimate soil resistance (P_u), and the subgrade modulus (K_s). The variation of two important parameters, subgrade modulus which defines the initial slope of p-y curve, and the ultimate resistance, which governs the pile response at large deflections, are controlled by the unit weight and angle of internal friction, which leads to modification of p-y curves of vertical piles in order to generate p-y curves of battered piles. Zhang et al. suggested that changes in subgrade modulus (K_s) and the soil's ultimate resistance for battered piles (P_{ub}) are proportional to the ratio of passive earth pressure coefficient for

battered piles to passive earth pressure coefficient for vertical pile as shown in equations (1) and (2) *[54]*.

$$P_{ub} = \Psi P_u \quad (1)$$

where, $\Psi = \lambda * \frac{K_{pb}}{K_p}$ (2)

$$K_p = \frac{sin^2(\theta-\phi)}{sin^2\theta \ sin(\theta+\delta)[1-\sqrt{\frac{sin(\phi+\delta)sin(\phi+\beta)}{sin(\theta+\delta)sin(\theta+\beta)}}]^2} \quad (3)$$

where, λ = coefficient that accounts for the size of the sand's passive soil wedge,

K_p = passive earth pressure coefficient for vertical pile,

K_{pb} = passive earth pressure coefficient for battered pile,

θ = wall inclination,

ϕ = internal frictional angel of the soil,

δ = soil-pile interface friction angle,

β = the ground slope angle.

Similarly, the initial subgrade modulus for the battered piles, K_{sb} is obtained by multiplying the vertical pile subgrade modulus, K_s, with the same factor, Ψ (i.e., $K_{sb} = \Psi^* K_s$). The value of Ψ factor for the modification can be estimated from Figure 3 and 4. The soil-pile interface friction angle δ has a dominant effect on the lateral resistance of battered piles. Jardine and Chow found that the value of δ is independent of the relative density and tends to decline with particle size *[55]*. It is noted that the soil-pile interface friction angle δ has a significant effect on the p-y curves. Specifically, the larger the δ value, the larger the K_{sb} and P_{ub} values for the positive battered piles and the smaller the K_{sb} and P_{ub} values for the negative battered piles versus vertical pile values. Figure 5 depicts the modified p-y curves for battered piles.

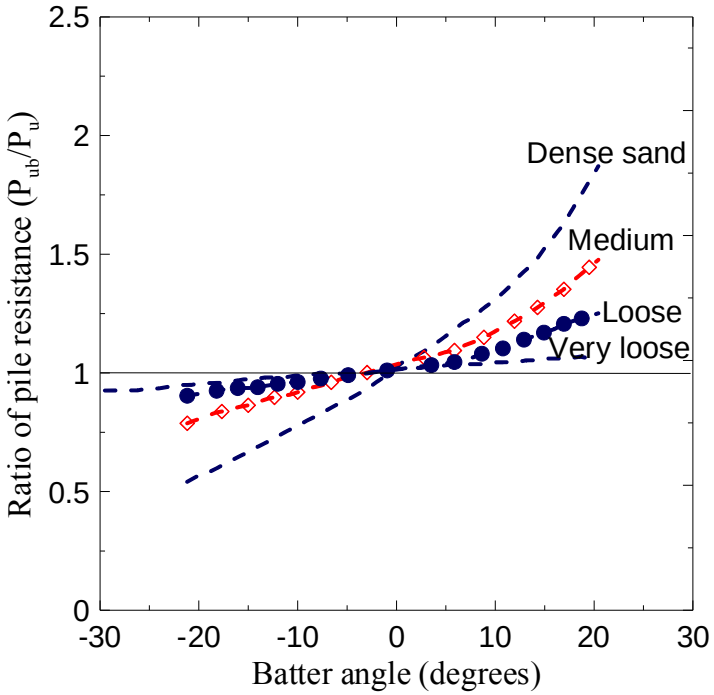

Figure 3

Influence of batter angle on pile resistance (after *[54]*)

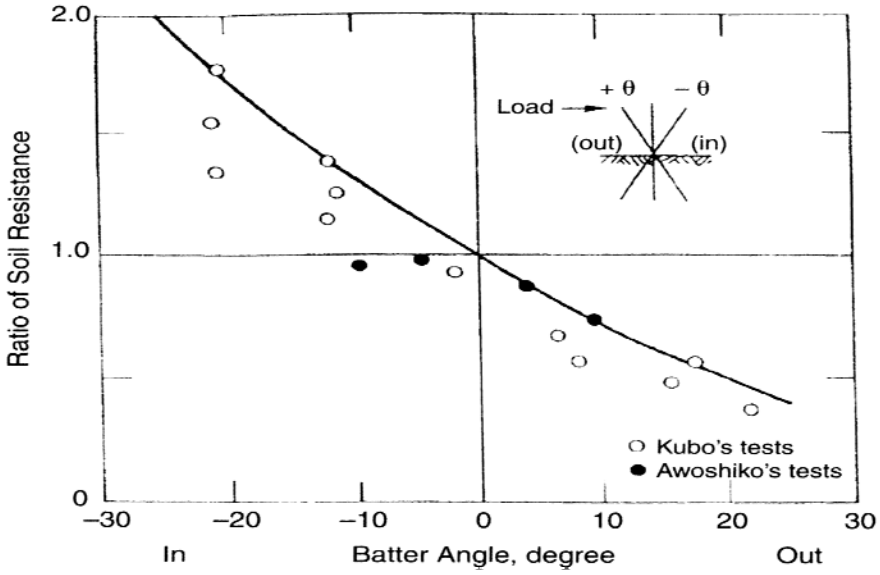

Figure 4

Influence of pile batter on pile resistance *[52]*

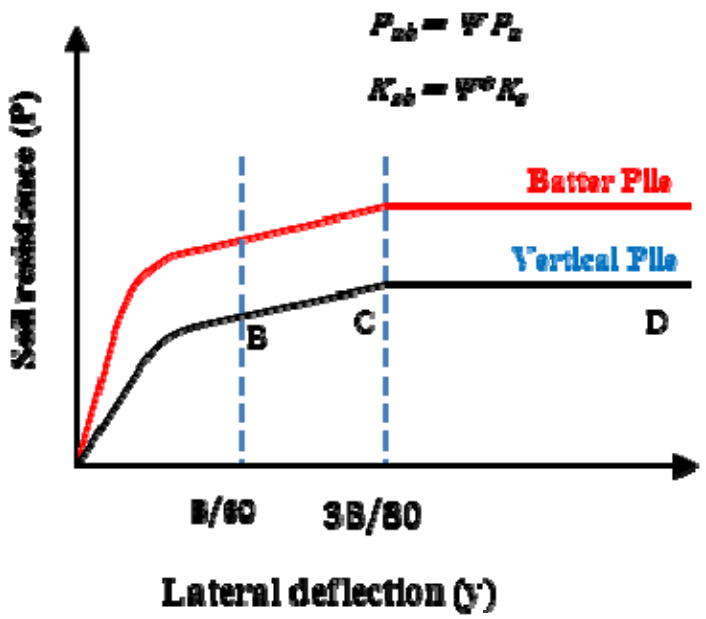

Figure 5
Modified P-y curves for battered pile in sand *[54]*

Numerical Simulations using Computer Programs

With the development of finite difference and finite element techniques, several computer programs such as COM624P/ GROUP, LPILE, FLPIER and FB-MultiPier were developed *[56], [57], [58], [59]*. The applicability and structures of these programs are discussed in detail in the following sub-sections.

Finite Difference Method Based Programs. COM624P and LPILE are two programs for laterally loaded single piles developed based on the finite difference method in which the soil is modeled using p-y curves. LPILE models the pile as a beam with lateral stiffness based on the modulus of elasticity and moment of inertia of the pile and models the soil as a non-linear spring. The program can calculate the pile's stiffness as either linear or non-linear, depending on the user input. Typically, concrete pile stiffness is assumed non-linear whereas steel pile stiffness is assumed linear. To analyze or calculate the displacements, shear forces, and bending moments in the laterally loaded pile, LPILE requires information of structural properties, soil properties including modulus of lateral subgrade reaction or lateral subgrade modulus, and *p–y* curve shapes.

The analysis of pile groups is more complicated than that for single piles because of pile-soil-pile interactions. GROUP program, the advanced form of COM624P, has incorporated *p-y* multipliers to predict the effect of pile-soil interaction and has been used by many researchers for the analysis of pile groups *[30]*, *[60]*.

Finite Element Programs. FLPIER, a non-linear finite-element program developed at the University of Florida for analyzing bridge pier structures, is a flexible program that can model different pile and pier configurations; for example, battered piles, variable spacing between piles, and missing piles. FLPIER is coupled with a graphical preprocessor, PIERGEN, to define the structure configuration and a postprocessor, PIERPLOT, to plot the deflected shapes, internal stresses, and forces *[27]*, *[61]*. The finite element program divides each pile into 16 two-node, three-dimensional elements consisting of 10 degrees of freedom, 3 degrees of translation, and 2 rotations at each node. At each node of the pile, lateral pile-soil interaction is modeled by nonlinear springs, p-y curves. The incorporated p-y curves included O'Neill's p-y curves for cohesionless soil and cohesive soil, default p-y curves similar to COM624P, and a user-defined p-y curves option for linear interpolation. The intensity of group interaction effect is modeled using p-multiplier values. The advancement of this program took place by incorporating cracking effects of reinforced and prestressed pile to consider the non-linearity behavior of pile, because not considering cracking effects generally overestimates the stiffness of a pile subjected to relatively high loadings. Charles at al. investigated the behavior of large-diameter bored pile groups and studied the design parameters for modeling the non-linear response of soil and bored piles using FLPIER *[62]*. Similarly, Zhang et al. simulated several centrifugal test models in FLPIER program in order to validate and improve it *[49]*. They concluded that this finite element program is a reliable and powerful tool for laterally loaded pile group analysis. With the success of FLPIER, the Florida Department of Transportation advanced this software by making some changes in interface and features that generated a more powerful tool called FB-MultiPier.

The FB-MultiPier program couples the non-linear structural finite element analysis with non-linear static soil models for axial, lateral, and torsional soil behavior to provide a robust system of analysis for coupled bridge pier structures and foundation systems. FB-MultiPier performs the generation of the finite element model internally given the geometric definition of the structure and foundation system as input graphically by the designer. This allows the user to work directly with the design parameters and lessens the bookkeeping necessary to create and interpret a mode. Possiel modeled the response of full-scale tests in FB-MultiPier and found that the model produced results within 10% error of the measured results for the desired 1.5 in pile deflection *[63]*. Similarly, McVay et al. performed numerical analysis using FB-MultiPier for time-domain analysis of soil- structure interaction from a full- scale vessel impact loading of a bridge pier *[64]*.

Interpretation of Measurements for Deriving p-y Curves

Load-deflection responses of laterally loaded piles depend on many factors, such as pile geometry, structure material properties, adjacent soil conditions, soil-structure interaction,

and loadings. The governing differential equations derived by Hetenyi for the lateral loaded pile are given in equation (4) and the typical profiles of displacement, bending moment, shear force and lateral soil resistance force per unit length are presented in Figure 6 *[65]*.

$$\theta = \frac{dy}{dz} \qquad M = EI\frac{d^2y}{dz^2}, \qquad V = EI\frac{d^3y}{dz^3} \quad P = EI\frac{d^4y}{dz^4} \tag{4}$$

where, θ = slope or rotation, y = lateral displacement, z = depth below , M = bending Moment, E = Young's modulus of concrete, I = moment of inertia, V = shear force, P = lateral soil resistance per unit length.

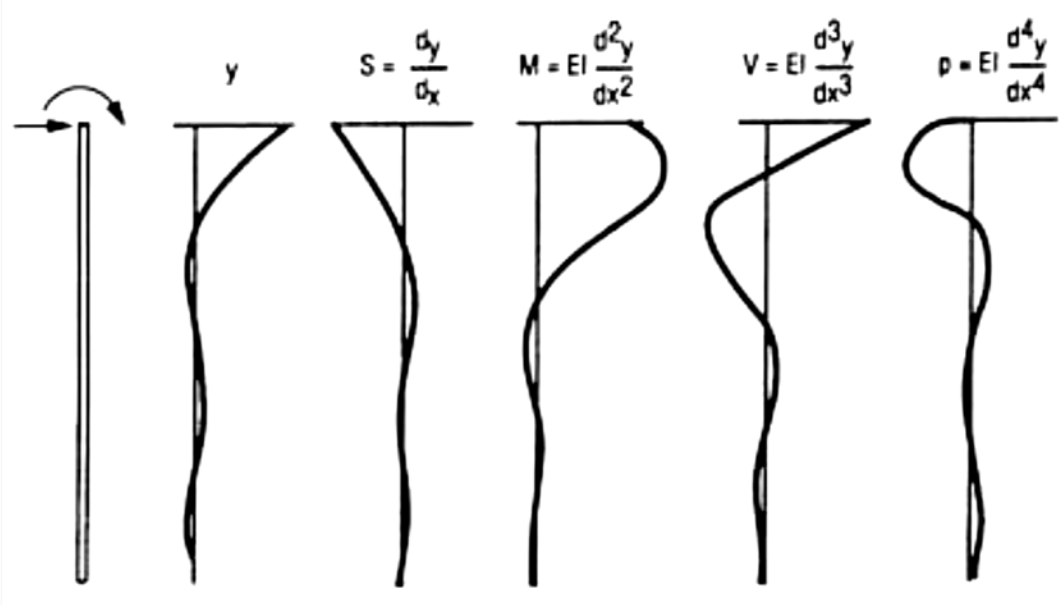

Figure 6
Typical profiles of y, θ, M, V, and P

The equation for soil reaction (P) is commonly solved by numerical methods such as finite difference method, finite element method, or modeling the soil reaction using p-y curves. In general, the raw data in the form of horizontal displacement or angular displacement obtained from the instruments, such as inclinometers and strain gauges, can be utilized to analyze the lateral responses of laterally loaded piles. Problems faced in such analysis are the difficulties during data interpretation obtained from inclinometers. It is essential to find a reliable method of data interpretation for deducing bending moment, shear force profile, and back-calculating p-y curves from the measured strain and deflection data.

The deflection from the inclinometers and strain gauges can be obtained by the following equations:

$$y = \iint \phi dz \ldots\ldots\text{..from stain gauges} \tag{5}$$

$$y = \int \theta dz \text{……..from inclinometer} \quad (6)$$

Where, θ is the slope or rotation measured from inclinometers and ϕ is the curvature (compression strain-tension strain) measured from strain gauges. The integration of discrete data such as rotation and curvature measurements provides fairly reliable results due to numerical stability during the process, but deducing bending moments and soil reaction from rotation measurements involves differentiation and amplifies errors. So far, several methods have been proposed to fit the data obtained by double differentiating to evaluate the p-y curves. Herein these methods are briefly reviewed: High order global polynomial curve fitting; Piecewise polynomial curve fitting; Weighted residual method; Brown least square error method; Energy Method; Cubic Spline; and Elastic Superposition Method *[66, 67, 68, 69, 70, 71, 72]*. Details on these methods are included in Appendix B.

OBJECTIVE

The main objective of this research project was to establish a bridge substructure health monitoring system for use in short-term and long-term monitoring purposes:

- Short-term monitoring: to validate the applicability of the FB-MultiPier analysis for predicting the performance of battered pile group systems under lateral loading and to develop (or back-calculate) the p-y multipliers for battered pile groups in similar soil conditions by conducting lateral static load test.
- Long-term monitoring: to evaluate the behavior of pile group structure under dynamic loads caused by selected events (wind, waves, and vessel collision).
- Provide a better approach in the design process of battered pile groups.

SCOPE

This study implemented a bridge health monitoring system for the new I-10 Twin Span Bridge including both superstructure and substructure. The monitoring system serves two purposes: long term monitoring of the bridge during next extreme events such as hurricane and ship impacts and short term monitoring of a lateral load test. The instrumented sensors include triaixal accelerometers and tiltmeters for pile cap motion, water pressure cells for water pressure of storm surges, corrosion meters for steel corrosion, strain gauges and IPI at piles for pile deformation, and strain gauges at bridge girders for deformation.

The lateral load test was conducted on the east bound bridge pier M19. The battered pile group response was recorded by the monitoring system. Data interpretation incudes analyses of IPI and strain gauge data. A high-order-polynomial curve fitting method was adopted to back-calculate battered pile group response from the measured IPI data and to derive p-y curves. FB-MultiPier program was used to simulate the lateral load test of the battered pile group. The simulation results were compared with measured data as well as the results from the back-calculation.

METHODOLOGY

Test Site

The old I-10 Twin Span Bridge, with an elevation of 9 ft, could not resist the storm surge generated in Lake Ponchartrain and suffered massive damage during Hurricane Katrina; consequently, most of the bridge remains unusable. In order to resist the high storm surge, the new bridge was built with an elevation of 30 ft. Figures 7 and 8 show the project site location.

Understanding the proper behavior of the superstructure and substructure of the newly built bridge under induced axial and lateral load is essential to ensure proper performance of the bridge during its service life. In order to study the lateral load mechanism of the pile foundation, a full-scale lateral load test was designed and conducted at the M19 eastbound pier. The M19 pier was selected as it is second pier from the marine traffic under pass and more susceptible to lateral load due to possible ship impact in addition to the wind and water waves. It consists of a 24 battered pile group in which some selected piles were instrumented with advanced instruments prior to the full-scale lateral load test.

Figure 7
Location of I-10 Twin Span Bridge site

Figure 8
Newly-constructed I-10 Twin Span Bridge

M19 Pier Foundation

The M19 pier supports 200 ft. long steel girders in the north side and 135 ft. long concrete girders in the south side. The M19 pier is the second pier south of the marine traffic underpass. The size of pile cap of the M19 piers is 44 ft. × 42.5 ft. × 7 ft. The view of M19 east and west bound piers are depicted in Figure 9. The foundation of M19 piers consist of 24 precast presetressed concrete (PPC) piles in a 6 × 4 configuration, 4 rows of piles in the direction of loading, and 6 rows of piles perpendicular to the direction of loading. The center-to-center spacing of piles in the direction of loading at the cap level was 13 ft. or 4.33 B and 7.5 ft. or 2.5 B in the direction of perpendicular to the loading. All 24 piles were 110 ft. long with an outer dimension of 36 in. including a circular void of 22.5 in. with the exception of the top 20 ft. which was solid section.

The average embedded length of the piles was 87 ft. The piles were battered at a 1:6 slope; the two rows of piles closer to the eastern side of pile cap (position of loading) were battered in the direction of loading and the two rows of piles closer to the western side of pile cap were battered against the loading. Each pile was reinforced with 36 number of 0.6 in. diameter strands with an initial tension of 43,980 lbs. The piles were designed to have a minimum compressive strength of 6000 psi at 28 days and of 4500 psi at the time of transferring the prestressed force.

Figure 9
M19 east and west bound piers site

Geotechnical Conditions

Geotechnical subsurface investigations were conducted by Fugro Inc. The generalized subsurface profile is presented in Figure 10. As a full-scale lateral load test was designed for M19 pier, five Cone Penetration Tests (CPT) and one soil boring test with several Standard Penetration Tests (SPT) were conducted in order to investigate subsurface soil properties and to determine the pile's tip elevation. Out of the five CPTs, four tests were conducted at distances 5 to 10 ft. from the four corners and one at the center of foundation, as shown in Figure 11. The depth of CPTs range from 160 ft. to 185 ft. below the mudline. The main purpose of performing CPTs were to define soil profiles more accurately, to observe any variation of soil properties across the foundation site, and to locate the depth of the bearing sand layer to support the piles. The approximate water depth measured at nearby M19 Pier was nearly 11 to 12 ft. The depth of bearing sand layer at the M19 pier was found to be at depths ranging from 100 ft. to 110 ft. below the water surface.

The CPT tests measured tip resistance (q_c), friction resistance (f_c), and pore pressure (u): the average q_c and f_c for top 20 ft. depth below mudline were 1.23 tsf and 0.028 tsf, respectively. The

undrained shear strength (S_u) was calculated and plotted using CPT soil classification software version 5 developed by Louisiana Transportation Research Center. The undrained shear strength based on CPT was computed using the following equation (7).

$$S_u = \frac{q_c - \sigma_{vo}}{N_{kt}} \quad (7)$$

where,

S_u = undrained shear strength

σ_{vo} = vertical overburden stress

N_{kt} = a bearing factor. The value of N_{kt} is chosen to be 15 based on the current Louisiana practice.

CPT soil classification was determined based on a probabilistic method *[73]*, which gives probability of soil behavior as sandy, silty, and clayey. The CPT result shows that the soil profile at the M19 pier foundation mostly consists of silty clay soil down to 45 ft. depth underlain by cohesionless soil from 45 to 57 ft. followed by clayey soil. Cohesionles soil below the depth of 100 ft. has limited influence on the lateral resistance force. Only the soil layer up to depth of 5 B to 10 B below pile tip influences pile-soil interaction *[74]*. The average undrained shear strength computed from CPT were, 162 psf for the top soil (12-20) ft. depth, 800 psf for 20-25 ft. depth, 1300 psf for 25-35 ft. depth, 902 psf for 35-45 ft. depth, and 1500 psf for 45-110 ft. depth. The summary of the CPT results and corresponding soil classification is presented in Figure 12.

One soil boring was drilled down to 200 ft. and SPT tests were performed in sandy soil layers. The soil samples were retrieved from the ground surface to the completion depth of the boring using Shelby tube samplers. Laboratory tests consisting of moisture content, Atterberg limits, and unconsolidated undrained (UU) triaxial tests were conducted on the collected samples for soil classification and evaluation of properties such as the undrained shear strength and compressibility characteristics of the foundation soils. The summaries of borings, SPT, and laboratory tests are also illustrated in Figure 12. Based on laboratory and in-situ tests results, the subsurface soils of M19 foundation are classified as:

- 0 to 35 ft. depth: medium to stiff gray and tan silty clay to clay soil with silt pockets. Laboratory testing indicates that the soils have undrained shear strength ranging from 140 to 1000 psf.
- 35 ft. to 47 ft. depth : soft to medium clay.
- 47 ft. to 57 ft. depth: medium to dense light gray sand. The SPT-N values ranged from 16 to 22.

- 57 ft. to 85 ft. depth: medium to stiff gray clay with sandy clay/silt pockets. The undrained shear strength ranged between 1700 psf to 2000 psf.
- 85 to 98 ft. depth: medium to very stiff clay having undrained shear strength of around 2000 to 2600 psf.
- 99 ft. to 160 ft. depth: medium dense to very dense sand with interlayers of silty sand, clayey sand and silty clay soil. The SPT-N values range from 3 for loose sand to 86 for the very dense sand.

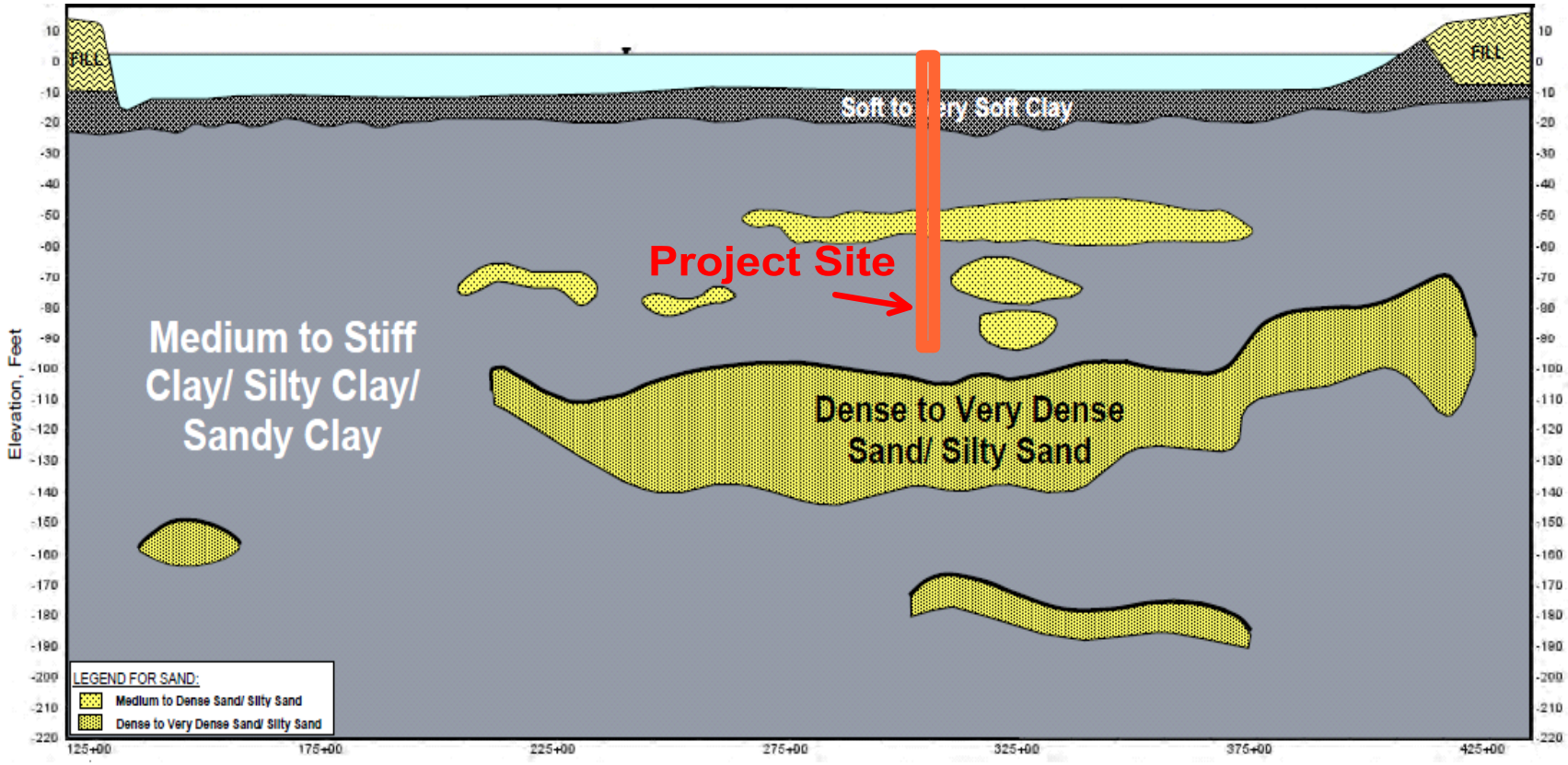

Figure 10

Generalized subsurface profile at Twin Span Bridge

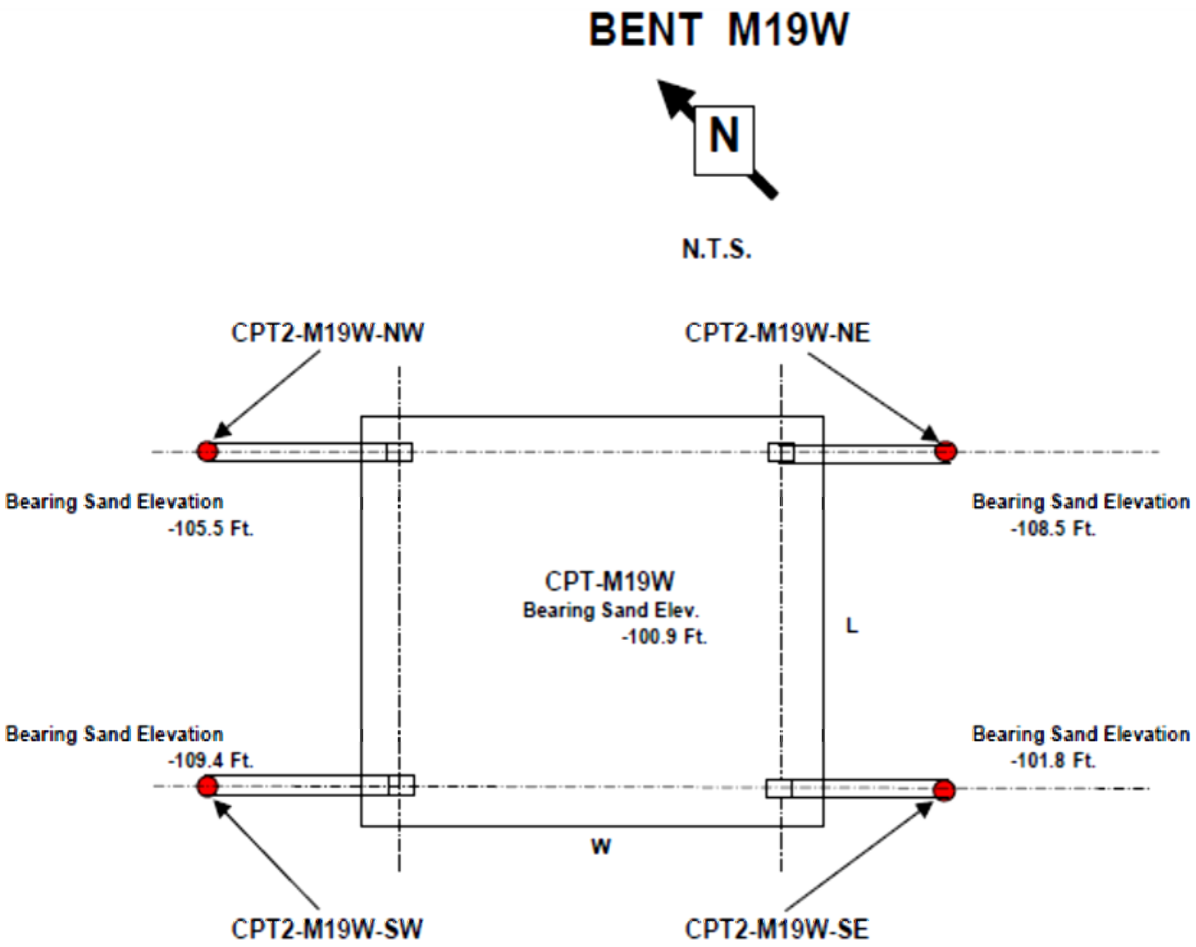

Figure 11
Location of CPT tests conducted at M19 Pier

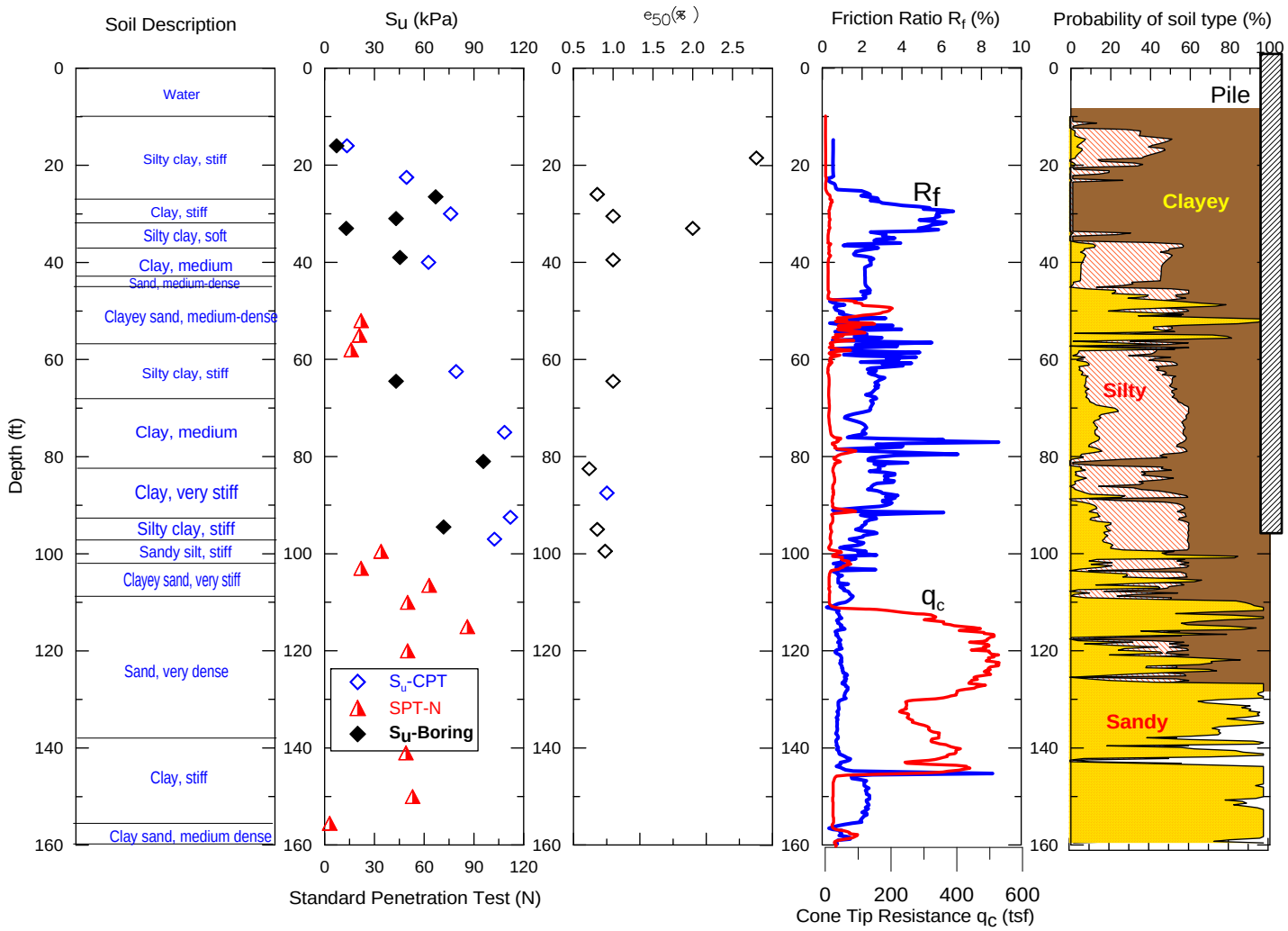

Figure 12

Summary of in-situ exploration and testing of site M19 pier

Instrumentation Program

In order to address some concerns raised during the design of the new I-10 Twin Span Bridge, DOTD engineers decided to install a structural health monitoring system on pier M19 Eastbound of the bridge. The system, which includes instrumenting both the substructure and superstructure of the pier, will be used for short-term and long-term monitoring of the bridge.

The substructure monitoring system includes instrumenting eight selected piles with inclinometers and strain gages, and instrumenting the pile-cap with accelerometers, tiltmeters, water pressure cells, and corrosion meters. A plan view of the M19 footing with a layout of the substructure instrumentation is presented in Figure 13. The superstructure monitoring system includes instrumenting the columns, bent cap, three steel girders, three concrete girders, and one diaphragm with strain gauges and corrosion meters. A Weigh-In-Motion (WIM) system was also installed at the concrete bridge deck of the M19 eastbound pier. This report will focus on the discussion of the substructure instrumentation plan of the M19 Eastbound pier and the subsequent lateral load test that was conducted on the pier.

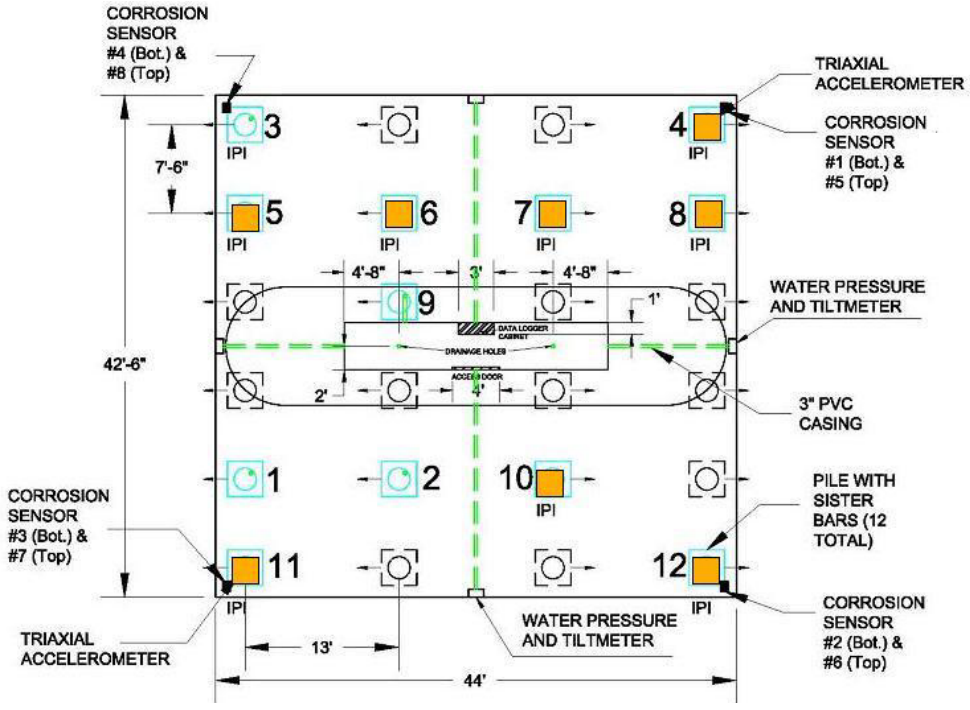

■ IPI, □ Sister Bars

Figure 13

Plan view of M19 pier footing with layout of substructure instrumentation

Instrumentation Plan of Piles

Eight selected piles (piles number 4, 5, 6, 7, 8, 10, 11, and 12) were instrumented with MEMS In-Place-Inclinometers (IPI). The IPI (Geokon model 6150) consists of a string "node" of tilt sensors connected together and placed in the pile foundation through a PVC casing. It can measure the position change (inclination) in each node in a direction perpendicular to the axis of the string. Each pile was instrumented with six inclinometer sensors located at elevations of -65, -45, -35, -25, -15, and -5 ft. from the bottom level of the pile cap. The measurements from the six IPIs can provide a profile with depth of the lateral deformation of the pile.

Twelve selected piles (piles number 1, 2, 3, 4, 5, 6, 7, 8, 9, 10, 11, and 12) were instrumented with resistance type sister bar strain gages (Geokon model 3911-4) to measure the strain distribution at the locations close to the pile cap caused by the applied lateral load. Each pile was instrumented with two pairs of strain gauges at -16 ft. and -21 ft. from the top of the pile in the casting yard. Measurements from strain gauges can be used to calculate the axial loads and bending moments transferred to the instrumented piles.

Instrumentation Plan of Pile Cap

Two triaxial accelerometers (Dytran model 7523A5) were installed on top of the pile cap at two corners across from each other (NE and SW corners). The accelerometers will be used to measure any applied dynamic load during the long-term monitoring of the M19 pier and to set up a trigger criterion system to start collecting and saving the data from other instrumentations in any event for future analysis.

Four uniaxial MEMS Tiltmeters (Geokon model 6160) were installed at the mid-width of the four sides of the pile cap. The tiltmeters will be used to measure any tilt or rotation of the pile cap during long-term monitoring. Eight water pressure transducers (Geokon model 3520) were installed mounted flush with the pile cap facings (two per facing) to measure the water wave force impact during selected events.

In addition, eight ECI corrosion meters (ECI-1 model) were installed in the pile cap, two corrosion meters at each corner at top and bottom of the pile cap, to measure any corrosion that might occur during the long-term monitoring. The corrosion meters are usually attached to support rebars with tie wraps at corrosion prone areas.

The complete development of the instrumented monitoring system was achieved in several phases as described below.

Pile Castings Phase

During this phase, a 100-ft., 3.34-in. diameter IPI casing was installed in each of the eight selected piles, in addition to one spare pile, for use to host the MEMS IPI sensors later. Two pairs of sister bar gauges were also calibrated and installed in each of the twelve selected piles with a total of 48 strain gauges. The strain gauges were installed at 16 ft. and 21 ft. below the pile tops, taking into consideration the possibility of pile cutoff after driving. Photos of pile instrumentations taken during the casting phase are presented in Figure 14. The piles' strain changes were monitored during casting, strand cutting, and storage. Figure 15 presents the measured strain changes during strand cutting and relocation of Pile 4. This phase also includes installing necessary conduits and wires to connect the strain gauges later to the data loggers. Pile 1 was instrumented with a data logger and a battery to monitor the strain change during storage and delivery. The recorded strain change of the pile is illustrated in Figure 16. It can be seen that the pile only experienced appreciable strain change when was moved for storage (August 2008) and when it was moved into the barge for delivery (end of October 2008).

Both the IPI casings and sister bar strain gages were installed at the casting yard in Memphis, TN. Two 3-in. PVC conduits were also installed in each pile to protect the instrument cables. A 16-ft. long PVC pipe with a 6-in. diameter was installed around the IPI casing to give enough space for splicing the IPI casing to extend it through the pile cap.

Pile Driving Phase

The strain gauges in the selected piles were tested post-delivery and after pile driving. Special care was taken to protect the strain gauge wires during piles' cutoff, which ranged from 6ft. to 7ft. The strain gauge readings before and after driving were recorded. The results showed that the influence of driving on the piles is minimal.

Pile Cap Instrumentation Phase

Instrumentation in this phase started immediately after placing the footing's rebar mesh reinforcements. This included: calibrating and installing two triaxial accelerometers at the north eastern (NE) and south western (SW) corners in the pile cap for measuring the dynamic load during long-term monitoring; calibrating and installing eight corrosion meters at the top and bottom of each corners in the pile cap; calibrating, installing, and housing four uniaxial MEMS tiltmeters at the four sides of the pile cap to measure the rotation of the pile cap; and calibrating and installing eight water pressure cells mounted flush with footing facing with two on each side of the pile cap. All these instrumentations were waterproofed and protected from salt water. Photos of pile cap instrumentations are presented in Figure 17.

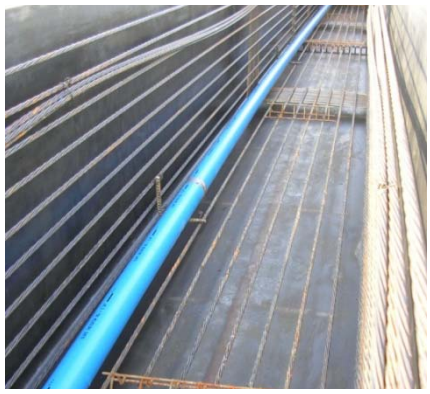

(a) Installed IPI Casing

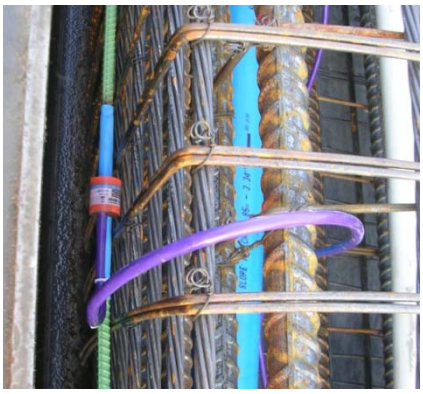

(b) Installed Strain Gauge

(c) Monitoring Strain Gauges

(b) Data Logger on Pile 1

Figure 14
Pile instrumentation during castings phase

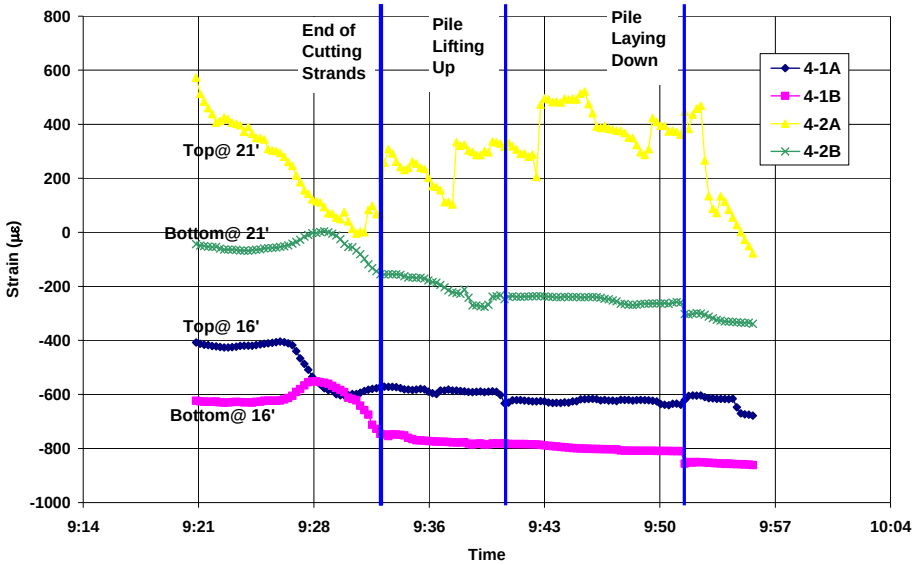

Figure 15
Strain changes during strand cutting and relocation of Pile 4

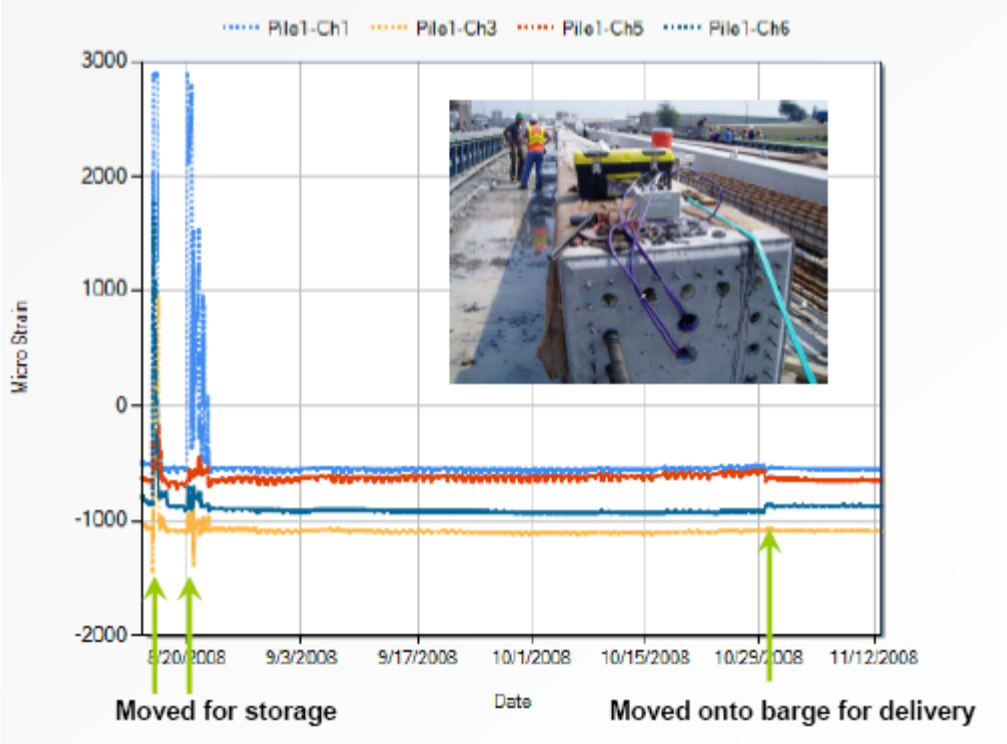

Figure 16
Recorded strain change for Pile # 1 during storage and delivery

To provide an access for the IPI array installation as well as for running the strain gage and IPI cables, 11 stainless steel junction boxes were installed flush with the top surface of the pile cap. These junction boxes were connected with the data logger room inside the protection wall with 3-in. PVC conduits for running the instrument cables. Eight stainless steel knock-out boxes were also installed flush with the sides of the pile cap to provide mounting space for the water pressure cells as well as the tiltmeters. These knock-out boxes were also connected with the data logger room with 3-in. PVC conduits for running the instrument cables.

In this phase, two 4-in. diameter PVC pipes were also installed in both the M19 eastbound and westbound piers for use later to run the steel strand tendons through it during the lateral load test. Two Freyssinet dead-end anchorages were installed at the M19 eastbound pier footing; each included a 19C15 trumplate and bursting steel spiral. A 20 in. × 20 in. × 1 in. plate was installed over each of the two 8 in. × 8 in. × 3 in. blockout on the live-end at M19 westbound pier footing. The plates were fixed to the footing by steel anchors drilled and anchored with epoxy.

(a) IPI Sensor

(b) Triaxial Accelerometer

(c) Water pressure cell

(d) Tiltmeter

Figure 17
Pile cap instrumentations

Design of Lateral Load Test

A fullscale lateral load test was designed and conducted on the M19 piers to evaluate the analysis method used to design the bridge pile foundations. The test was conducted by pulling the M19 eastbound and westbound piers toward each other using high strength steel tendons that were run through the pile caps. Each steel tendon includes 19-0.62 in. diameter strands of low relaxation, high yield strength steel (Es = 28,500 ksi).

Preparation of the site for the lateral load test started almost a week before the designated test day. This included assembling the substructure monitoring system as well as preparation and setup of the lateral load test.

The deformation profiles of casings for the selected piles were determined, prior to installing the IPI sensors, using traditional vertical inclinometer probe. Six IPI MEMS inclinometer sensors were calibrated and properly installed in each of the eight selected piles at the specified depths of 5, 15, 25, 35, 45, and 65 ft. from the bottom level of the pile cap with the lowest one tied to an anchor point at the bottom of PVC casing at 85 ft. from the bottom of the pile cap.

The substructure monitoring system was temporarily assembled two days before the test to allow collection of the data from all instruments during the lateral load test. This includes connecting the IPI sensors and strain gauges to data loggers that were placed inside the eastbound pier protection wall. The data loggers were then connected via internet phone to the data acquisition server at Geocomp headquarters, located in Boxborough, MA. The assembled monitoring system was tested to ensure that it worked properly prior to testing and that the data from all instrumentations could be recorded and retrieved in the data acquisition software. The initial readings of all instrumentations were recorded before the load test. Survey station prisms were installed at M19 eastbound and westbound, M17 eastbound, and M20 eastbound to monitor the movements of footings and bent caps of the M19 piers using an automated laser survey system.

Setup of the lateral load test started two days before the test (Figures 18 and 19). Two floating barges were deployed to the site. One barge was placed between the two pile caps to allow access and to provide support to steel strand tendons to eliminate slack and keep them out of water. Another barge was placed next to M19 westbound to carry equipment setup and to allow access to the live-end side. The steel strands were run through the 4-in. PVC pipes, which were pre-installed inside M19 footings, one by one from the dead-end at M19 eastbound toward the live-end at M19 westbound. The steel strands were first anchored at the dead-end side. A 600-ton jack with piston-end facing, 12 in. × 12 in. × 1 in. plate, an anchor block, and a 19 × 0.62 in. wedge-seating plate were installed for each steel tendon at the live-end. The strands were anchored at the live-end, and then each strand was pre-loaded to 2 kips using two 10-ton monostrand jacks, one for each tendon. Setup preparation for the load test was then completed, one day before load test, by connecting the hydraulic pumps, hoses, gauges, and manifolds to the two 600-ton jacks. The jacks' gauges were also connected to the data acquisition system for actual measurements of applied load. The jacking system at the live-end of the M19 westbound pier is presented in Figure 19(a).

Figure 18
Load test site at M19 eastbound and westbound Piers

The designed loading and unloading sequence of the lateral load test included pre-loading each tendon to 300 kips, increasing the load by 50 kips increments to 500 kips/tendon, unloading by 100 kips to 300 kips/tendon, re-loading by 100 kips increments to 1000 kips/tendon, unloading again to 300 kips/tendon, and finally cutting the strands. The duration time per load increment ranged from 5 min. for smaller loads to 30 min. for larger loads with a total estimated testing time of 6 hrs. During testing, the horizontal movements of footings and bent caps of the two M19 piers were monitored using an automated laser survey system with station prisms. This was in addition to monitoring the strains and IPI deformation measurements within the foundation piles after each load increment. The elongations of selected strands were also recorded after each load increment. DOTD bridge engineers setup two different criteria to start unloading the test at any time before reaching the intended max-applied load of 2000 kips: (1) if the maximum lateral displacement of the M19 westbound bent cap reaches 3/4 in. or (2) if the maximum change in tension strain at the top two strain gages in Pile 8 reaches 160 microstrains (1.6×10^{-4}), which corresponds to a maximum negative moment of 750 kip-ft. None of these criterion occurred during the lateral load test; however, the test was unloaded earlier at a maximum applied load of 1870 kips when the stroke in one 600-ton jack reached its maximum. The detailed adjusted loading/unloading sequence during the test is shown in Table 1.

(a) Jacking system at the live-end of w. pier

(b) E. Pier with steel strand tendons

(c) Dead-end at the eastbound pier

(d) Automated laser survey

Figure 19
Setup of lateral load test

Table 1
Loading sequence of the lateral load test

No	Lateral loads(kips) per cable	Total Lateral loads(kips)	Load Duration (min)	No	Lateral loads(kips) per cable	Total Lateral loads(kips)	Load Duration (min)
Pre-Load	300	600	90	10	700	1400	15
1	350	700	5	12	800	1600	20
2	400	800	5	13	850	1700	20
3	450	900	5	14	900	1800	20
4	500	1000	15	15	935	1870	20
5	400	800	5	16	800	1600	10
6	300	600	5	17	550	1100	10
7	400	800	5	18	300	600	10
8	500	1000	10	19	**Strands cut**		
9	600	1200	15				

Method of Data Analysis

The laterally loaded piles have been successfully analyzed using back-calculation from p-y curves of the measured data obtained using inclinometers and strain gauges. As discussed previously, various approaches such as piecewise polynomial curve fitting, high order polynomial curve fitting method and weighted residual method have been developed for p-y curve back-calculation. These methods can be applied to the bending moment data calculated from strain gauge measurements. For the interpretation of inclinometer results, Brown et al. proposed the best fit curve method using a least square technique based on a finite difference model of soil-pile *[69]*. Liao and Lin derived the deflection function of lateral loaded piles based on the energy conservation concepts *[70]*. Nip et al. assumed a fourth order polynomial to represent the shape of soil reaction profile and derived the function of the deflection profile to the match measured lateral deformation profile obtained from inclinometer measurements *[33]*.

In this study, the interpretation of inclinometer readings is performed using a high order polynomial curve fitting method; the p-y curves were then back-calculated in order to understand the lateral load behavior of the battered pile group. In addition, the moment values obtained from strain gauge readings were used in this study to compare with the moments derived by inclinometer readings in order to check the accuracy of the curve fitting method used to back-calculate p-y curves. In this section, the method of analysis is introduced in detail.

Interpretation of Inclinometer Data

The MEMS inclinometer measures rotation at selected depths along the pile for each load increment during lateral load test. The lateral displacement profile can be derived by integrating the rotation profile with depth (z) according to the following equation.

$$y = \int \theta dz \tag{8}$$

Considering pile as a flexible elastic beam on an elastic foundation, the lateral responses of the pile can be evaluated by solving the following differential equations for deflection-curve (or rotation).

$$\mathrm{M} = \mathrm{EI}\frac{\mathrm{d}^2\mathrm{y}}{\mathrm{dz}^2} = \mathrm{EI}\frac{\mathrm{d}\theta}{\mathrm{dz}} \tag{9a}$$

$$V = EI\frac{d^3y}{dz^3} = EI\frac{d^2\theta}{d^2z} \tag{9b}$$

$$\mathrm{P} = \mathrm{EI}\frac{\mathrm{d}^4\mathrm{y}}{\mathrm{dz}^4} = \mathrm{EI}\frac{\mathrm{d}^3\theta}{\mathrm{d}^3\mathrm{z}} \tag{9c}$$

where *y* is the pile lateral deflection, *z* is the depth below the pile top, θ is rotation, *M* is the bending moment, *V* is the shear force, *P* is the soil reaction force per unit length and *EI* is the flexural stiffness of the pile.

High-Order Polynomial Curve Fitting. Among the several methods mentioned earlier, only the least square technique, energy method, and high order method were used to interpret the inclinometer data for lateral load test *[33, 69, 70]*. Considering the non-uniformity of the soil distribution at the M19 pier along with the limitation of available data and inclination of pile, Nip et al.'s back-analysis method, which assumes the shape of the soil reaction profile rather than the shape of p-y curve method *[33]*, is found to be the most suitable method for interpreting the measured inclinometer data from the full-scale lateral load test of the M19 east bound pier.

The shape of soil reaction profile with depth z (P_z) is assumed to follow a 4th order polynomial, similar to Nip et al. *[33]*, which is defined as:

$$P_z = az + bz^2 + cz^3 + dz^4 \quad (10)$$

Since inclinometer sensors provide rotation data, rotation profile can be obtained by integrating equation (10) three times with depth (θ_z). This yields a 7th order polynomial function as follows:

$$\theta_z = a_1 z + a_2 z^2 + a_4 z^4 + a_5 z^5 + a_6 z^6 + a_7 z^7 \quad (11)$$

Where, coefficients a_1, a_2, and a_4 through a_7 need to be determined through curve fitting. Equation (11) was used in this study to perform non-linear fit of the measured rotation profiles obtained from the IPI measurements at different load increments using a reduced chi-square minimization of residual error regression analysis (Origin Pro program). The chi-square minimization method minimizes the deviations or errors of the theoretical curves from the experimental data in order to select the appropriate parameter values for best fitting that yield least square of errors. In order to reduce the chi-square value, an iteration procedure was performed. The Origin Pro Program uses Levenberg-Marquardt (L-M) algorithm, a combination of Gauss-Newton method and the steepest descent method for iteration. The reduced chi-square value is simply the mean deviation for all data points. The precision or the goodness of the fitted values is measured by standard error; R-square (R^2).

Some boundary condition assumptions were made to develop a rotation profile from the measured IPI data. Since the pile cap is 7 ft. thick reinforced concrete, the pile-cap connection was considered to be a fixed end with zero rotation. In addition, the IPI measurements showed that the rotations at 65 ft. are minimal thus were treated as zero rotation ($\theta_{z=65} = 0$). Examples of curve fitting of rotation for pile 8 (row 4) obtained at 1870 kips and pile 11 (row 1) obtained at 1745 kips lateral load are depicted in Figure 20.

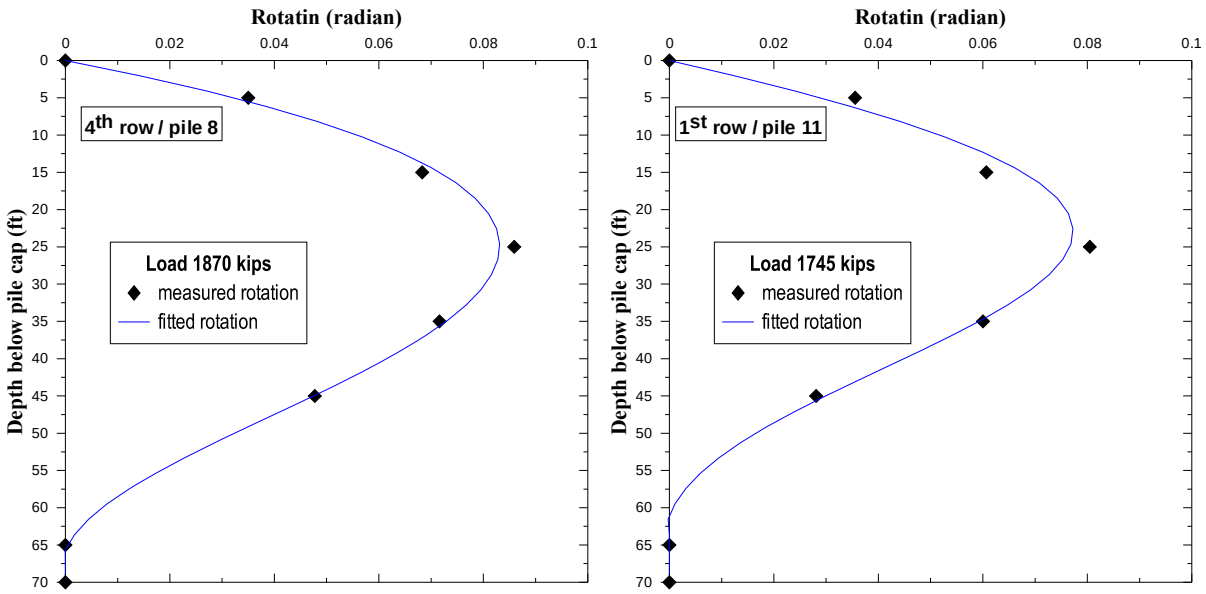

(a) (b)

Figure 20
Example of curve fitting of IPI measurements with polynomials

Derivation of Lateral Displacement Profile. Lateral deflection profiles can be calculated directly from the measured rotation by IPI sensors using the following trigonometric equation.

$$y = \Delta l \, sin\theta \tag{12}$$

Where, Δl is the depth between two rotation values.

In order to check the accuracy of the derived lateral displacement profile, the measured deflections from the inclinometer are compared with lateral deflections derived from high order polynomial fitted rotation curve for Piles 8 and 11 as shown in Figure 21. It clearly shows that the derived lateral displacement profiles obtained from high order polynomial curve fitting matches very well with the measured displacement profiles which demonstrates that the 7th order polynomial fitted function was capable of capturing the measured rotation profiles and hence can be used to deduce the displacement profiles, moment profiles, shear force profiles and soil reaction profiles with minimal errors.

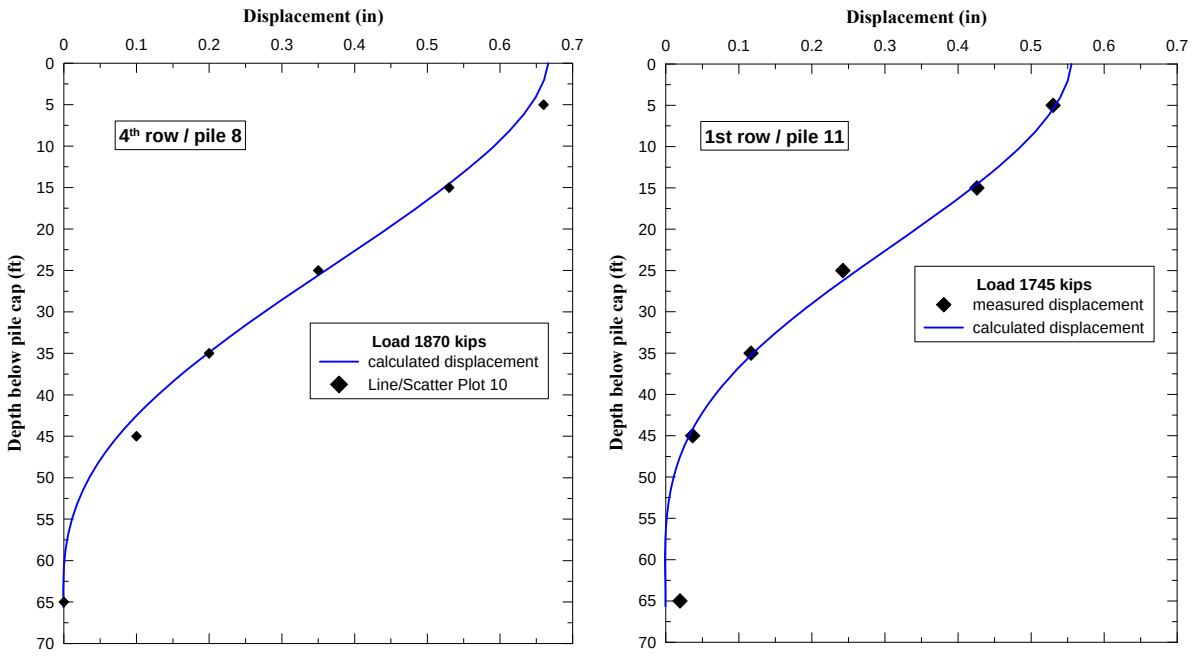

(a) (b)

Figure 21
Comparing the measured displacement with the derived displacement profile

Development of Moment, Shear, and Soil Reaction Profiles. Once the rotation profile (θ_z) is fitted into the function and polynomial coefficients are determined, moment, shear force and soil reaction profiles can be deduced by differentiating equations (9a) through (9c) with respect to rotation and multiplying the result by the flexural stiffness (EI) of the PPC pile. The resulting expressions are as follows.

$$M_z = (a_1 + 2a_2z + 3a_3z^2 + 4a_4z^3 + 5a_5z^4 + 6a_6z^5 + 7a_7z^6) \times \text{EI} \quad (13)$$

$$V_z = (2a_2 + 6a_3z + 12a_4z^2 + 20a_5z^3 + 30a_6z^4 + 42a_7z^5) \times \text{EI} \quad (14)$$

$$P_z = (6a_3 + 24a_4z + 60a_5z^2 + 120a_6z^3 + 210a_7z^4) \times EI \quad (15)$$

The flexural rigidity or stiffness depends on the properties of the pile, its cross section and the moment developed along the length of the pile. Thus, it needs to be appropriately calculated for accurate prediction. The piles are composed of two different sections: solid and void. The first portion of the pile is solid whereas the second portion of the pile consists of 22.5 in. concentric void. The moment of inertia (I) was calculated based on the geometry as:

$I_{\text{solid pile (no void)}} = 139{,}968 \text{ in}^4$

$I_{\text{Hollow pile (with void)}} = 128{,}475 \text{ in}^4$

The modulus of elasticity for the concrete (E_c) was calculated using an empirical formula as

$$E_c = 57{,}000 \times \sqrt{f'_c} \quad (16)$$

Where, E_c is expressed in psi and f'_c is the average 28-day compressive strength of the concrete in psi. f'_c was calculated based on the average of six compression tests conducted on cylindrical specimens at the time of testing (f'_c = 8000 psi). The calculated elastic modulus ($E_c = 5.098\times10^6$ psi) was assumed to be a constant since the piles' deformation were within the elastic range. However, in reality, the behavior of piles is somehow non-linear and the cracking of the pile reduces its stiffness. Nip et al. developed a curve of flexural stiffness and bending moment from strain compatibility and the equilibrium of forces to describe the relation of EI with bending moments as illustrated in Figure 22 *[33]*. It clearly demonstrates that the flexural stiffness reduces gradually for partially cracked to cracked state of concrete. However, in the present study, the calculated highest moment was 1200 kips-ft., which is nearly equal to 1.4 MN-m from where the flexural stiffness starts reducing as shown in Figure 22. The E_c value estimated from the results of 28 days compression strength tests on cylindrical specimens were increased by 5% ($E_c = 5.35\times10^6$ psi) to incorporate the increase in strength/stiffness at the time of lateral load testing (6 months).

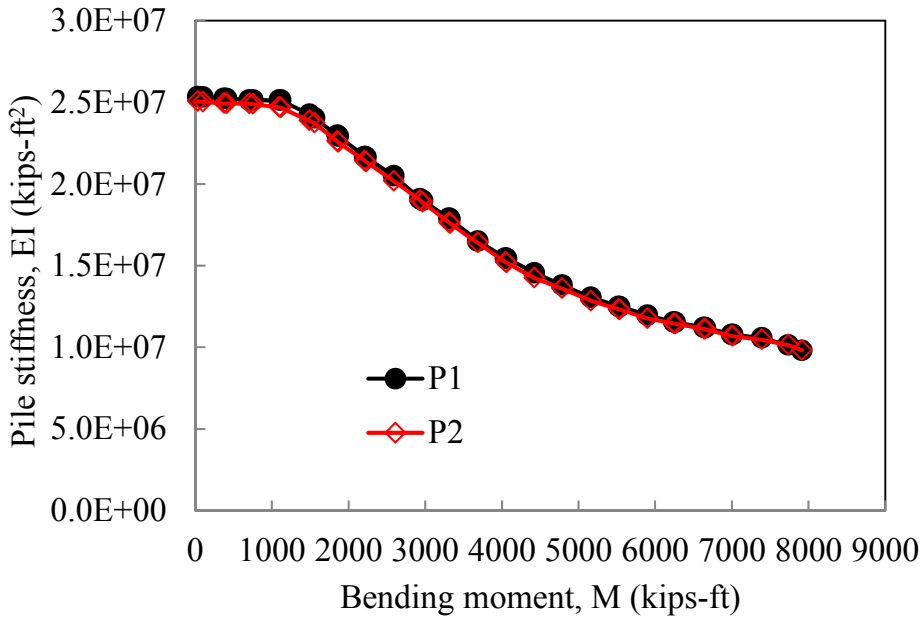

Figure 22
Relationship between EI and M (after *[33]*)

Back-calculating p-y Curves. The back-calculation of p-y curves from results of lateral load test is important since the back-calculated p-y curves can be used to analyze the lateral behavior of pile installed in similar types of soil where lateral load tests are not feasible. The p-y curves can be derived from the inclinometer readings through the derivation of lateral displacement profiles and the soil reaction profiles for each load increment. Once the lateral displacement profile (y) and soil resistance profile (P_z) are derived, the p-y curves at different depths can be deduced. In summary, the back-calculation of the p-y curves from inclinometer data involves the following five steps:

Development of the rotation profile (θ_z) for each load increment by using high order polynomial curve fitting to measured inclinometer rotation data.

Derivation of the displacement profiles (y) with depth (z) for different load increments through single integration of the rotation profiles ($y = \int \theta dz$).

Development of moment profile (M_z) for each load increment with depth by single differentiation of rotation profile and multiplying by EI ($M = EI\frac{d\theta}{dz}$).

Calculation of soil resistance (P_z) for different load increments by double differentiation of the developed moment profile($P = EI\frac{d^2M}{d^2z}$).

Construction of p-y curves for selected depth by taking displacement and corresponding soil resistance value for each load increment.

Using the fitted rotation profile, the lateral displacement profile was obtained from equation (12) and the soil reaction profile corresponding to each load increment was calculated using equation (15). Thereby, using the soil reaction per unit length obtained at different load levels and the corresponding lateral depth at selected depths, the p-y curves at selected depths were back-calculated.

Interpretation of Strain Gauge Measurements. Two pairs of strain gauges (SG1 and SG2) were installed at two different depth levels in twelve selected piles during casting as discussed previously. The main purpose of installing the strain gauges was to calculate the transfer of axial loads and bending moments at strain gauge locations along the pile length. The strain distribution measured by the strain gauges is the summation of the axial strain and the bending strain as given in equation (17) and depicted in Figure 23.

$$\text{Strain}_{\text{measured}} = \text{Strain}_{\text{due to axial}} + \text{Strain}_{\text{due to bending}} \quad (17)$$

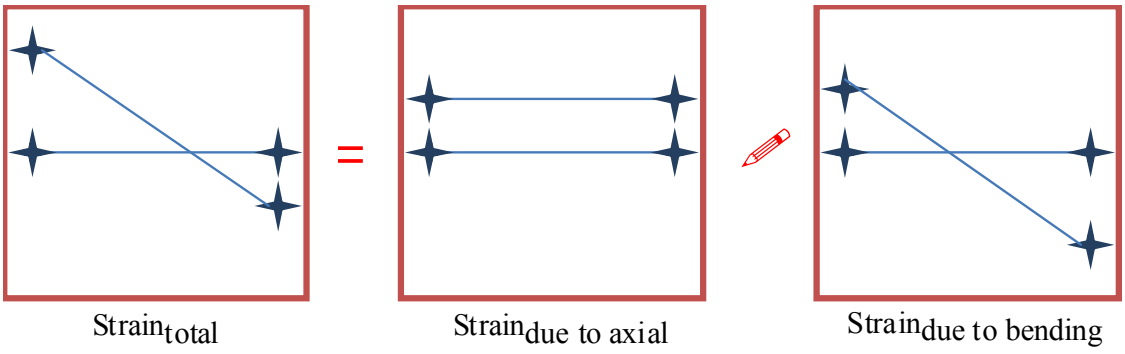

Figure 23
Strain distribution due to axial load and moment

Calculation of Moment from Strain Gauge Measurements. The moments of the pile at corresponding strain gauge locations were calculated from the strain gauges using equation (18). According to Rollins et al., this approach cancels out any contribution due to axial strain, leaving strains only due to bending, and makes it possible to accurately compute the bending moment *[24]*.

$$M = \frac{EI(\varepsilon_t - \varepsilon_c)}{h} \quad (18)$$

where, ε_t is tensile strain (+ve), ε_c is compressive strain (-), and h is the horizontal distance between the two gauges spaced at equal but opposite distances from the neutral axis.

Calculation of Axial Load from Strain Gauge Measurements. The load transfer mechanism of battered piles is different than for vertical piles. In vertical piles, the total applied lateral load is transferred to soil media only. However, for battered piles, the lateral load will also be transferred to axial compression or tension force as shown in Figure 24. The part of lateral load transferred to axial load reduces the developed bending moment along the pile and decreases the lateral soil resistance. The induced axial loads can be calculated from the strain gauge data as:

$$Q_A = \frac{EA(\varepsilon_t + \varepsilon_c)}{2} \quad (19)$$

where, A is the cross section area of pile. The axial load is compression when $\varepsilon_t < \varepsilon_c$ and tension when $\varepsilon_t > \varepsilon_c$. Figure 25 presents a summary flow chart for the analysis of the inclinometer and strain gauge measurements obtained during the lateral load test.

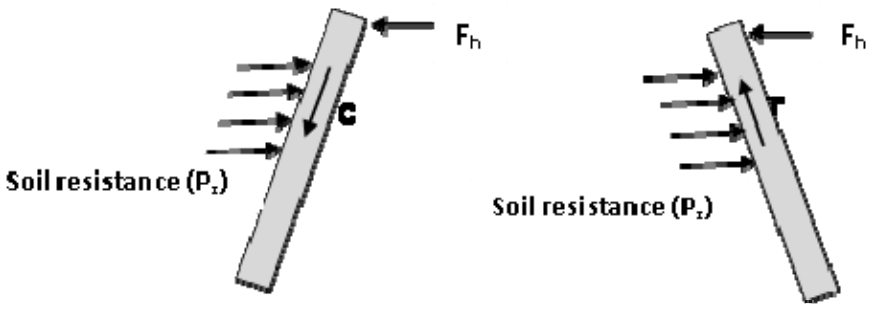

Figure 24
Decomposition of applied lateral load on battered pile

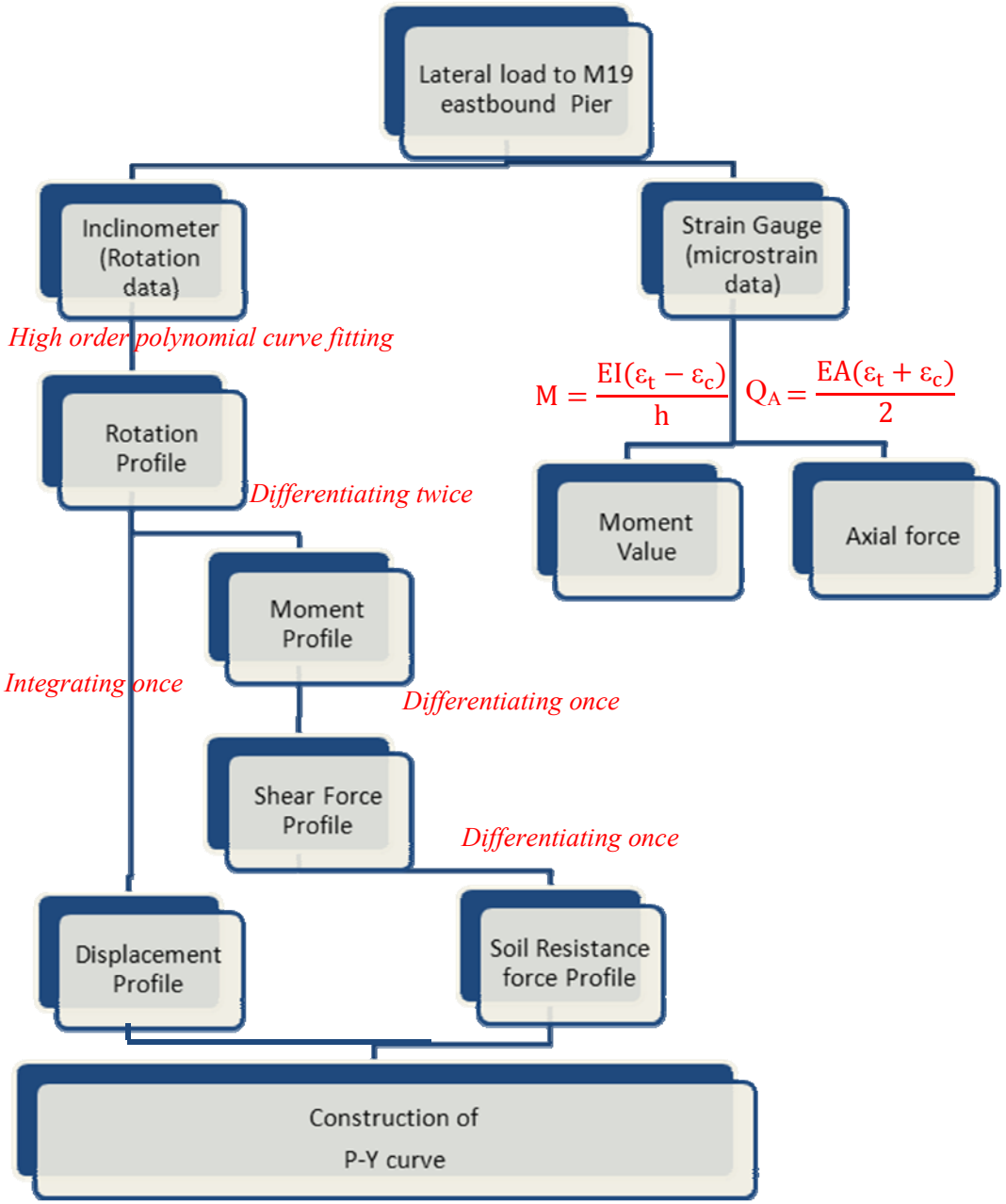

Figure 25

Flow-chart of analysis for battered pile group

FB-MultiPier Design Analyses

The FB-MultiPier was selected to perform the numerical analysis of the battered pile group foundation at the M19 eastbound pier. The FB-MultiPier was preferred for numerical analysis because the entire I-10 Twin Span Bridge design was done using this software. The

objective of the FB-MultiPier analysis was to evaluate its design capacity of battered pile groups with the results of full-scale lateral load test.

Introduction of FB-MultiPier. The FB-MultiPier program can be used to analyze the entire components of the bridge from the bridge slab to the soil layer by incorporating a finite-element analysis. It performs the analysis by generating the finite element models for given geometric descriptions of the structure and the foundation system. For the generation of finite element models, the FB-MultiPier incorporates several types of elements such as membrane element, flat shell element, plate element, and a special element generated by adding normal rotational stiffness to the shell element, which accounts for the torsional force transmitted from pile to pile cap. The soil modeling in the FB-MultiPier provides the ability to define the soil layers at varying depths. Each soil layer can be modeled either as sand or clay using one of the several built in p-y curves or by applying user-supplied p-y curves to the respective layers. The p-y curves incorporated in the FB-MultiPier and their input parameters are summarized in Table 2.

The pile-soil interaction in a pile group is characterized by user defined p-multipliers to account for group effect. FB-MultiPier uses an iterative solution technique to predict the lateral displacements. During iteration, it calculates stiffness of soil and piles, and eventually generates the stiffness matrix to predict the lateral displacement of the pile as output. The displacement is then used to predict the internal forces of the structures' members.

Table 2
Summary of input parameter of p-y curves used in FB-MultiPier

Soil type	Soil stiffness	Soil location relative to ground water table	Parameters	p-y curve
Sand	Loose–dense	Above	ϕ, K_s, γ	O'Neill and Murchison *[75]*
		Below	ϕ, K_s, γ	Reese et al. *[40]*
Clay	Soft/medium stiff	Above	S_u, ε_{50}	O'Neill and Gazioglu *[76]*
		Below	S_u, ε_{50}	Matlock *[25]*
	Stiff	Above	S_u, ε_{50}	Reese and Welch *[66]*
		Below	S_u, ε_{50}, K_s, γ	Reese and Van Impe *[74]*

Modeling of M19 Eastbound Pier Foundation using FB-MultiPier. The M19 eastbound pier structure was modeled with 24 battered piles, pier cap, 2-pier column, shear wall, and a cantilever bent as illustrated in Figure 26. The piles are modeled as 3D discrete elements. The discrete element models the non-linear behavior of concrete material by using input or default stress-strain curves that are a function of compressive stress of concrete (f'_c) and modulus of elasticity of concrete (E_c). The input data defining the pile geometry and

structural properties such as f_c, E_c, pile length and width, reinforcement area, were input to generate the pile model. The fixed head pile cap was modeled using nine nodded shell elements which is based on Mindlin's theory that can take into account the bending and shear deformations. Similarly, each soil layer surrounding the piles was modeled as an attached non-linear spring which can be characterized by selecting a proper p-y curve. The p-y curve was selected based on soil type and properties. The inputs required for modeling soil layers are undrained shear strength (S_u), strain corresponding to 50% of the maximum stress (ε_{50}), unit weight of the soil (γ) and the subgrade modulus of soil (K_s) for clayey soil; or friction angle (ϕ), K_s and γ for sandy soil.

The values of these soil input parameters were based on laboratory and in-situ test results. The undrained shear strengths (S_u) were obtained from unconsolidated undrained (UU) triaxial tests that were conducted on undisturbed samples obtained from soil borings. The S_u were also estimated from CPT tests. The value of strain that corresponds to 50% of the maximum principle stress (ε_{50}) was determined from UU tests, and were compared with the typical values of ε_{50} recommended by Matlock (1970) as presented in Table 7. The subgrade soil modulus (K_s) was estimated based on undrained shear strength value as given in Table 8.

Similarly, SPT blow counts (N_{60}) were used to estimate the internal friction angle for sand. The values of soil parameters for each layer and selected p-y curve for that layer are presented in Table 3 and Figure 27.

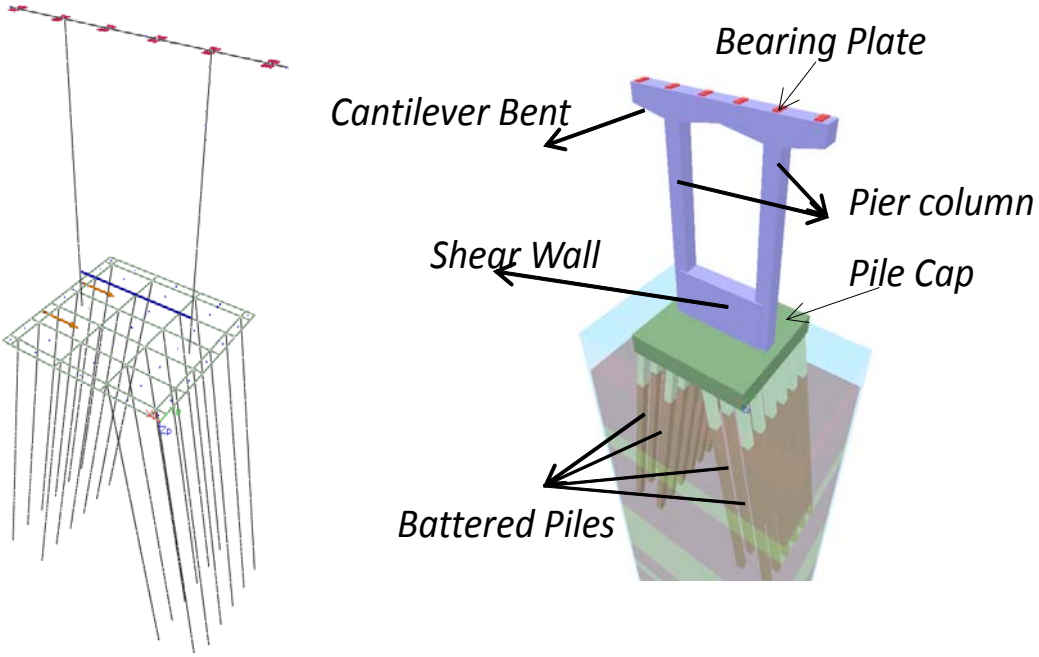

(a) Structure view (b) 3D pier view

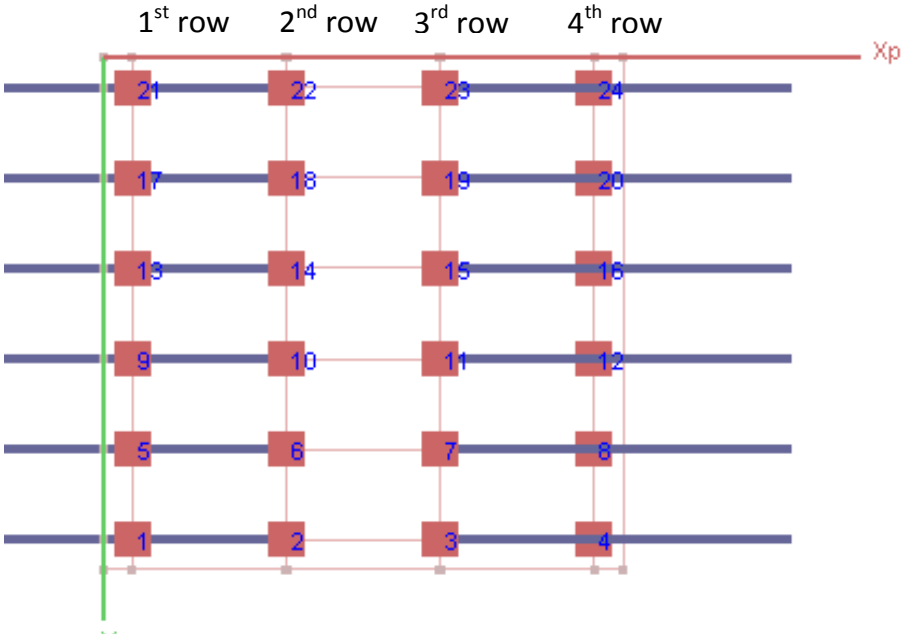

(c) Top view of Pile layout

Figure 26
FB-MultiPier model for M19 Pier

Table 3

Value of input parameters for FB-MultiPier Analysis (based on soil boring)

Depth below excavated ground (ft)		Soil type	Lateral model (p-y curve)	Unit weight (pcf)	Undrained shear strength (psf)	Friction angle ϕ(deg)	Subgrade modus K_s (ksi)	Strain ε_{50}
15	23	Cohesive		120	150			0.028
23	30	Cohesive		120	1400		186	0.008
30	32			120	900		150	0.010
32	35			118	280			0.02
35	45		Clay soft	108	950		150	0.01
45	57	Cohesionless	Sand (Reese)	120		33	64	
57	73	Cohesive	Clay soft	114	900			0.01
73	93		Clay stiff	123	2000		266	0.007
93	99	Cohesive	Clay stiff	128	1500		200	0.008
99	101	Cohesive	Clay soft	124	1140			0.009
101	105	Cohesionless	Sand(Reese)	120		31	64	
105	138	Cohesionless	San (O'Neil)	120		38	123	
138	145	Cohesive	Clay stiff	113	1400		186	0.008
145	155	Cohesive	Clay stiff	107	1900		253	0.007
155	163	Cohesionless	Sand (Reese)	127		28	46	
163	174	Cohesive	Clay stiff	115	2600		346	0.006
174	178	Cohsieve	Clay stiff	127	1600		213	0.007
178	186	Cohesinless	Sand (Reese)	120		29	64	
186	194	Cohesinless	Sand (ONeill)	120		38	149	

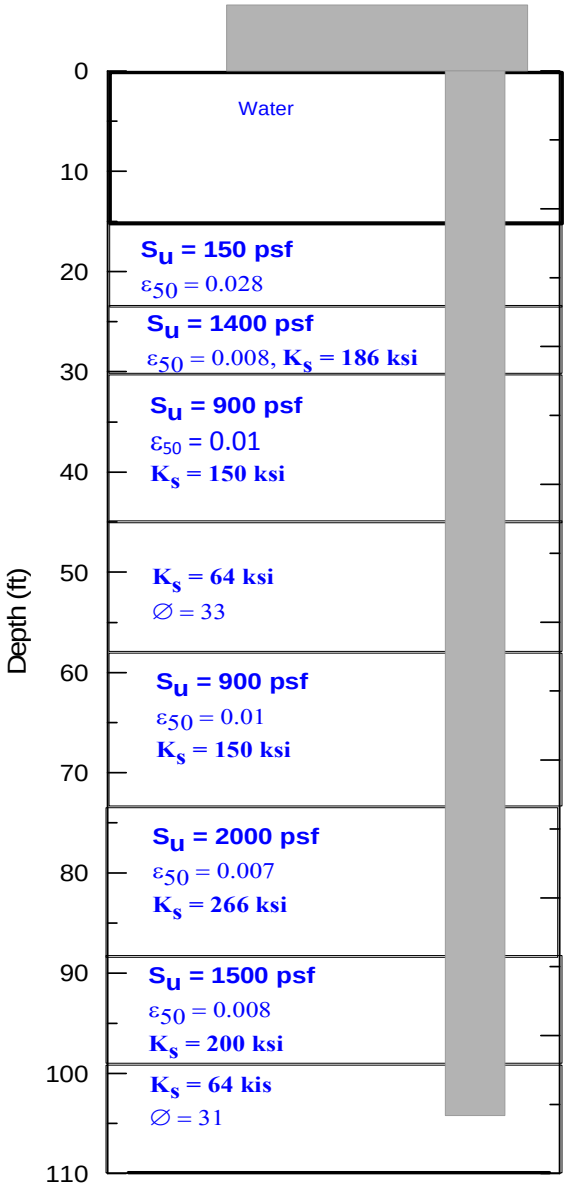

Figure 27

Soil input values used for generating FB-MultiPier model

.

DISCUSSION OF RESULTS

Lateral Load Test Results

Displacement Measurements

Figure 28 presents the horizontal deflection profiles obtained for the selected piles. Data from Pile 5 was not presented because the MEMS sensors were damaged at two depths. The deflection profiles indicate that most of the lateral deformation occurred within the upper 50 ft. of the piles' length. The maximum lateral deformation measured at 5 ft. below the bottom level of the pile cap ranged from 0.59 in. to 0.67 in. This is in agreement with the measured lateral deformations of the pile cap using the automated laser survey, which were 0.58 in. and 0.66 in. for the southwest and northwest corners of the M19 eastbound pier, respectively, as shown in Figure 29.

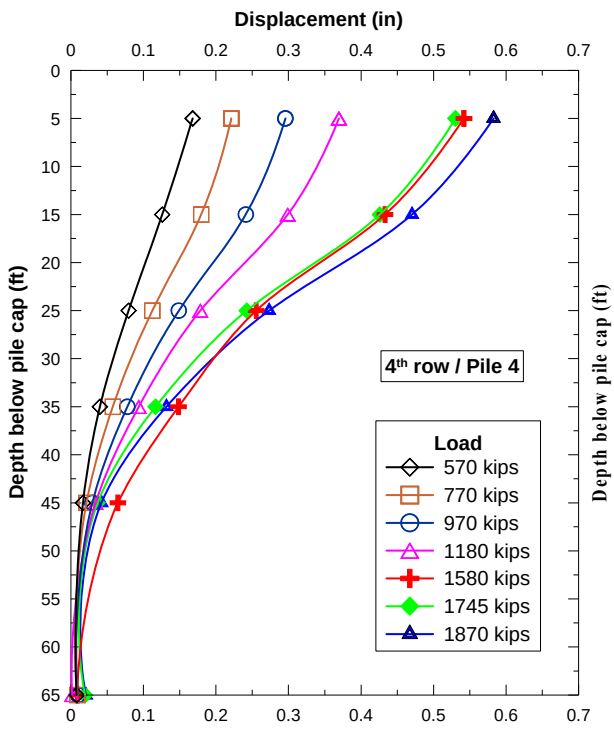

(a) Pile 4

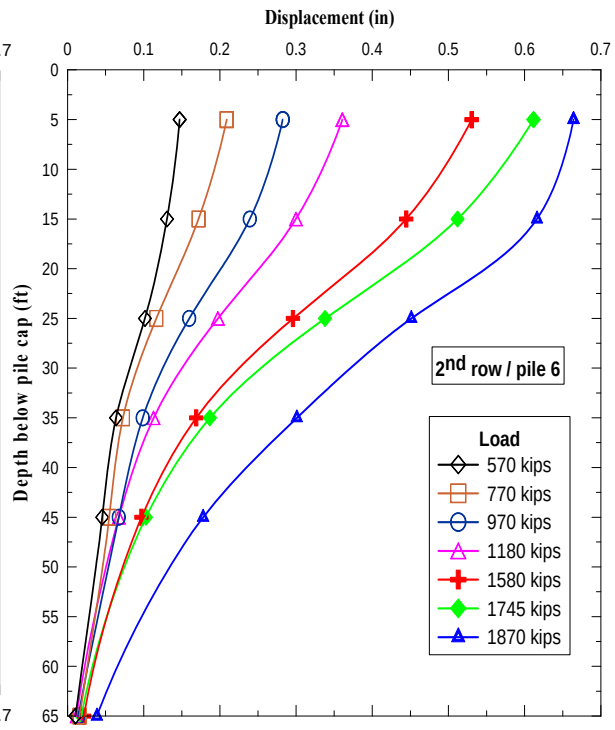

(b) Pile 6

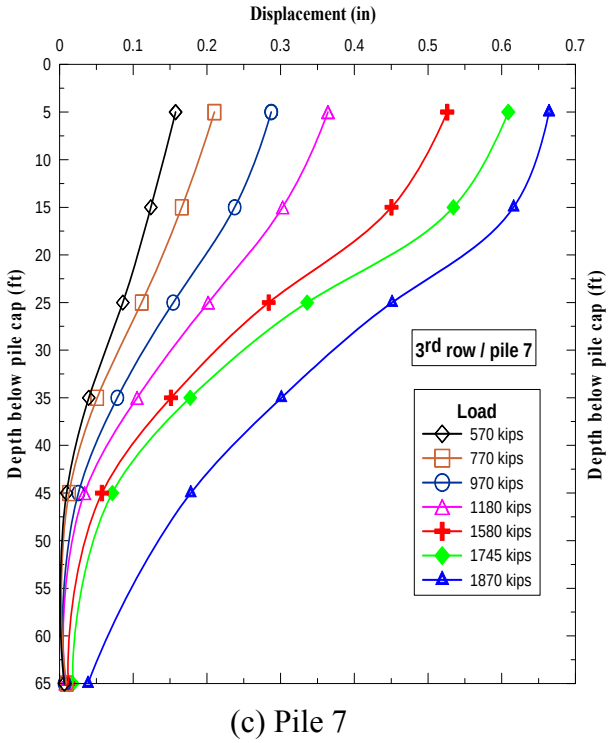

(c) Pile 7

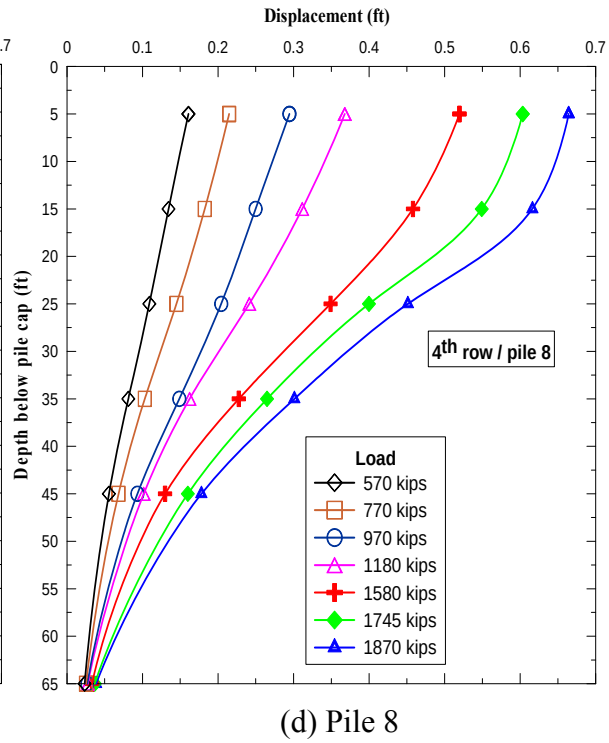

(d) Pile 8

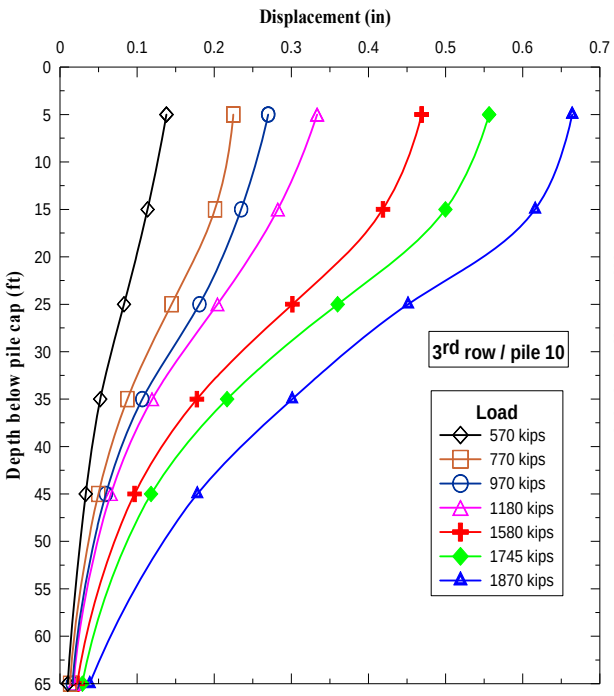

(e) Pile 10

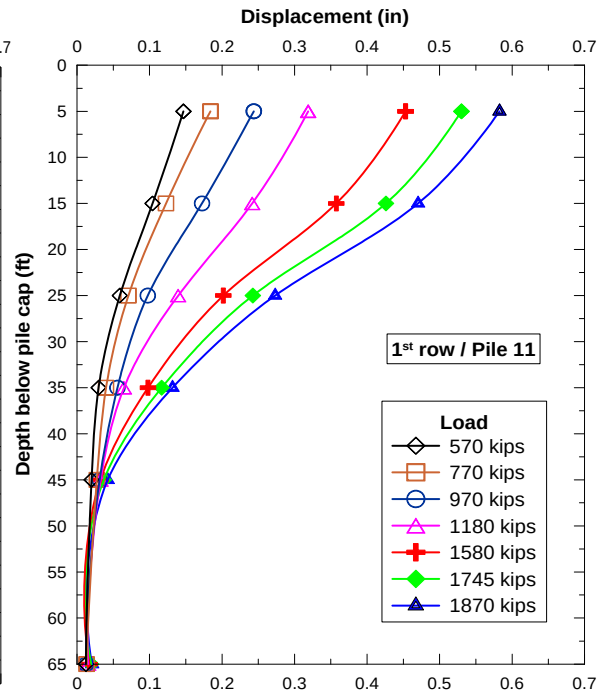

(f) Pile 11

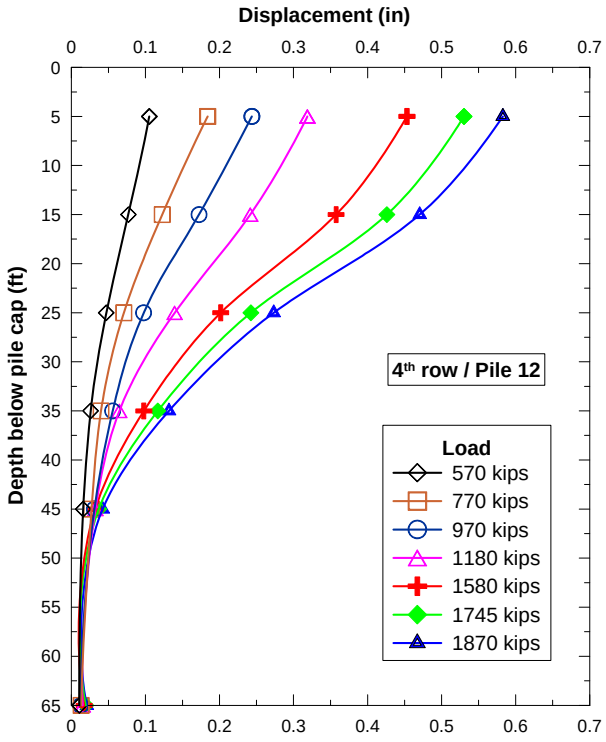

(g) Pile 12

Figure 28

Profile of lateral deformation of piles

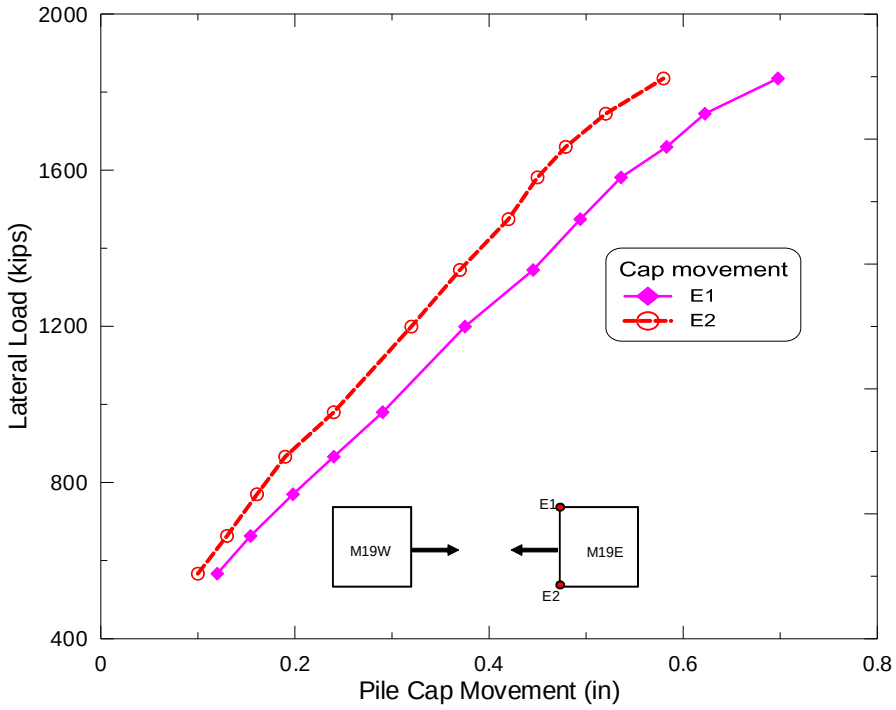

Figure 29

Profile of lateral deformation measured from survey prism

Strain Measurements

During testing, some strain gauges were incapable of capturing the strain at the applied maximum load of 1870 kips. Also, some strain gauges, such as SG1 of Pile 2 and SG2 of Pile 7, were inactive. Similarly, some measured data from SG1 of Pile 8 and SG II of Pile 1 were deemed unreliable as the difference between compression and tension strains were found to be substantially high. Figure 30 presents the measured strains obtained for the instrumented piles at two lateral loads, 570 kips and 1780 kips, respectively.

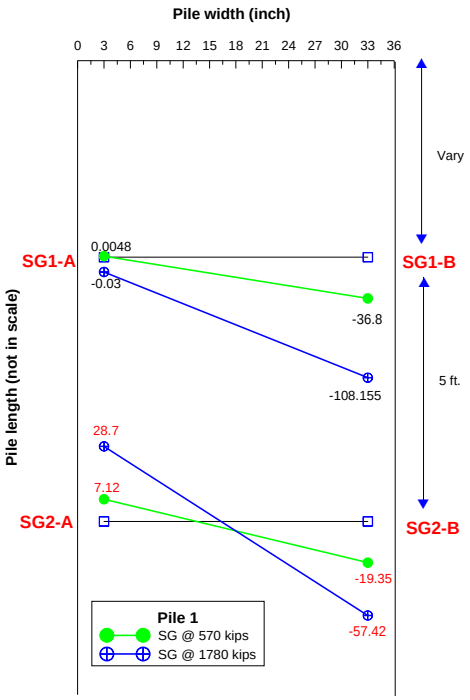

(a) Pile 1

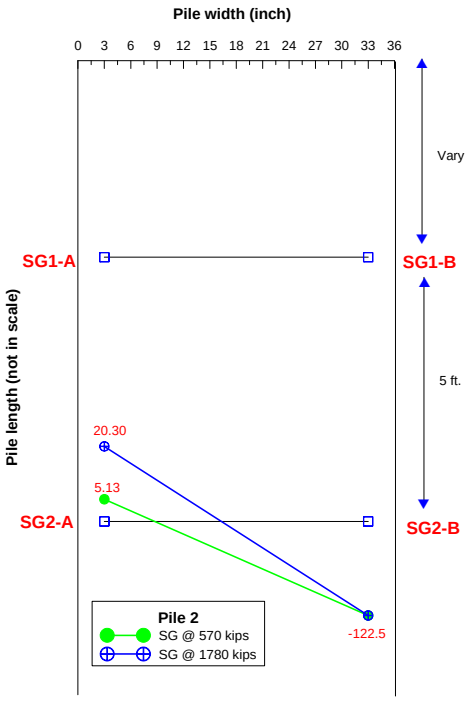

(b) Pile 2

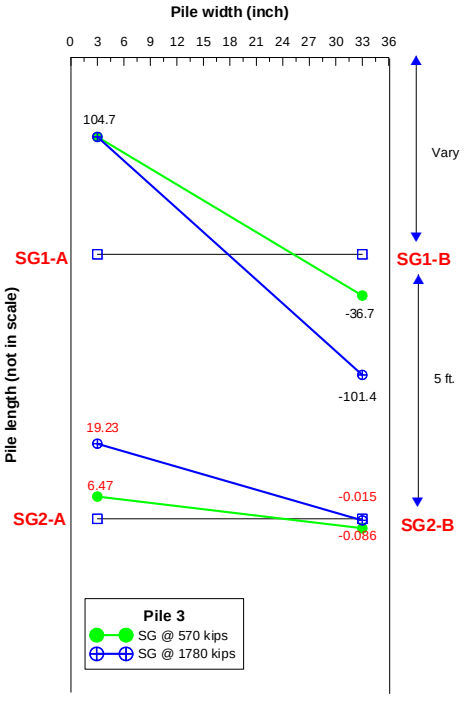

(c) Pile 3

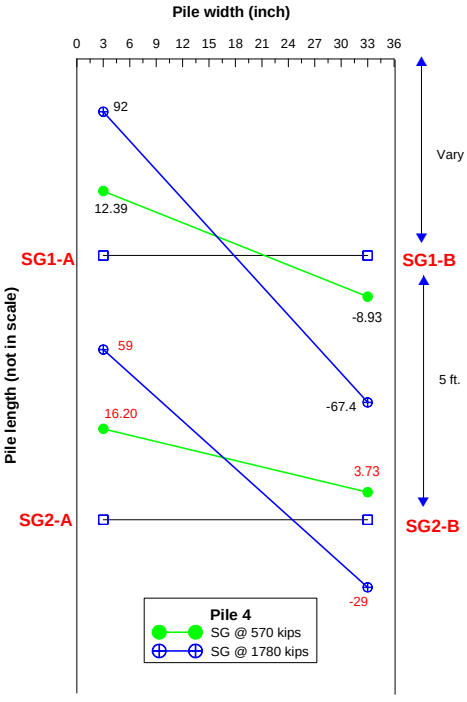

(d) Pile 4

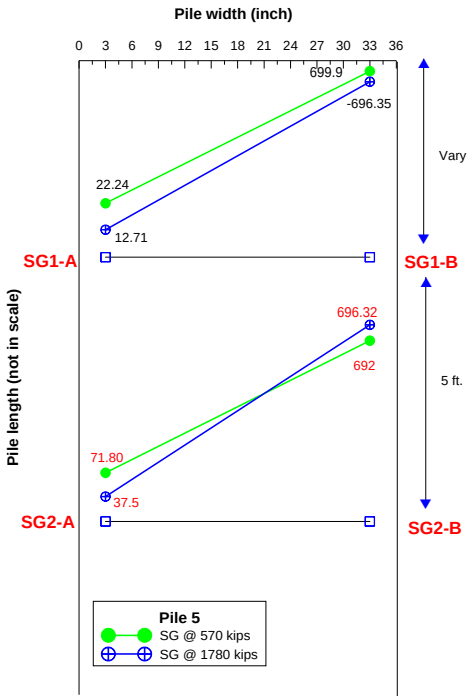

(e) Pile 5

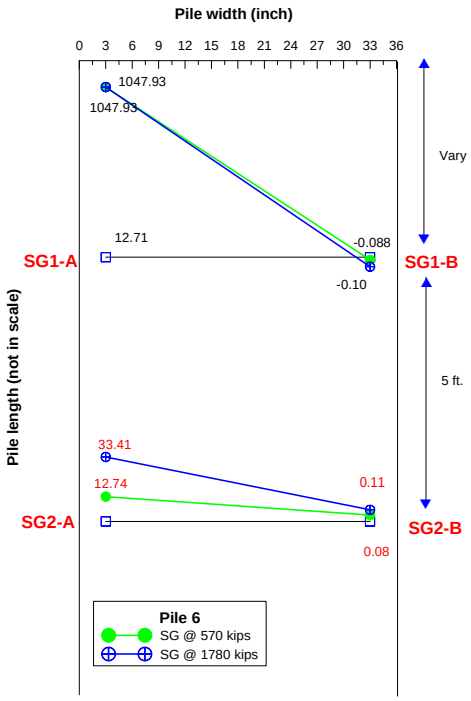

(f) Pile 6

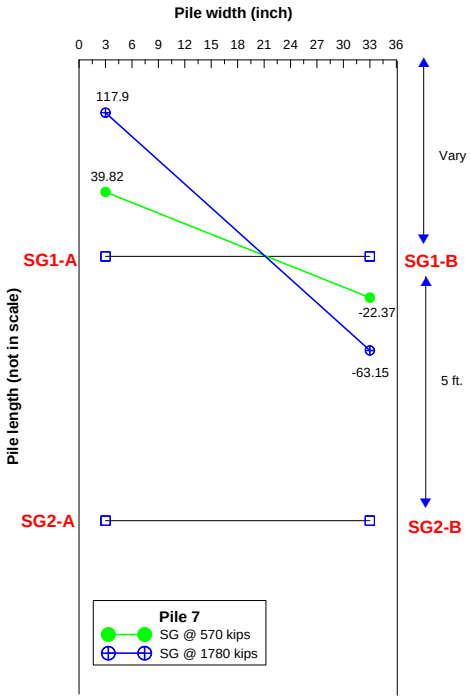

(g) Pile 7

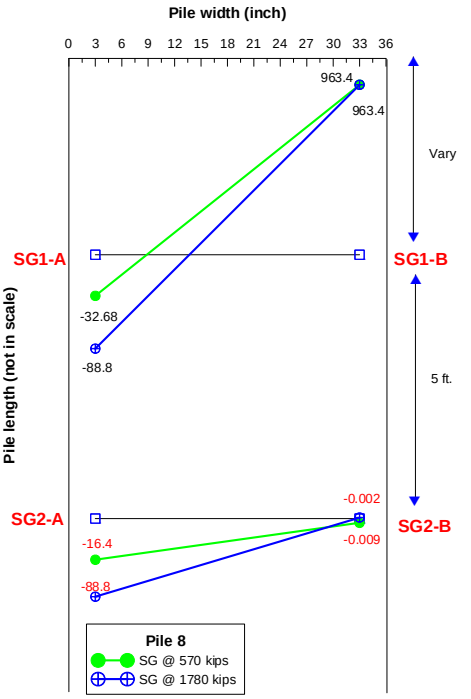

(h) Pile 8

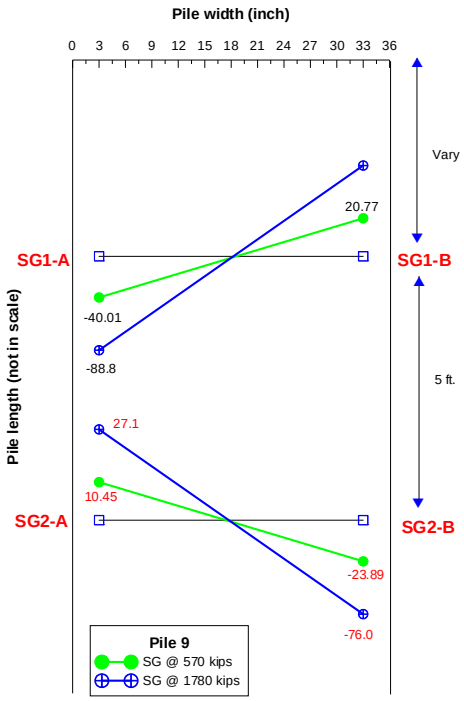

(i) Pile 9

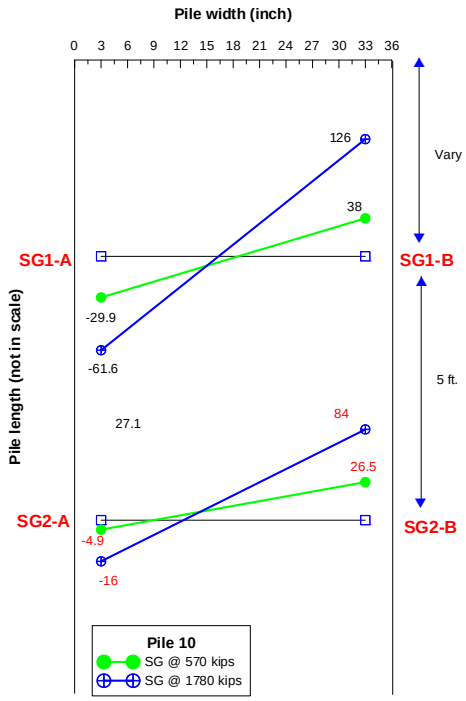

(j) Pile 10

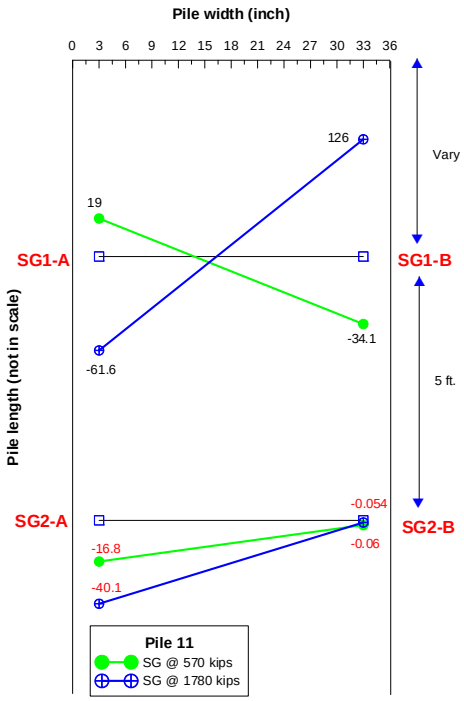

(k) Pile 11

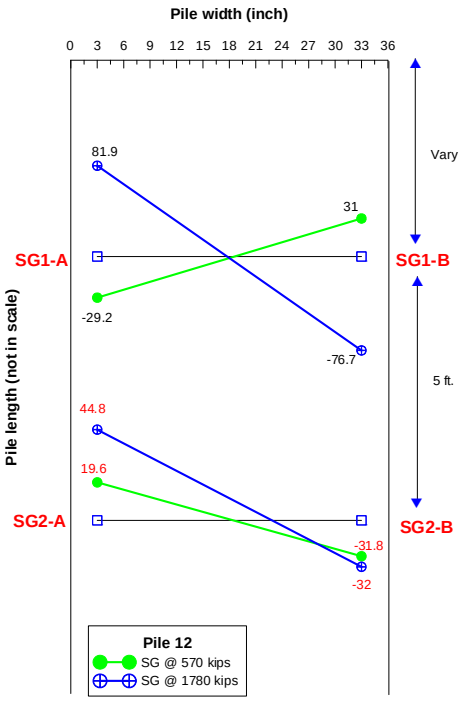

(l) Pile 12

Figure 30
Measured strains at two peak load

Back-Calculation Analysis of Measured Pile Deflections

The measured IPI data were analyzed using the high-order-polynomial method introduced previously. The measured rotation profiles were fitted using the curve-fitting technology offered in the program Pro Origin. Then, the deflection profiles were obtained by converting rotations to horizontal displacements using equation (12). With fitted rotation profiles, the bending moment profile, shear force profile, and soil resistance profile were calculated using equation (4). Finally, p-y curves at each depth were obtained by combining the resistance profiles and horizontal deflection profiles at different load levels.

For the convenience of clear presentation of the analyses results, a schematic drawing as shown in Figure 31 is used to illustrate some of the terms used later in this section. The pile results are discussed with regard to row positions as well as the position within each row in order to study the pile group effect. The individual piles are classified based on their locations within the foundation as illustrated in Figure 31. Across the loading direction, the row of piles located at the position closest to the loading points is termed as the 4th row (back row or trailing row); whereas the row located at the position farthest away from the loading points is termed as the 1st row (front row or leading row). The piles located at the edge of the pile group in both directions are called corner piles (i.e., Piles 3, 4, 11, and 12). All others are designated as inner piles.

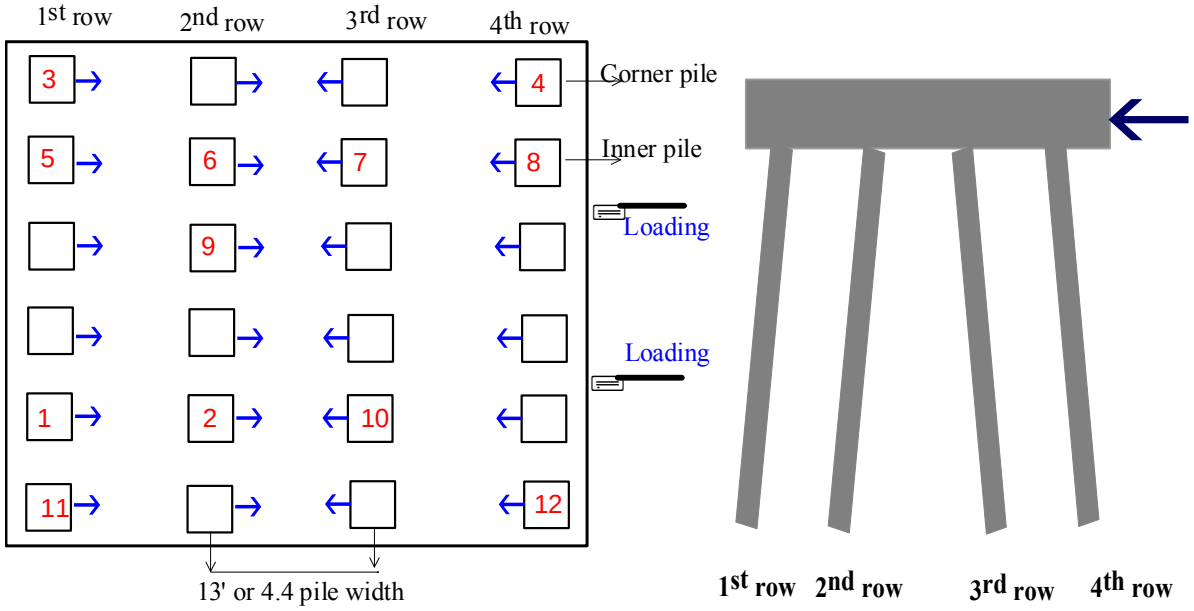

(a) (b)

Figure 31

(a) Plan view of pile layout (b) side view of pile layout

Lateral Deflection Profiles

The horizontal deflection profiles derived from fitted rotation profiles were verified by the deflection calculated from IPI measurements as shown in Figure 21. In order to investigate the effects of pile location and spacing on pile deflection behavior, pile lateral deflection profiles were compared between piles located in different rows and piles located in the same row.

Lateral Deflection for Piles Located in Different Rows

Figure 32 presents the profiles determined for piles 11, 6, 7, and 8. The maximum displacement values obtained at the peak lateral load of 1870 kips for the piles located at the back row when compared to the front row do not differ; the variation of displacements is within 10%. The maximum displacement at the pile head of 4th row and 1st row are 0.67 in. and 0.6 in., respectively. This is in excellent agreement with the result of the automated survey measurements, which were 0.58 in and 0.66 in, respectively as shown in Figure 29.

Further examination of the derived displacement profiles reveals that the depth from pile head to the zero displacement for piles depends upon the magnitude of loading and location in the pile group. At higher loading, the depth from the pile head to zero displacement for the 4th row pile is about 55-60 ft. (18B to 20B, where B is pile width), whereas, it is about 45-50 ft. (15B-16B) for the 1st row pile. The depth to the zero displacement for the 2nd row and the 3rd row piles are similar; this may be due to the increased spacing between the opposite battered piles (positive battered pile in 2nd row and negative battered pile in 3rd row) along the depth.

In order to have a better understanding of the load-displacement relationship, the curve of total load applied at the pile cap versus derived peak displacement at the pile head is plotted. It is then compared with the automated laser survey measurements as shown in Figure 33.

Figure 33
Pile head lateral displacement along with applied lateral load

The figure demonstrates the linear nature and is also a slight indication of bi-linear behavior of the piles. All piles exhibit a similar lateral displacement profile. It is noteworthy, as shown in Figure 32, that the front row pile (Pile 11) comparatively takes more lateral load at the same displacement, whereas, the 4th row pile has larger lateral deformation at a similar load. The margin, however, is not substantial. The graph does not have a peer peak load point. The load seemed to increase not yet reaching the yield point.

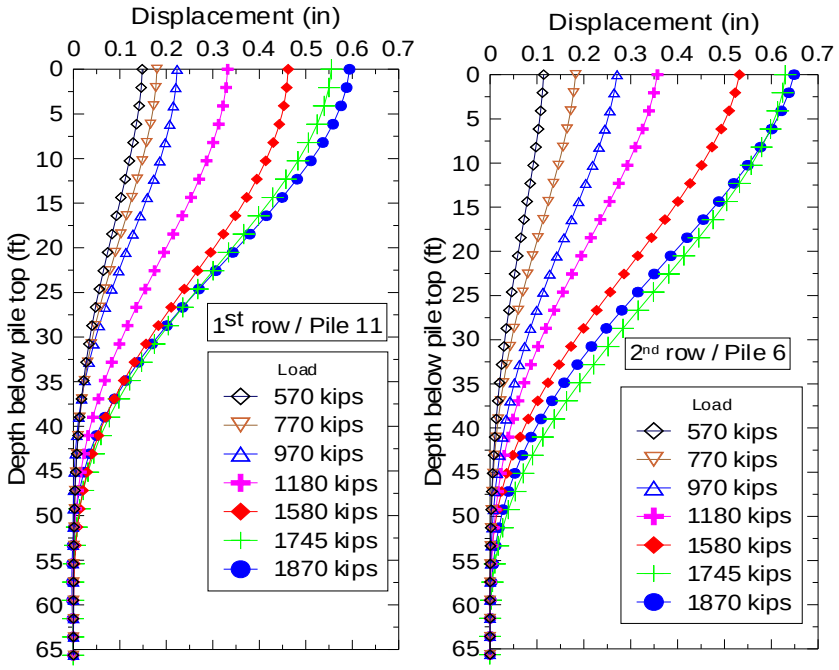

(a) Pile 11(row 1) (b) Pile 6 (row 2)

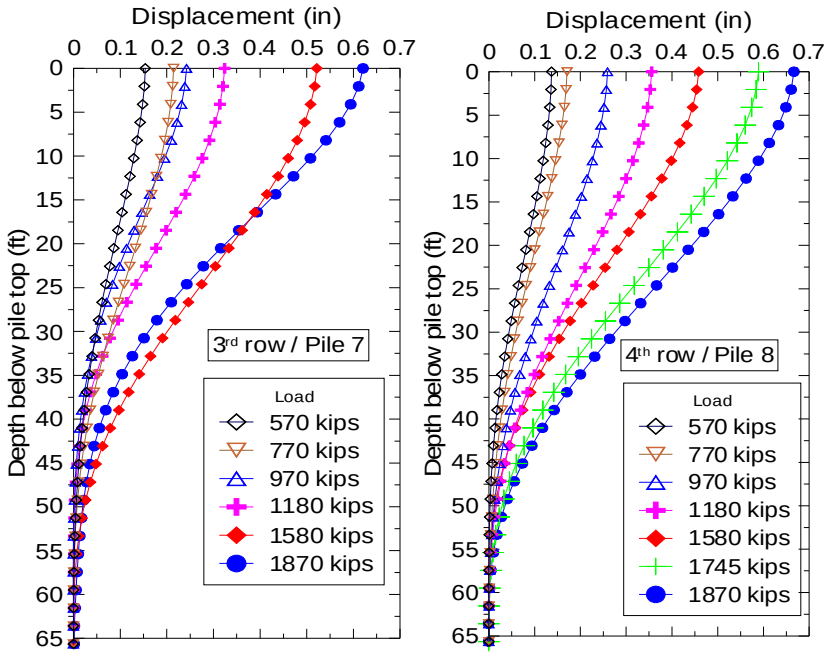

(c) Pile 7 (row 3) (d) Pile 8 (row 4)

Figure 32

Lateral displacement profiles for piles in different rows

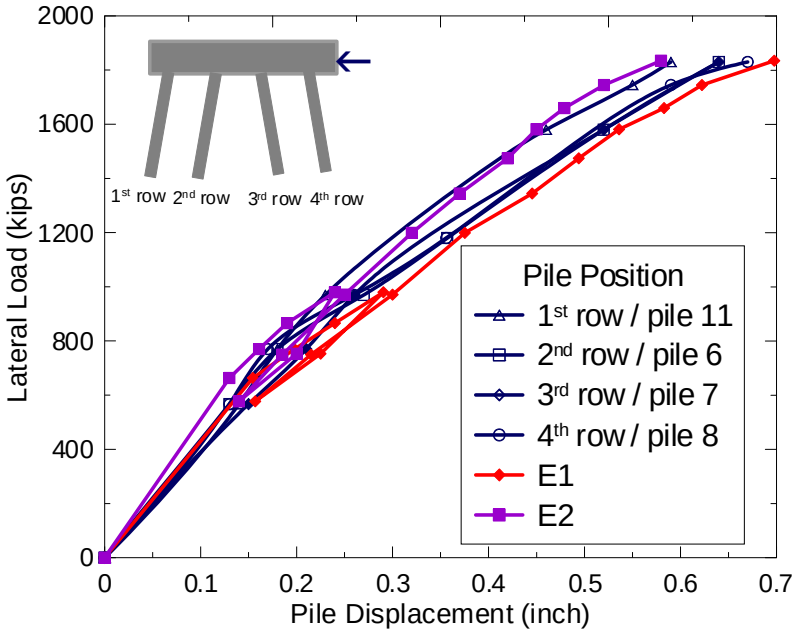

Figure 33

Pile head lateral displacement along with applied lateral load

Lateral Deflection for Piles Located in the Same Rows. In order to understand the lateral load behavior of piles within the same row, the lateral deformation profiles of three instrumented piles, 4, 8, and 12 located in the 4th row are derived as depicted in Figure 34. Figure 34 shows that Piles 4 and 12 have similar head displacement since they were both located at the corner and symmetric to the loading. On the other hand, the corner piles have smaller pile deflections under the same load level than the inner Pile 8, as shown in Figure 34(d). This can be explained by the pile group effect in the same row. Corner piles have larger soil support from the surrounding soil as compared to inner piles. Figure 35 shows the load-displacement determined at pile head and at ground level for piles in the 4th row. It indicates that all three piles in the 4th row overall exhibit similar load-displacement behavior.

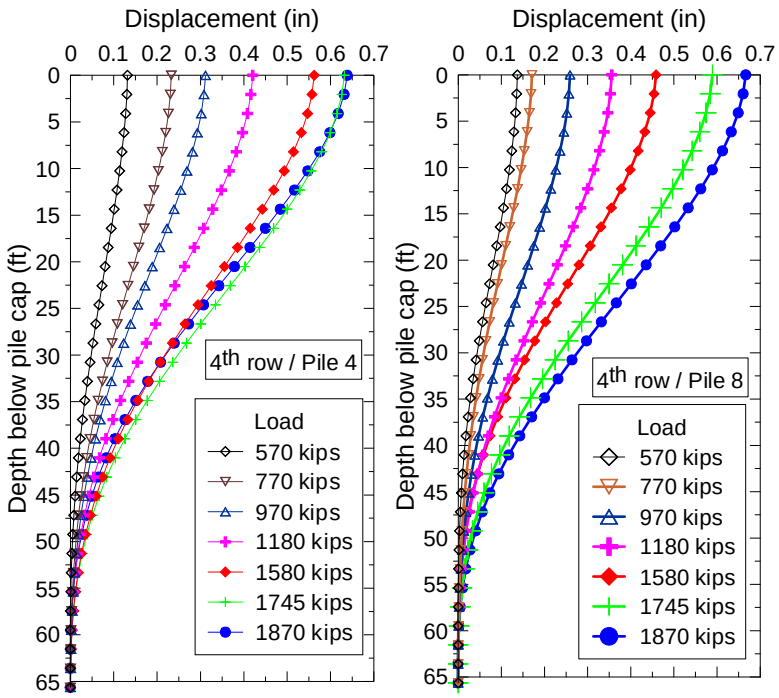

(a) Pile 4

(b) Pile 8

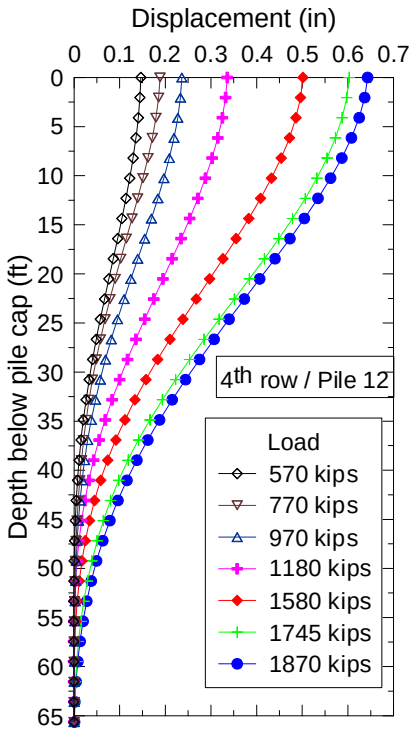

(c) Pile 12

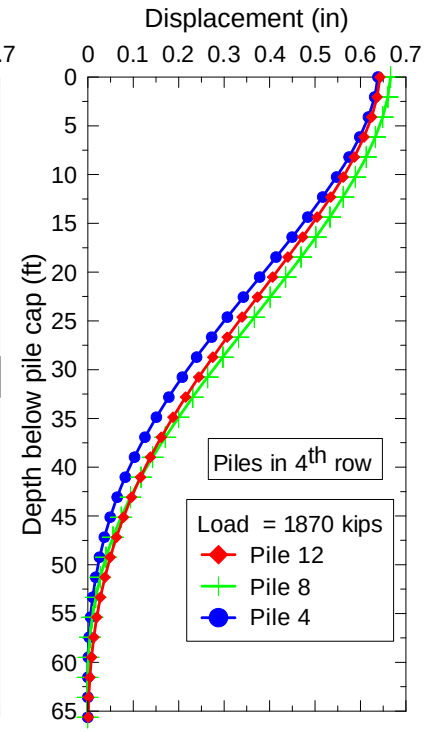

(d) Piles 4, 8, and 12 at same load level

Figure 34
Lateral displacement profiles for piles located in 4th row

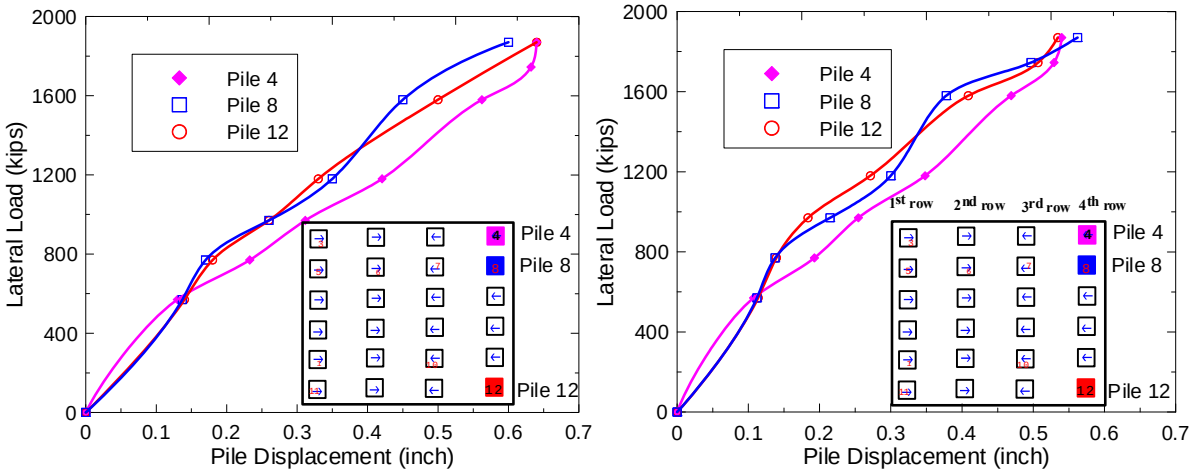

(a) At pile head (b) At mudline

Figure 35

Comparison of load-displacement behavior between piles in the same row

Bending Moment Profiles

Bending Moment of Piles Located in Different Rows. The moment profiles for Piles 11, 6, 7, and 8 are shown in Figure 36. It is evident that the maximum positive bending moments occur at the pile head for all piles due to the rigid pile-cap connection. It is inferred from Figure 36 that the magnitude of the moment and the depth to the first zero moment increases with the increment of applied lateral loads.

Comparatively the 1st row pile has the highest moment value, whereas the 4th row pile has the lowest moment value. Also, the depth to the zero moment for the 1st row pile occurred at a shallower depth than the 4th row pile. This trend is also observed for the depth from the pile head to the maximum negative moment. This finding is consistent with a previous study on the analysis of laterally loaded vertical pile groups *[31]*. The 3rd row pile has a larger moment than the 4th row pile at all loads. However, the rate of increase of the moment value is comparatively reduced at higher loads. At lower applied loads, the 3rd row pile has about a 15% larger moment than the 4th row pile, whereas the rate of variation is limited to 5-7% at higher applied loads. Similarly, the 1st row pile moment exceeds the 4th row pile moment by 30 to 40% at 570 and 770 kips, 10% at 970 and 1180 kips, but it only exceeds by 3% at 1745 and 1870 kips. Some unexpected results might be attributed to some minor measurement error, as seen for the 2nd row pile, which has larger moments than 1st row pile at 970 and 1180 kip loads.

To examine the effects of row position on moments, moment profiles for piles in different rows are plotted in the same figure at selected load levels as Figure 37shows. As expected, all piles display a similar profile except Pile 11 of the 1st row, which exhibits larger negative

moments when compared to other piles. Figure 37 also indicates that the depth to zero moment as well as the depth to the maximum negative moment increases as the load increases.

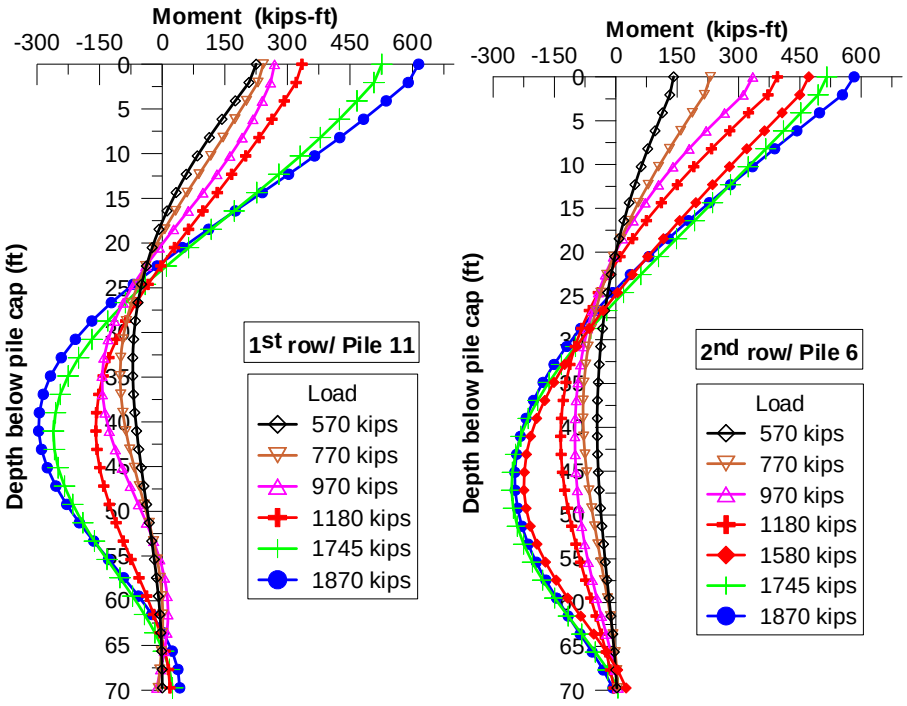

(a) 1st row / Pile 11 (b) 2nd row / Pile 6

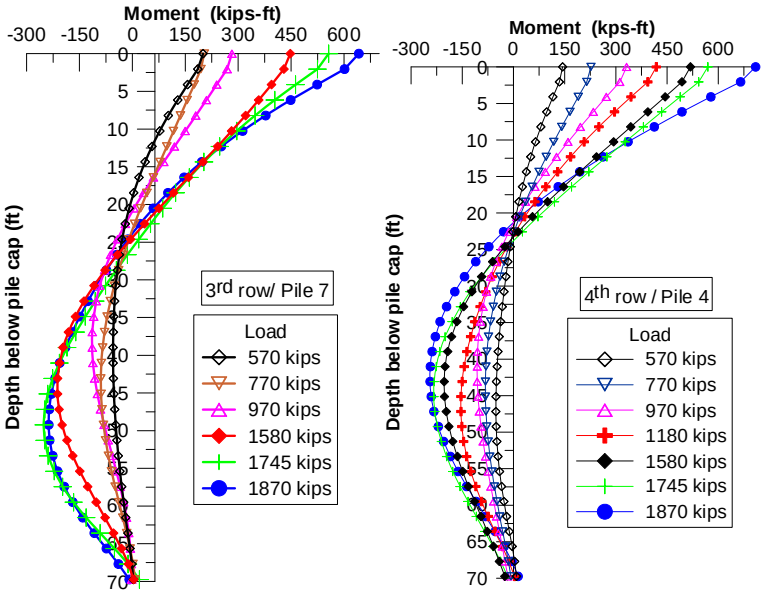

(c) 3rd row / Pile 7 (d) 4th row / Pile 4

Figure 36
Profile of bending moment for different piles

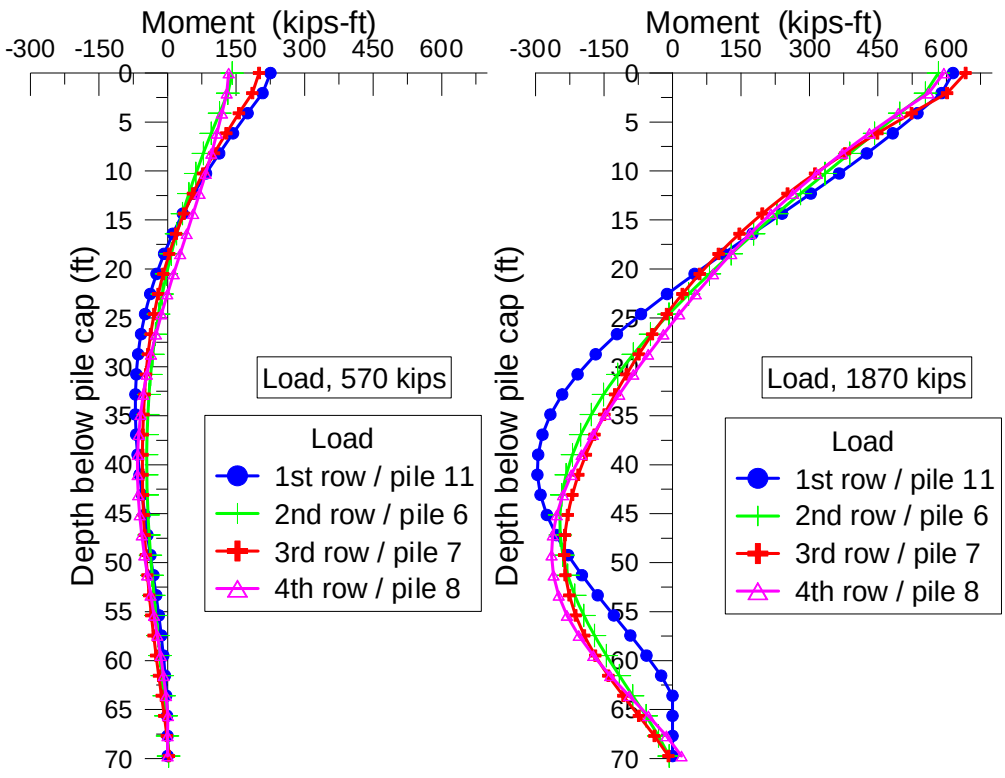

(a) at 570 kips load (b) at 1870 kips load

Figure 37

Comparison of derived moment profile of different row piles

Similar to the trend of the load-displacement curve, the moment–load curve also shows bi-linear behavior. The curve of applied lateral load versus moment developed at near to ground level (12 ft. from pile head) is also shown in Figure 38. The bending moment at ground level is found to be 50 to 55% lower than the moment at pile head. However, the variation of moment within the piles at ground level is not negligible. The variation of moment remains within the range of 15%.

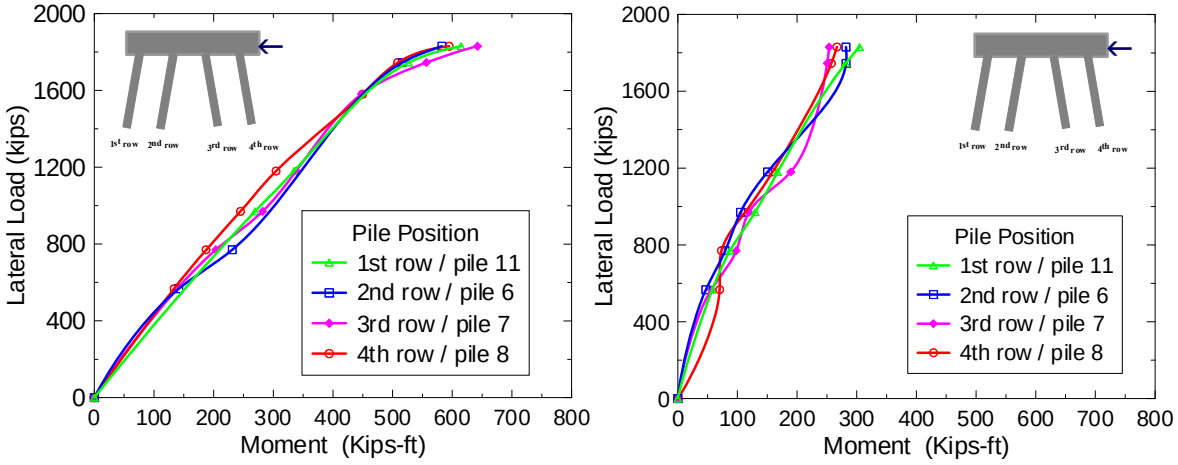

(a) At pile head (b) At ground level

Figure 38
Variation of bending moment with lateral load

Bending Moment of Piles Located in Same Row. The bending moment profiles for piles located within the 4th row were determined. The displacement profiles for Piles 4, 8, and 12 are presented in Figure 39. The outer Piles, 4 and 12, have almost similar moment profiles. The maximum moment of Pile 4 is about 700 kips-ft. while the maximum moment of Pile 12 is about 630 kips-ft. The inner pile also shows a similar bending moment profile; however, the moment values at the pile head as well as at the ground level are found to be 7% to 25% smaller than the corner pile as shown in Figure 40.

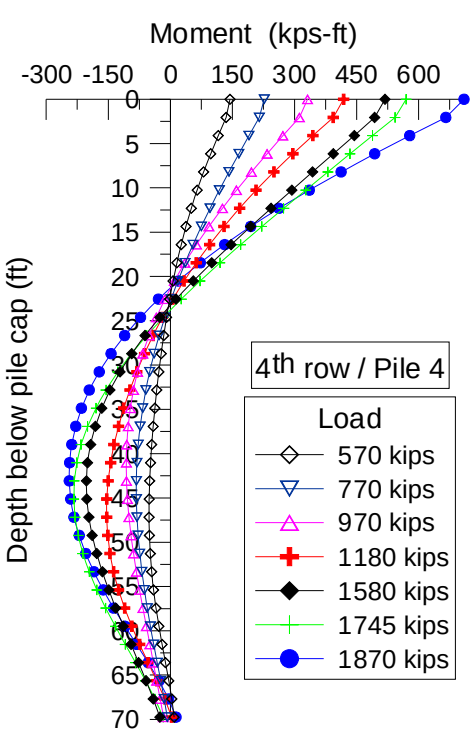

(a) Pile 4

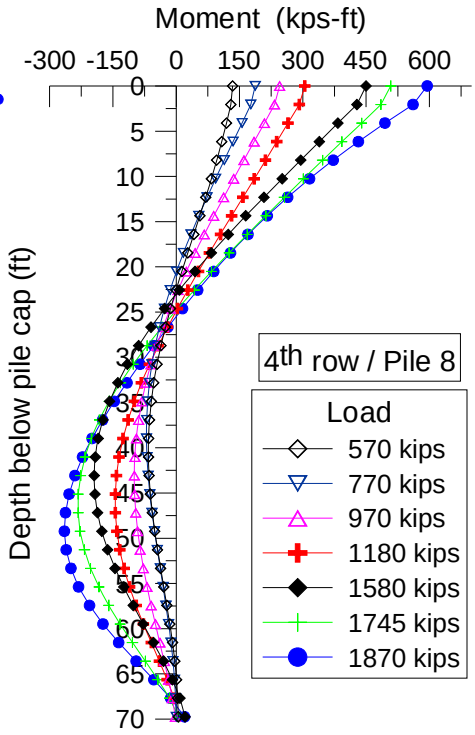

(b) Pile 8

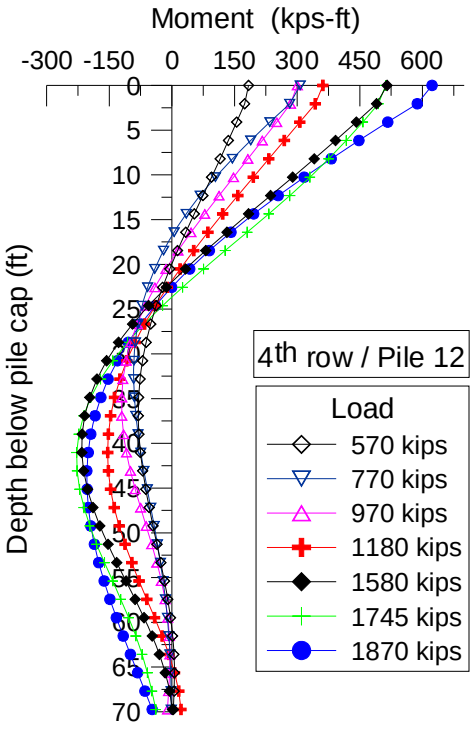

(c) Pile 12

Figure 39
Bending moment (kip-ft.) profiles of piles of the 4th row

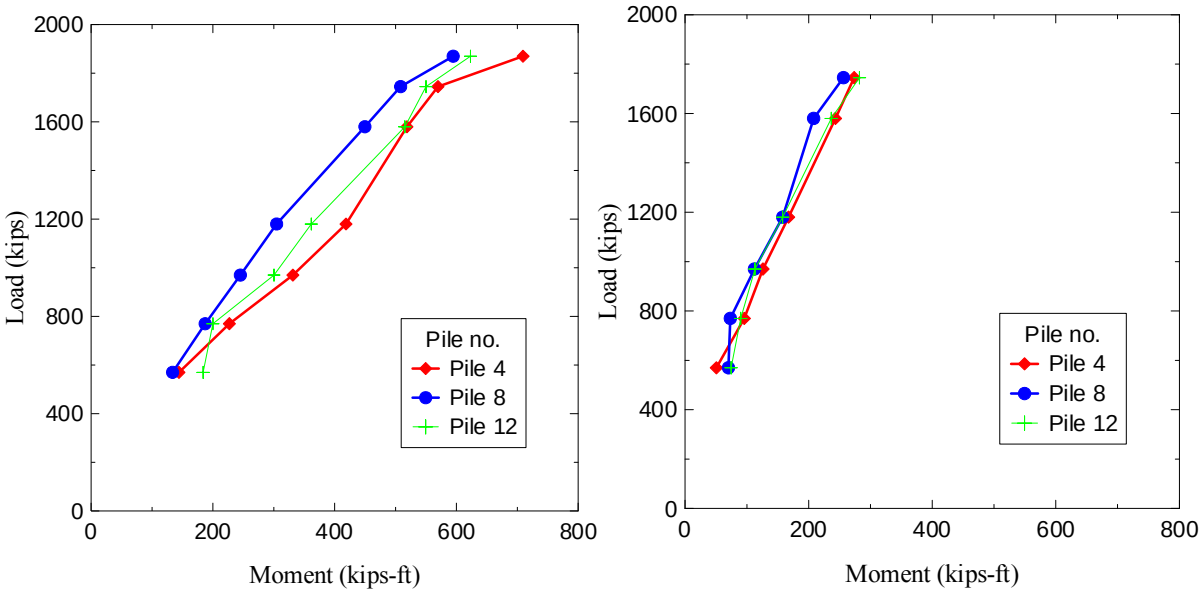

(a) at pile head (b) at ground level

Figure 40
Comparison of moments of piles located in the 4th row

Bending Moment Derived from Strain Gauge Measurements. The sister bar type of strain gauges was installed at two depths on selected piles. One pair of strain gauges (designated as SG1) were installed at 10 to 12 ft. from the pile head, depending upon length of pile, whereas, another pair (designated as SG2) were installed at 5 ft. below SG1. The bending moments were calculated from strain gage measurements using equation (18). The measured moments are compared with the moments derived from inclinometer readings. The comparison of moments from strain gauge readings and inclinometer readings for Piles 4, 7 and 12 are shown in Figure 41. These figures show the moments calculated from both instrument measurements have a strong agreement.

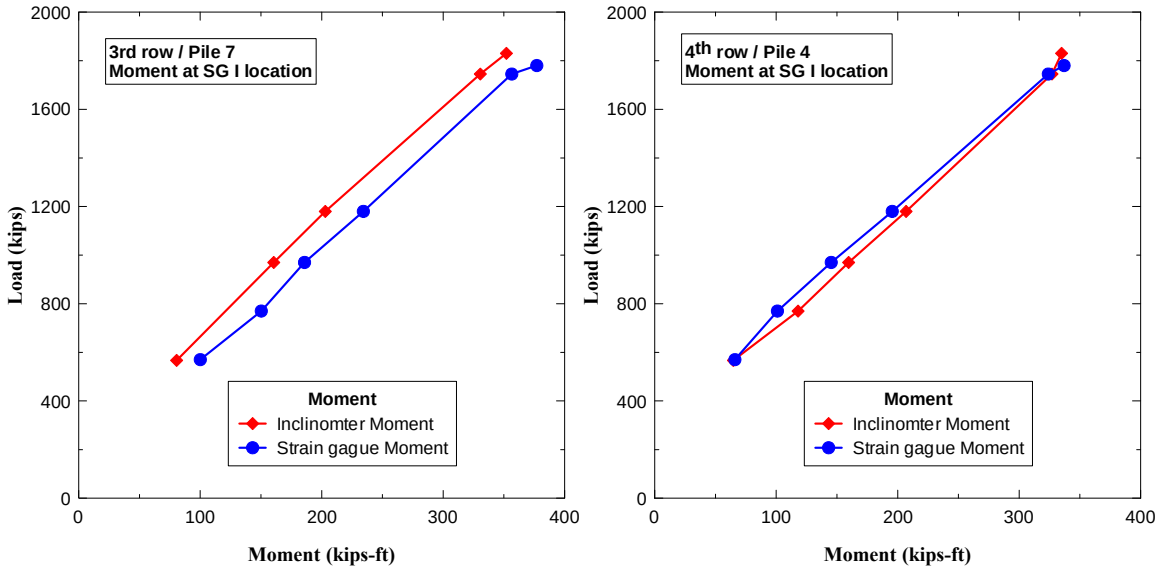

(a) Pile 7 at SG1 location

(b) Pile 4 at SG1 location

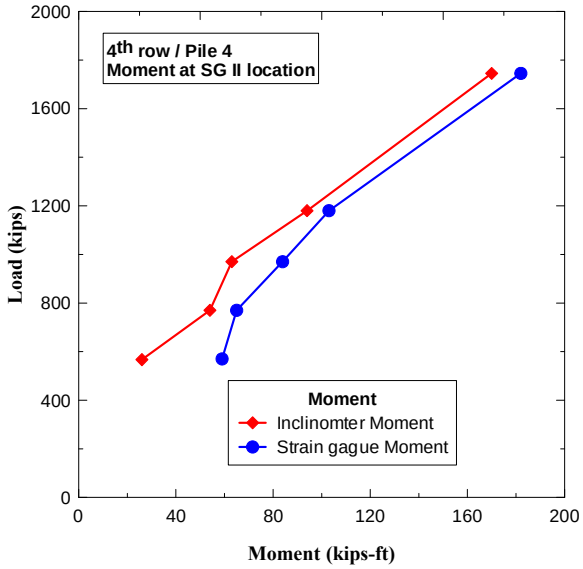

(c) Pile 4 at SG2 location

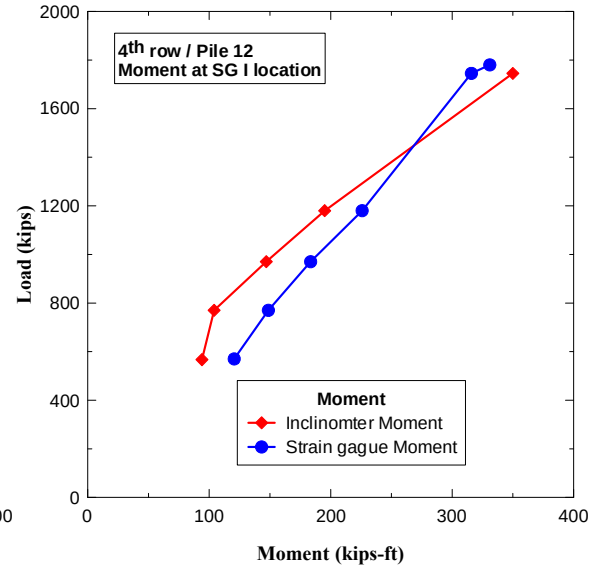

(d) Pile 12 at SG1 location

Figure 41
Comparison between moments derived from IPI measurements and strain gauge measurements

Pile Axial Load

The axial forces in piles are calculated at increasing static loads as shown in Figure 42. The axial forces in piles derived from strain gauge readings are due to the applied lateral load only, since the strain gauges were set to zero prior to the lateral load test. Figure 42 indicates that the magnitude of measured axial loads is approximately linearly proportional to the

increase of applied lateral loads with the exception of Pile 12. In general, nearly 5% to 12% of the applied lateral load was transmitted to axial load in all piles; however, the direction of developed axial loads depends upon the row position. It is also observed that that the piles inclined in the direction of lateral loading (row 3 and 4) are subjected to tension and those inclined in the opposite direction of loading (row 1 and 2) are subjected to compression.). Furthermore, Pile 4 has 90 kips tension load at SG1 location whereas Pile 12 has 30 kips in tension at SG2 location. This was expected since the laser survey shows that the north side of the pile foundation undergoes larger deformation than the south side of the pile foundation.

At the SG1 location for Pile 11 in the 1st row, a compressive axial load of about 50 kips and 100 kips were developed at the applied lateral load of 570 kips and 1780 kips, respectively. This indicates that about 8% and 5% of the applied lateral load was transmitted to the compressive axial load at lower and higher loads respectively as shown in Figure 43(a). However, at the SG2 (5 ft. below the SG1) location for that pile, only 6% of lateral load was transmitted to the axial load at the higher load, and 5% for the lower load as illustrated in Figure 43(b). Hence, the rate of transmitting the applied lateral load to the axial pile loads decreases with pile depth.

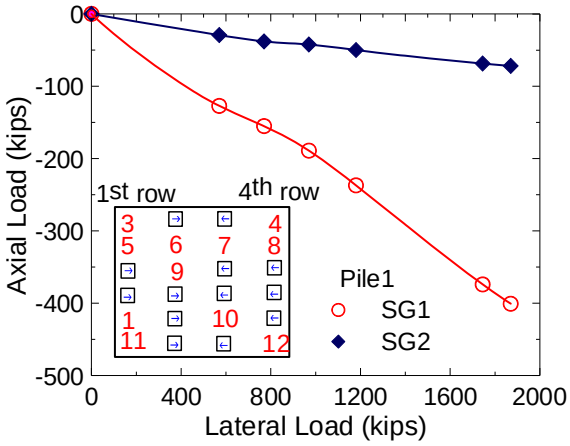

(a) Pile 1

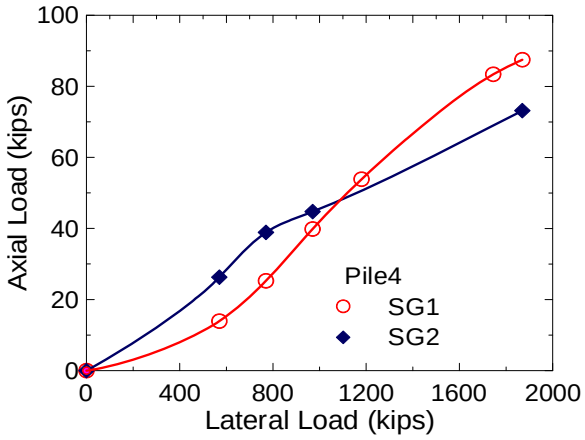

(b) Pile 4

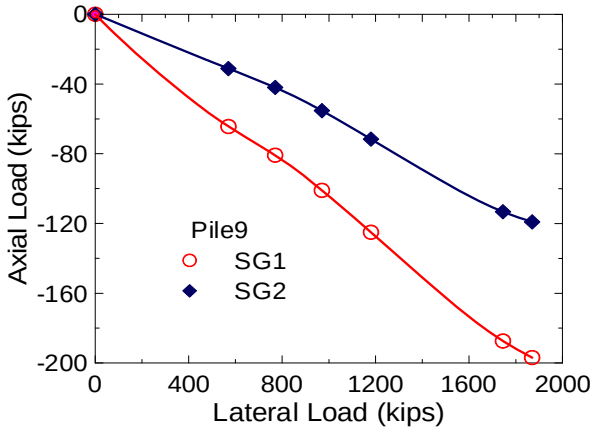

(c) Pile 9

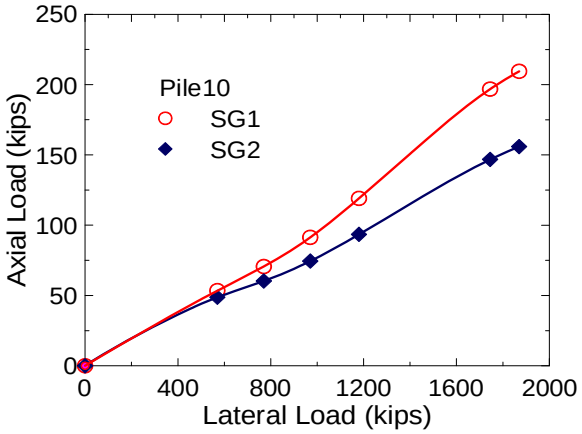

(d) Pile10

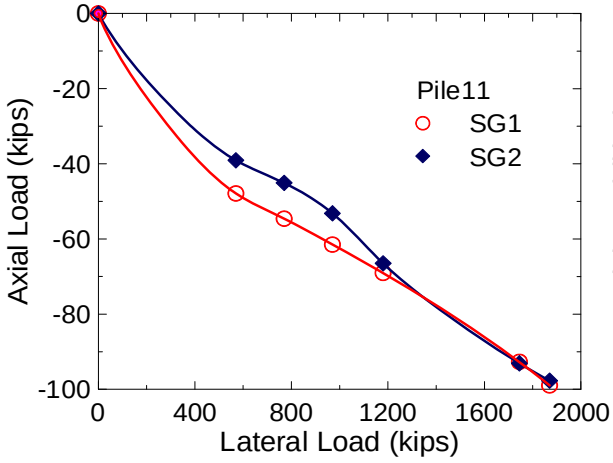

(c) Pile 11

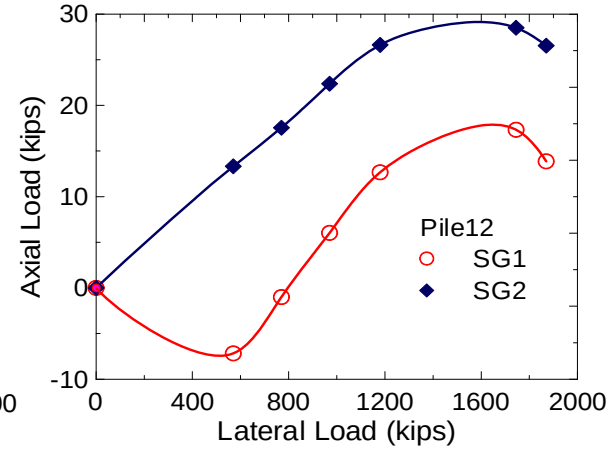

(d) Pile 12

Figure 42

Pile axial load calculated from strain gauge measurements

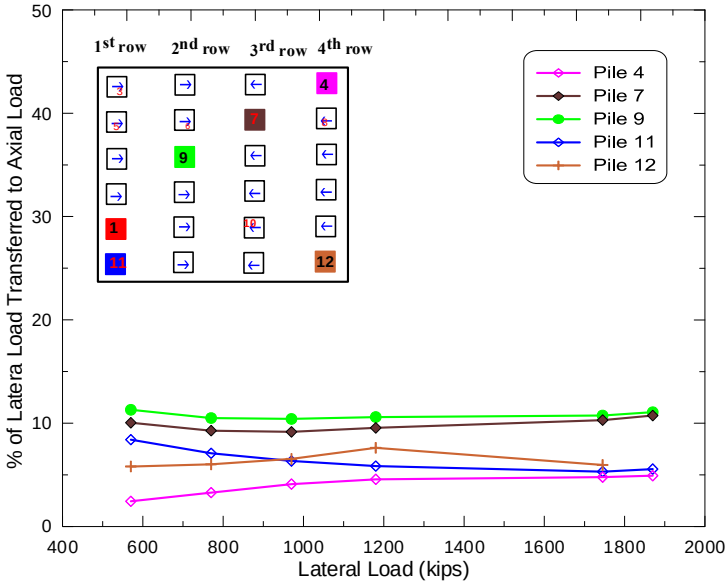

(a) Percentage of lateral load transferred to axial load at SG1

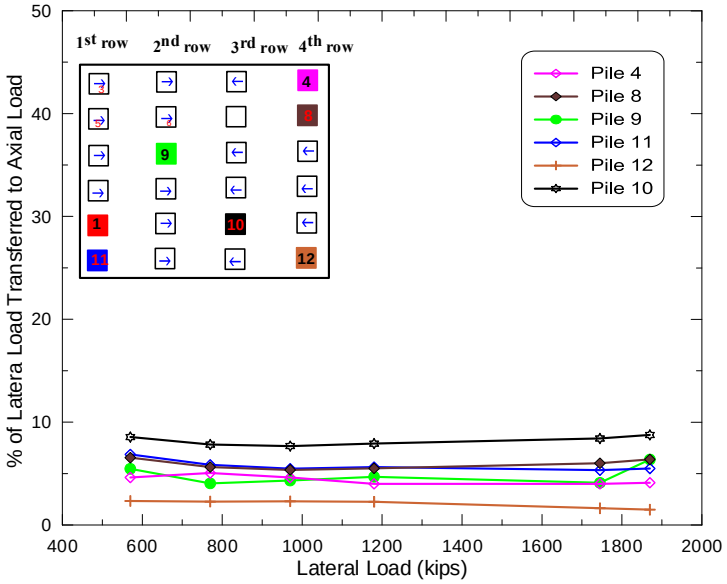

(b) Percentage of lateral load transferred to axial load at SG2

Figure 43
Transfer of lateral load to axial load in piles

Figure 44(a) presents axial loads for piles located in the 1st row. Some exceptions were found for Pile 1. It was noticed that the maximum compression axial load developed for Pile 1 at the SG1 location is 400 kips or 22% of lateral load, which simply suggests the overestimation or malfunction of the installed strain gauges at SG1 of Pile 1. However, the results obtained at the SG2 location of Pile 1 shows a good trend, but indicates a 15-22% lower compressive load than Pile 11 as shown in Figure 44(a).

Figure 44(b) is presented to show the axial loads for piles (Piles 7 and 10) located in a middle row, the 3rd row. As can be seen, the axial loads in Pile 7 and Pile 10 are almost similar, but higher than the piles in the outer rows. At the peak lateral loading of 1870 kips, the axial loads developed in Piles 7 and 10 at SG1 location are close to 200 kips. It should be noted that the developed axial load for piles in the 3rd row was tensile. As shown in Figure 44(b), Piles 7 and 10 of the 3rd row have almost the same amount of axial load at the SG1 location. The past experimental results show that the row closer to the point of loading develops a tensile force *[77]*.

The aforementioned results explicitly suggest that the statically induced axial forces in the piles are non-uniform and depend on row position: the piles located in the row nearby the applied lateral and induced tensile forces and piles located at the farthest row, such as 1st row, induced compressive forces, which is consistent with the results of previous studies *[58, 78]*. The bar chart showing induced axial force in piles corresponding to the applied lateral load is presented in Figure 45. It can be explained that the lateral displacement along with the rotation of the rigidly connected pile group cause the back row piles (Pile 7 and Pile 8) to move upward subsequently inducing tensile force, whereas it cause the front row piles (Piles 9 and 11) to move downward resulting in compressive forces. The schematic diagram illustrating the compressive and tensile movement of piles is depicted in Figure 46.

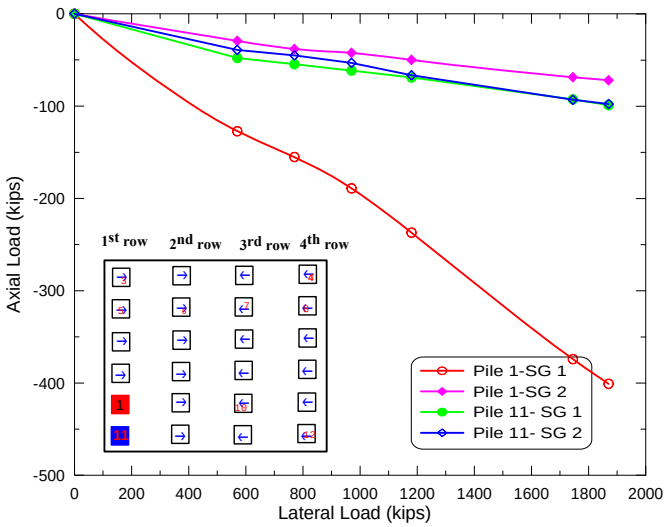

(a) Piles 1 and 11

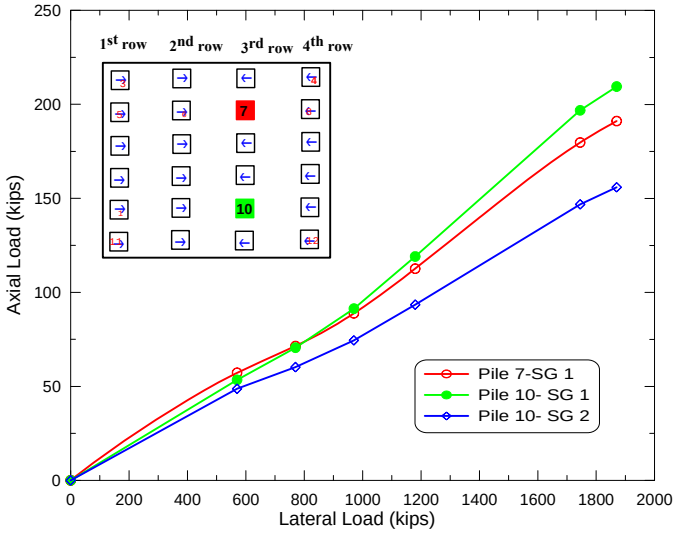

(b) Piles 7 and 10

Figure 44
Comparison of induced axial load for piles located in the same row

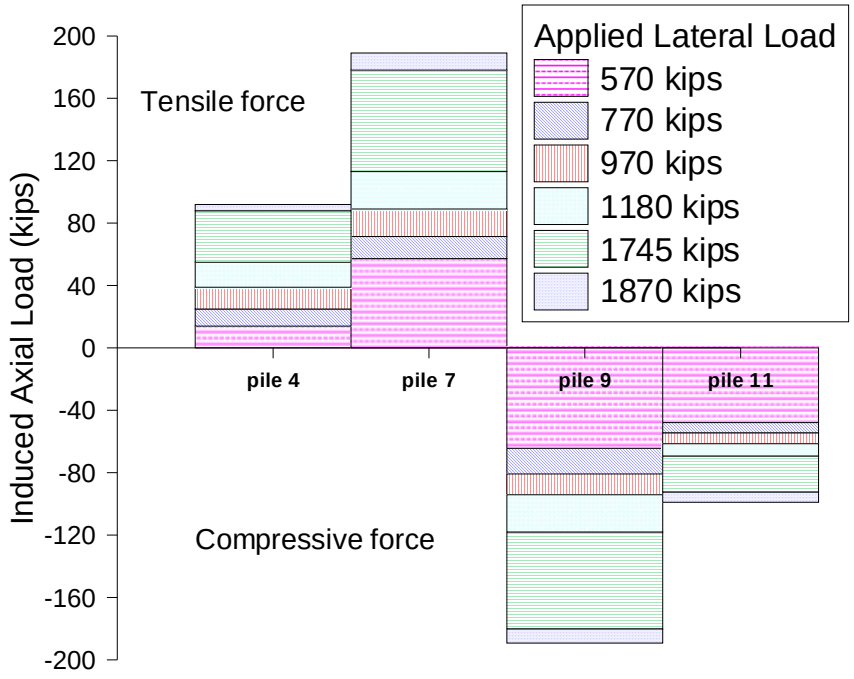

Figure 45

Induced axial force in pile under lateral loading

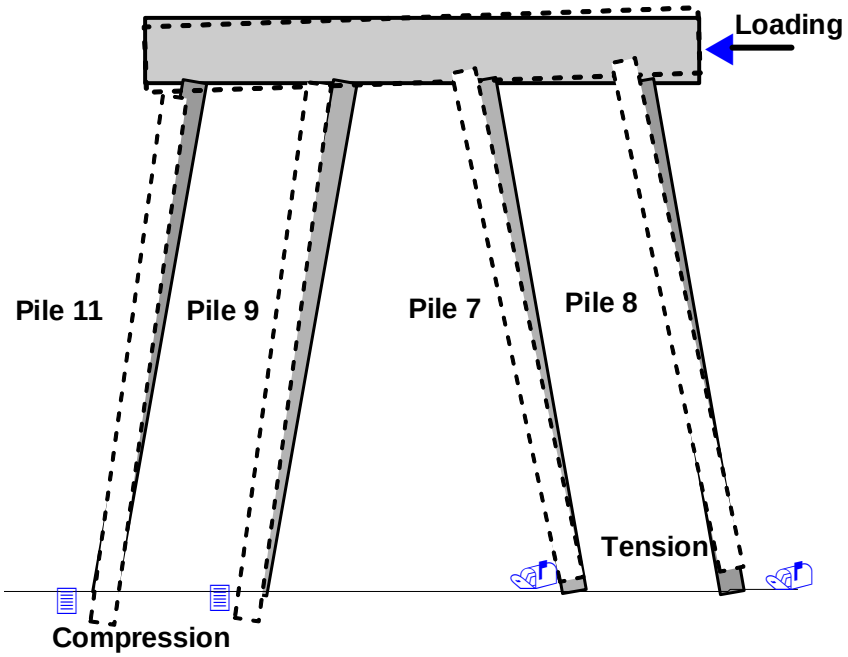

Figure 46

Schematic diagram illustrating the movement of pile under lateral loading

In addition, the distribution of axial forces along the pile length is also not uniform since the induced axial force at the SG2 location is lower than the axial force induced at the SG1

location. The reason is evident, since the SG1 is located near the ground level where the soil is too soft, thus the tendency of the pile to deform laterally is larger due to the low lateral soil resistance. With the depth of soil, the soil lateral resistance increases due to the increment of the stiffness of soil, thus lower axial forces as compared to SG1 is induced. However, due to the lack of sufficient number of strain gauges at the lower level of the piles, the distribution of the axial force along the length of the pile could not be illustrated.

Soil Resistance

The profiles of soil resistance (force per unit length) for piles were derived by differentiating the moment profiles twice as described in equation (9). The soil resistance profiles of Piles 11, 6, 7, and 8 are illustrated in Figure 47. The 1st row exhibits the maximum soil resistance value; approximately 20% to 40% higher than the 4th row pile. However, the value of soil resistance corresponding to the same depth for all the piles in the rows does not vary substantially; only 7-8% variation is observed.

Similar to moment profiles, the value of soil resistance increases with increasing the applied lateral load. The depth from pile head to the position of maximum soil lateral resistance developed in the pile also increases as the applied load increases. On the other hand, the maximum soil resistance developed at the applied loads of 970, 1180, 1745 and 1870 kips are 0.50, 0.77, 1.22, and 1.4 kips/ft., respectively. These maximum soil lateral resistances occurred at around 29 ft. (9.67B), 32 ft. (10.67B), 34 ft. (11.33B), and 34 ft. (11.33B), respectively. Hence, the greater the applied load, the deeper the maximum soil resistance occurred. Such a trend is also seen in piles in the other rows.

In comparison to the other piles, the depth to the maximum soil resistance is found to be the lowest in the 1st row piles, as depicted in Figure 47(a). It also indicates that the distributing range of soil resistance along the pile length is smaller for the front row pile (Pile 11) than the other row piles. The soil resistance distribution extends to 16B in the back row pile (Pile 8), whereas the soil resistance distribution for the front row piles extends to 14B depth (Pile 11). Thereby, it can be inferred that the soil resistance depends upon the loading and position of the row.

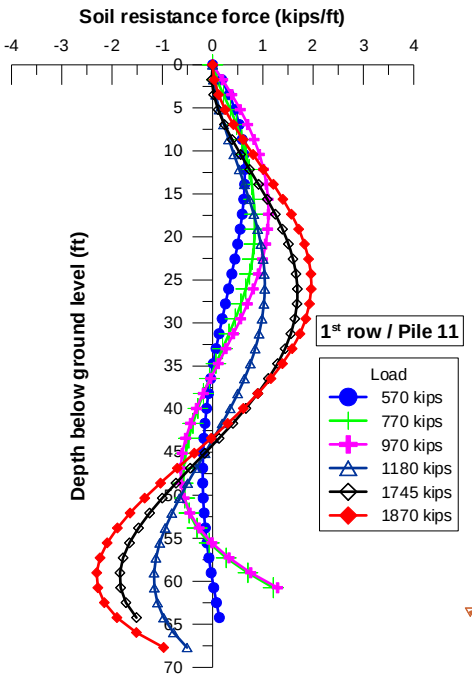

(a) 1st row/ Pile 11

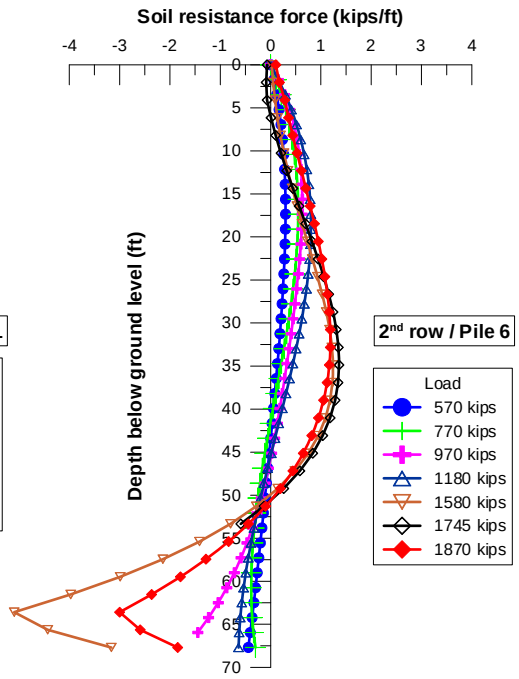

(b) 2nd row / Pile 6

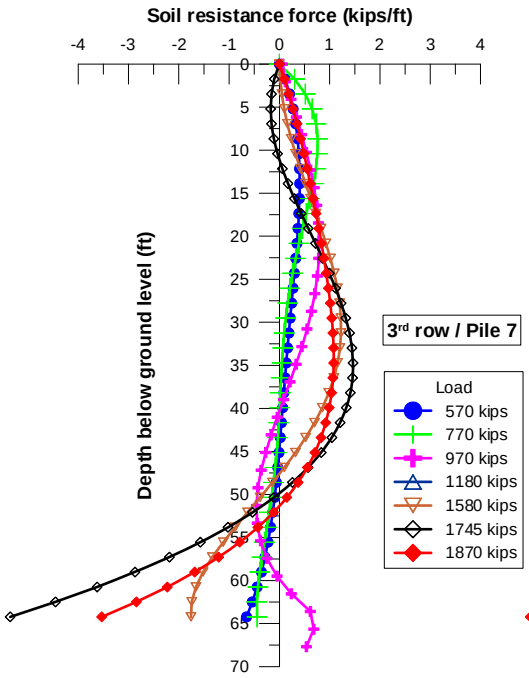

(c) 3rd row / Pile 7

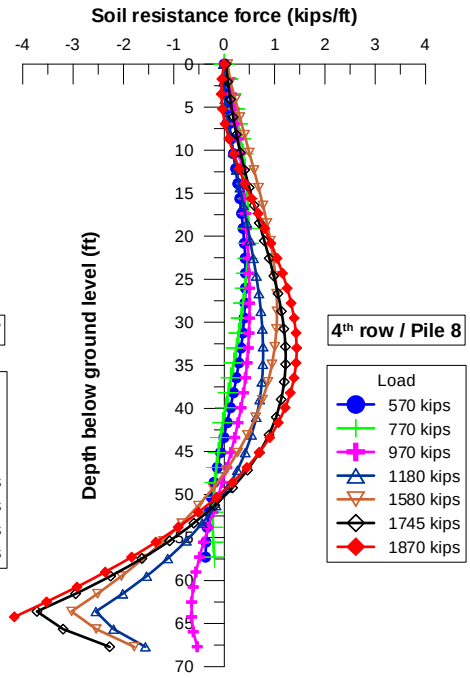

(d) 4th row / Pile 8

Figure 47
Soil resistance force profile for each row in pile group

The soil resistance profiles for the 4th row piles, i.e. Piles 4, 8, and 12, are presented in Figure 48. The outer piles in the same row, Piles 4 and 12 have higher soil resistance at the upper piles. This clearly indicates the outer piles are less affected by pile group effects and thus have larger soil resistances. The depth to the maximum soil resistance differs between piles. The depth to the maximum soil resistance is within 20-25 ft. below ground level for Piles 4 and 12, whereas the depth to the maximum soil resistance for Pile 8 is in the range of 30-35 ft. below ground level

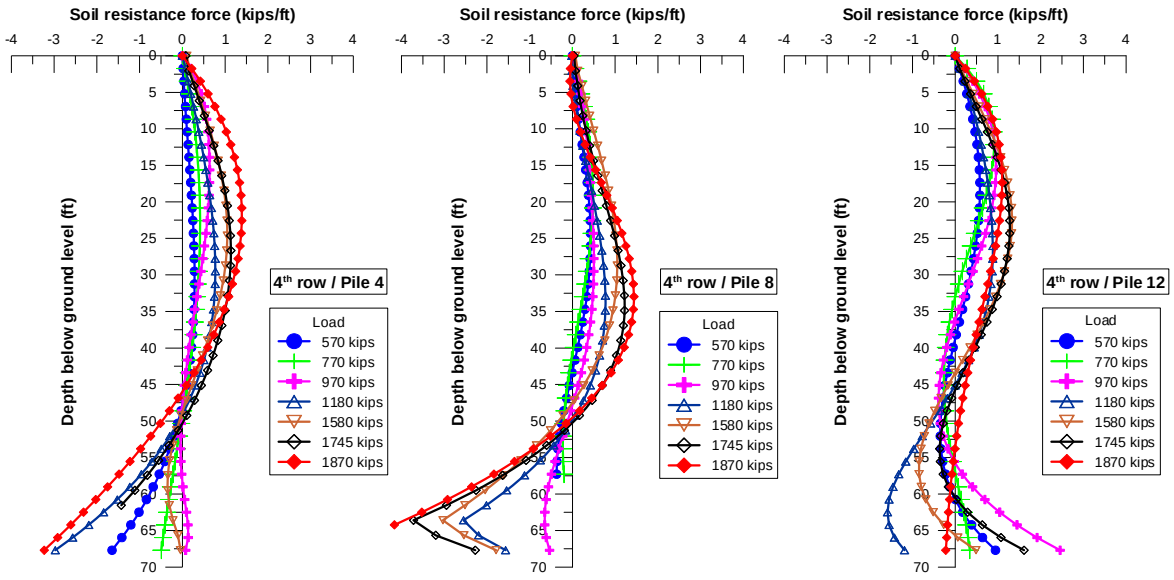

(a) Pile 4 (b) Pile 8 (c) Pile 12

Figure 48
Soil resistance force profile of piles within 4th row of pile group

Back-Calculation of p-y Curves

The p-y curves for depths of 5 ft., 10 ft., 15 ft., and 20 ft. below ground level were developed for piles in different rows, Piles 6, 7, 8, and 11, as shown in Figure 49. It is shown that that the 1st row pile has the largest soil reaction with respect to the same pile displacement. However, the 2nd, 3rd, and 4th row piles display similar p-y curves at all depths. This observation agrees with the current pile group theory: piles in the leading row are less affected by the group effect, thus having larger soil reaction. Besides the pile group effect, the soil horizontal variation also causes an increase of soil resistance at Pile 11 as the CPT soundings showed that soil profile close to Pile 11 has a higher undrained shear strength compared to the soil close to other pile locations.

Figure 49 also indicates that the determined p-y curves were fully developed only at 5 ft. and 10 ft. depth. The p-y curves below 10 ft. depth were not fully developed. With an increase of

depth, the p-y curves become stiffer as the soil strength increases. This conforms to the findings of experiments that were conducted by McClelland and Focht for Louisiana offshore soils *[79]*. The p-y curves of the leading row Pile 11 are slightly stiffer than the p-y curves of piles in other rows. Considering the center-to-center pile spacing in the loading direction, which is 4.3B, it is inferred that the group effects in the loading direction are minimal. However, further study is needed to verify this statement.

The p-y curves for piles 4, 8, and 12 located in the same 4^{th} row are compared at the depth intervals of 5 ft., 10 ft., 15 ft., and 20 ft. as shown in Figure 50, which shows that the outer Pile 12 has the largest soil reaction, with approximately 30% larger than the inner Pile 8. This indicates that the pile group effect within the same row is much larger than the group effect for different rows, which may be explained by that the pile spacing in the loading direction is greater than the pile spacing in the transverse direction of the loading.

In addition, the p-y curves for Piles 11 and 12 are also compared since both piles have similar lateral displacement. It can be seen that Piles 11 and 12 develop similar p-y curve at 5 ft. and 10 ft. below ground level as shown in Figure 51(a). However, with the increase of depth, Pile 11 exhibited larger later soil resistance, and hence producing stiffer p-y curves compared to Pile 12 as presented in Figure 51(b).

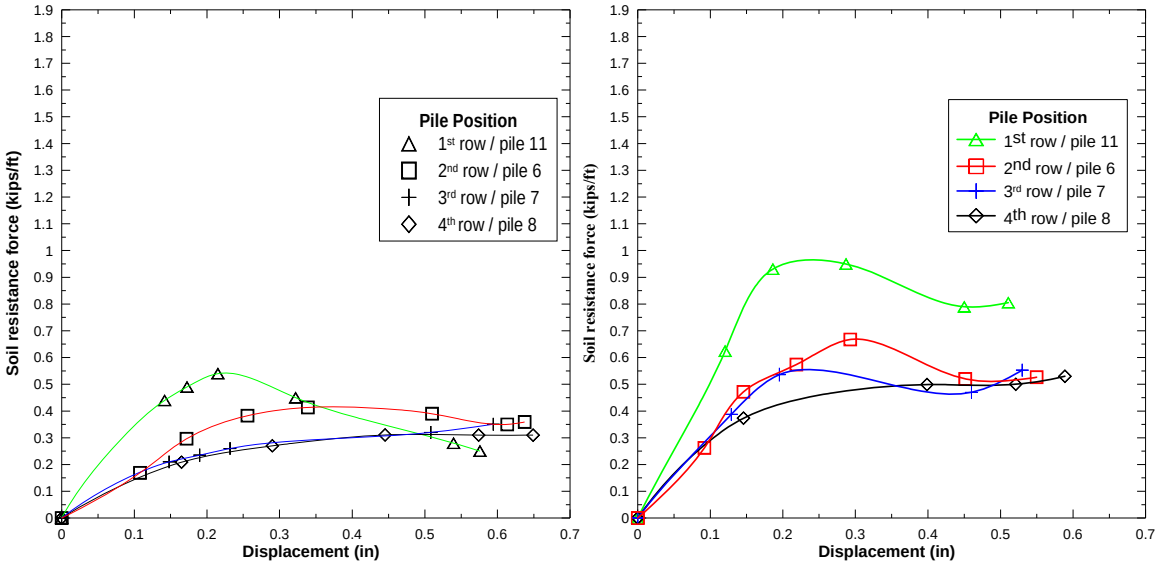

(a) 5 ft. below ground level

(b) 10 ft. below ground level

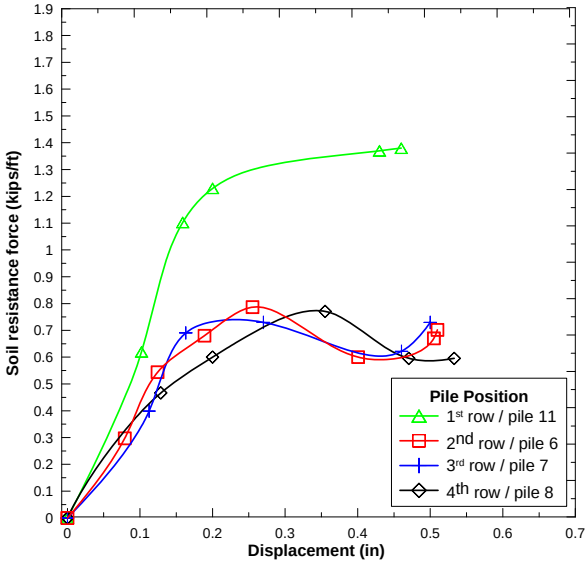

(c) 15 ft. below ground level

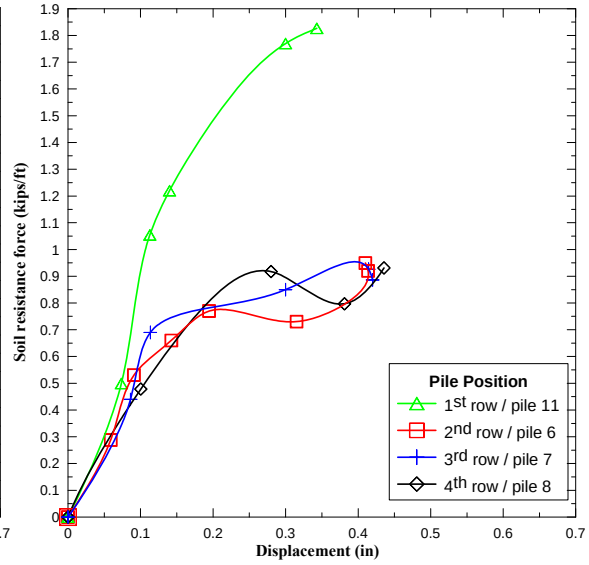

(d) 20 ft. below ground level

Figure 49
Comparison of p-y curves of piles in different rows

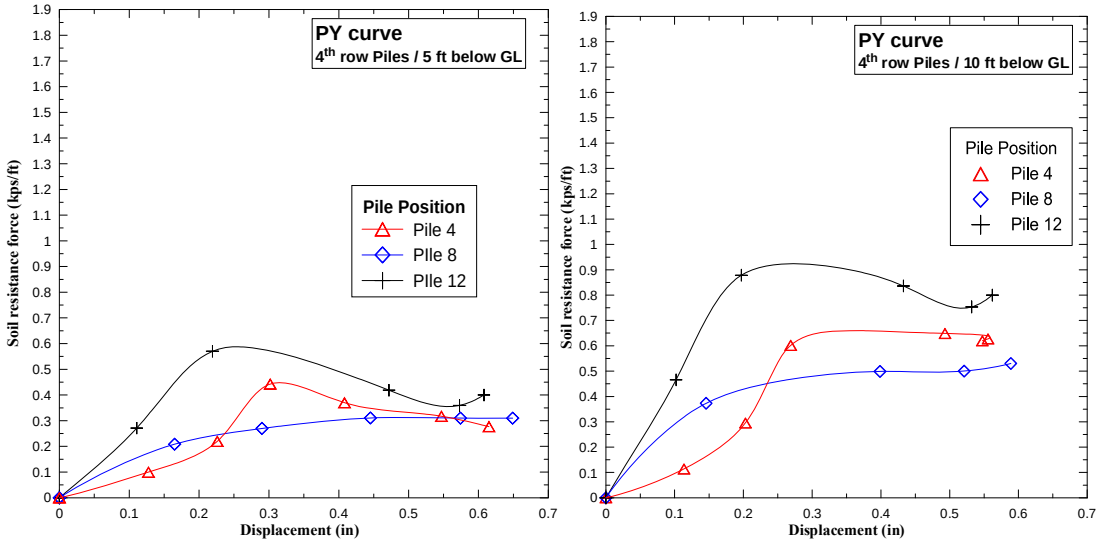

(a)

(b)

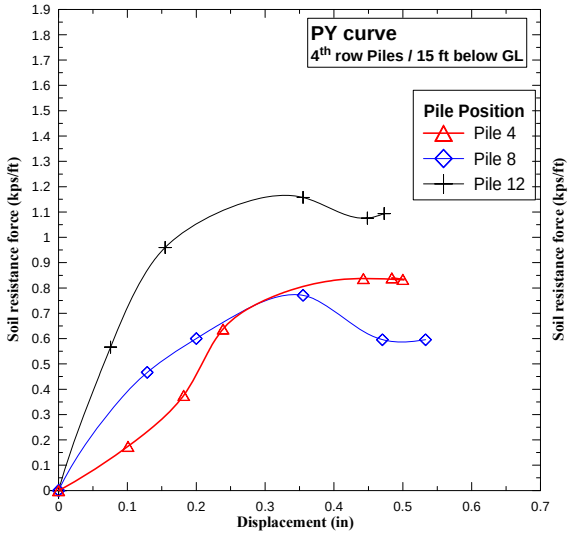

(c)

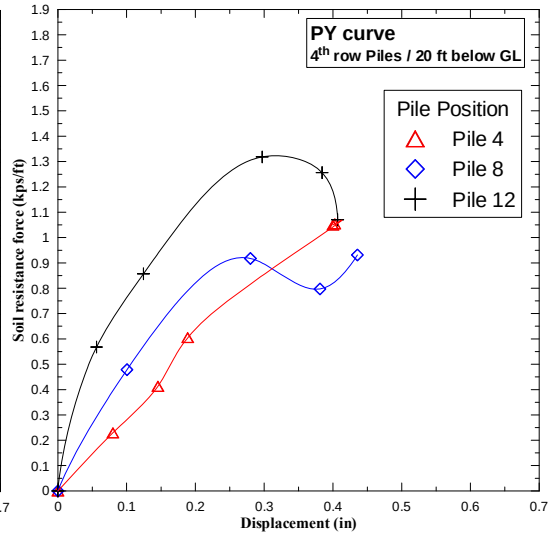

(d)

Figure 50

Comparison of p-y curves of same row piles

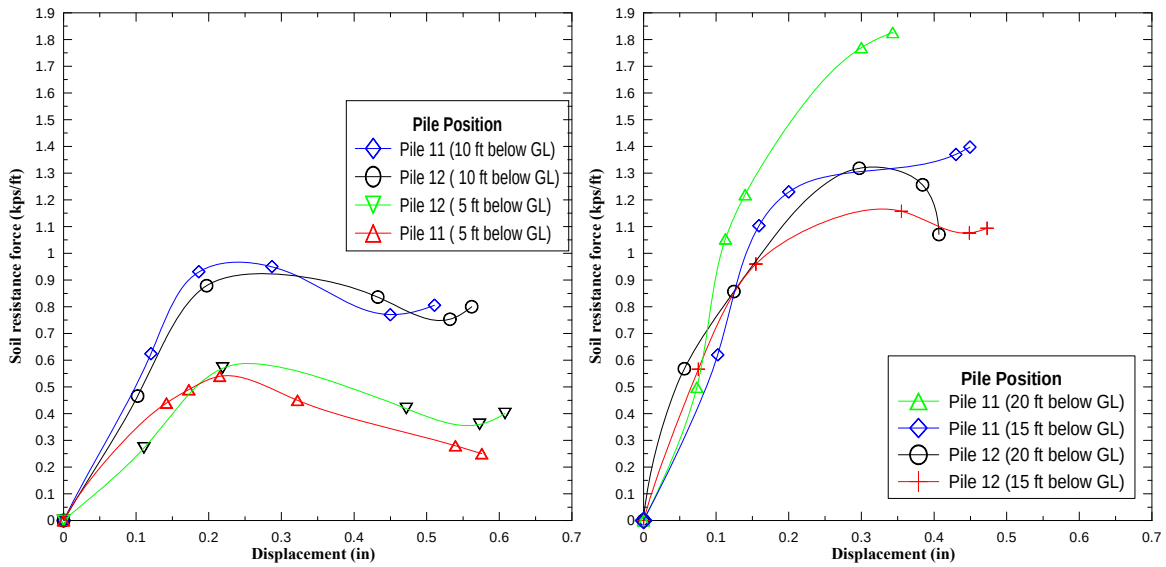

(a) (b)

Figure 51
Comparison of p-y curves of Pile 11 and Pile 12

FB-MultiPier Analysis

Sensitivity Study on FB-MultiPier Input Parameters

Sensitivity analyses of these input parameters are important for choosing the input values. S_u, ε_{50}, and K_s are selected as representative input parameters for sensitivity analyses. The base analysis showed a large discrepancy in the analyzed lateral displacements from the measured values recorded during the lateral load test. Therefore, before analyzing the lateral load behavior of the M19 pier, a sensitivity analysis was first performed based on these input parameters.

Undrained Shear Strength (S_u)

Three cases, in which undrained shear strength for cohesive soils were increased or decreased by the same ratio of its corresponding initial strength, were considered: (1) S_{u_lab} determined from undrained unconsolidated (UU) test as given in Table 3; (2) $2S_{u\_lab}$; and (3) $\frac{1}{2} S_{u\_lab}$, while all other parameters remain the same. It was observed that the variation of S_u highly affects the lateral displacement profile. As shown in Figure 52, the pile head deflection is sensitive to the change of S_u. With S_u doubled, the pile head deflection reduces from 1.4 in. to 1 in., whereas with S_u reduced by half, the pile head deflection increases to 1.9 in. Figure

53 presents the p-y curves for these three scenarios. It shows that the change of S_u greatly affects the initial slope and peak strength of the p-y curves for both soft and stiff clay.

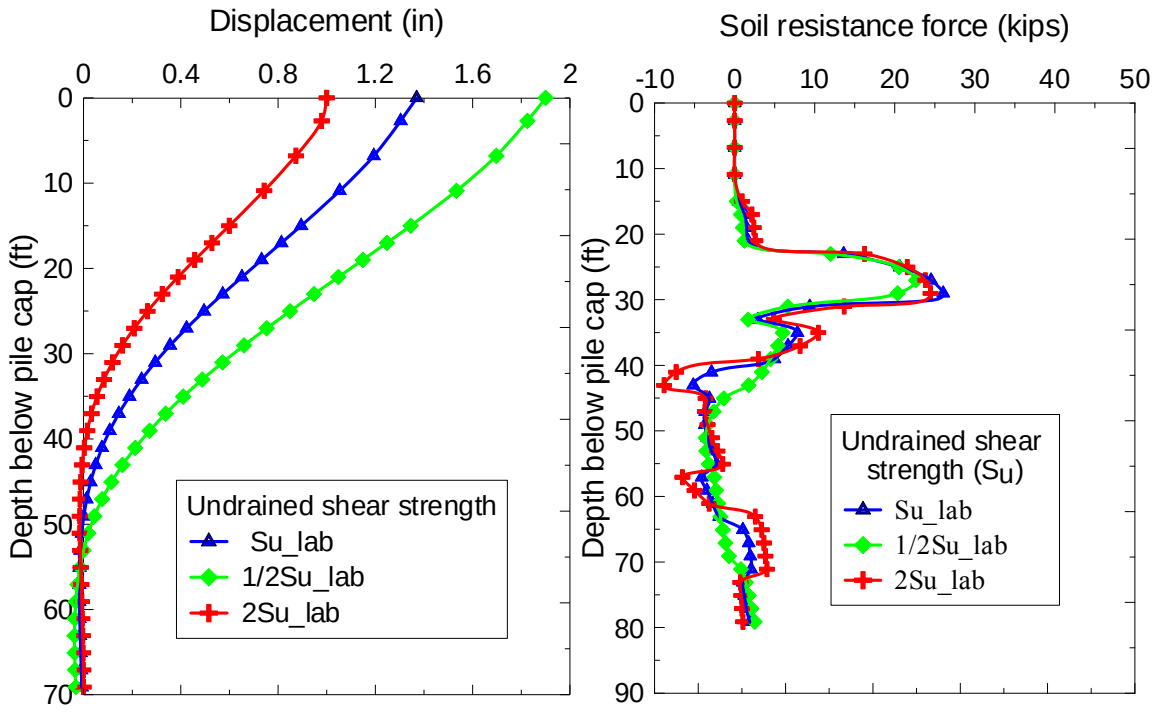

(a) Lateral deformation (b) Soil resistance force

Figure 52
Behavior of pile at varying undrained shear strength of Pile 11

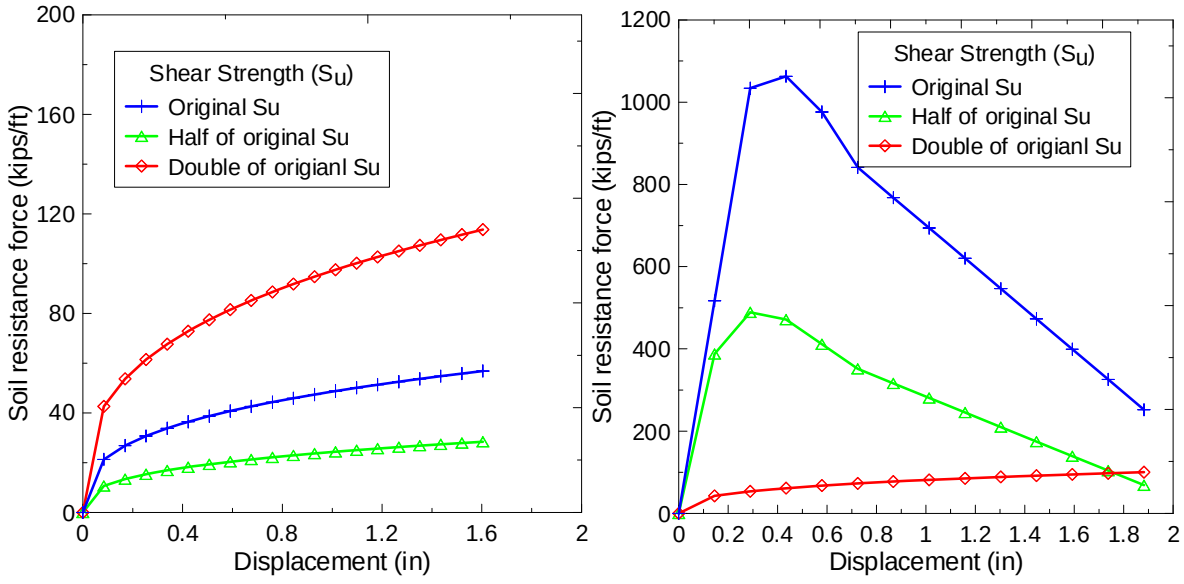

(a) soft clay layer (b) stiff clay layer

Figure 53
P-y curves at varying undrained shear strength

Strain at 50% Stress (ε_{50}). Similar to the analyses of the effect of S_u, three cases were also analyzed by considering ε_{50_lab}, $2\varepsilon_{50\_lab}$ and $\frac{1}{2}\varepsilon_{50\_lab}$ with ε_{50_lab} as the values shown in Table 3, while keeping the other parameters unchanged. The deflection profiles are presented in Figure 54. The results of the analyses indicate that reducing the ε_{50_lab} does not have substantial influence on the magnitude of the lateral deformation as the displacement is merely reduced by 3% to 4%. However, the lateral displacement is increased by 10% when the ε_{50_lab} value is doubled. For soft soil, an increase of ε_{50} reduces soil resistance as shown in Figure 55, while the shape of the p-y curves remains the same. For stiff clay, the increase ε_{50} mainly affects the location of peak strength while the magnitude of the peak strength remains the same. Figure 55 indicates that change of ε_{50} causes less change of p-y curves than it does by the change of S_u.

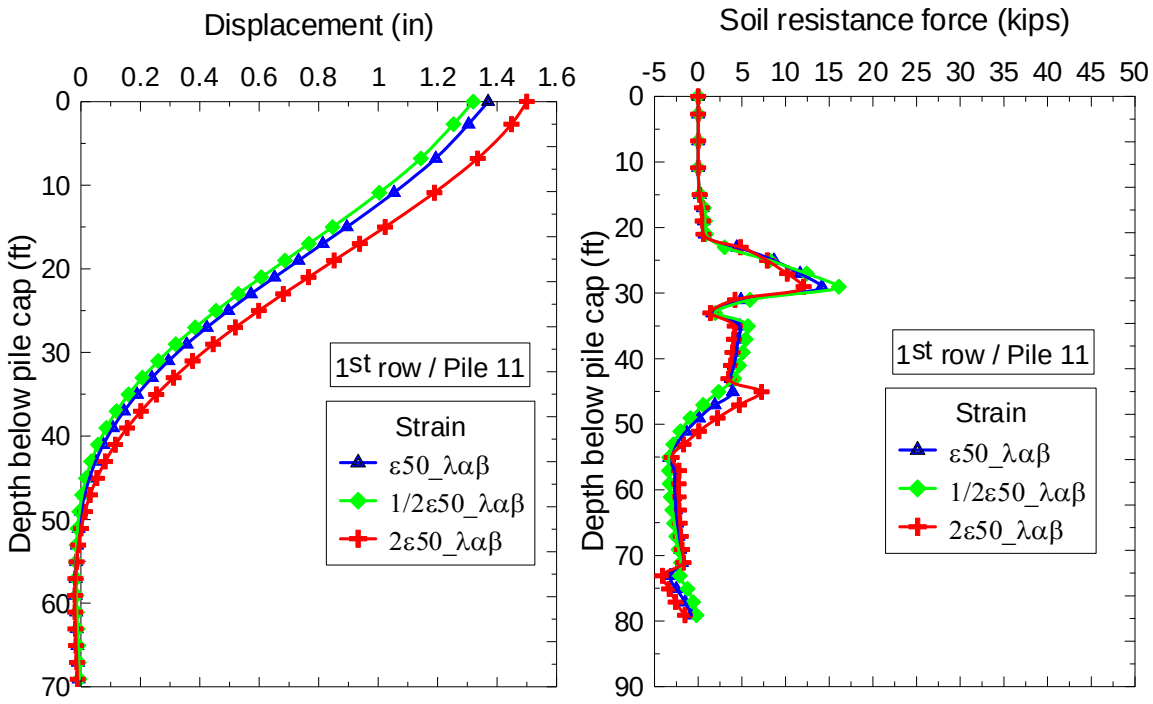

(a) Lateral deflection (b) Soil resistance force

Figure 54
Pile deflections at varying strain values

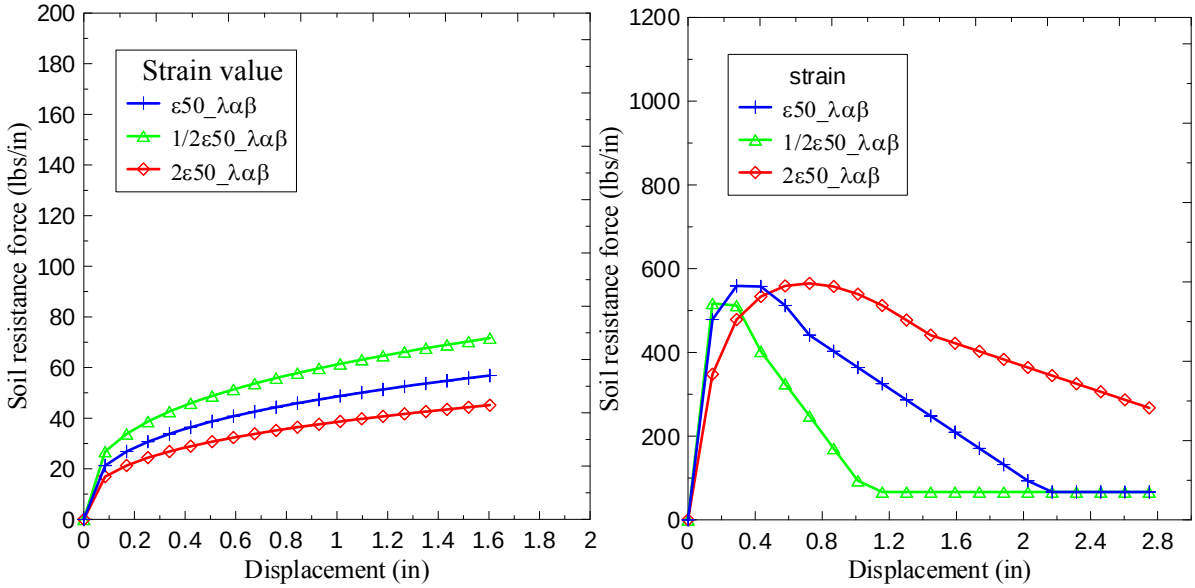

(a) soft clay (b) stiff clay

Figure 55
p-y curves at varying strain values (ε_{50})

Young's Modulus of Concrete (E_c). The results are shown in Figure 56. The figure suggests that increasing E_c from 5090 ksi to 7000 ksi resulted in decreasing the lateral deformation by 23% to 25% for the top 20 ft. of pile. However, when E_c is further increased to 10000 ksi, the lateral deformation is reduced by 40%.

Subgrade Modulus (K_s). The results of the analysis are presented in Figures 57 and 58. It shows that K_s has no noticeable effects on the pile deflection as explained by Figure 58, where the change of K_s has no obvious effect for both soft and stiff soil.

Battered Pile Groups versus Vertical Pile Groups. To study the performance of battered pile groups in comparison with vertical pile groups, a vertical pile group was modeled in FB-MultiPier with the same inputs as for the battered pile group with the only exception of changing battered piles to vertical piles. For simplification, no pile group effect was considered in both models. The comparison of battered group and vertical pile group at the load of 1870 kips is shown in Figure 59. As shown in the figure, the battered pile group has much smaller pile head deflections along with smaller pile head moments and shear forces. This observation agrees with the fact that battered pile groups have much larger lateral resistance.

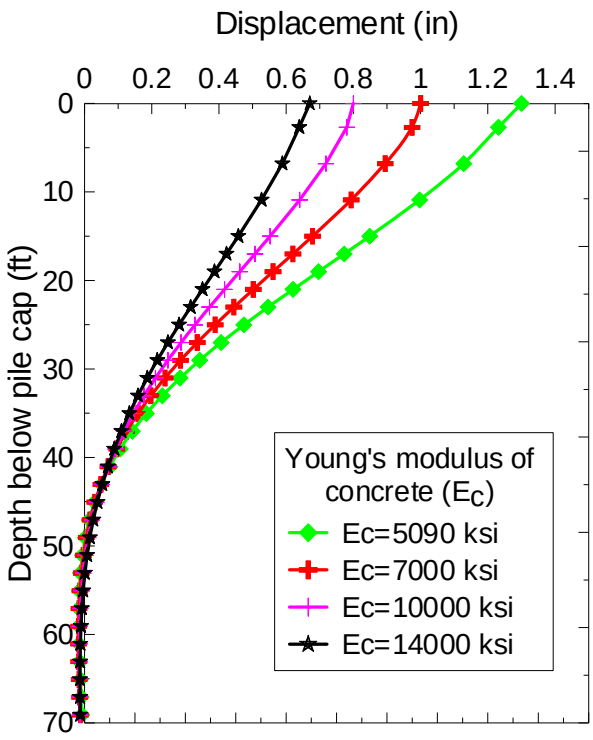

Figure 56

Effect of E_c of the pile concrete on pile deflections

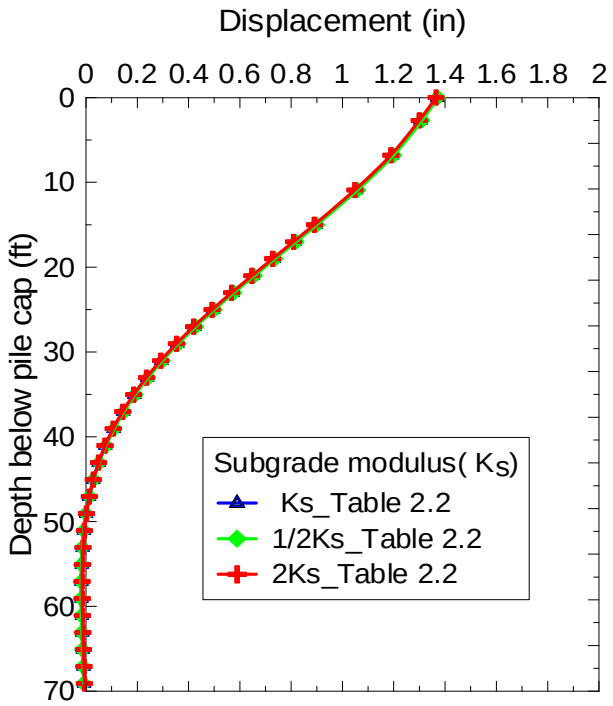

Figure 57

Effect of the subgrade modulus, K_s, on pile deflections

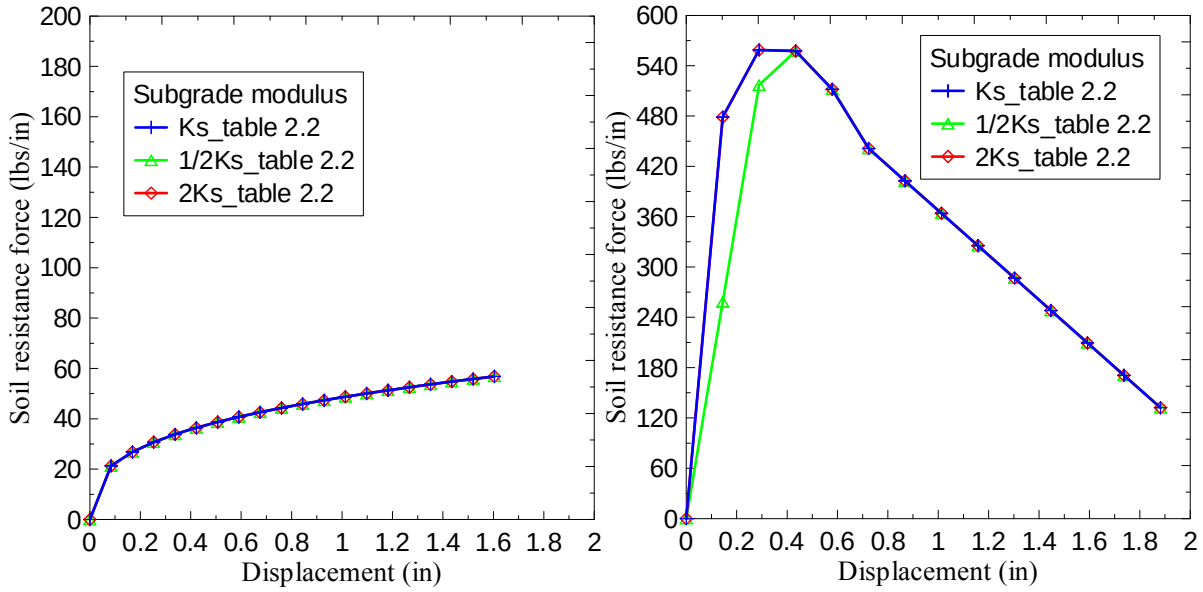

(a) Soft clay layer (b) Stiff clay layer

Figure 58

P-y curve at varying subgrade soil modulus (K_s)

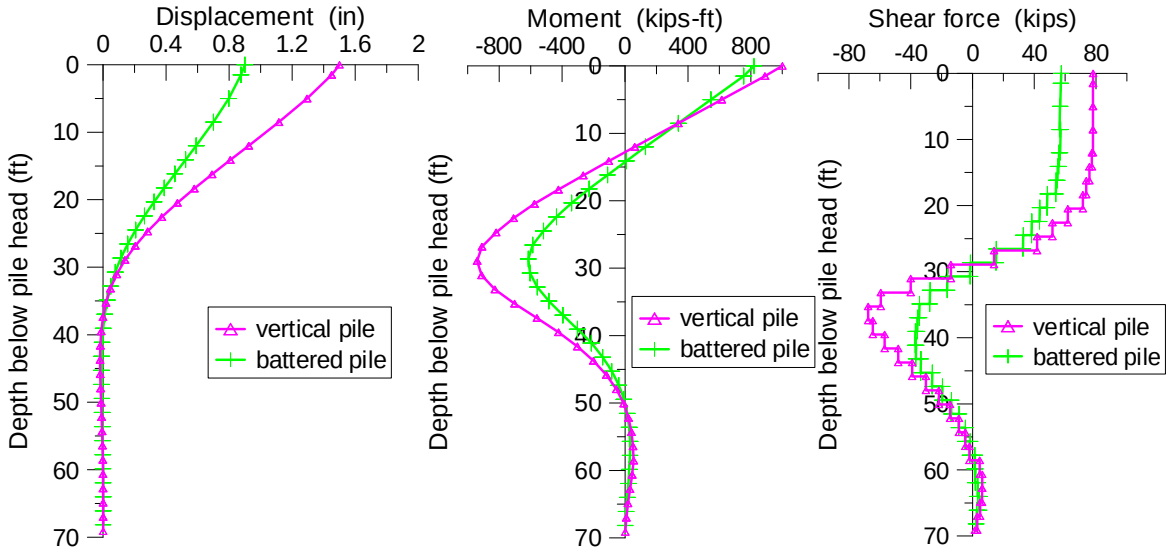

(a) Displacement profile (b) Moment profile (c) Shear force profile

Figure 59

Comparison of battered pile group versus vertical pile group (lateral load = 1870 kips)

Effects of Mudline Depth. The top soil layer below the mudline was identified as silty clay with low undrained shear strength. Among the five CPT tests and one soil boring, the thickness of the top soil layer varies due to the variation of the mudline depth. Since the top soil layer is the closest soil layer to the pile head, it may have considerable influence on the pile-soil interaction despite its low undrained shear strength.

An analysis using FB-MultiPier was conducted to investigate the effects of the mudline depth. The mudline depth was varied between 10 ft. to 15 ft. below the water level, which leads to a change in the top soil layer thickness from 15 ft. to 10 ft. Other FB-MultiPier input parameters were kept constant when changing the mudline depth. A lateral load of 1870 kips was applied for all the FB-MultiPier runs in this analysis.

Figure 60 shows the variation of pile head deflection with the mudline depth below water level. As can be seen, changing the mudline depth from 10 ft. to 15 ft. in the FB-MultiPier analysis resulted in a variation of pile head deflection in the amount of about 0.2 in.

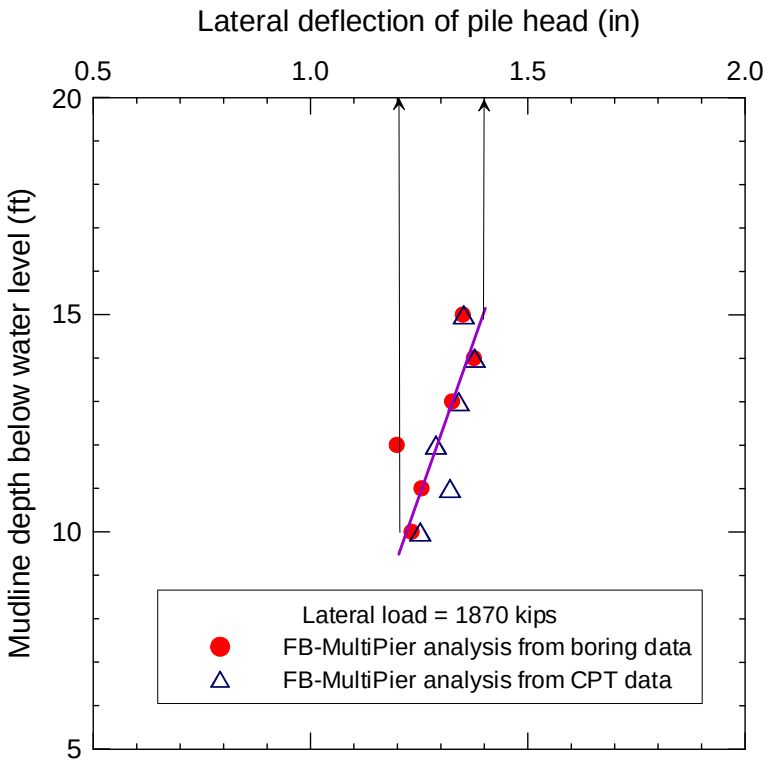

Figure 60

Variation of pile head deflection with mudline depth for Pile$_{FB}$20/Pile 8

The profiles of pile deflection and moment with mudline depth varying from 10 ft. to 15 ft. in FB-MultiPier analysis are presented in Figure 61. The deflection at pile head showed a minimal amount of variation with the mudline depth, which is demonstrated in Figure 61

as well. In addition, the change in pile moment profiles caused by the change of mudline depth is negligible as indicated in Figure 61(b).

Figure 62 shows the soil lateral resistance force along the depth below the pile cap. It was found that effects of the change in mudline depth on soil lateral resistance force are minimal. This is probably due to the fact that the top soil layer was much softer compared to underlying soil layers.

In summary, the variation of mudline depth from 10 ft. to 15 ft. or the change of the first soil layer thickness between 15 ft. and 10 ft. did not show significant impacts on the behavior of battered pile in the FB-MultiPier analysis, except for that the pile head deflection varied in a small amount of 0.2 in. For the subsequent analysis using the FB-MultiPier, the mudline depth from the water level was determined to be 10 ft. or 12 ft. from the bottom of pile cap as illustrated in Figure 63.

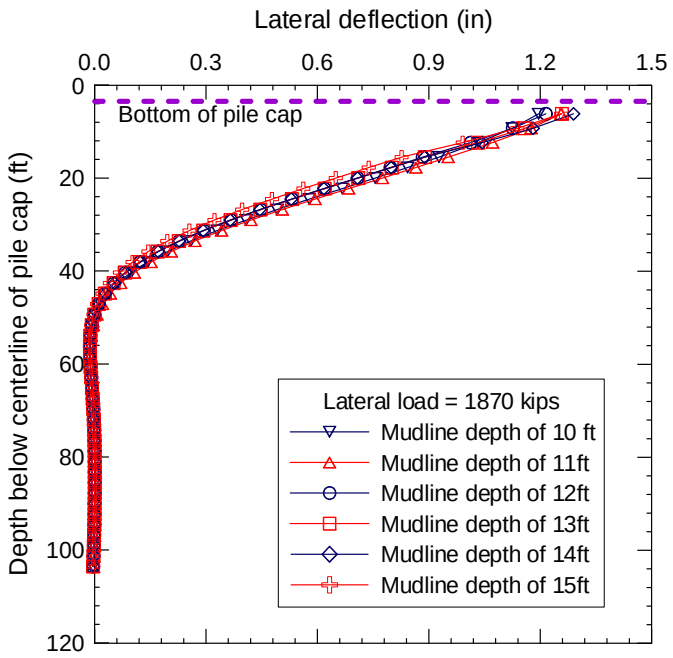

(a) Deflection profile of $Pile_{FB}20$/Pile 8

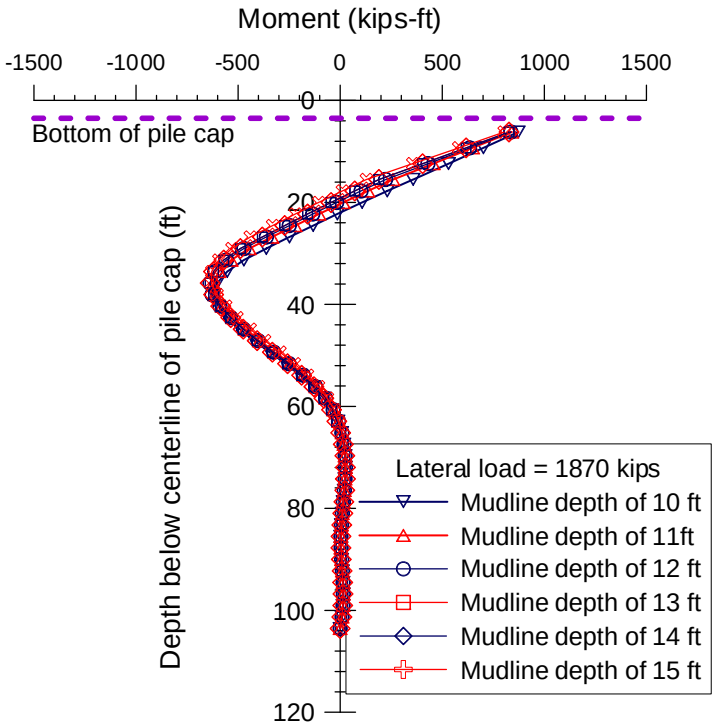

(b) Moment of $Pile_{FB}20$/Pile 8

Figure 61
Effects of mudline depth on profiles of pile deflection and moment in FB-MultiPier analysis

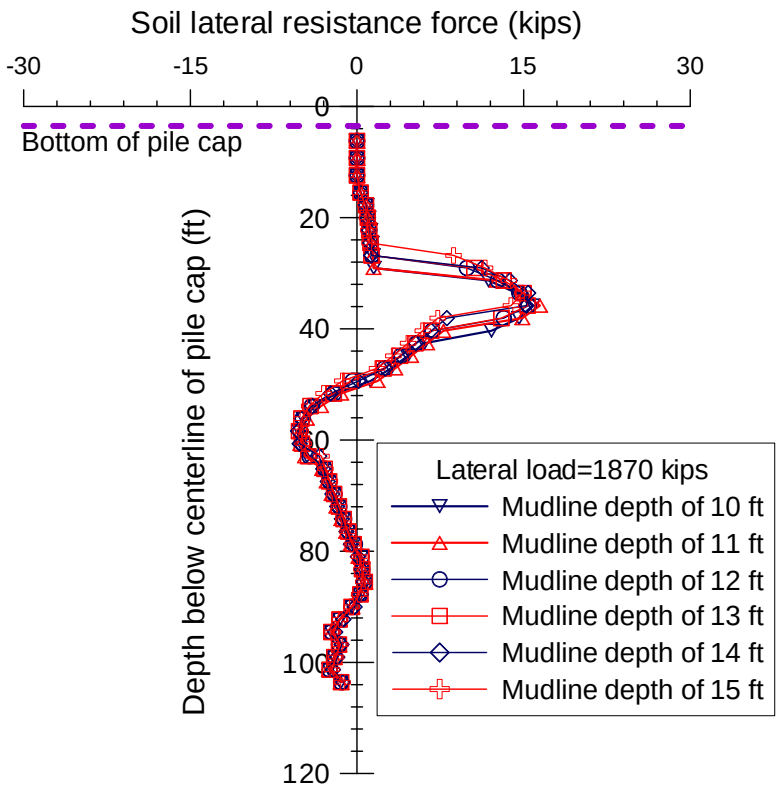

Figure 62

Effects of mudline depth on soil lateral resistance force in FB-MultiPier analysis

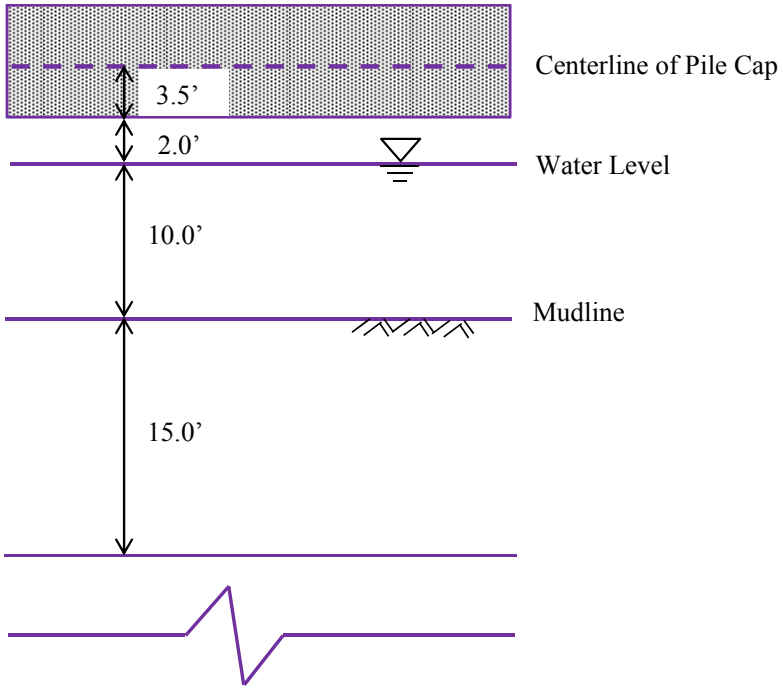

Figure 63

Mudline depth in FB-MultiPier analysis

Analysis of Battered Pile Groups

The FB-MultiPier analyses were performed to predict pile lateral deflections, moments, axial forces, soil resistances, and shear forces. Comparisons were then made between the results from the FB-MultiPier analysis and the measurements from instruments or the derived results based on instrumentation measurements.

Figure 64 presents a plan view of the pile layout. It illustrates the numbering system in the FB-MultiPier models and the numbering during the instrumented lateral load tests. The input parameters used in the FB-MultiPier for modeling the pile and the pile cap are summarized in Table 4. Table 5 lists input parameters for the pier.

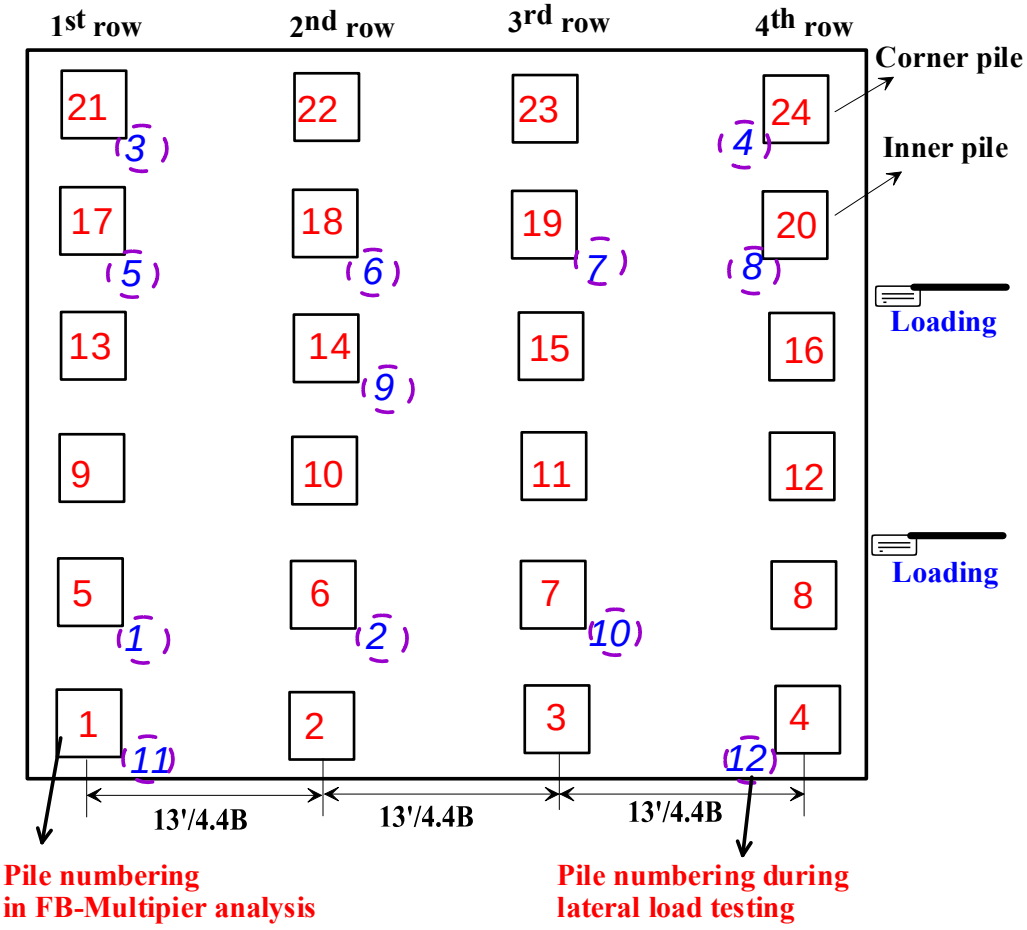

Figure 64

Plan view of pile layout modeled in FB-MultiPier

Table 4
Input material properties of pile and pile cap

Input parameter	Unit	Pile	Pile Cap
Breadth (B)	ft.	3	44
Width (W)	ft.	3	42.5
Height (H)	ft.	105-107	7
Unit weight(γ)	pcf	150	150
Elastic modulus(Ec)	ksi	5090	5090
Poisson's ratio (v)		N/A	0.2
Thickness(t)	ft.	N/A	7
Compressive strength (f'c)	ksi	8	6

Table 5
Input parameters of pier columns

Pier height (ft.)	Cantilever length (ft.)	Column spacing (ft.)	Column offset (ft)	Number of Pier Column	Elastic Modulus (Ec) (ksi)	Compressive strength (f'c) ksi
68	13.5	31.25	58.75	2	4696	8

The geotechnical investigation on the site conditions through CPT tests and soil boring showed some discrepancies in soil profiles and soil undrained shear strength. The discrepancies were probably caused by horizontal variation of the subsurface soil as the location of CPT is about 200 ft. from the borehole. The CPT data are considered more accurate to characterize the subsurface soil condition of the M19 pier because the CPT tests were carried out at locations where the test pier was installed later. However, in order to examine the effects of soil profile on the pile behavior, FB-MultiPier analyses were performed using soil properties estimated from CPT data and soil boring, respectively.

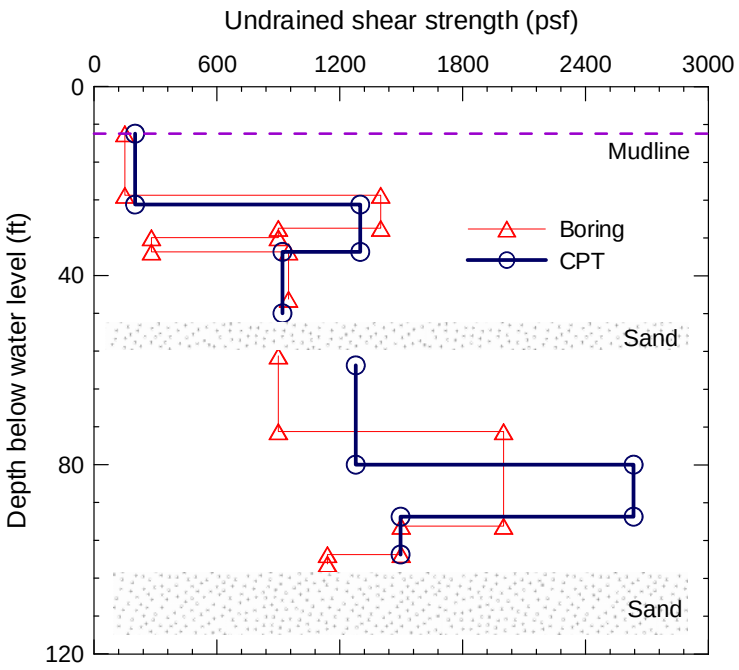

Figure 65
Comparison of soil undrained shear strength obtained from CPT and UU tests on boring samples

For characterizing pile group effects, the following two different conditions were considered:

(1) Including the pile group effect (*p*-multiplier < 1),

(2) Neglecting the pile group effect (*p*-multiplier = 1)

FB-MultiPier facilitates the use of the PY multiplier value for different row piles to characterize the pile group effect, and such effect can be ignored if unit PY multipliers are chosen for all row piles. The rationale behind considering no group effect in this study are: a) The measured lateral displacement under maximum load was small (0.66 in) and within the elastic deformation range of piles; b) the back-calculated p-y curves from lateral load test showed no group effect especially between rows 2, 3, and 4; and c) the pile spacing in the loading direction is 4.4 times of the pile width at cap level and increases with depth between row 2 and row 3, which is deemed to be relatively insignificant to cause considerable group effects. Nevertheless, FB-MultiPier analysis with assumed PY multipliers was carried out to evaluate the group effects on the pile behavior. The *p*- multipliers adopted in this analysis using FB-MultiPier were determined based on relevant information from the literature and engineering judgment. From 1st row to 4th row, the assigned *p*-multiplier in FB-MultiPier for each row was 0.7, 0.5, 0.35, and 0.35, respectively.

The pile head deflection predicted by FB-MultiPier are compared with the measured deflection from the automated survey and deflection derived using high order polynomial curve fitting methods as shown in Figure 66. As can be seen, pile head lateral deflection predicted by the adopted FB-MultiPier is larger than the measured deflection at the same load level. The predicted pile head deflection from FB-MultiPier with soil properties determined by CPT data and soil boring showed only minimal difference, which is in agreement that the soil profiles estimated from CPT tests and the borings were similar. Between the predicted pile head deflections with and without group effects, the results from the FB-MultiPier analysis by ignoring group effects showed significantly less deflection, indicating that the group effects with the PY multipliers chosen in this study have considerable influence on the pile behavior.

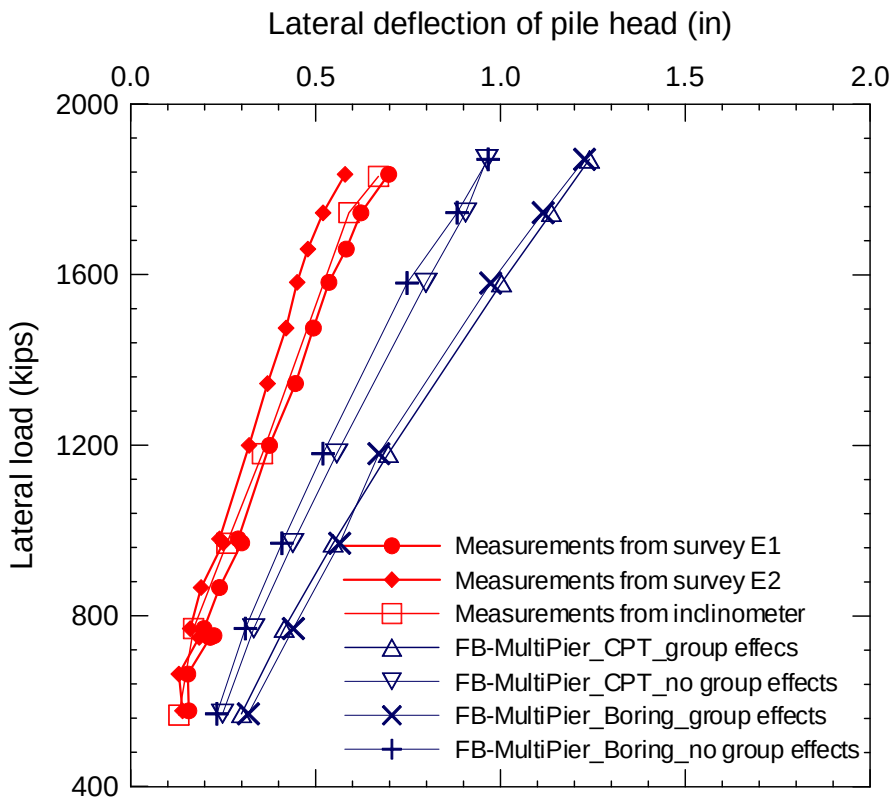

Figure 66
Comparison of pile head lateral deflection ($Pile_{FB}20$/Pile 8) between measurements and prediction from FB-MultiPier analysis

The lateral deflection profiles predicted at the maximum applied lateral load of 1870 kips by the FB-MultiPier analyses using the aforementioned different conditions are compared with

the IPI measured and polynomial derived displacement profiles developed at same load as shown in Figure 67(a) and Figure 67(b) for Pile 4 and Pile 8, respectively. When group effects are neglected, the predicted pile deflection is larger than the measured deflection for the portion from the pile head to a depth of 25 ft. and smaller below the depth of 25 ft. When group effects were taken into consideration and the assumed p-multipliers were incorporated in the adopted FB-MultiPier analysis, the predicted deflection is overall larger than the measurements for the portion from the pile head to a depth of around 40 ft. and smaller below the depth of around 40 ft.

The predicted pile deflection profiles using the adopted FB-MultiPier model for various conditions showed overall noticeable differences from the measured deflection profiles. It should be pointed out that there are a wide range of factors that cause the discrepancies between the prediction and measurements. For example, uncertainties or errors may exist in the measurements from instruments although measures such as using an automated survey were taken to verify the instrumentation measurements. The soil property inputs in FB-MultiPier may not completely represent the in-situ soil conditions under which the lateral load tests were carried out. The effects of pile installation on changing soil properties were not taken into account by implementing the soil properties into FB-MultiPier from CPT tests and soil boring conducted before the pile construction.

On the other hand, by implementing Winkler's approach with the assumption of discrete soil-pile units (a beam connected to a series of springs), the actual soil-pile-soil interaction during the lateral load testing may not be fully simulated in FB-MultiPier although empirical *p*-multipliers were used to account for the "shadow effects" in the loading direction. The "edge effects" in the transverse direction of loading were not able to be considered in FB-MultiPier despite that the piles were closely spaced in the transverse direction. In addition, the restriction of pile-cap connection at the centerline of the pile cap does not allow modeling the actual pile embedment length of 2 ft. in the cap where the pile-cap connection is 1.5 ft. below the cap centerline, which may particularly contribute to the discrepancies with respect to the bending moment.

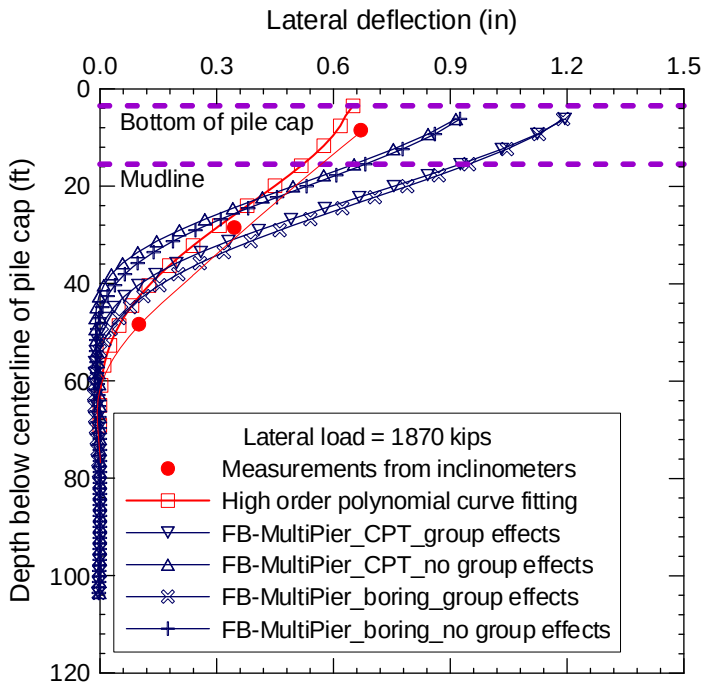

(a) Pile$_{FB}$24/Pile 4

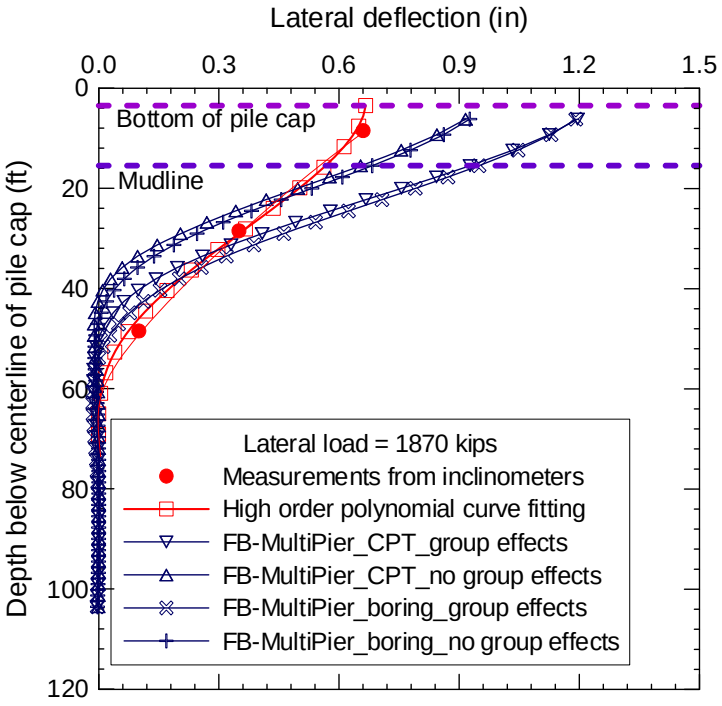

(b) Pile$_{FB}$20/Pile 8

Figure 67
Pile lateral deflection from measurements and FB-MultiPier analysis with different conditions

Profiles of Lateral Deflection. Since the predicted displacement profiles for piles in all different rows are similar, results are presented only for Pile 11 and Pile 8 in Figure 68(a) and 68(b), respectively. The FB-MultiPier predicted 0.30 in displacement at 570 kips and 1.20 in displacement at 1870 kips at the pile head for all piles. For $Pile_{FB}20$/Pile 8, the results suggest that the predicted deformation is larger than the measured one, which is 0.66 in. In addition, the depth at which the lateral displacement gradually reduced to zero was found to be smaller than the measured one. The depths to the zero displacement of predicted profiles were in the range of 40-45 ft. from pile top proportioning to magnitude of loads, whereas this range is 45-60 ft. for the measured displacement profiles.

Profiles of Bending Moments. Bending moment profiles at different load levels are presented in Figure 69 for Pile 11and Pile 8. The maximum positive moment is located at the pile head level, as expected, where the pile and pile cap are rigidly connected.

The moment profiles for piles in different rows are presented in Figure 70. It shows that bending moment profiles are approximately the same for piles in different rows, indicating that the direction of batter has minimal effects on bending moments of piles.

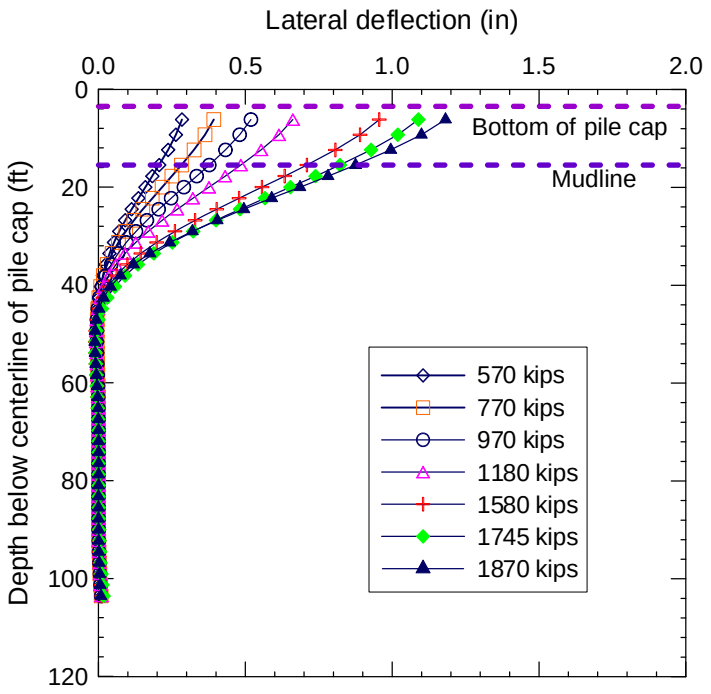

(a) $Pile_{FB}1$/Pile 11 in 1st row

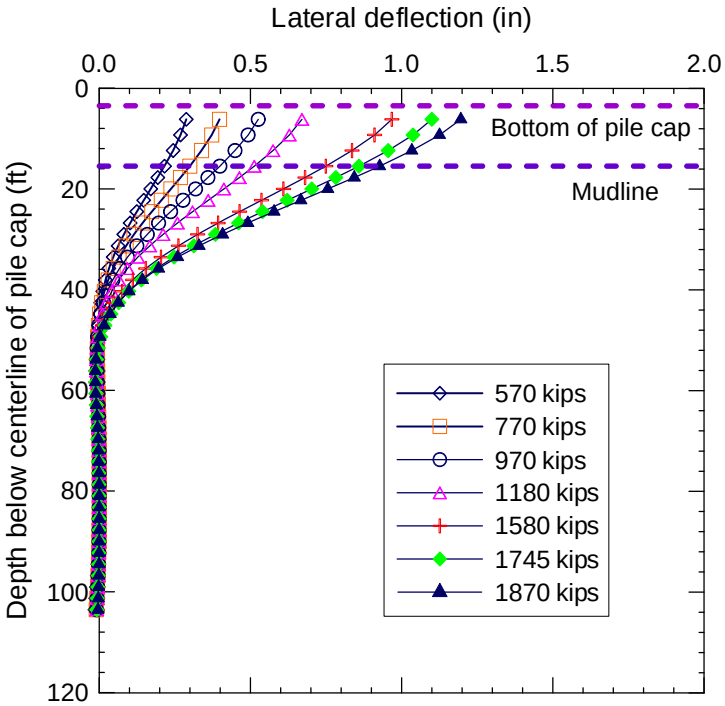

(b) $Pile_{FB}20$/Pile 8 in 4th row

Figure 68
Pile deflection at various load levels in FB-MultiPier analysis

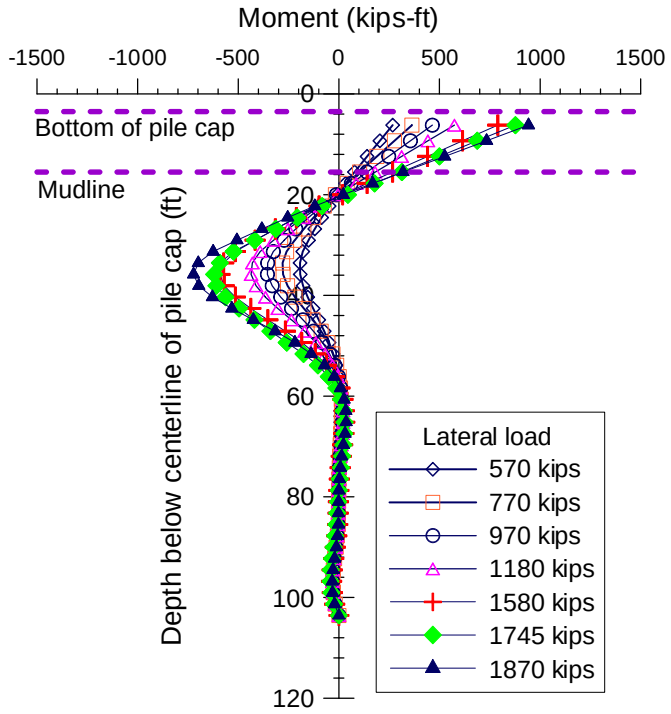

(a) $Pile_{FB}1$/Pile11 in 1st row

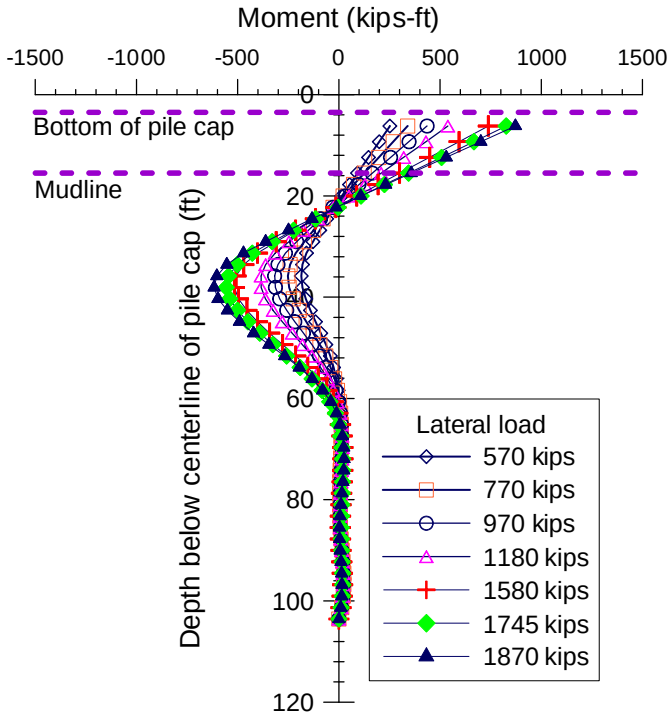

(b) $Pile_{FB}20$/Pile8 in the 4th row

Figure 69

Pile moments at various load levels in FB-MultiPier analysis

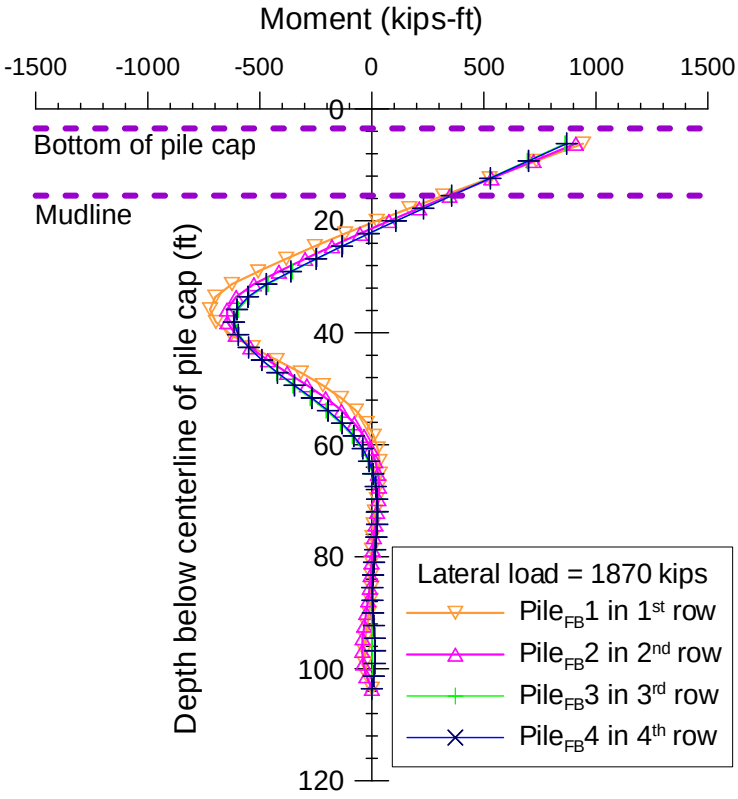

Figure 70
Comparison of moments at 1870 kips

The moment profiles predicted from the FB-MutiPier are compared with the measured moments by strain gauges and those back-calculated from IPI data as shown in Figure 71. The figure shows that both the moments predicted by the FB-MultiPier and the back-calculated moments from IPI are in good agreement with the moments calculated from strain gauge measurements at the two different instrumented depths. However, the maximum negative moments predicted by FB-MultiPier are larger than the corresponding back-calculated negative moments, and the maximum positive moments predicted at the pile head are nearly 50% larger than back-calculated moments for all loads. Unfortunately, due to unavailability of enough strain gauges, the actual moment profile was not calculated and verified.

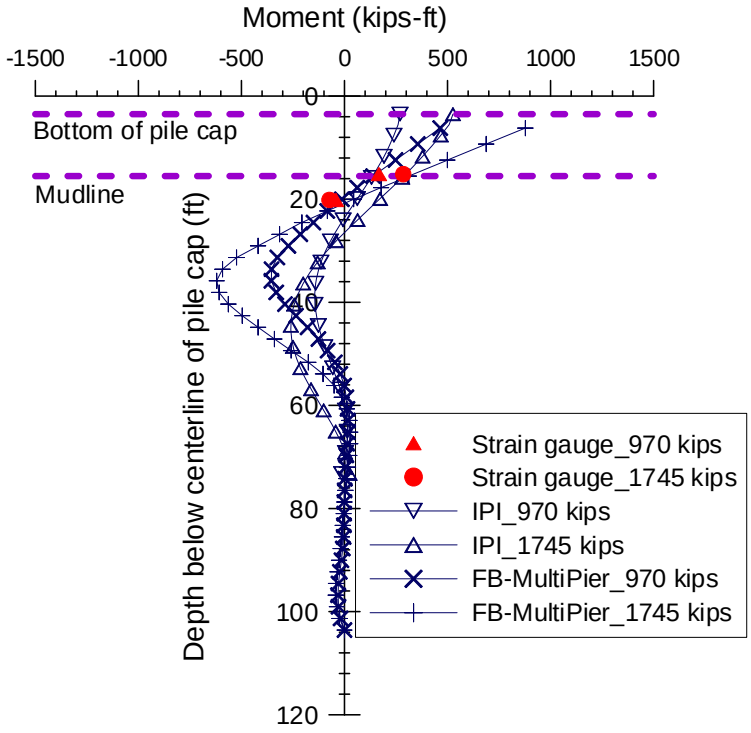

(a) $Pile_{FB}1$/Pile 11 in 1st row

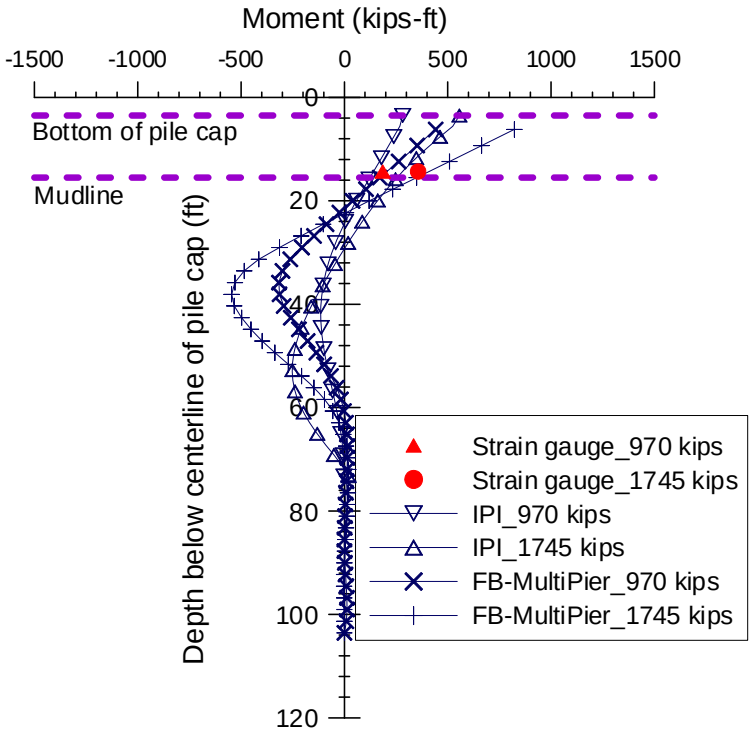

(b) $Pile_{FB}19$/Pile 7 in 3rd row

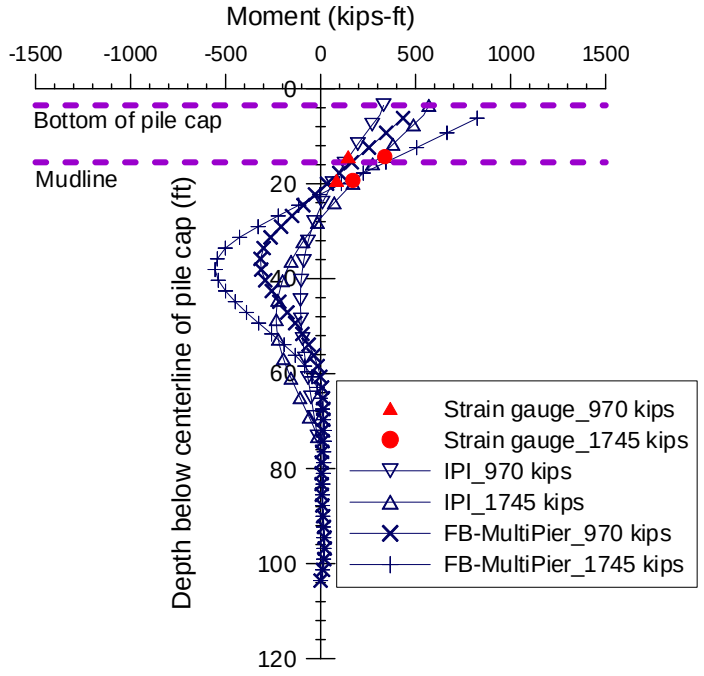

(c) $Pile_{FB}4$/Pile 12 in 4th row

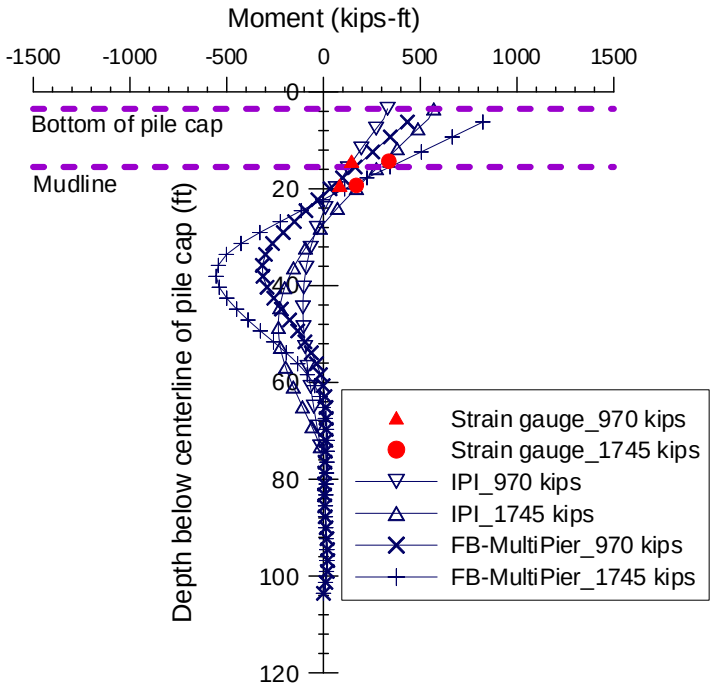

(d) $Pile_{FB}24$/Pile 4 in 4th row

Figure 71

Pile moments derived from strain gauge measurement, IPI measurement, and from FB-MultiPier analysis

Profiles of Lateral Soil Resistance. The profiles of soil resistance force predicted by the FB-MultiPier at the different lateral loads for the 1st row pile and 4th row pile are presented in Figure 72(a) and Figure 72(b), respectively. The figures indicate that the maximum soil resistance predicted by FB-MultiPier was 25 kips at the maximum load of 1870 kips, which occurred at about 26-33 ft. below the pile head. It is also observed that the positive soil resistance force changes to negative at 45-47 ft. from pile head depending on the magnitude of applied load. The figure shows that at higher applied load such as 1870 and 1745 kips, the soil resistance changes to negative at deeper depths than that at lower applied load.

Figure 73 presents the soil lateral resistance forces for piles in different rows at the lateral load of 1870 kips in FB-MultiPier analysis. The 1st row piles showed highest lateral soil resistance forces and then the piles in 2nd row. Piles in the 3rd and 4th rows showed almost the same soil lateral resistance forces.

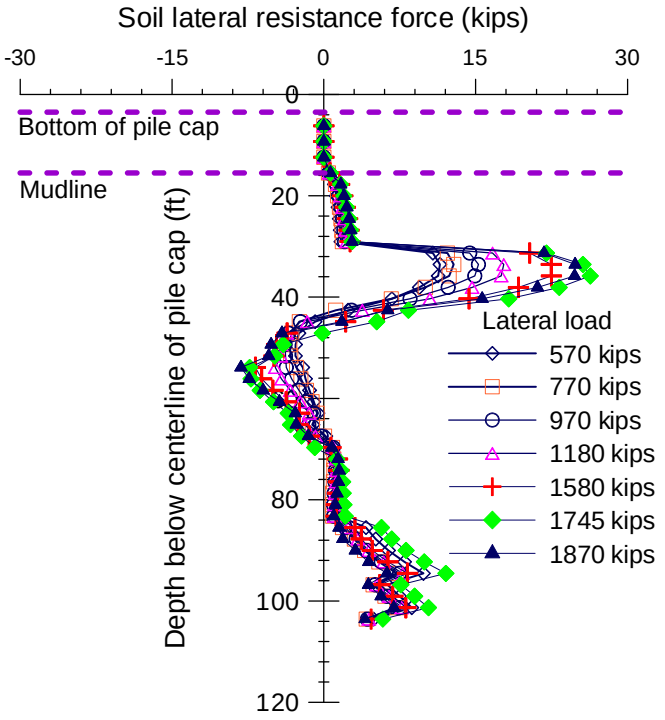

(a) $Pile_{FB}1$/Pile 11 in 1st row

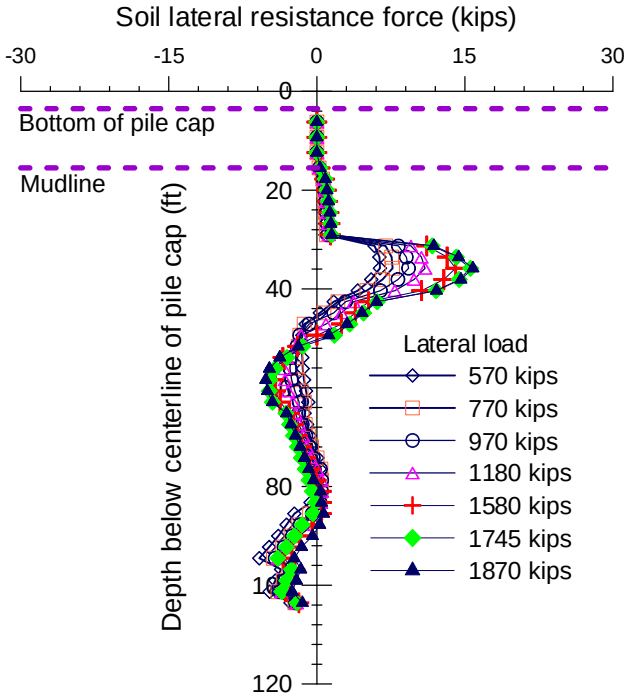

(b) $Pile_{FB}20$/Pile 8 in 4th row

Figure 72

Soil lateral resistance force at different loading levels in FB-MultiPier analysis

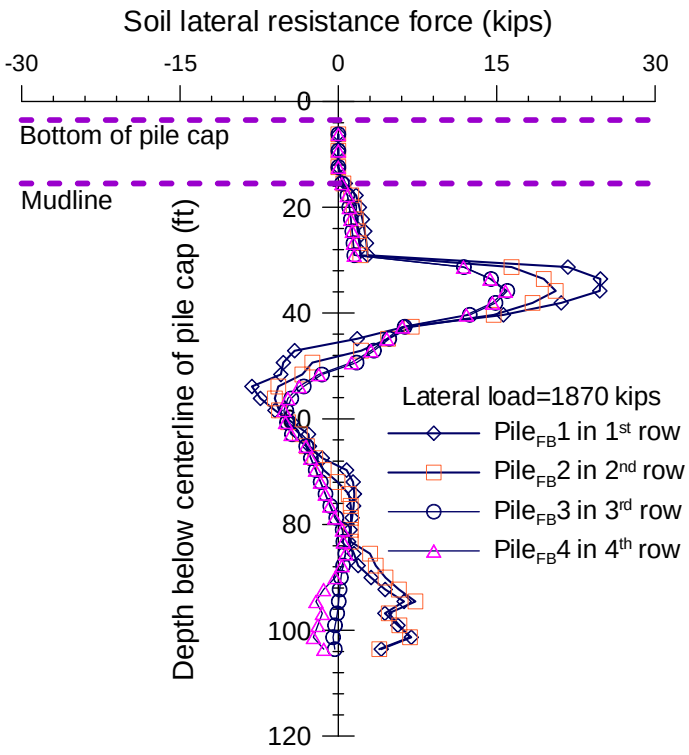

Figure 73

Soil lateral resistance force for piles located in different rows in FB-MultiPier analysis

The soil lateral resistance force per unit length predicted by FB-MultiPier were compared with the soil lateral resistance force per unit length derived using the high order polynomial method as shown in Figure 74(a) and Figure 74(b) for Pile 11 and Pile 8, respectively. The figures indicate that the FB-MultiPier predicted maximum soil resistance forces are greater than those calculated by high order polynomial curve fitting. In addition, the maximum soil resistances derived by the polynomial method occurred at deeper depths than the predicted values. Moreover, the calculated resistance profiles gradually reduces to zero at larger depths than the predicted soil resistance profile for piles in both 1st and 4th rows.

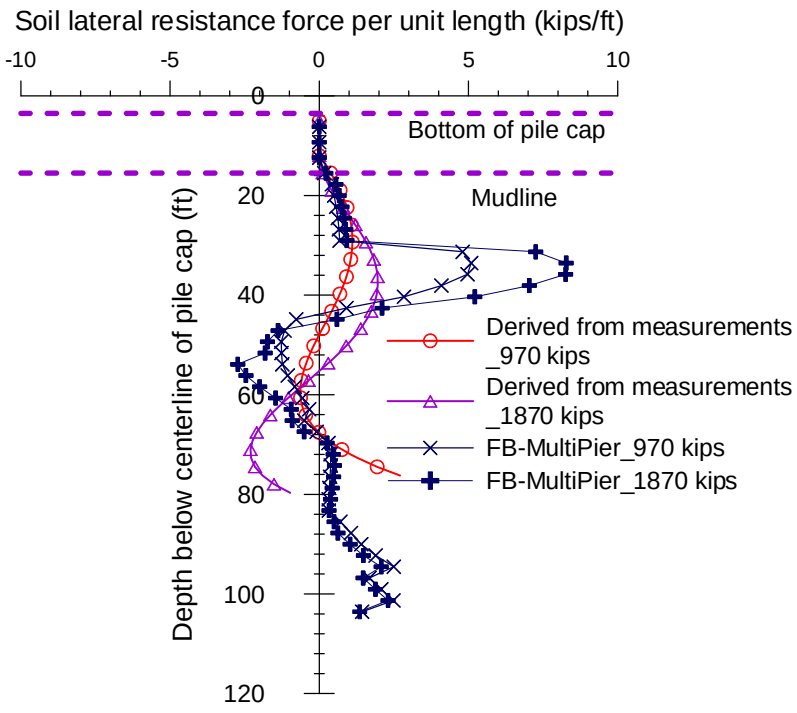

(a) $Pile_{FB}1$/Pile 11

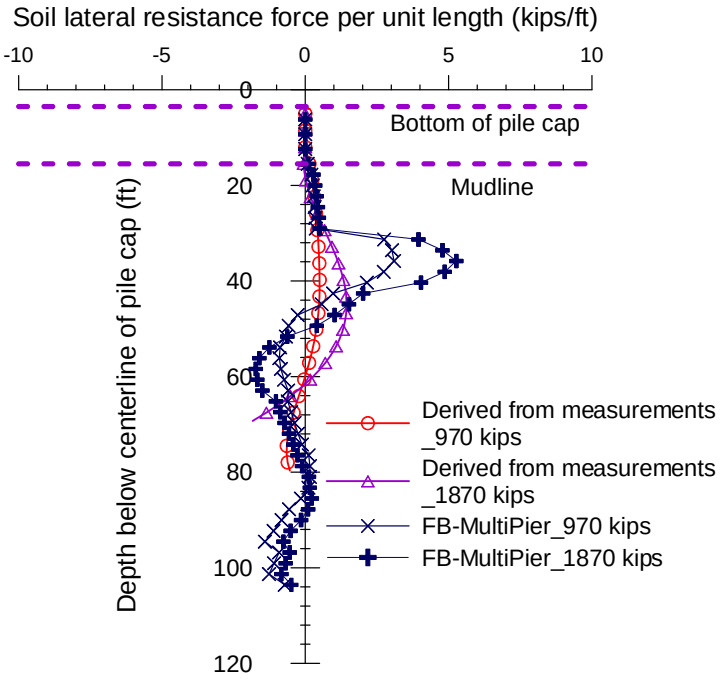

(b) $Pile_{FB}20$/Pile 8

Figure 74
Soil lateral resistance force per unit length derived from measurements and predicted by FB-MultiPier analysis

Pile Axial Force. The axial force profiles developed along the piles located in different rows at the applied lateral loads of 570 kips and 1870 kips are presented in Figure 75. As expected, the back row piles have developed tensile axial force, whereas the front row piles have developed compressive axial force. This observation agrees with the axial forces computed from strain gauge data. The axial forces predicted by FB-MultiPier at static lateral load increment were compared with those measured from the strain gauges located at different depths of the piles. As explained earlier, a pair of strain gauges (SG1) was located at 10 ft.-12 ft. from the pile top, depending on the pile cut-off length, and another pair of strain gauges (SG2) was located at 5 ft. below the strain gauges, SG1. The comparison between the predicted axial forces at SG1 and SG2 locations of the piles subjected to increasing static lateral load to the measured axial forces are presented in Figure 76. The figures show that the axial forces at both depths (SG1 and SG2) predicted from FB-MultiPier are very close, which is somehow different from the measured axial forces at these same depths. However, in general there is an acceptable level of agreement on trend and range of predicted axial forces, compared to measured axial forces.

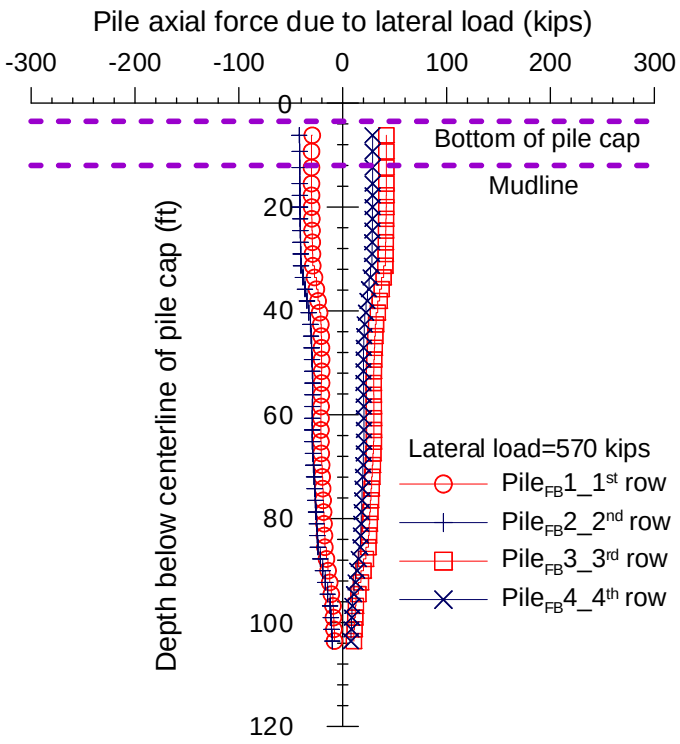

(a) Lateral load of 570 kips

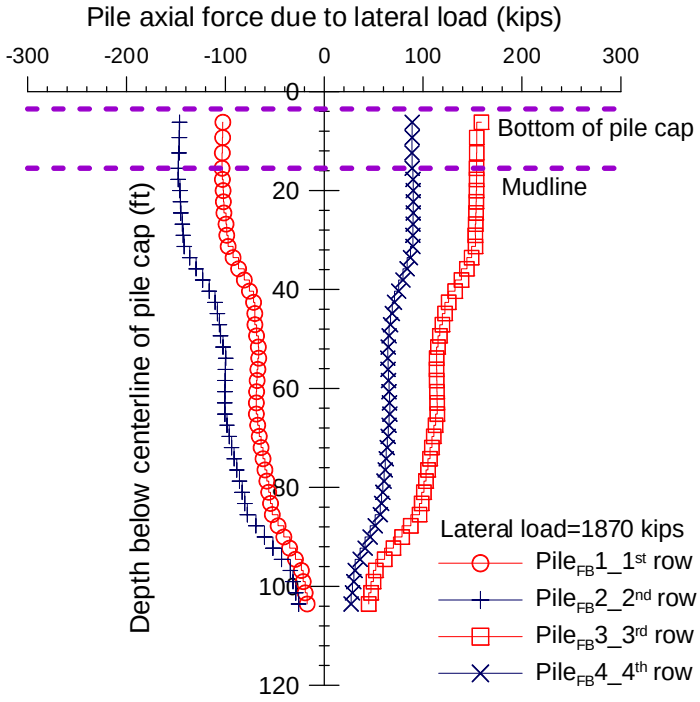

(b) Lateral load of 1870 kips

Figure 75

Pile axial force due to lateral load in FB-MultiPier analysis

The axial forces predicted for the 1st row piles are in good agreement with the measured axial forces at SG2 as shown in Figure 76(a). Since the measured axial forces at SG2 location are not varied significantly from SG1, it can be said that the predicted axial forces are in a good agreement with the measured axial forces for the 1st row pile. The predicted axial forces for the 2nd row pile [Figure 76(b)] are somehow larger than the measured axial forces at SG2, and smaller than the measured axial force at SG1. However, the variation between the measured axial forces at SG1 and SG2 for piles in the 2nd row are a little high compared to piles in other rows. The 3rd row pile's [Figure 76(c)] predicted axial forces are smaller than the axial forces at SG1, but, it almost matches the measured axial forces at SG2. Similar to the 1st row pile, the predicted axial forces for the corner pile ($Pile_{FB}24$/Pile 4) of 4th row with increased lateral load are found to be within the range of measured axial forces at SG2 as shown in Figure 76(d).

In general, the predicted axial forces by FB-MultiPier agree reasonably well with the measured axial forces. It is worth pointing out that the proper distribution of axial force along the pile length were not distinctly defined, since the predicted axial forces at SG1 and SG2 location are very close, which was only 5 ft. apart.

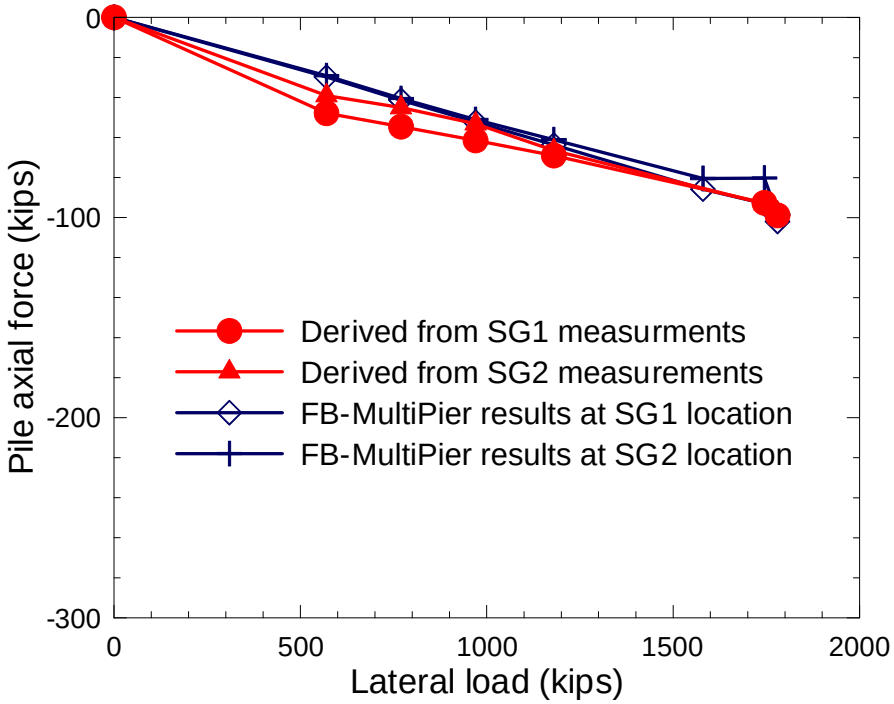

(a) $Pile_{FB}1$/Pile 11 in 1st row

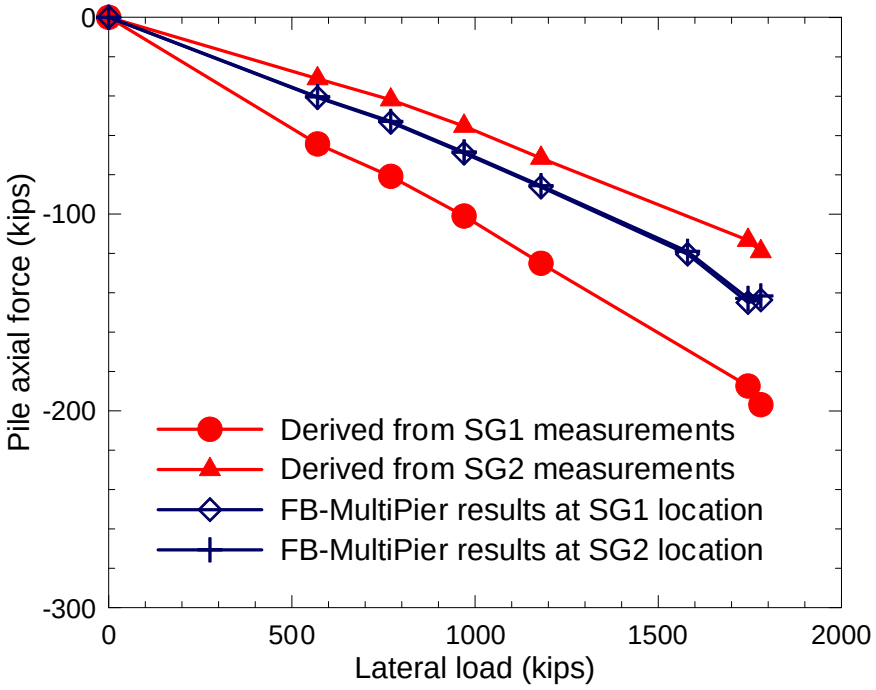

(b) $Pile_{FB}14$/Pile 9 in 2nd row

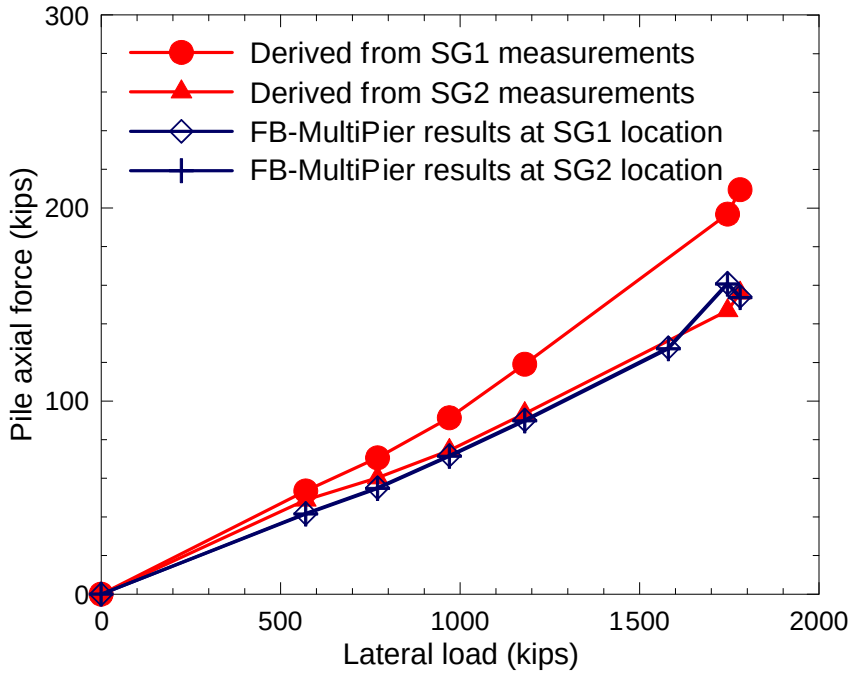

(c) Pile$_{FB}$7/Pile 10 in 3rd row

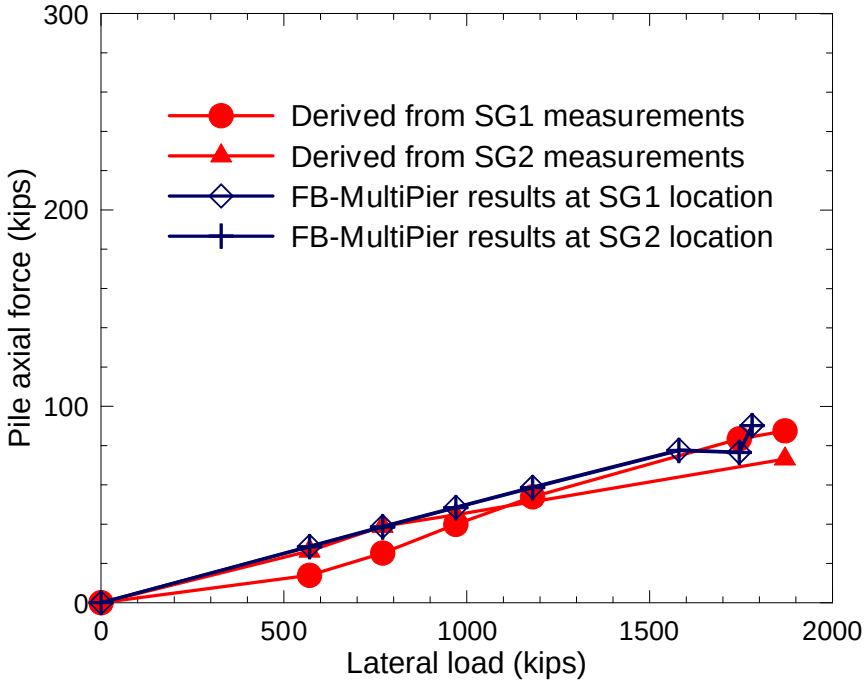

(d) Pile$_{FB}$24/Pile 4 in 4th row

Figure 76
Comparison of predicted and measured axial force of piles

Profiles of Shear Force. The profiles of shear force predicted by FB-MultiPier at different applied lateral loads are presented in Figure 77. Since the shear force predicted for all piles are very close, only the profiles of shear forces for the 1st row and 4th row piles are presented in Figure 77(a) and Figure 77(b) respectively. The shear force predicted at the pile head are 16 to 20 kips and 55 to 66 kips corresponding to the applied lateral load of 570 kips and 1870 kips, respectively. It can be observed that the depth to the first zero shear force occurred between 35-38 ft. from pile top for both row piles.

The shear force predicted shear by FB-MultiPier is compared with the shear force derived using the high order polynomial curve fitting. The comparisons are made at the applied lateral loads of 970 kips and 1870 kips as shown in Figure 78. The figures indicate that the predicted shear forces are larger than the derived shear force from polynomial fitting curve. However, we do not have field measurements to verify either result. The maximum shear force predicted for the $Pile_{FB}1$/Pile 11 in the 1st row is about 66 kips, whereas the maximum shear force calculated for the same pile is less than half. Such a trend is also observed for all piles. Moreover, the depths to the first zero shear force derived by using high order polynomial are also larger than the predicted profiles. The profiles of predicted shear force have a similar trend and shape at all applied loads. However, the derived profiles do not follow the same trend and shape. For example, the shape of shear force profiles derived for $Pile_{FB}1$/Pile 11 in the 1st row are very different from the shape of other piles' derived shear force profiles.

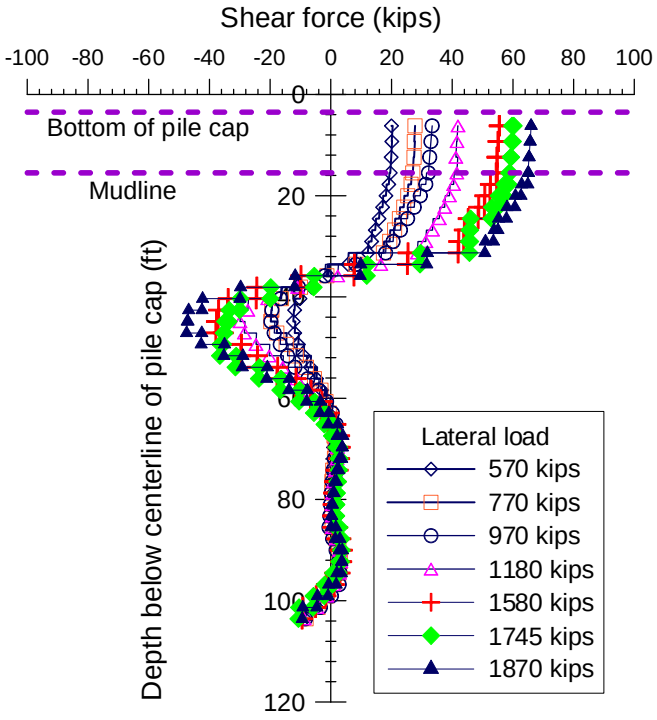

(a) $Pile_{FB}1$/Pile 11

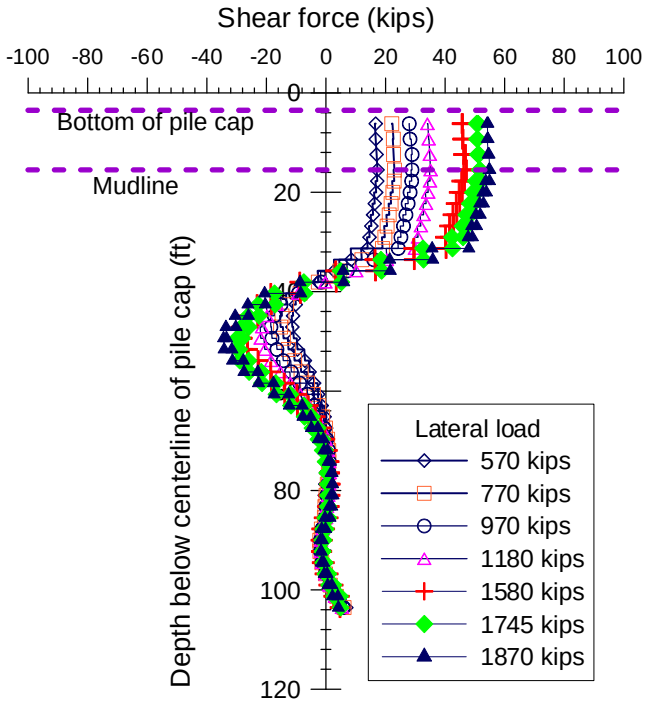

(b) $Pile_{FB}20$/Pile 8

Figure 77
Predicted Shear force profiles at different loads

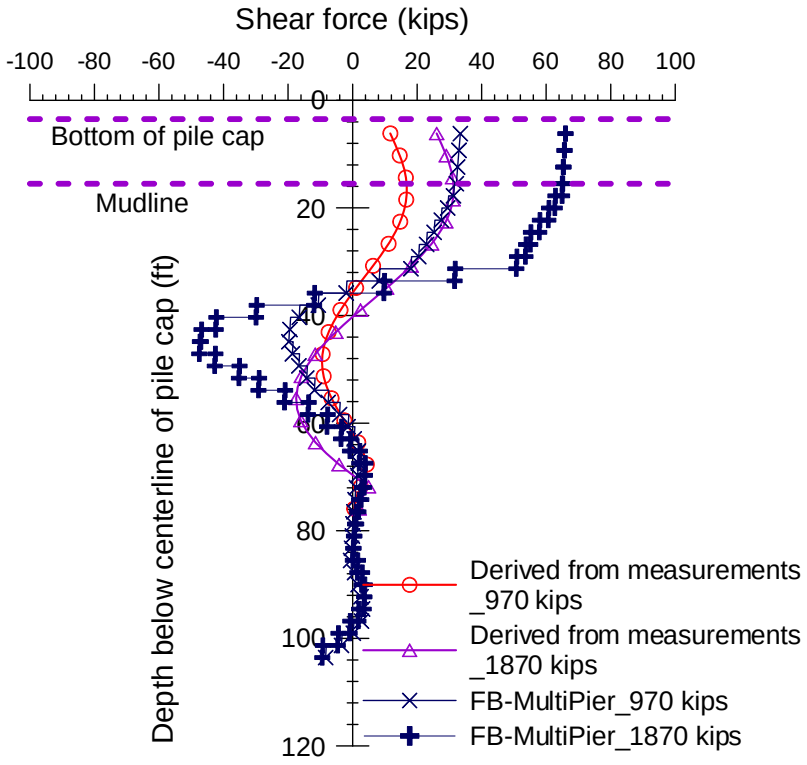

(a) $Pile_{FB}1$/Pile 11 in 1st row

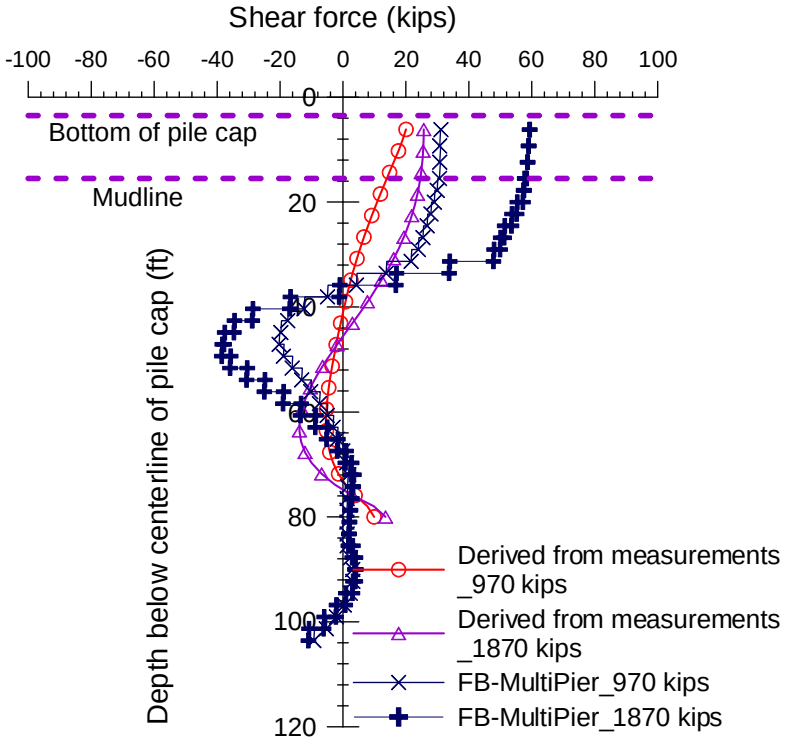

(b) $Pile_{FB}18$/Pile 6 in 2nd row

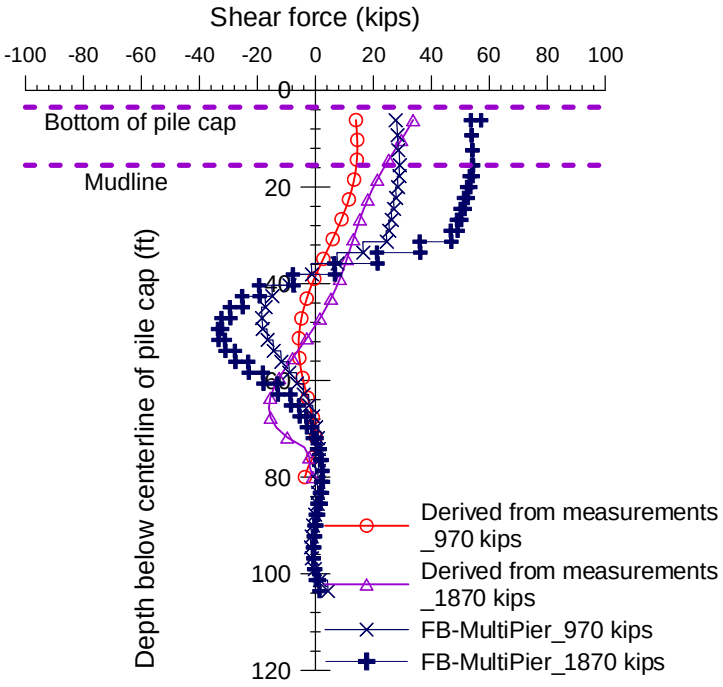

(c) $Pile_{FB}19$/Pile 7 in 3rd row

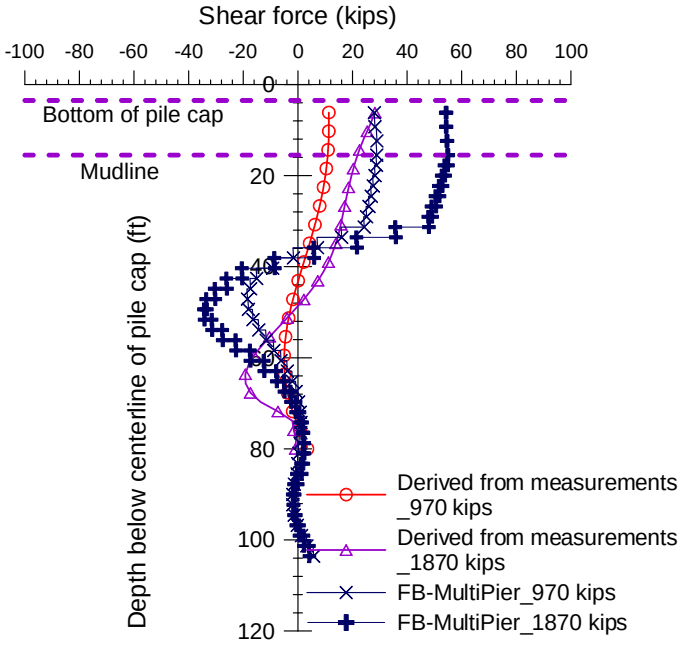

(d) $Pile_{FB}20$/Pile 8 in 4th row

Figure 78

Pile shear forces derived from measurements and from FB-MultiPier analysis

Effects of Pile Installation

In the previous analyses using FB-MultiPier, the soil property inputs were estimated from CPT tests conducted before the construction of the test pier. After the completion of pier construction, it is generally believed that the soil strength can be significantly improved due to the effects of pile driving and pile setup. The upper soil stratigraphy mainly consists of clay and silty clay. The pile driving process can replace soil and thus increase soil strength by squeezing the soil surrounding the piles. Pile setup has been commonly observed from the previous construction practice in the state of Louisiana.

The lateral load test was conducted about six months after the completion of the pile driving. Therefore, it is rational to assume that the in-situ soil strength at the M19 pier was increased by 20% of its original soil strength in a conservative estimation. It is also expected that the compressive strength of the pile concrete also increased during the time period of six months. It is assumed that the compressive strength of the pile increased from 8000 psi to 9000 psi at the time of the lateral load test. From the discussion of the results from back-calculation analyses of the IPI data, the pile group effects are minimal in the loading direction. Considering the uncertainties in the design process, it is rational to assume *p*-multiplier of 0.9, 0.8, 0.8, and 0.7 for piles in the 1st row, 2nd row, 3rd row, and 4th row, respectively.

Lateral Deflection. The FB-MultiPier analysis was conducted to account for the increase of soil strength due to pile setup and the concrete strength gained along with time. Figure 79 presents the lateral pile head deflection with the increase of lateral load. As can be seen, by incorporating the effects of pile installation on soil properties and increase of pile strength, the predicted pile head deflection by FB-MultiPier became closer to the measured deflection although there is still some difference between them.

Figure 80 shows the profiles of pile deflection for Pile$_{FB}$20/Pile 8. The figure indicates that predicted pile deflection for the portion above the mudline became closer to the measured deflection after increasing the soil shear strength and concrete strength in FB-MultiPier analysis. However, the prediction of pile deflection from FB-MultiPier still showed some discrepancies from measurements. It appears that increasing the overall soil strength only resulted in the shift of the deflection profile while the shape of the deflection profiles are still different between the prediction and measurements.

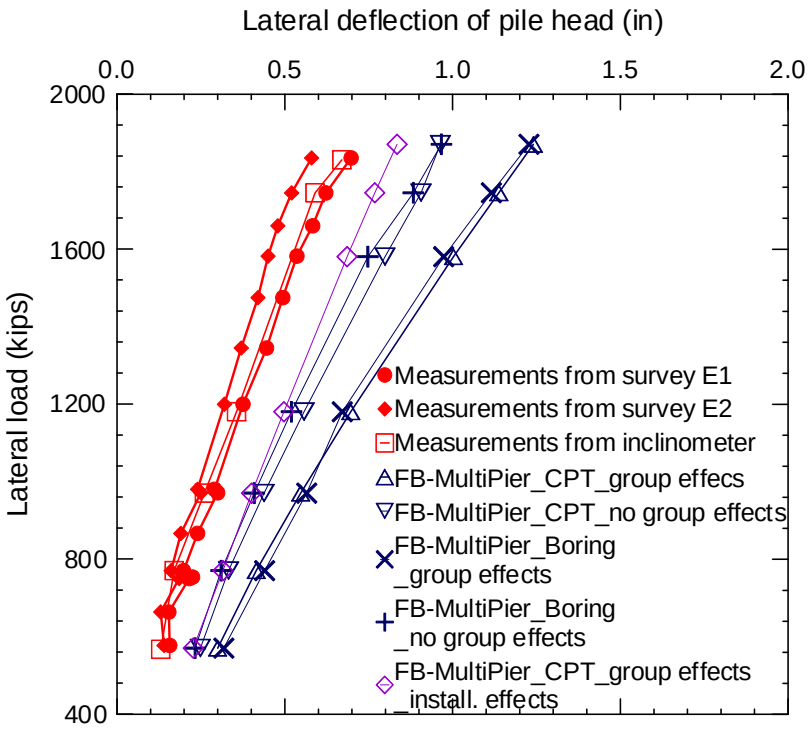

Figure 79

Predicted and measured pile head deflection for Pile$_{FB}$20/Pile 8

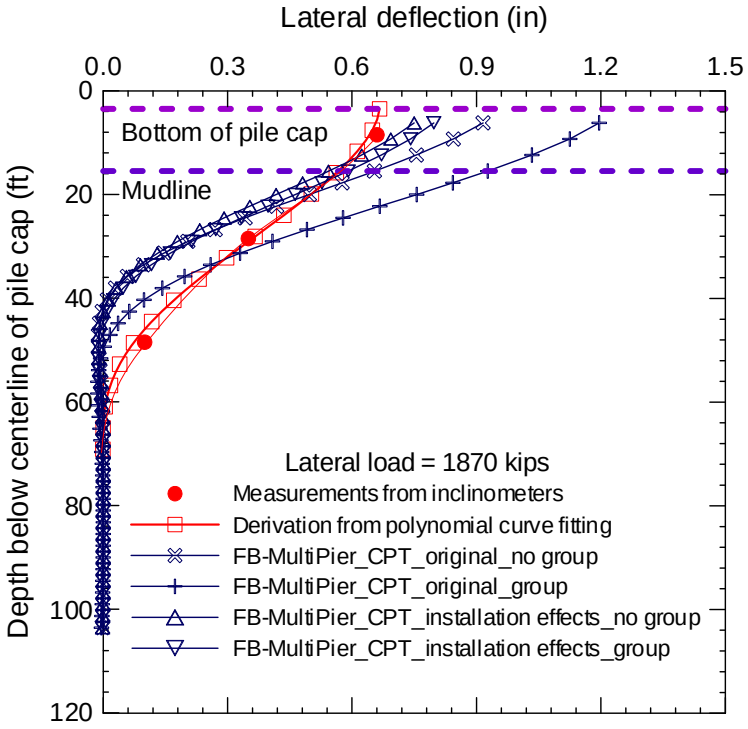

Figure 80

Pile deflection profile from FB-MultiPier with different conditions for Pile$_{FB}$20/Pile 8

Pile Bending Moments. Figure 81 presents the pile moment profiles for piles 4, 7, 11, and 12 to examine the installation effects on pile moments. At the load level of 970 kips, no significant changes are observed in pile bending moments between the original FB-MultiPier analysis and the analysis taking into account for installation effects. When the lateral load increases to 1745 kips, compared to the original analysis, bending moments decrease below the depth of 35 ft. while the maximum bending moment remains the same.

Soil Lateral Resistance. The change of soil lateral resistance force due to the installation effects is illustrated in Figure 82. For piles located in the inner rows and trail row (rows 2, 3, and 4), there is considerable increase of soil lateral resistance at a lateral load of 1870 kips while the change of soil resistance at a 970-kip lateral load is not noticeable. It indicates that increasing soil shear strength results in the increase of soil lateral resistance at high load level where the soil resistance capacity is mobilized. Pile 11/$Pile_{FB}1$ located in the lead row (1^{st} row) does not exhibit a significant increase of soil lateral resistance at 1870-kip lateral load probably because the soil is not fully mobilized around the piles in the lead row.

Pile Axial Force. The axial forces developed at various load levels for piles located in different rows are presented in Figure 83. After accounting for the installation effects and increasing the undrained soil shear strength in the FB-MultiPier analysis, the axial load in the piles located in the inner rows (rows 2 and 3) decreases significantly as shown in

Figure 83(a), Figure 83(b), and Figure 83(c). On the other hand, piles located in the lead row and trail row are not influenced by the installation effects as Figure 83(a) and Figure 83(d) indicate. Since there are more lateral loads transferred to axial loads for piles located in inner rows as indicated by previous observations (see Figure 43 and Figure 45), it would be expected that the change of soil conditions has a greater influence on the axial loads of the piles in the inner rows.

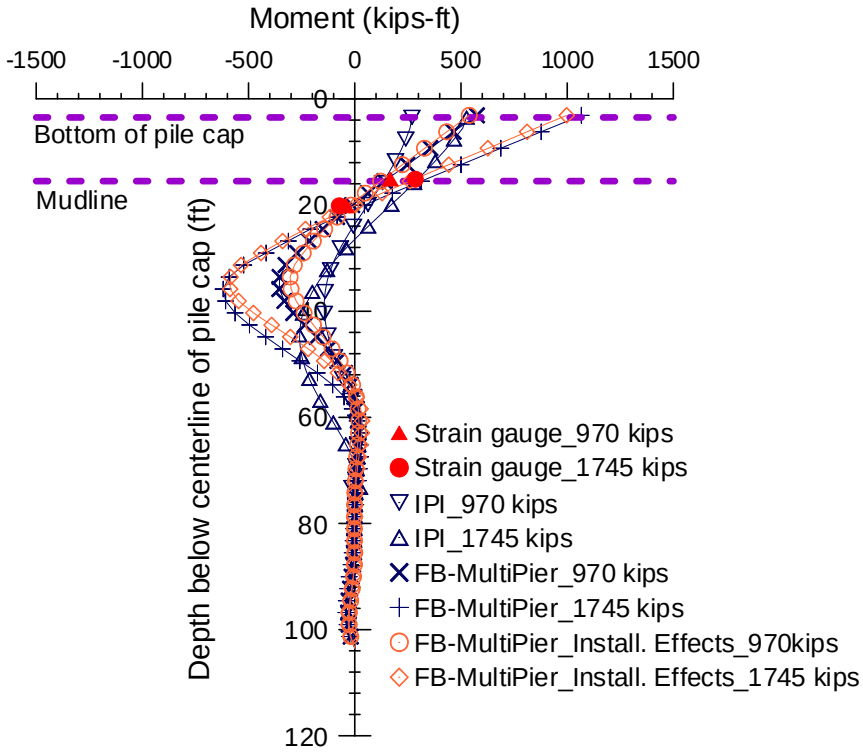

(a) $Pile_{FB}1$/ Pile 11

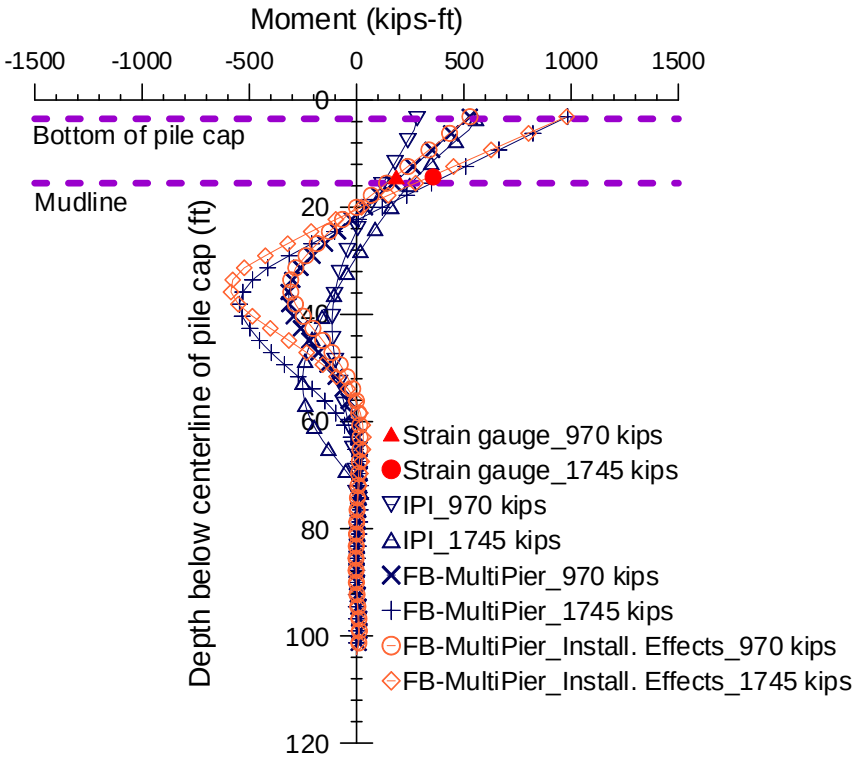

(b) $Pile_{FB}19$/ Pile 7

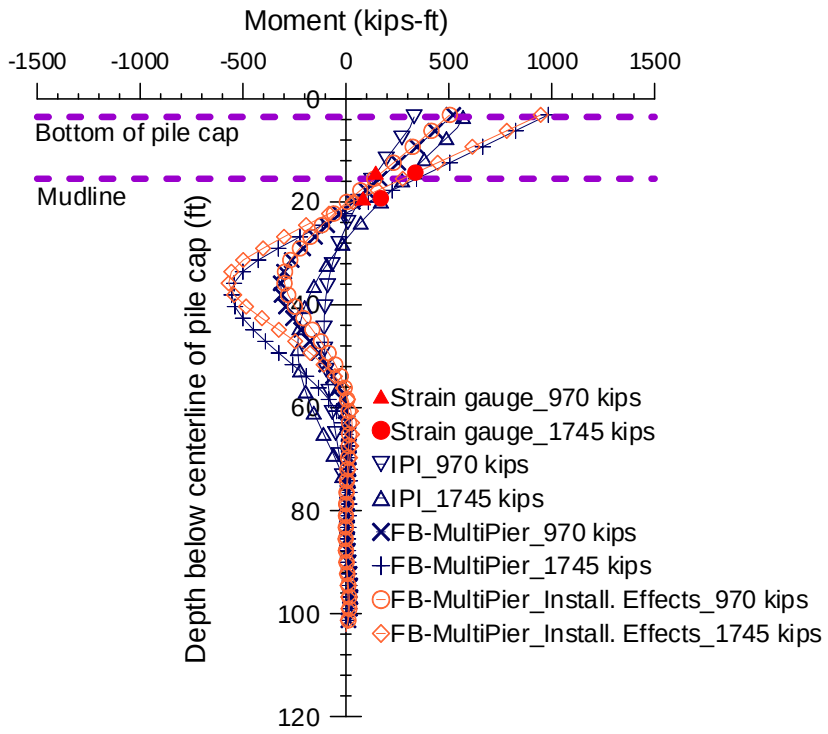

(c) $Pile_{FB}24$/Pile 4

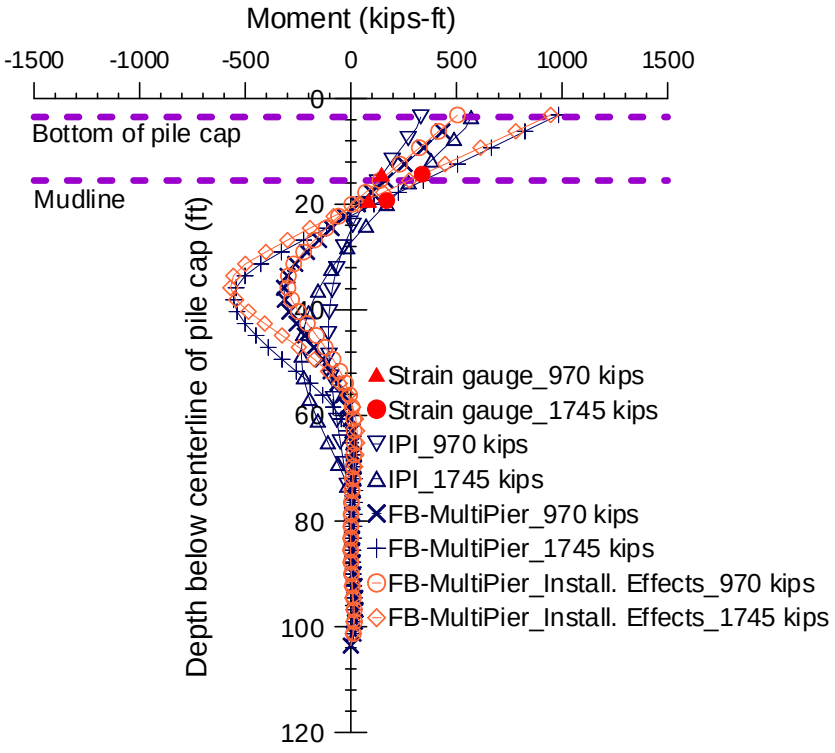

(d) $Pile_{FB}4$/Pile 12

Figure 81

Pile moment profiles from FB-MultiPier with different conditions

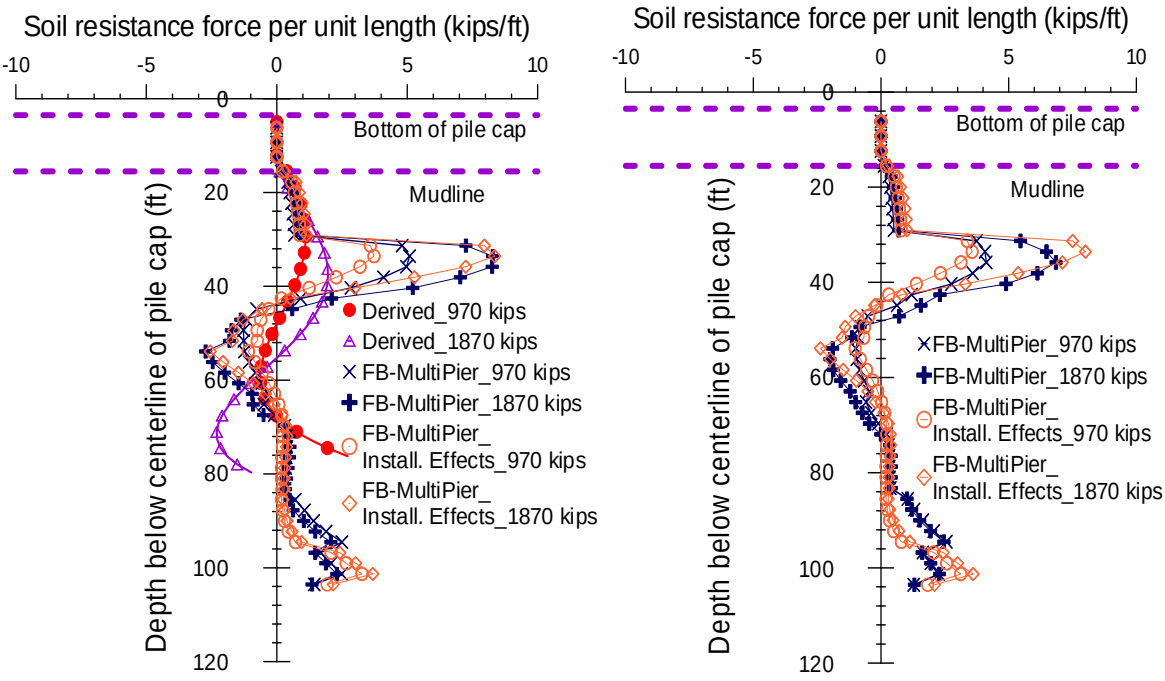

(a) $Pile_{FB}1$/ Pile 11 in 1st row

(b) $Pile_{FB}18$/ Pile 6 in 2nd row

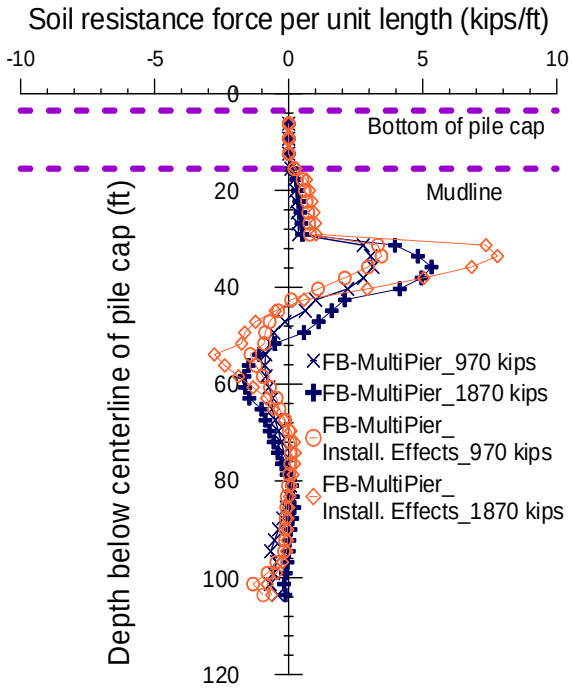

(c) $Pile_{FB}19$/ Pile 7 in 3rd row

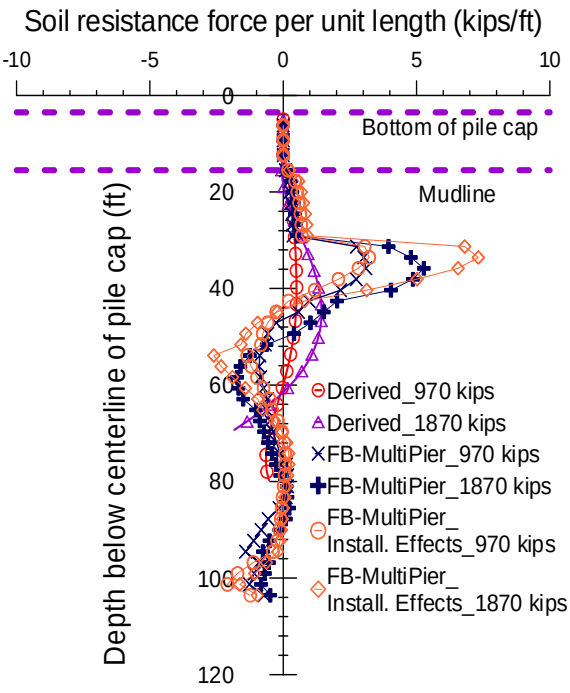

(d) $Pile_{FB}20$/ Pile 8 in 4th row

Figure 82

Soil lateral resistance from FB-MultiPier analysis with different conditions

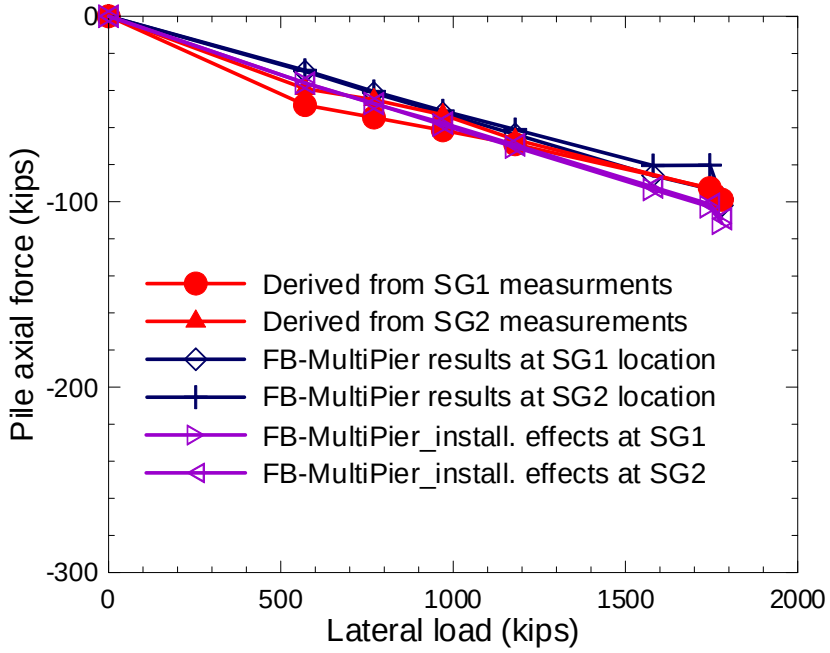

(a) $Pile_{FB}1$/ Pile 11 in 1st row

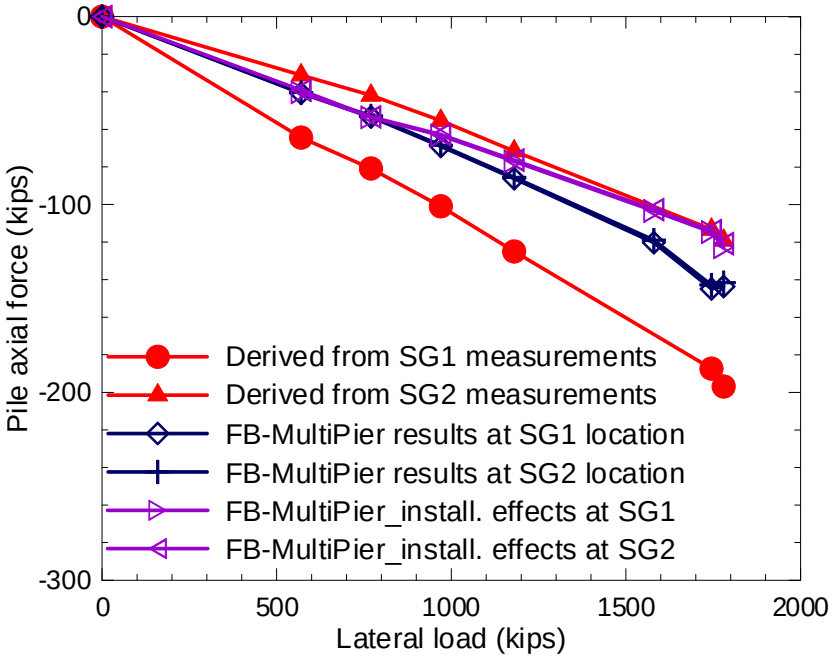

(b) $Pile_{FB}14$/ Pile 9 in 2nd row

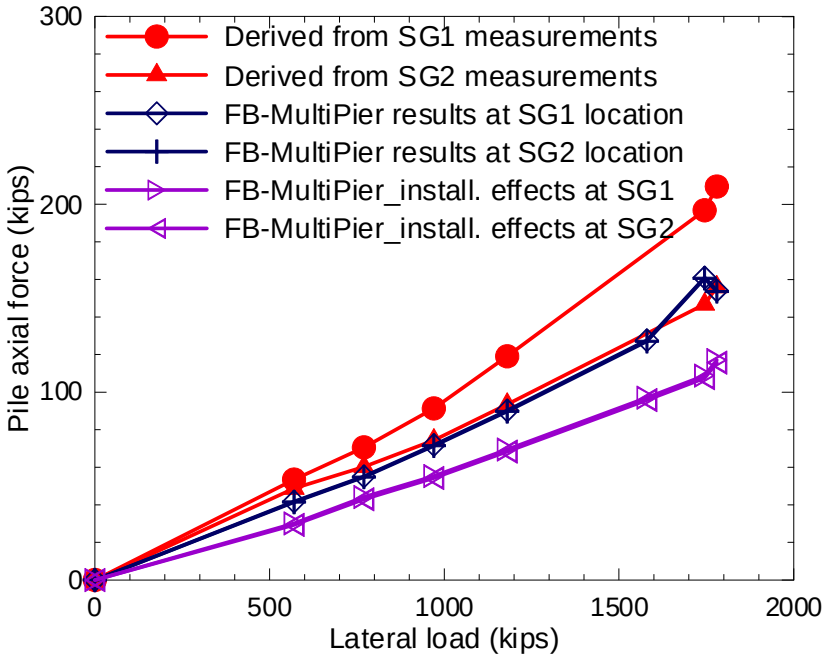

(c) $Pile_{FB}7$/Pile 10 in 3rd row

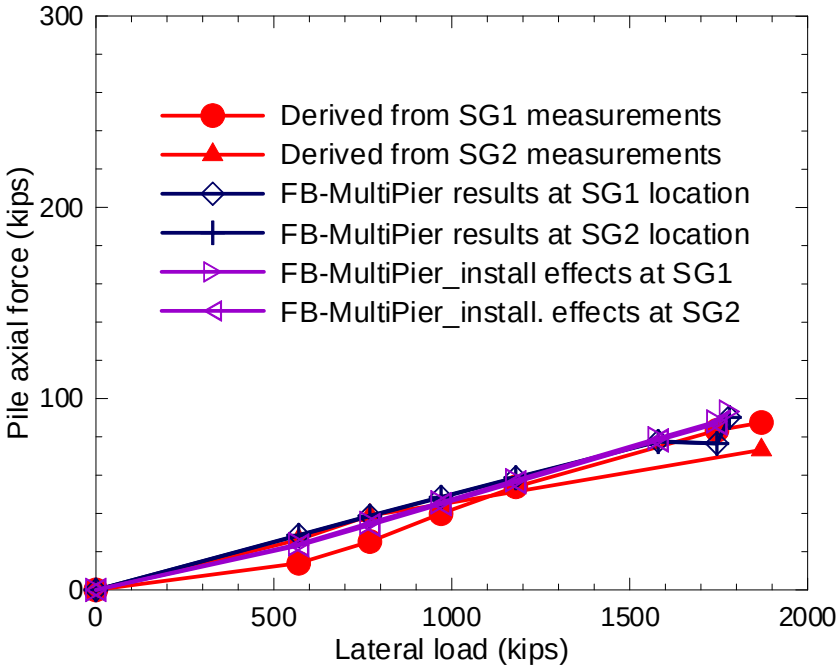

(d) $Pile_{FB}24$/Pile 4 in 4th row

Figure 83
Axial load for piles located in different rows

FB-MultiPier Analysis using Modified Meshes

In the FB-MultiPier program, the connection between the pile cap and the pile head is only allowed to be at the center of the cap with the options of a fixed or a pinned connection. Thus, in this study, the pile head is assumed to be rigidly connected to the center of the pile cap, i.e. 3.5 ft. into the cap since the thickness of the cap is 7 ft. However, the actual embedment length of each pile into the cap is about 9 in. and the lateral load is applied at the center of the pile cap. This may contribute to the discrepancies between the field measurements and the results from the FB-MultiPier analysis. Modified meshes were created for the FB-MultiPier analysis in attempt to address the issue discussed above. Figure 84 illustrates the original and modified meshes. The elevation of the pile cap was lowered for 3.5 ft. while the elevation of the lateral load was kept the same. As a result, the distance between the lateral load and the pile head became 3.5 ft. approximately representing the actual distance between the load and the pile head. Since the actual lateral load was applied at the pile cap instead of the pier column as Figure 84 shows, multiple artificial shear wall beam elements were added to the mesh to create a rigid part for the modified mesh 1 [Figure 84(b)] and a single shear wall beam element was added to the mesh to transfer the applied load for the modified mesh 2 (Figure 84c). The concrete properties of the pile cap were applied to the artificial shear wall beams.

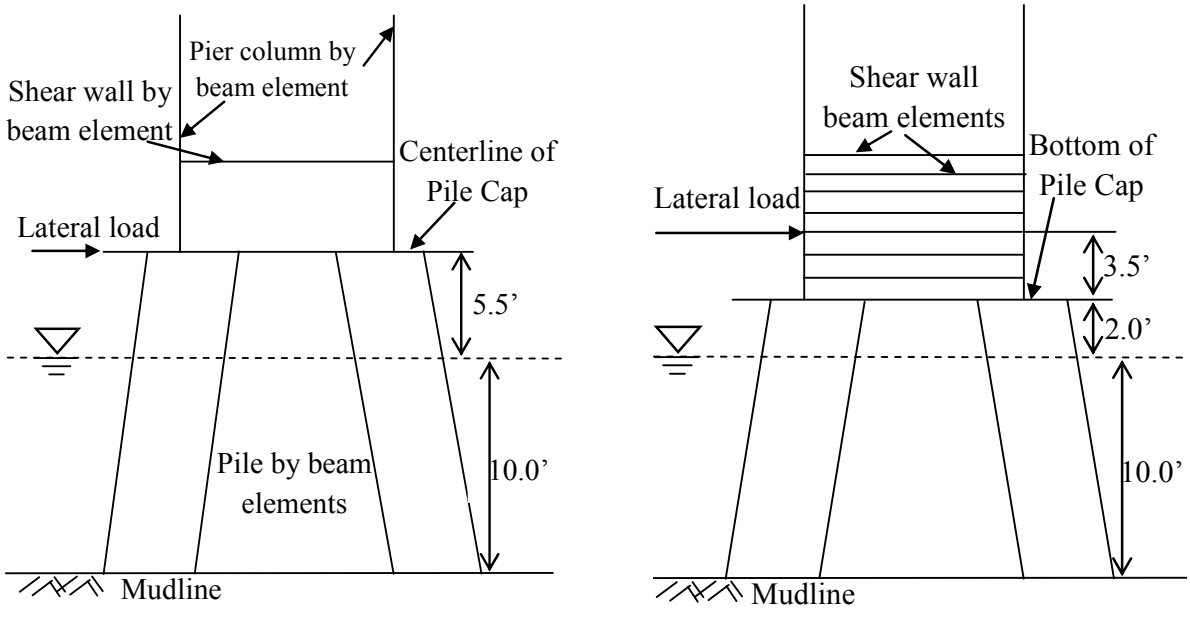

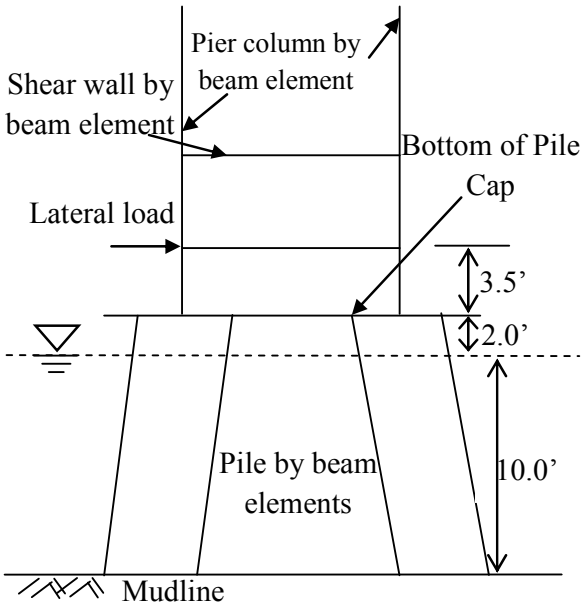

(c)

Figure 84

Discretization of the pier: (a) original mesh; (b) modified mesh 1; (c) modified mesh 2

Lateral Deflection. Figure 85 presents the pile deflection profile from the analysis using the modified meshes. As can be seen from the figure, both modified meshes give close results on the pile deflection profile. Based on the modified meshes, the FB-MultiPier analysis showed a pile head deflection of about 0.6 in. which is close to the measured pile head deflection. However, as can be seen in Figure 85, the FB-MultiPier analysis based on the modified meshes overall underestimates the lateral pile deflection. Similar to other FB-MultiPier analyses, the predicted depth of fixity is shallower than that from the field measurements. It is worth pointing out that, unlike other FB-MultiPier analyses, the shape of the deflection profiles from the analysis based on the modified meshes is similar to the measurements.

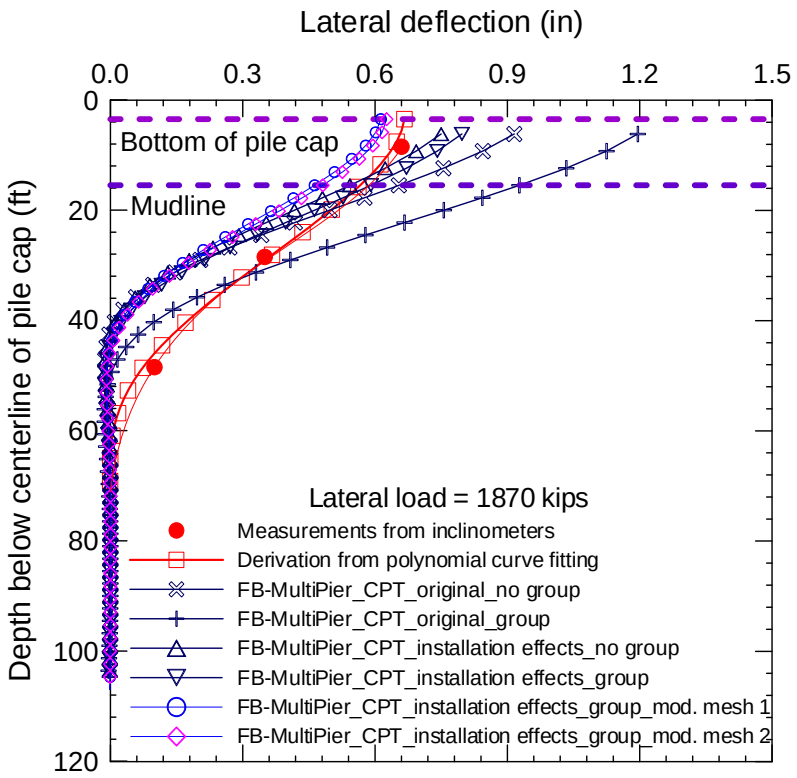

Figure 85

Profile of pile deflection from analysis using modified mesh for $Pile_{FB}$20/Pile 8

Pile Bending Moments. Figure 86 presents the profiles of the pile bending moments from the FB-MultiPier analysis based on the modified meshes. The moment profiles predicted from the FB-MultiPier using modified meshes are compared with the other FB-MultiPier analysis and those from the back-calculations from IPI data and the moments measured by strain gauges. Under the lateral loads of 970 kips and 1745 kips, the maximum moments for $Pile_{FB}$1/Pile 11 in the 1st row predicted by FB-MultiPier are 245 kips-ft. and 468 kips-ft., respectively, by using the modified mesh 1, and 259 kips-ft. and 500 kips-ft., respectively, by using the modified mesh 2; while the FB-MultiPier analysis based on the original mesh showed a maximum moment of 355 kips-ft. and 620 kips-ft., respectively. Both modified meshes again give close results on the profiles of the pile bending moments. The predicted moments from the modified mesh showed good agreement with the moments calculated from strain gauge measurements at the two different instrumented depths.

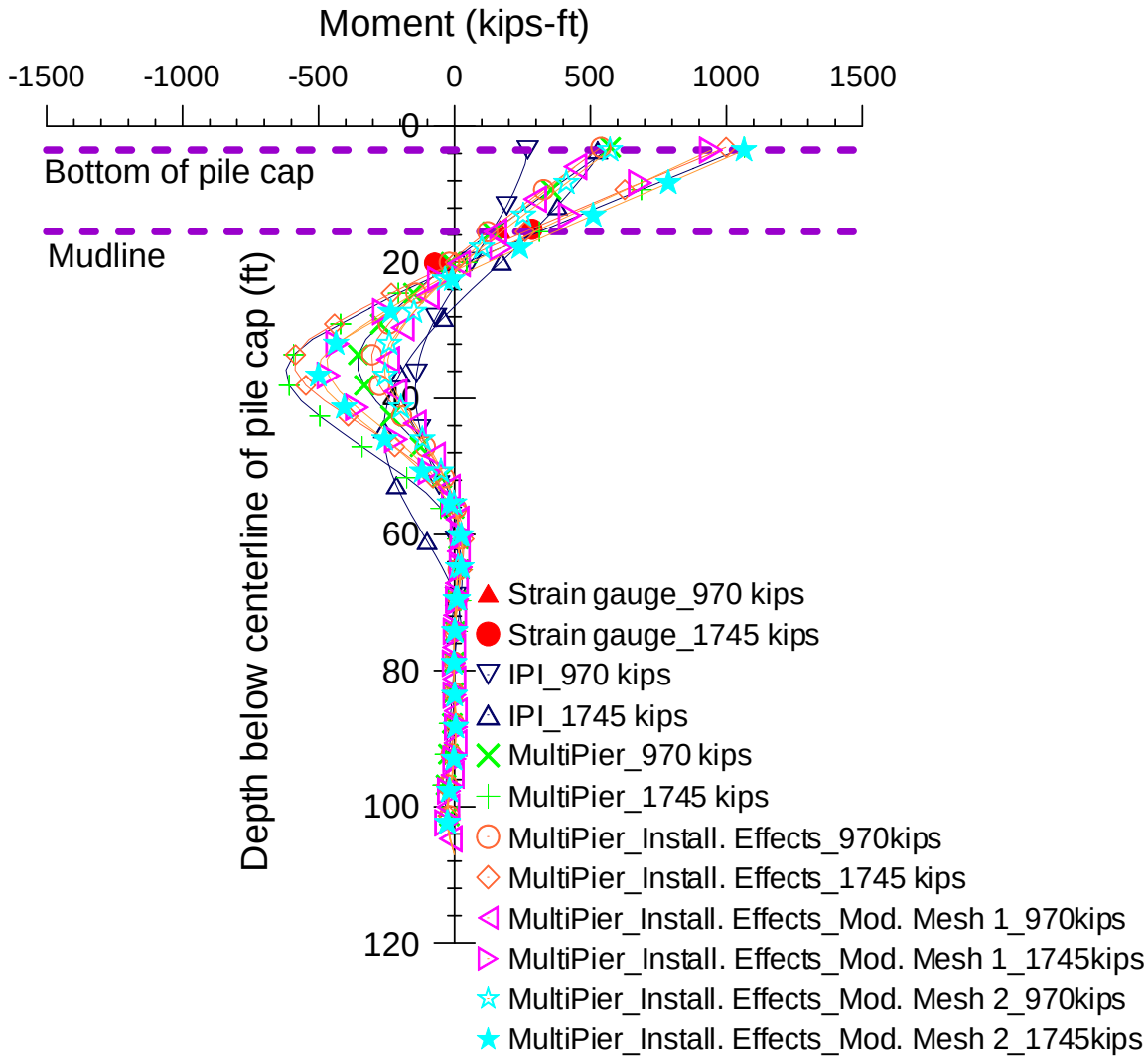

Figure 86

Profile of moment from analysis using modified mesh for $Pile_{FB}1$/Pile 11

SUMMARY AND CONCLUSIONS

An SHM (structural health monitoring) system was successfully installed at the M19 eastbound pier of the new I-10 Twin Span Bridge over Lake Pontchartrain. The system consisted of instrumenting both the substructure and the superstructures of the bridge. The substructure instrumentation system was used to monitor the M19 eastbound pier during the unique lateral load test that was conducted to investigate the lateral behavior of the M19 pier and to verify the analysis method used to design the battered pile group foundations using the FB-MultiPier software. The SHM system will be used for long-term health monitoring of the bridge during selected events such as storm surge, extreme wind and vessel impact.

A high-order-polynomial curve fitting was adapted to best-fit the IPI measured rotation profiles with depth for the instrumented piles using a reduced chi-square minimization of residual error regression method. The bending moments, shear forces, and soil reactions were then derived from the fitted rotation polynomial functions based on the beam on elastic foundation theory. The strain gauge measurements were used to calculate the bending moments and the axial loads of the instrumented piles at two depth locations.

The FB-MultiPier software was also used to analyze the lateral response of the M19 pier under lateral loading using two different soil profiles, soil boring data and CPT soundings. Three different FB-MultiPier models were used in this analysis that vary by the way the pile cap rigidity and its connection with the piles are modeled [typical model used by DOTD [Figure 84(a)], modified mesh model 1 [Figure 84(b)], and modified mesh model 2 [Figure 84(c)]. The effect of pile installation was then incorporated into the FB-MultiPier models through increasing the undrained shear strength of the surrounding soil by 20%. In this model, the p-multipliers of 0.9, 0.8, 0.8, and 0.7 for the 1st, 2nd, 3rd, and 4th row piles, respectively, were adopted.

Based on the findings of this study, the following conclusions can be drawn:

- The maximum lateral deformation of the M19 eastbound pier cap corresponding to the maximum applied lateral load of 1870 kips, as measured using the laser survey, was 0.66 in. at the northwest corner and 0.58 in. at the southwest corner. The maximum lateral deformation of piles measured at 5 ft. below the bottom level of the pile cap using the IPI sensors ranged from 0.65 in. to 0.72 in. The success rate of strain gauges and IPI sensors instrumentation were about 70 %.
- The measured lateral deformations of the piles indicate that the pile horizontal movements mainly occur within the upper 50-60 ft. below the pile cap. The lateral deflection profiles for different row piles seemed to have similar shapes, which indicate that the pile group effects in the loading direction are somehow minimal.

- The strain gauge measurements showed that the pile axial loads due to lateral loading are in compression or tension, depending on the battered pile direction. This shows that the battered pile system can improve the horizontal resistance of pile group by transferring a portion of the applied lateral load into pile axial loads.
- The back-calculated moments deduced from the curve fitting of IPI measurements were compared with the moments calculated from strain gauge measurements, and the results indicated good agreement between them. The results also showed that the moments developed at the ground level (mudline) were about 50-55% lower than that at the bottom of pile cap, and the depth to the first zero moment increases as the load increases.
- The measured axial loads showed that inner row piles (i.e., 2^{nd} and 3^{rd} rows) carry higher axial loads compared to piles in the other two rows (i.e., 1^{st} and 4^{th} rows).
- The p-y curves at different depths for the IPI instrumented piles were back-calculated from the derived soil reaction profiles (p) and the pile lateral deflection profiles (y) obtained at different load increments. The comparison of p-y curves for piles in different rows indicates slight pile group effects for the leading row piles, with the outer piles in the same row having slight pile group effects (i.e., p-multiplier ≈ 1).
- The sensitivity analyses conducted using the FB-MultiPier indicated that the undrained shear strength S_u has the greatest influence on the piles' lateral behavior compared to other input parameters.
- The analysis of the typical FB-MultiPier model using the borehole input data showed overestimating of the lateral deformations, and the use of CPT input data yielded slightly better prediction than the soil boring data. However, the analyses without considering group effect have better predictions of the measured lateral deformations than the case with group effect, which might suggest again that the pile group effects in the loading direction of the battered pile group might not be significant.
- The results of the typical FB-MultiPier analysis considering the installation effect showed improvement in the prediction of the piles' lateral behavior. However, the FB-MultiPier analysis based on the modified models when considering the installation effect showed much better prediction of the measured lateral deformations, and the shape of the deflection profiles is similar to the measurement values.
- The FB-MultiPier predicted moments showed good agreement with the moments calculated from the strain gauge measurements at the two different instrumented depths. The comparison between the FB-MultiPier predicted moments and the back-calculated moments from IPI measurements showed that the FB-MultiPier predicted moment

profiles have larger negative moments and the depth corresponding to the peak negative moment is shallower compared with the back-calculated IPI moment profiles using high order polynomial curve fitting. However, there are no strain gauges installed below 20 ft. deep to verify either of the two moment profiles.

RECOMMENDATIONS

Based on the findings of this research study on instrumentation and lateral load testing of the battered pile group foundation at M19 eastbound pier of I-10 Twin Span Bridge, the following recommendations have proposed:

- It is recommended that DOTD bridge design engineers consider using less conservative *p*-multipliers (as presented in Table 6) when using the FB-MultiPier software for analysis and design of battered pile group foundations loaded laterally along the batter direction. Since the pile spacing increases with depth between row 2 and row 3, the selection of *p*-multipliers should be based on average pile spacing within a depth of 8B (B is the pile width) below the ground surface (or mudline).

Table 6
Recommended values for *p*-multipliers

Spacing	Row 1	Row 2	Row 3	Row 4
3B	0.7	0.6	0.6	0.5
4B	0.8	0.7	0.7	0.6
5B	0.9	0.8	0.8	0.7
6B	1.0	0.9	0.9	0.8
7B	1.0	1.0	1.0	0.9
8B	1.0	1.0	1.0	1.0

- It is recommended that DOTD bridge design engineers consider using the modified FB-MultiPier meshes as presented in Figures 84(b) and 84(c) (e.g., pile cap modeled using single or multiple artificial shear wall beam shell elements to simulate rigidity of pile cap) for improving the analysis and design of pile group foundations.
- The DOTD engineers need to be aware of the effect of pile installation and the subsequent soil densification, consolidation and set-up on the increase of strength properties of the surrounding soils. Whenever it is possible to evaluate these effects, it is recommended to incorporate the pile installation effect through the selection of proper input soil properties for analysis and design of large pile group foundations.
- For future instrumentation of bridges in general and bridge foundations in particular, the authors recommend instrumenting selected piles with a series of strain gauges along the depth (in addition to inclinometers) in order to be able to measure the moment distribution along the pile during testing and monitoring. In addition, the authors recommend using additional sensors/instrumentation at key locations for redundancy in case damage occurs to some instrumentation. Also, the authors recommend adopting wireless systems for instrumentation.

- It is recommended that a future research project use a continuum-based non-linear finite element numerical modeling using ABAQUS software to study the lateral behavior of the battered pile group foundation and its interaction with the surrounding geomaterials under both static and impact type lateral loads. The FE analysis can accurately model the group effects, the "shadow effects" in the loading direction as well as the "edge effects" in the transverse direction of loading, without the need of assuming a constant *p*-multiplier for the entire pile depth. The back-calculation from results of FE analysis can be used to determine the p-y curves for different layers along the pile length.

ACRONYMS, ABBREVIATIONS, AND SYMBOLS

CI	cyberinfrastructure
CPT	Cone Penetration Tests
DOTD	Department of Transportation and Development
FE	finite element
FHWA	Federal Highway Administration
ft.	foot (feet)
in.	inch(es)
IPI	In-Place-Inclinometers
L-M	Levenberg-Marquardt
LTRC	Louisiana Transportation Research Center
MEMS	microelectromechanical system
NBI	National Bridge Inventory
NBIS	National Bridge Inspection Standards
NE	north eastern
PPC	precast presetressed concrete
SHM	structural health monitoring (
SPT	Standard Penetration Tests
SSHM	substructure health monitoring
SW	south western
UU	undrained unconsolidated
WIM	weight-in-motion

REFERENCES

1. FHWA. Status of the Nation's Highways, Bridges, and Transit: Conditions & Performance. Technical Report No. FHWA-PL-03-004, Federal Highway Administration, Washington D.C., 2010.
2. Moore, M., Phares, B., Graybeal, B., Rolander, D. & Washer, G. Reliability of Visual Inspection for Highway Bridges, Technical Report No. FHWA-RD-01-020, Vol. 1, Federal Highway Administration, Washington D.C., 2001.
3. Wardhana, K. & Hadipriono, F. C. "Analysis of recent bridge failures in the United States." *Journal of Performance of Constructed Facilities*, Vol. 17, No. 3, 2003, pp. 144-150.
4. Salane, H.J., J.W. Baldwin, and Duffield, R. C. "Dynamics Approach for Monitoring Bridge Deterioration." In *Transportation Research Record 832*, TRB, National Research Council, Washington D.C., 1981, pp. 21–28.
5. Kato, M. and Shimada, S. "Vibration of PC Bridge During Failure Process." *ASCE Journal of Structural Engineering*, Vol. 112, 1986, pp. 1692–1703.
6. Turner, J.D. and Pretlove, A.J. "A Study of the Spectrum of Traffic-Induced Bridge Vibration." *Journal of Sound and Vibration*, Vol. 122, 1988, pp. 31–42.
7. Doebling, S.W., Farrar, C.R., Prime, M.B., and Shevitz, D.W. *Damage Identification and Health Monitoring of Structural and Mechanical Systems from Changes in Their Vibration Characteristics: A Literature Review*. Report No. LA-13070-MS, Los Alamos National Laboratory, 1996.
8. Sohn, H., Farrar, C. R., Hemez, F. M., Shunk, D. D., and Stinemates, D. W. "A Review of Structural Health Monitoring Literature: 1996–2001." Report No. LA-13976-MS, Los Alamos National Laboratory, 2004.
9. Aktan, A.E., Catbas, F.N., Grimmelsman, K.A., and Pervizpour, M. Development of a Model Health Monitoring Guide for Major Bridge. Report submitted to FHWA Research and Development, contract No. DTFH61-01-P-00347, U.S. Department of Transportation, 2003.
10. Chang, P.C., Flatau, A. and Liu, S.C. "Review paper: health monitoring of civil infrastructure." *Structure Health Monitoring*, Vol. 2, 2003, pp. 257-267.
11. Elgamal, A., Conte, J.P., Masri, S., Fraser, M., Fountain, T., Gupta, A., Trivedi, M. and El Zarki, M., Health monitoring framework for bridges and civil infrastructure, in Proceedings of the 4th International Workshop on Structural Health Monitoring, pp. 123-130, edited by F.-K. Chang, Stanford, CA, USA, September 15-17, 2003.
12. Lynch, J.P., Kim, J.H., Zhang, Y., Wang, M., Sohn, H., and Yun, C. B. "Advance Sensor Technologies on Korean Bridges: Field Benchmark Opportunities." Bridge Maintenance,

Safety, Management, Health Monitoring and Informatics – Koh & Frangopol (eds), 2008, pp. 3306-3313.
13. James, G. and Karoumi, R. *Monitoring of the New Svinesund Bridge*, Brobyggnad, KTH Byggvetenskap, KTH, SE-100 44, Stockhom, Sweden, 2003.
14. Jonsson, F. ,and Jonsson, D. "Finite Element Model Updating of the New Svinesund Bridge." Master's Thesis, Chalmers University of Technology, Goteborg, Sweden, 2007.
15. Zhang, R. R. and Olson, L. D. "Dynamic Bridge Substructure Condition Assessment with Hilbert–Huang Transform Simulated Flood and Earthquake Damage to Monitor Structural Health and Security." In *Transportation Research Record 1892*, TRB, National Research Council, Washington, D.C., 2004, pp. 153–159.
16. Pando, M. A., Ealy, C. D., Filz, G. M., Lesko, J.J., and Hoppe, E.J. "A Laboratory and Field Study of Composite Piles for Bridge Substructures." Report No. FHWA-HRT-04-043, Federal Highway Administration, Washington D.C., 2006.
17. Fellenius, B.H., Kim, S. R., Chung, S. G. "Long-Term Monitoring of Strain in Instrumented Piles." *Journal of Geotechnical and Geoenvironmental Engineering*, Vol. 135, No. 11, 2009, pp. 1583-1595.
18. Collins, J. D. "Remote monitoring systems for substructural health monitoring." Master's Thesis, University of South Florida, 2008.
19. Fealing, L.B. Lateral Pile Loading Test. "Lateral pile loading test." Transactions, ASCE, Vol. 102, Paper No. 1959, 1937, pp. 236-254.
20. Kim, J.B., Brungraber, R.J. "Full Scale Lateral Load Tests of Pile Groups." *Journal of the Geotechnical Engineering Division*, ASCE Vol. 102, No. GTI, 1976, pp. 87-105.
21. Kim, J.B., Brungraber, R.J., Singgh, L.P. "Pile Cap Soil Interaction from Full-Scale Lateral Load Tests." *Journal of the Geotechnical Engineering Division*, ASCE, Vol. 105, No. 5, 1979, pp. 643-653.
22. Matlock, H., Ingram, W.B., Kelley, A.E., Bogard, D. "Field Tests of the Lateral Load Behavior of Pile Groups in Soft Clay." *8th Texas Conference on Soil Mechanics and Foundation Engineering*. Austin, Texas, 1980.
23. Brown, D. A., Reese, L. C., and O'Neill, W. M. "Cyclic lateral loading of a large-scale pile group." *Journal of Geotechnical and Geoenvironmental Engineering*. Vol. 114, No.11, 1987, pp. 1261–1276.
24. Rollins, M. K., Peterson, T. K., and Weaver, J. T. "Lateral load behavior of full scale pile group in clay." *Journal of Geotechnical and Geoenvironmental Engineering*. Vol. 124, No. 6, 1998, pp. 468-478.
25. Matlock, H. "Correlations for Design of laterally loaded piles in soft clay." 2nd Offshore Technology Conference, Houston Texas, 1970.

26. Brown, D. A., Morrison, C., and Reese, L. C. "Lateral load behavior of pile group in sand." Journal of Geotechnical Engineering, Vol. 114, NO. 11, 1988. pp. 1261-1276.
27. Ruesta, F., and Townsend, C. F. “Evaluation of laterally loaded pile group at Roosevelt Bridge.” *Journal of Geotechnical and Geoenvironmental Engineering*. Vol. 123, No.12, 1998, pp. 1153-1161.
28. Huang, A., Hsueh, C., O’neill, M.W., Chern, S., and Chen, C. “Effects of construction on laterally loaded pile groups.” *Journal of Geotechnical and Geo-environmental Engineering*, Vol. 127, No. 5, 2001, pp. 385-397.
29. Rollins, K., Olsen, R., Egbert, J., Olsen, K., Jensen, D., and Garrett, B. “Response, analysis and design of pile groups subjected to static and dynamic lateral loads.” Utah Department of Transportation Research and Development Division, Report No. UT-03.03, 2003.
30. Rollins, M. K., Lane, D. J., and Gerber, M. T. “Measured and computed lateral response of a pile group in sand.” *Journal of Geotechnical and Geoenvironmental Engineering*, Vol. 121, 2005, pp. 103-114.
31. McVay, M., Zhang, L., Molnit, t., and Lai, P. “Centrifuge testing of large laterally loaded pile groups in sands.” *Journal of Geotechnical and Geo-environmental Engineering*, Vol. 124, No. 10, 1998, pp. 1016-1026.
32. Rollins, K.M. and Sparks, A. “Lateral resistance of full-scale pile cap with gravel backfill.” *Journal of Geotechnical and Geoenvironmental Engineering*, Vol. 128, No. 9, 2002, pp. 711-723.
33. Nip, N, C, D., and Ng, W, W. C. “Back analysis of laterally bored piles.” *Geotechnical Engineering*, Vol. 158, No. 2, 2005, pp. 63-73.
34. Cox, W. R., Reese, L. C., and Crubbs, B. S. “Lateral load tests of 25.4 mm diameter piles in very soft clay in side-by-side and in-line groups.” *Laterally Loaded Deep Foundations: Analysis and Performance*, ASTM, West Conshohoken, PA, 1984, pp. 122–139.
35. McVay, C. M., Shang, I. Te., and Casper, R. “Centrifuge Testing of Fixed-Head Laterally Loaded Battered and Plumb Pile.” *ASTM Geotechnical Testing Journal*, Vol. 19, 1996, pp. 41-50.
36. Moss, R. E. S., Caliendo J.A., and Anderson L.R. “Investigation of a cyclic laterally loaded model pile group.” *Soil Dynamics and Earthquake Engineering*, Vol. 17, 1998, pp. 519-523.
37. Llyas, T., Leung, C. F., Chow, Y. K., and Budi, S. S. “Centrifuge model study of laterally loaded pile groups in clay.” *Journal of Geotechnical and Geoenvironmental Engineering*, Vol. 130, No. 3, 2004, pp. 274–283.

38. Poulos, H.G. and Davis, E. H. *Pile Foundation Analysis and Design*, John Wiley and Sons, New York, 1980.
39. Poulos, H.G. "Behavior of laterally loaded piles;II-Pile groups." *Journal of Soil Mechanics and Foundation*, Vol. 97, No. 5, 1971, pp. 733-751.
40. Reese, L. C., Cox, W.R., and Koop, F.D. "Analysis fo laterally loaded piles in sand." Proceedings of 6th Offshore Technology conference, Houston TX, 1974.
41. Norris, G. M. "Theoretically based BEF laterally loaded pile analysis." Proceedings, 3rd International Conference on Numerical Methods in Offshore Piling, TECHNIP, Ed., Paris, 1986, pp. 361-386.
42. Ashour, M., Norris, G., and Pilling, P. "Lateral loading of a pile in layered soil using the strain wedge model". *Journal of Geotechnical Engineering*, Vol. 124, No. 4, 1998, pp. 303-315.
43. Tschebotarioff, G.P. "The resistance to lateral loading of single piles and pile groups." ASCE special publication, No 154, ASTM, West Conshohocken, 1952, pp. 38-48.
44. Murthy, V. N. S. "Behavior of battered piles embedded insand subjected to lateral loads." Proceedings of Symp. on Bearing Capacity of piles CBRI, Roorkee, India, pp. 142-153, 1964.
45. Prakash, S., and Subramanyam, G. "Behavior of battered piles under lateral loads." Journal of Indian National Society of Soil Mechanis and Foundaiotn Engineering, New Delhi, Vol 4, 1965, pp. 177-196.
46. Manoliu, l., Botesa, E., and Constaninescu, A. "Behavior of pile foundations submitted to lateral loads." International Proceedings, 9th Conference, ICSMFE: 437-440, Tokyo, 1977.
47. Ranjan, G., Ramasamy, G., and Tyagi, R. P. "Latearl response of battered piles and pile bents in clay." *Indian Geotechnical Journal*, New Delhi, 1980, Vol. 10, No. 2, pp: 135-1742.
48. Lu, S.S. "Design load of bored pile laterally loaded." Proceeding, 10th International conference on Soil mechanics and Foundation Engineering, Balkema,Rotterdam. The Netherlands, Vol. 2, 767-770, 1981.
49. Zhang, L., McVay, M.C., Han, J. H.,Lai, P. W. "Centrifuge modeling of laterally loaded single battered piles in sand." *Canadian Geotechnical Journal*, Vol. 36, No. 6, 1999, pp. 561-575.
50. Rajashree, S. S, and Sitharam G.T. "Nonlinear finite-element modeling of batter piles under lateral load." *Journal of Geotechnical and Geoenvironmental Engineering*, Vol. 127, No. 7, 2001, pp. 604-612.

51. Pinot, P., McVay. M., Hoit, M., and Lai. P. "Centrifuge testing of plumb and battered pile groups in sand." In *Transportation Research Record 1569*, TRB, National Research Council, Washington, D.C., 1997, pp. 8-16.
52. Kubo, K. "Experimental study of the behavior of laterally loaded piles." Proceeding, 6th International Conference on soil Mechanics and Foundation Engineering, Montreal, QC, 1965.
53. Awoshika, K. *Analysis of foundation with widely spaced piles*. Ph.D thesis, University of Texas, Austin, Texas, 1971.
54. Zhang, L., McVAy, M.C., Han, J.H., Lai,P.W. "Numerical Analysis of laterlly loaded 3×3 to 7×3 pile groups in sands." *Journal of Geotechnical and Geoenvironmental Engineering*, ASCE, Vol. 125, No. 11, 1999, pp. 936-946.
55. Jardine R.J. and Chow F.C. New design methods for offshore piles MTD Publication 96/103, Marine Technology Directorate, London, 1996.
56. Wang, S. T. and Reese, L. C. COM624P-lateraly loaded pile analysis program for the microcomputer, version 2.0, Ensoft, Inc., Austin, Texas, 1993.
57. Reese, L.C., Wang, S.T., Arrellaga, J.A., and Hendrix, J. LPILE Plus 3.0 for windows, Ensoft, Inc., Austin, Texas, 1997.
58. Mcvay, M. C., Shang, T. and Casper, R. "Centrifuge testing of fixed head laterally loaded battered and plumb pile groups in sand." *ASTM, Geotechnical Testing Journal,* Vol. 19, No. 1, 1996, pp. 41-50.
59. FbMultipier-Bridge Software Institute, University of Florida.
60. Walsh, J. M. *Full-scale lateral load test of a 3 x 5 pile group in sand*, Master Thesis, Brigham Young University, Provo, UT, 2005.
61. Hoit, I. M., McVay, M., Hays, C., and Andrade,W. P "Nonlinear Pile Foundation Analysis Using Florida-Pier." *Journal of Bridge Engineering*, Vol. 1, No. 4, 2005, pp. 135-142.
62. Charels, W., Ng, W., Zhang, L., and Dora C. N. Nip. (2001) "Response of Laterally Loaded Large-Diameter Bored Pile Groups," *Journal of Geotechnical and Geoenvironmental Engineering*. Vol. 127(8): 658‐669.
63. Possiel, B. A. *Point of Fixity Analysis of Laterally Loaded Bridge Bents*, Master's Thesis, North Carolina State University, Raleigh, NC, 2008.
64. McVay, C. M., Wasman, J. S., Consolazio, R. G., Bullock, J. P., Cowan, G. D., and Bollmann, T. H. (2009). "Dynamic Soil–Structure Interaction of Bridge Substructure Subject toVessel Impact." *Journal of Bridge Engineering*, Vol. 14, No. 1, 2009, pp. 7-16.
65. Hetenyi, M. "Beams on elastic foundation," University of Michigan Press, Michigan, 1946.

66. Reese, L.C. and Welch, R.C. “Lateral Loadings of Deep Foundations in Stiff Clay.” *Journal of Geotechnical Engineering*, Div, ASCE, Vol. 101, No. 7, 1975, pp. 633-649.
67. Matlock, H., and Ripperger, E. A. “Procedures and instrumentation for tests on a laterally loaded pile.” Proceedings, 8th Texas Conference on soil Mechanics and Foundation Engineering, Austin Texas, 1956.
68. Wilson, D. “Soil-Pile-Superstructure interaction in liquefying sand and soft clay.” Ph.D. Dissertation, University of California at Davis, 1998.
69. Brown, D. A., Hidden, A. S., and Zhang, S. “Determination of p-y curves using inclinometer data.” *Geotechnical Testing Journal*, Vol. 17, 1994, pp. 150-158.
70. Liao, C. J., and Lin, S. S. “An analytical model for deflection of laterally loaded piles.” *Journal of Marine Science and Technology*, Vol. 11, No. 3, 2003, pp. 149-154.
71. Dou, H. and Bryne, P.M. “Dynamic Response of single pile and soil-pile interaction.” *Canadian geotechnical Journal*, Vol. 33, 1996, pp. 80-96.
72. Yamin, M., and Liang, R. Y. “Limiting equilibrium method for slope/drilled shaft system.” *International Journal of Numerical Analysis and Methods of Geomechanics*, Vol. 34, No. 10, 2009, pp. 1063–1075.
73. Zhang, Z.,and Tumay, M. “Statistical to fuzzy approach toward CPT soil classification.” *Journal of Geotechnical and Geoenvironmental Engineering*, Vol. 125, No. 3, 1999, pp. 179-186.
74. Reese, L. C. and Van Impe, W. F. *Single Piles and Pile Groups under Lateral Loading*, Balkema, Brookfield, VT, 2001.
75. O'Neill, M.W. and Murchison, J.M. An evaluation of p-y relationships in sands, University of Houston - University Park, Depart of Civil and Environmental Engineering, Report No. GT-DF02-83, 1983
76. O'Neill, M.W. and Gazioglu, S.M., An evaluation of p-y relationships in clays, University of Houston - University Park, Depart of Civil and Environmental Engineering, Report No. UHCE-84-3, 1984.
77. Zhang, L.M. and McVay, M.C. "Response of a laterally loaded 4x4 battered pile group." Geotechnical Engineering - Meeting Society's Needs, Vols 1 and 2, Proceedings, 2001, pp. 605-610
78. Pinto, P., McVay, M., Hoit, M., and Lai, P. "Centrifuge testing of plumb and battered pile groups in sand." Transportation Research Record, No. 1569, pp. 8-16.
79. McClelland, B. and Focht, J. "Soil modulus for laterally loaded piles." Journal of the Soil Mechanics and Foundations Division, Vol. 82, No. 4, 1956, pp. 1-22.
80. Terzaghi, K. “Evaluation of coefficients of subgrade reaction.” *Geotechnique*, Vol. 5, 1955, pp. 297-326.

81. Matlock, H., and Reese, L.C. "Generalized solution for laterally loaded piles." *Journal of Soil Mechanics and Foundation*, Div., ASCE, Vol. 86, No. 5, 1961, pp. 673-694.
82. Davisson, M.T. "Lateral load capacity of piles." *Highway Research Record 333*, Highway Research Board, Washington, D.C., 1970, pp. 104-112.
83. Francis, A.J. "Analysis of pile groups with flexural resistance." *Journal of Soil Mechanics Foundation Division*, ASCE, Vol 90, No. SM3, 1964, pp. 1-32.
84. Broms, B. "The lateral resistance of piles in cohesionless soils." *Journal of Soil Mechanics Foundation*, Vol. 90, No. 2, 1964, pp. 27-63.
85. Broms, B. "The lateral resistance of piles in cohesionless soils." *Journal of Soil Mechanics Foundation*, Vol. 90, No. 3, 1964, pp. 123-156.
86. Reese, L.C. "Discussion of Soil modulus for laterally loaded pile analysis." Proceeding, third International Conference on Numerical Methods in offshore Piling, Edicitons Tecnhip, Paris, France, pp. 361-386, 1958.
87. O'neill, M. W. and Dunnavant, T. W. "A study of effect of scale, velocity, and cyclic degradability on laterally loaded single piles in overconsolidated clay". *Report No. UHCE 84-7*, Dept. of Civil Engineering, University of Houston, Texas, 1984.
88. Salgado, R. The Engineering of Foundations, 2008, The McGraw-Hill Companies, Inc., New York.
89. Ashour, M., and Norris, G. "Modeling lateral soil-pile response based on soil-pile interaction." *Journal of Geotechnical and Geoenvironmental Engineerin*g, Vol. 126, No. 5, 2000, pp. 420-7428.
90. Mokwa, R. L., and Duncan, J. M. "Laterally loaded pile group effects and p-y multipliers." *ASCE special publication No. 113*, Foundation and Ground Improvement, 2001, pp. 729-742.
91. King, G. J. "The interpretation of data from test on laterally loaded piles." *Proceedings of the International Conference*: Centrifuge 94, Singapore, pp. 485-490, 1994.
92. Wilson, D. "Soil-Pile-Superstructure interaction in liquefying sand and soft clay." Ph.D. Dissertation, University of California at Davis, 1998.
93. Nip, N, C, D., and Ng, W, W. C. "Back analysis of laterally bored piles." *Geotechnical Engineering*, Vol. 158, Issue GE2, 2005, pp. 63-73.
94. Yang, K., and Liang, R. "Methods for deriving p-y curves from instrumented lateral load tests." *Geotechnical Testing Journal*, Vol. 30, 2006, pp. 1-8.
95. Dunnavant, T.W. "Experimental and analytical investigation of the behavior of single piles in overconsolidated clay subjected to cyclic lateral loads." *Ph.D. Dissertation*, University of Houston, TX, 1986.

96. Janoyan, D.K., Stewart, P. J., and Wallace, W.J. “Analysis of p-y curves from lateral load test of large diameter drilled shaft in stiff clay.” *Porceeding, 6th Seismic Design Workshop*, Sacramneto, 2001.
97. Han, J.D., and Frost, J.D. “Load-Deflection Response of Transversely Isotropic Piles Under Lateral Loads.” *International Journal for Numerical and Analytical Methods in Geomechanics*, Vol. 24, No. 7, 2000, pp. 509-529.
98. Mezazigh, S. and Levacher, D. “Laterally loaded piles in Sand: slope effect on p-y reaction curves.” *Canadian Geotechnical Journal,* Vol. 35, No. 3, 1998, pp. 433-441

APPENDIX A

Methods of Analyzing Laterally Loaded Piles

Winkler Approach

The Winkler approach, also called the subgrade reaction theory, is illustrated in Figure 87. The pile-soil system is simplified as an elastic beam on discrete elastic springs. The coefficient of the springs represents the soil response which is termed as the coefficient of subgrade reaction (k).

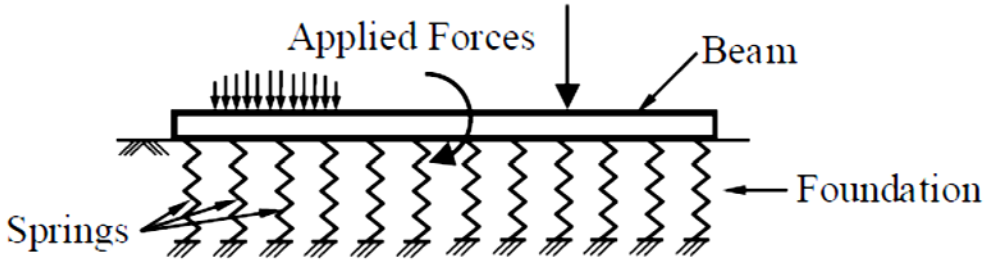

Figure 87
Winkler concept of a beam lying on elastic soil (after *[38]*)

As illustrated in Figure 87, the force induced on the spring is,

$$F = k \times y \tag{20}$$

where, F = force, k = spring stiffness coefficient, and y = spring displacement or ground displacement.

Terzagi related the spring coefficient to the modulus of subgrade reaction of a soil mass *[80]*. If P (F/L^2) is the pressure applied at the interface of soil and beam due to the applied load and y is the deflection then

$$P = k_h \times y \tag{21}$$

where, k_h = modulus of subgrade reaction = P/y (F/L^3), hence spring coefficient $k = k_h / y$

If P (F/L) is soil resistance force per unit length,

$$P = K_s \times y \tag{22}$$

where, K_s = subgrade modulus = $k_h z$, z = depth below the ground level.

Since the value of subgrade reaction (k_h) may represent the exponential function of the depth and pile deflection as illustrated in Figure 88, the subgrade modulus ($K_s = k_h z$) should be a non-linear function of depth z and the pile deflection y; i.e $K_s = f(z,y)$.

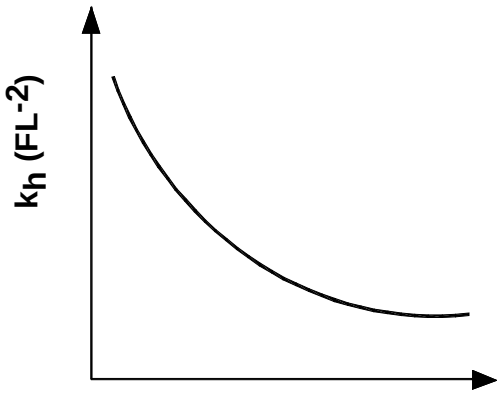

Figure 88
Exhibiting k_h as nonlinear function of *z* and *y* (after *[45]*)

Other researchers (e.g., *[83], [84], [85], [86])* applied the Winkler concept on laterally loaded piles by considering the pile as a beam against lateral (transverse) loading. Winkler's assumption was that the behavior of soil is elastic linear; however, there is complexity in the behavior of soil under the lateral load due to the non-linearity behavior of the soil.

p-y Curve Method

The p-y curve method is considered an improvement to the Winkler approach, where p is the soil resistance and y is the displacement of the soil. The soil springs have nonlinear response depicted by p-y curves. Several approaches have been made to develop or to derive the p-y curves from field load tests or laboratory tests. Matlock and Reese incorporated non-linearity behavior of soil in the model developed by modifying Winkler's approach, assuming pile as a flexible beam and the soil continuum as a set of independent non-linear springs *[81]*. The varying characteristics of these springs reflect the non-linearity behavior of soil. Several researchers suggested that the non-linearity behavior in the p-y curves can be represented by different mathematical functions such as power, exponential and hyperbolic. The suggested p-y curves is typically comprised of three segments: straight line, parabola, and straight line. The initial straight portion of the p-y curves represents the elastic behavior of soil and the slope is the constant of horizontal subgrade reaction, whereas the middle parts reflect the non-linear portion of the in-situ stress strain curve. Many studies were performed to predict the middle portion of a p-y curve; however, there is no widely accepted analytical procedure for the standard shape of the middle portion. The third segment is again a straight horizontal

line which represents the plastic behavior of soil. The typical p-y curve of a single pile is presented in the Figure 89.

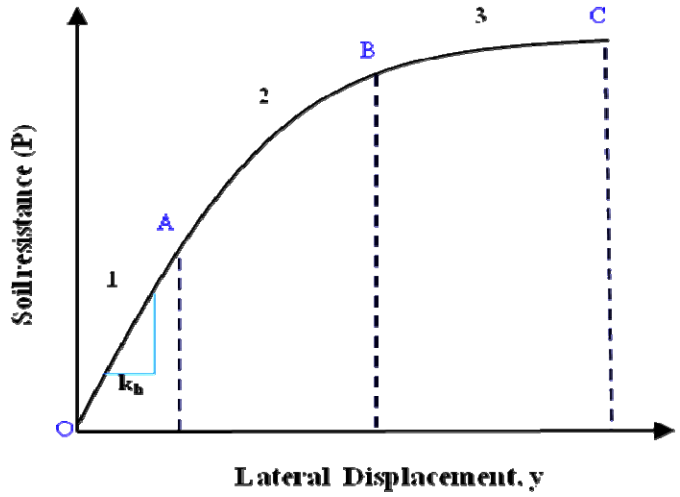

Figure 89
Typical p-y curve shape

Since p-y curves depend on the soil, and the soil through which pile is embedded is comprised of different layers with varying properties such as variation in classification, undrained shear strength, these varying properties of soil influence the shape of p-y curves. Many researchers including Matlock, Reese and Welch, Reese, and O'Neil developed p-y curves of different shapes for different soil conditions *[25]*, *[66]*, *[57]*, *[87]*.

P-y Curves for Soft Clay Soil. Matlock produced a p-y curve for soft clay for static loading, as shown in Figure 90, where the water level was above the ground surface *[25]*. The geotechnical parameters necessary for the development of the p-y curves are the undrained shear strength (S_u) and axial strain at 50% of failure load (ε_{50}). The initial slope of the p-y curves can be established by using k_h.

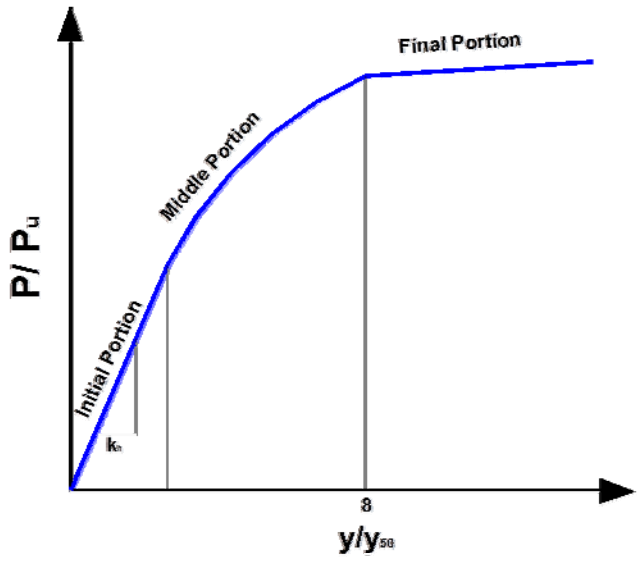

Figure 90
Characteristics shape of p-y curves for soft clay (after *[25]*)

The equation for the middle portion of curve is given by

$$\frac{P}{Pu} = (\frac{y}{y50})^{1/3} \quad (23)$$

where, P = lateral soil resistance per unit length, P_u = ultimate lateral soil resistance per unit length, y = lateral displacement, y_{50} = lateral displacement corresponding to one half of the ultimate lateral soil resistance.

The ultimate soil resistance per unit length of pile is computed using equations (24) and (25) and the smaller value is used for the p-y curve.

$$P_u = S_u * B(3 + \frac{\gamma'}{S_u} + {}^{j_e}/_{B} * z) \quad (24)$$

$$P_u = 9\, S_u B \quad (25)$$

where, γ'= average effective unit weight from ground surface to p-y curves, z = depth from ground surface to p-y curves, B = pile width or diameter of pile, j_e = experimentally derived unit parameter normally has a value between 0.25- 0.8.

According to Matlock, the value of J_e is 0.5 for soft clay and about 0.25 for medium clay *[25]*. The value of 0.5 is frequently used for J_e. The value of P_u is computed at each depth where a p-y curve is desired based on the undrained shear strength at that depth.

The lateral displacement y_{50} corresponding to one half of the ultimate soil resistance is computed as $y_{50} = 2.5\, B\varepsilon_{50}$, where the value of ε_{50} can be obtained from the stress-strain

curve or taken from Table 7 in the absence of a stress strain curve. Then p-y curves can be developed using equation (24) or equation (25) and the value of P remains constant beyond $y/y_{50} = 8$ as shown in the Figure 90.

Table 7

Matlock (1970) recommended values of ε50 based on the consistency of clay *[25]*

Consitency of Clay	Undraiend shear strength(kPa)	ε_{50}
Very soft	<12	0.02
Soft	12-24	0.02
Medium	24-48	0.01
Stiff	48-96	0.006
Very stiff	96-192	0.005
Hard	>192	0.004

P-y Curves for Stiff Clay. Reese et al. generated a p-y curve by conducting lateral load tests on overconsolidated stiff clay as described in Figure 91 *[66]*. The initial straight portion of the line is evaluated from the equation P = (kh z)y, where the value of kh is proportional to the undraiend shear strength. The reasonable suggestion is made that the initial slope of the p-y curves be established using k_h from Table 8.

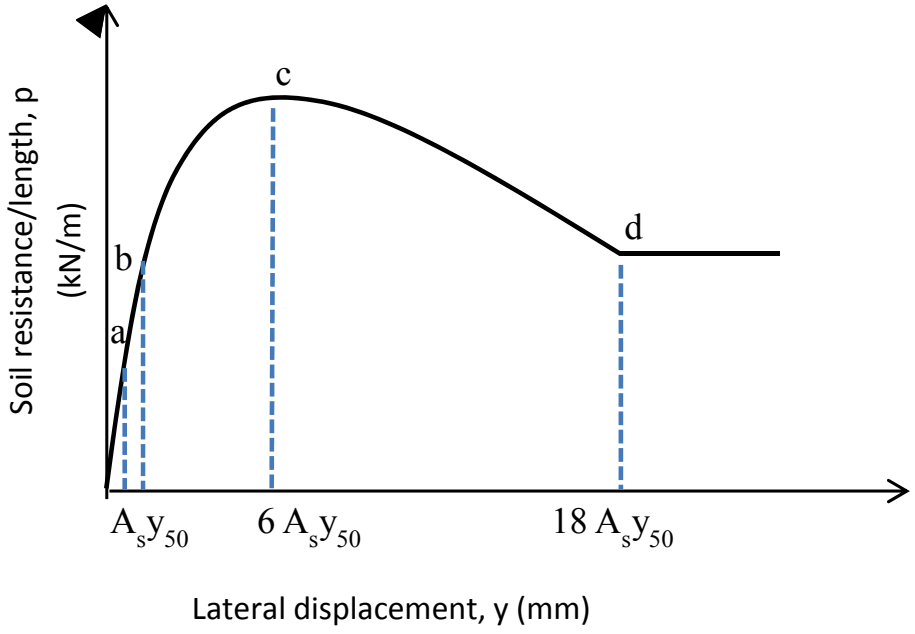

Figure 91

Characteristics shape of P-y curves for stiff clay (after *[74]*)

Table 8
Value of k_h corresponding to the undrained shear strength

Undrained Shear Strength (kPa)	50-100	200-300	300-400
k_h (MN/m^3)	135	270	540

The ultimate soil resistance per unit length (P_u) is computed according to the following equations and the lesser value is used in developing the p-y curves.

$$P_u = 2S_u B + \gamma B z + 2.83 S_u z \quad (26)$$

$$P_u = 11 S_u B \quad (27)$$

The value of y_{50} is computed from $y_{50} = \varepsilon_{50} B$ and the first parabolic portion (a-b) can be obtained according to the following equation.

$$P = 0.5 P_u (\frac{y}{y_{50}})^{0.5} \quad (28)$$

Similarly, the second parabolic portion (b-c) is given as:

$$P = 0.5 P_u (\frac{y}{y_{50}})^{0.5} - 0.0055 P_u (\frac{y}{y_{50}})^{0.25} \quad (29)$$

The third inclined straight line is obtained from the following equation:

$$P = 0.5 P_c (6A_s)^{0.5} - 0.411 P_c - P_c (\frac{0.0625y}{y_{50}})(y - 6A_s y_{50}) \quad (30)$$

The final straight line is developed by the following equation

$$P = p_u (1.225 A_s^{0.5} - 0.75 A_s - 0.411) \quad (31)$$

where, S_u = average undrained shear strength over depth, A_s = area correction factor given in Figure 92.

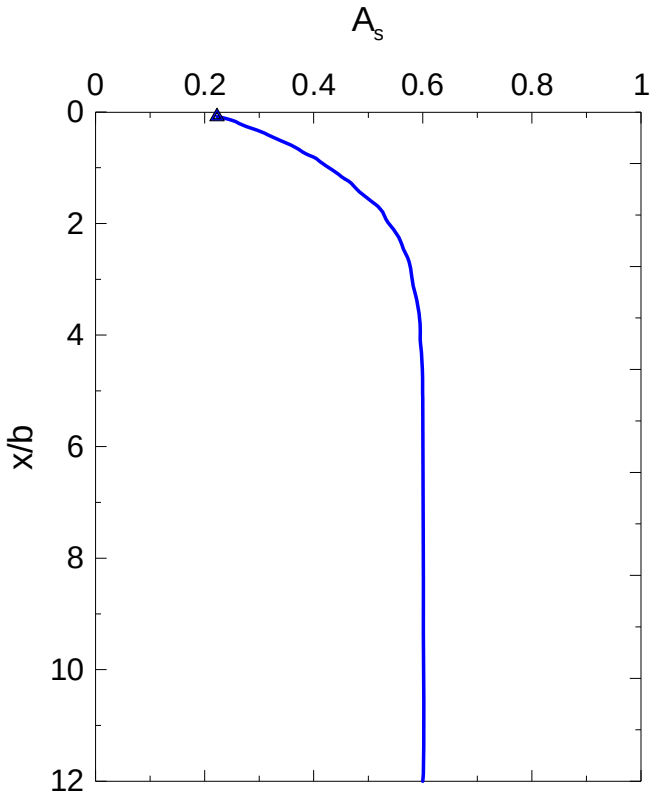

Figure 92
Parameter values (after *[74]*)

P-y Curves for Sand. a) Reese Model. The ultimate resistance per unit length (P_u) is computed from equations (32) and (33) and the lesser value is used in developing the p-y curves as shown in Figure 93 *[74]*.

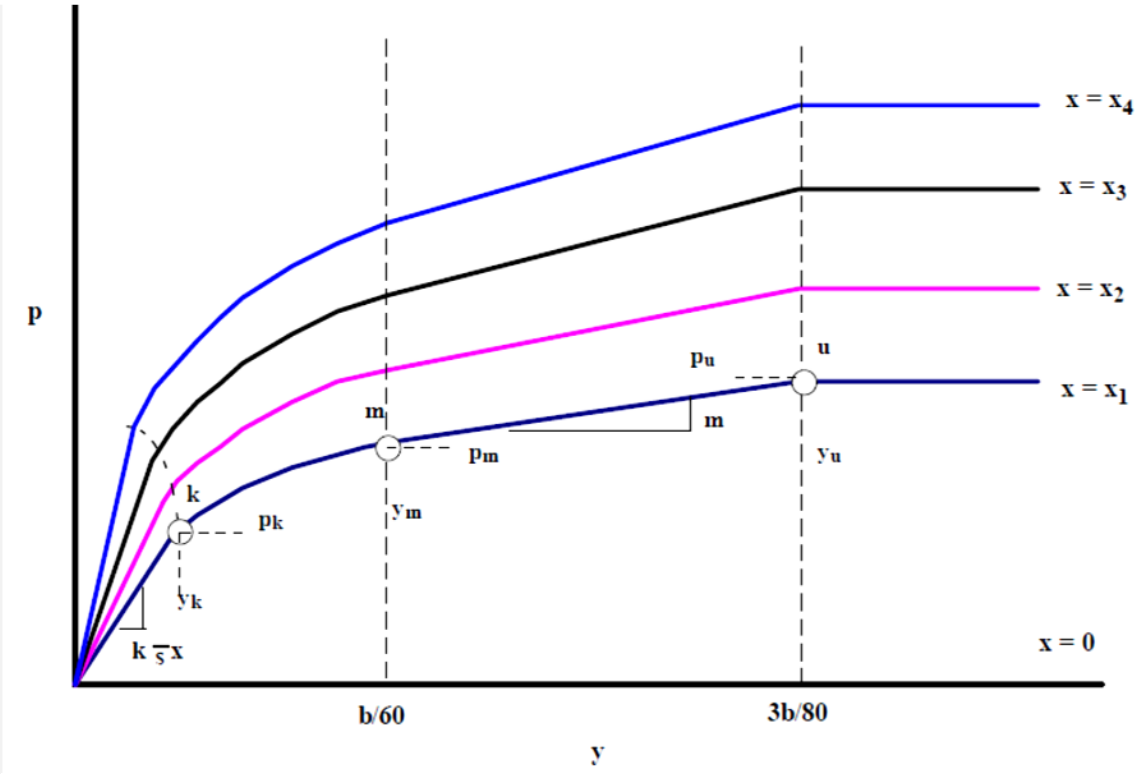

Figure 93
P-y curves for sand (after *[74]*)

$$P_u = \gamma\, z[\frac{K_o.tan\phi.tan\beta}{\tan(\beta-\phi).\cos\left(\frac{\phi}{2}\right)} + \frac{tan\beta}{\tan(\beta-\phi)} * \left(B + z\, tan\beta \tan\left(\frac{\phi}{2}\right)\right) + K_o\, z\, tan\beta \left(tan\phi sin\beta - \tan\left(\frac{\phi}{2}\right)\right) - K_a B] \quad (32)$$

or

$$P_u = K_a B\, \gamma\, z[\tan\beta^8 - 1) + K_o B\, \gamma\, z\, tan\phi.tan\beta^4 \quad (33)$$

where, K_a = Rankine active earth pressure coefficient=(1-sinϕ)/(1+sinϕ), K_o = Rankine coefficient of earth pressure at rest=1-sinϕ, ϕ =angle of internal friction, β=ground surface slope angle =45^0+ϕ/2, B=Pile width or diameter.

The ultimate resistance is modified with a constant A's, $P = P_{ut}\, A'_s$, where the area correction factor A'_s can be estimated from Figure 94 (a). Then using $P_m = B_s\, P_u$ to calculate the value of P_m in Figure 93, where the value B_s is obtained Figure 94 (b). The parabolic section (k-m) of the curve can be obtained from $C'y^{1/n}$, where the value of n can be found from $n = \frac{P_m}{my_m}$ and the value $C' = \frac{P_m}{y_m^{1/n}}$. The slope of linear line between u and m section is

$m = \frac{P_u - P_m}{y_u - y_m}$. The initial straight line is P = (k_hz)y, where k_h is proportional to the relative density of sand and can be obtained from Table 9. The point y_k is calculated as $y_k = \frac{C\prime}{K_{py}z}$.

Table 9
The value of k_h (MN/m^3)

Relative Density	Loose	Normal	Dense
Unsubmerged	6.8	24.4	61
Submerged	5.4	16.3	34

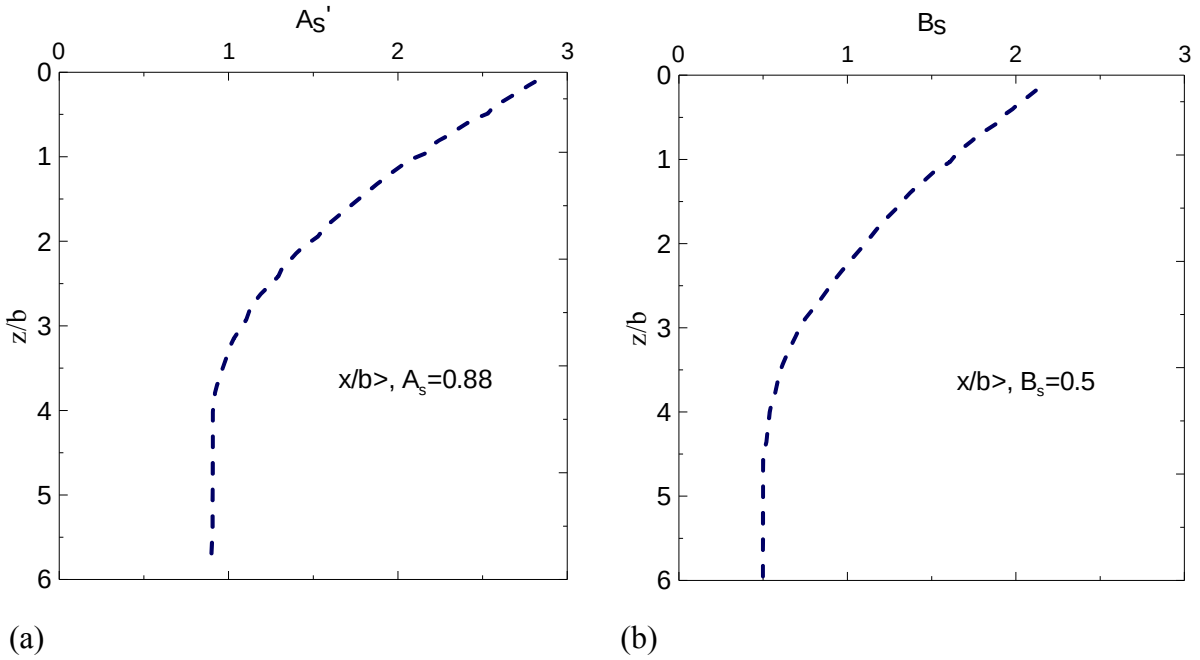

(a) (b)

Figure 94
Value of parameter (a) value of A_s'; (b) value of B_s (after *[74]*)

(b) O'Neil Model. In O'Neil, the ultimate soil resistance P_u is determined as the lesser value of equations (34) and (35) *[87]*.

$$P_u = \gamma z[D((K_p - K_a) + zK_p tan\phi\ tan\beta) \quad (34)$$

$$P_u = \gamma Dz(K_p^3 + 2K_oK_p^2 tan\phi + tan\phi - K_a) \quad (35)$$

where, K_p= Ranking passive earth pressure coefficient: $(^1/_{K_a})$

The soil resistance per unit length (P) is calculated using equation (36). The p-y curve shape obtained from this equation is presented in Figure 96 and the comparison of O'Neil and Reese p-y curve is shown in Figure 97.

$$P = \eta\, A\, P_u tanh[\left(\frac{k_h z}{A\, \eta\, P_u}\right) y] \tag{36}$$

where, η = a factor used to describe pile shape generally taken as 1.0 for circular piles; A = 0.9 for cyclic loading, and 3-0.8z/D≥0.9 for static loading.

The value of ϕ is obtained from the SPT as shown in Figure 95 (a) and the value of the k_h is obtained from the ϕ as shown in Figure 95 (b).

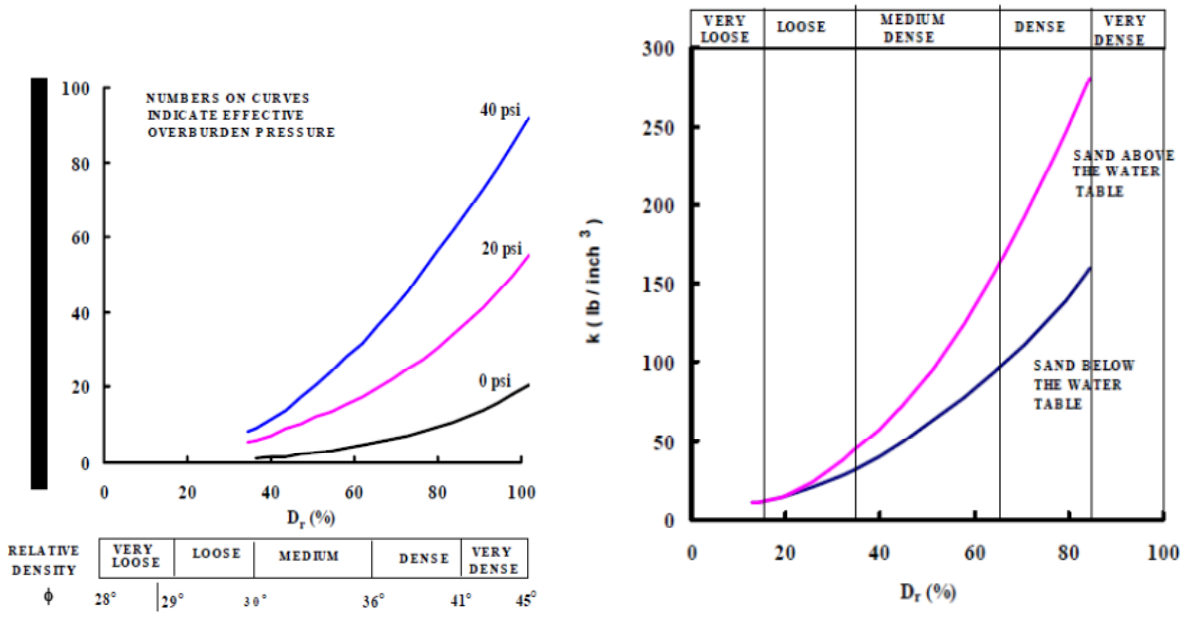

(a) (b)

Figure 95

(a) SPT blow count versus ϕ and relative density, D_r; (b) kh versus D_r

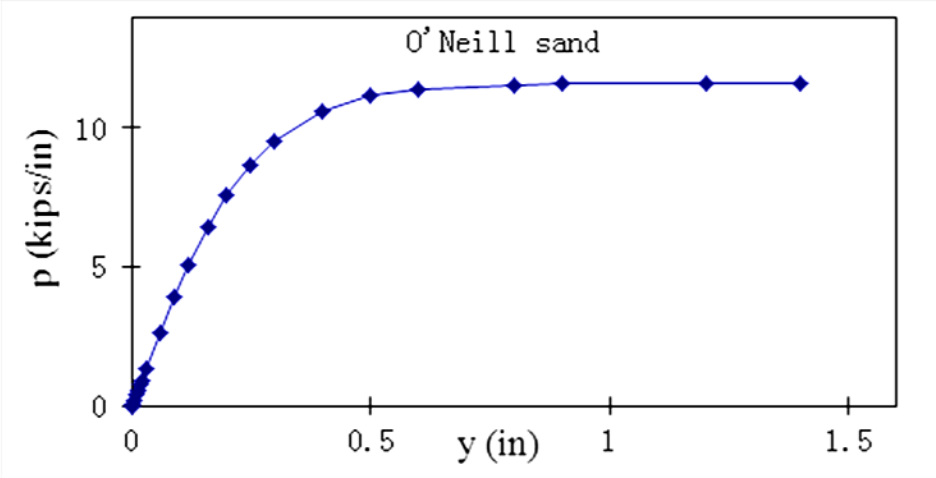

Figure 96
P-y curve according to O'Neill Method (after *[87]*)

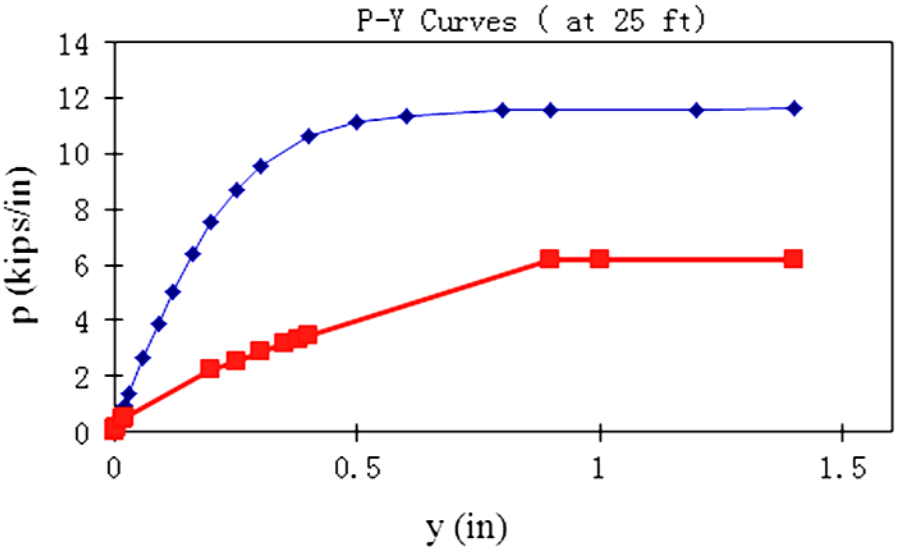

Figure 97
Comparison chart of p-y curves of Reese and O'Neill Methods

P-y Curves for Pile Groups. The application of the lateral load causes piles to move in the loading direction. For the pile group, the soil in front of the leading row resists the lateral movement of pile, whereas the piles in the trailing rows push the soil which in turn pushed on the piles in front of them, eventually reducing the lateral resistive force for trailing rows *[42]*, *[45]*, *[88]*. The soil-pile-soil or group interaction effect reduces with the increasing of center-to-center spacing between the piles.

Brown et al. introduced the concept of p-multipliers, and the value of p-multipliers represents the intensity of group interaction *[23]*. The p-y curves for group piles are developed by

multiplying the p-multiplier value to p-y curves of single pile as shown in Figure 98. Similarly, Ruesta and Townsend evaluated the behavior of laterally loaded pile groups at Roosevelt Bridge and observed similar value of p-multipliers suggested by Brown for prestressed pile in both free and fixed head conditions in the soil profile consisted of loose sand (Figure 99) *[26, 27]*. McVay et al. found that p- multipliers are independent of soil densities and only a function of the pile group geometry *[31]*. However, Ashour and Norris, assumed that the mobilization of p-multipliers appears to be a function of soil types, soil densities, pile spacing, pile location with respect to loading direction, and pile head connections *[89]*. Mokwa recommended that the piles in a group be modeled as an equivalent single pile with a flexural stiffness equal to the number of piles in the group multiplied by the flexural stiffness of a single pile within the group *[90]*. The summary of p-multiplier observed form the several researchers in literature are presented in Table 10.

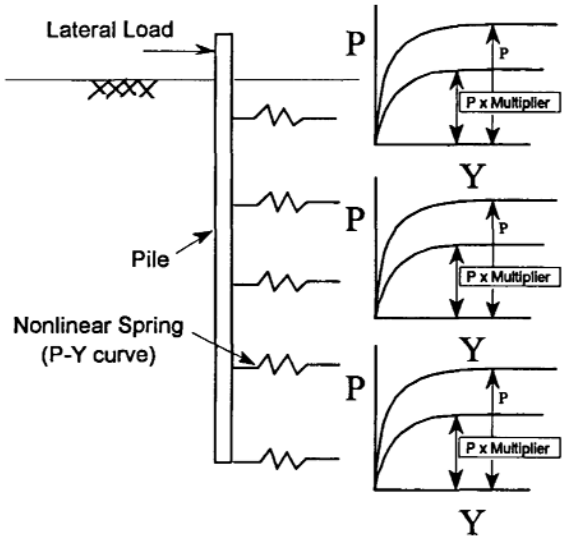

Figure 98
P-Y curves of piles in group pile using p-multiplier approach *[23]*

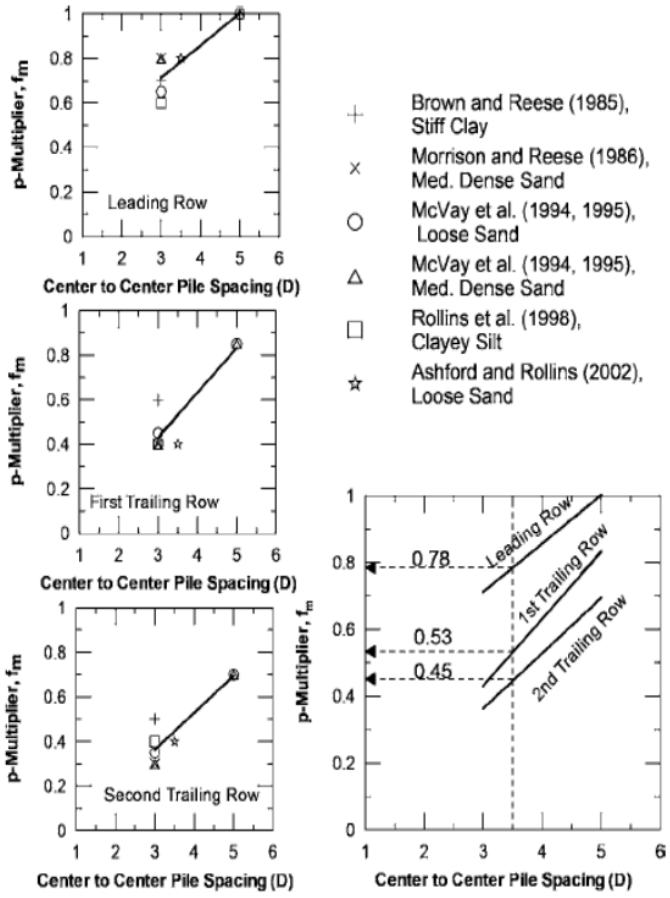

Figure 99

Relationship between the p-multiplier and the pile spacing for each row in the group *[90]*

Table 10
Literature values of p-multipliers

Reference	Test type	Pile			Values of p-multiplier						
		pattern	spacing	head fixity	Row1	Row 2	Row 3	Row 4	Row 5	Row 6	Row 7
Brown et al. *[27]*	Full scale	3x3	3D	Pinned	0.8	0.4	0.3				
Brown et al. *[23]*	Full scale		3D	Pinned	0.7	0.5-0.6	0.4-0.5				
McVay et al. *[35]*	Centrifuge	3x3	3D	Pinned	0.8	0.4	0.3				
	Centrifuge	3x3	3D	Pinned	0.65	0.45	0.35				
	Centrifuge	3x3	5D	Pinned	1	0.85	0.7				
Ruesta and Townsend *[26]*	Full scale	4x4	3D	Fixed	0.8	0.7	0.3	0.3			
McVay et al. *[31]*	Centrifuge	3x3	3D		0.8	0.4	0.3				
	Centrifuge	3x4	3D		0.8	0.40	0.3	0.3			
	Centrifuge	3x5	3D		0.8	0.40	0.3	0.2	0.3		
	Centrifuge	3x6	3D		0.8	0.40	0.3	0.2	0.2	0.3	
	Centrifuge	3x7	3D		0.8	0.40	0.3	0.2	0.2	0.2	0.3
Rollines et al. *[24]*	Full scale		3D	Pinned	0.6	0.4	0.4				
Rollines et al. *[29]*			2.8D		0.6	0.38	0.43				
			5.65D	-	0.98	0.95	0.88				
Rollines et al. *[30]*		3x3	3D		0.82	0.61	0.45				
		3x5	3.3		0.82	0.61	0.45	0.45	0.46		
		3x4	4.3		0.90	0.81	0.69	0.73			
		3x3	5.6		0.94	0.88	0.77				

APPENDIX B

Methods for Deriving p-y Curves

High Order Global Polynomial Curve Fitting Method

Broms assumed that the reaction profile could be described by a polynomial, which is generally true for long piles *[84], [85]*. King stated that fitting simple polynomials to the discrete data points and differentiating the polynomials might not be realstic and smooth, hence a high order polynomial becomes essential *[91]*. Many researchers have interpolated discrete measurements of moment or curvature of a pile and double differntiated their interpolating fucntions to calculate the lateral resistances along the pile *[67]*, *[71]*. Ruesta et al. used a third order polynomial to fit bending moment profiles *[27]*. Wilson applied three methods: cubic splines, polynomial functions, and finite element techniques to fit the data obtained from the strain gauges *[92]*. In polynomial technique, Wilson fitted 5^{th} and 6^{th} order polynomial equations to the discrete bending moment data using the least square method *[92]*.

$$M = a + bz + cz^2 + dz^3 + ez^4 + fz^5 \quad (37a)$$

$$M = a + bz + dz^3 + ez^4 + fz^5 \quad (37b)$$

$$M = a + bz + cz^{2.5} + dz^3 + ez^4 + fz^5 \quad (37c)$$

Equation (37a) has five lowest order integer terms used to fit seven recorded moment points along the pile, whereas equation (37b) includes five fitting terms but assumes the lateral resistance is zero at the surface of the soil, leaving out the quadratic term. Equation (37c) contains non-integer fitting terms by assuming zero lateral resistance at ground surface. Furthermore, Wilson used these equations and concluded that equation (37b) is clearly inconsistent with the other methods, whereas equation (37a) is the most reasonable approximation *[92]*. Similarly, Llyas et al. analyzed the bending moment profile using a 7^{th} order polynomial curve fitting method *[37]*.

All polynomial equations are used for the discrete moment data obtained directly from the strain gauge measurements using $\mathrm{M} = \mathrm{EI}\frac{\mathrm{d}^2\mathrm{y}}{\mathrm{dz}^2}$. The moment from strain gauge data can be easily calculated from strain gauge measurements, whereby neither integration nor differentiation is necessary. However, data obtained from the inclinometer needs to be integrated and differentiated to deduce deflection and bending moment profiles. Nip et al. introduced a 4^{th} order polynomial to interpret inclinometer data in which non-liner flexural concrete behavior is also considered *[93]*. The fourth order polynomial was chosen on the

basis of three known boundary conditions and one reasonably assumed boundary condition at the pile head. By introducing the 4th order polynomial, Nip et al. calculated the shape of a soil reaction profile and by back-analysis the p-y curves were generated *[93]*. The 4th order polynomial function for the soil reaction (P_z) is given as:

$$P = az^4 + bz^3 + cz^2 + dz \tag{38}$$

$$V = \frac{az^5}{5} + \frac{bz^4}{4} + \frac{cz^3}{3} + \frac{dz^2}{2} + F_0 \tag{39}$$

$$M = \frac{az^6}{30} + \frac{bz^5}{20} + \frac{cz^4}{12} + \frac{dz^3}{6} + F_0 z + M_0 \tag{40}$$

$$\theta = \sum_{z_{i=z_0}}^{z} \left(\frac{az^6}{30} + \frac{bz^5}{20} + \frac{cz^4}{12} + \frac{dz^3}{6} + F_0 z + M_0\right) * dz/EI \tag{41}$$

At the pile head rotation, the shear force (V_o) is known and bending moment (M_o) is calculated by multiplying the measured lateral force with the eccentricity of the force above the pile head for a free head pile. It is also assumed that the bending moment, shear force, and soil reaction are assumed to become zero at the same particular depth z_o, to provide the three necessary constraints. In the pile load test, z_o lies approximately between 1.5 to 3.5 m, which equal to 1-2 times the pile diameter below the depth of zero rotation. By assuming zero depth, the coefficient values a, b, c, and d can be easily calculated from Equation 2.28 and then the moment, and hence the rotation value, is also analyzed. This technique allows the evaluation of the coefficient of the horizontal subgrade reaction (k) and p-y curves. This method assumes a shape of soil reaction profile instead of a shape of p-y curves. Since the shape of p-y curves in complex soils, such as silty soil or clayey soil with sand lenses, are difficult to obtain, this method appeared good for such soils.

Piecewise Cubic Polynomial Function

Yang et al. evaluated four methods: global fifth-order polynomial curve fitting, piecewise cubic polynomial curve fitting, weighted residuals, and smoothed weighted residuals method, and recommended the use of the piecewise cubic polynomial curve fitting method (See Figure 100) for deriving p-y curves from instrumented lateral load tests and recommended the piece wise cubic polynomial curve fitting method for deriving p-y curves *[94]*. Matlock and Ripperger and Dunnavant employed a similar method of moment discrete data *[67]*, *[95]*. In this method, every five successive moment data points along the pile length are fitted to one cubic polynomial curve. This method requires at least five points of strain gages deployed at five different depths along the shaft. The double differentiation of the local fitted polynomial curve with respect to middle point yields p at that point.

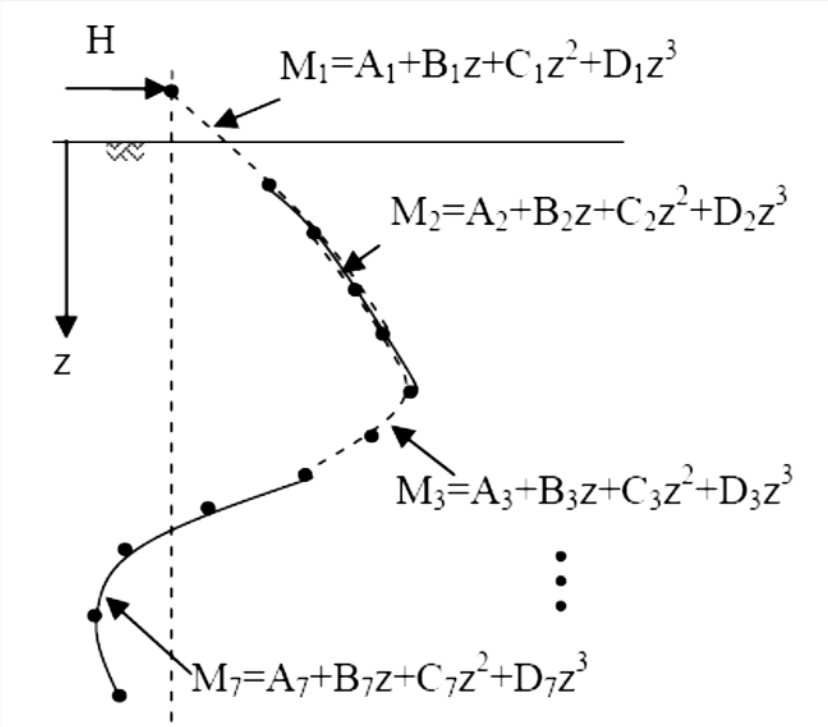

Figure 100
Procedure for reducing moment data to *p* using piecewise polynomial

Weighted Residual Method

Wilson developed this finite element approximation method based on minimizing weighted residuals to deduce soil resistance from strain gauges *[92]*. The residual function R(x) is considered zero in average as shown in equation (42).

$$\int_0^L R(x)\Psi(x)dx = 0 \qquad (42)$$

Where, Ψ(x) is an arbitrary weighting function.

The pile is assumed as, discretized finite elements with nodes at each bending moment gauge location. Wilson invoked this weighted residual method in his dissertation and compared it with the polynomial method and cubic spline method. He found that the weighted residual method appeared to be the most reliable one *[92]*. Janoyan et al. examined cubic spline method, polynomial, and weighted residual method for fitting smooth curves through profile data and concludes that the weighted residual method provides the most satisfactory results *[96]*.

Brown Method

Brown proposed an FEM based method to derive the p-y curves from simple inclinometer data using the least squares regression technique *[69]*. The p-y curves are assumed following specified functions containing unknown coefficients which are the subject of the fitting process. The unknown coefficients are related to soil strength and stiffness parameters, undrained shear strength (S_u) and strain corresponding to half ultimate stress (ε_{50}) for clays, angle of internal frictional (ϕ) and subgrade modulus (K_s) for sands. Other parameters could be used as the unknown fitted variables. The lateral deflection (y) was computed from the soil parameters, using the COM624 program by solving a set of nonlinear equations. Also, the deflections are known from the test. Then the value of the soil parameters is estimated by using the least squares "inversion" technique similar to that used for interpreting geophysical data. Brown successfully used this technique and concluded that this method is a rigorous and reliable method of interpreting a lateral load test on piles or drilled shafts using inclinometer data *[69]*.

Energy Method

The energy conservation concept has been used by some researchers to derive the deflection function from the inclinometer data of laterally loaded piles *[70]*, *[97]*. The total energy for a pile embedded in the soil is the sum of strain energy (U) and work (V). The strain energy is a function of the deflection, and the potential energy depends upon the soil pressure and the applied lateral load. Liao and Lin expressed the total energy as equation 43 and generated the deflection function as per the Rayleigh-Ritz method *[70]*. Han and Frost derived an equation for the total energy considering the shearing deformation effect using Timoshenko Beam theory solutions for load-deflection responses *[97]*.

$$TE = 1/2 \int_0^L EI(y")^2 dz + 1/2 \int_0^L P(z) y dz - Hy(L) \quad (43)$$

Where,

L = embedded length of pile

H = lateral forces applied at the pile head

Liao and Lin verified this method by analyzing the data from a full-scale lateral load test conducted by Washington DOT and a lateral load test on H piles *[70]*. The authors claimed that this method delivered a reasonable prediction of pile performance in both single piles and pile groups in comparison to the Brown method. A simple spreadsheet is required for the iteration, whereas the Brown method requires the COM624 program *[69]*.

Cubic Spline Method

Mezaziagh and Levacher employed the cubic spline method to fit the discrete moment data points *[98]*. It is considered as the simplest interpolation of discrete test data that can be double differentiated. However, it is more prone to any potential measurement error. Dou and Byrne used cubic splines to derive p-y relationships from dynamic hydraulic gradient model tests with good results *[71]*.

Elastic Superposition Method

Yamin and Liang (2009) proposed an analytical solution based on the classic theory of elastic superposition of the laterally loaded drilled shafts undergoing elastic deformations *[72]*. The shaft deflections were available through inclinometer measurements. Using the available deflection measurements, the proposed method can provide the soil resistance profile along the drilled shafts by solving the linear algebra equation (44).

$$[Y] = [f][R] \tag{44}$$

Where, [Y] is a vector of measured shaft deflection at variant depth along drilled shaft at a certain load level, [f] is the flexibility matrix, and [R] is the vector of assumed net applied load (both external load and soil reaction) on drilled shaft at the location where has deflection measurements. Applying equation (44) to the measured deflection profile at different load level, the soil resistance profile can be obtained and thus p-y curves at the chosen depth can be determined.

This method has the merits of being simple and computation efficient which does not require complicated finite element modeling yet provides accurate solutions. Yamin and Liang verified this method with cases created using the LPILE program and also several engineering cases in Ohio *[72], [23]*. However, more case studies are needed to verify the capability of this method for more complicated engineering case scenarios.